THESE de DOCTORAT de l'ECOLE POLYTECHNIQUE

présentée par

Johannes QUAAS

L'effet indirect des aérosols: Paramétrisation dans des modèles de grande échelle et évaluation avec des données satellitales.

The aerosol indirect effect: Parameterization in large-scale models and evaluation with satellite data.

Soutenue le 17 novembre 2003, devant le jury composé de :

M. Olivier BOUCHER	Co-Directeur de thèse
M. Jean-Louis BRENGUIER	Membre invité
M. Yves FOUQUART	Rapporteur, Président du jury
M. Hervé LE TREUT	Directeur de thèse
Mme Ulrike LOHMANN	Rapporteur
M. Serge PLANTON	Examinateur
M. Michael SCHULZ	Examinateur

LMD
Laboratoire de Météorologie Dynamique

Sciences de l'environnement
Institut Pierre Simon Laplace
Institut Pierre Simon Laplace

Ecole POLYTECHNIQUE
École Polytechnique

Contents

Part I.

Introduction

1. Introduction

1.1. The climate system and climate change

Global climate change is considered to be one of the most serious concerns of humankind (*United Nations*, 1992; *United Nations*, 2002). Anthropogenic greenhouse gases and aerosols impact considerably the energy balance of the Earth system, possibly provoking adverse effects on social, ecological, and economical equilibria. This is one of the main reasons why the understanding of the Earth's climate system is of major importance. If better predictions of the response of the climate system to anthropogenic perturbations were available, political decisions against negative impacts could be taken, and social adaptations to changed climate conditions would be possible.

The main scientific tools to understand the climate system and to simulate climate change on a global scale are Earth System Models (ESMs). An ESM is composed of several parts, each of which describes a component of the climate system, as atmosphere, ocean, continental surfaces, biosphere, sea ice, or cryosphere, to mention the most important ones. In the present work, we focus on the atmospheric part of the climate system, which is represented by a general circulation model (GCM) of the atmosphere. Numerically solving the basic equations that describe the circulation, and incorporating diabatic physical processes by parameterizations, GCMs of the atmosphere are able to simulate a multitude of atmospheric processes. However, due to limited computer power and limited understanding of processes, simulations remain unrealistic in many aspects. Techniques to improve the computational efficiency in climate modeling (e.g., *Quaas*, 2000), and improved computer hardware may help to increase resolution and complexity of the models. The present work is meant to contribute to the improvement of the understanding of the physical processes focusing on the aerosol indirect effects.

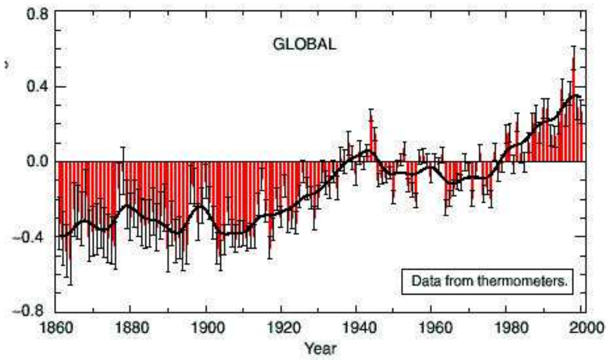

Figure 1.1.: Evolution of the global mean surface temperature, shown as the deviation from the 1960 to 1990 average from (from *Folland et al.*, 2001).

1.2. Anthropogenic impacts on climate

Two main perturbations of the atmosphere composition are provoked by humankind. The first and most important one is the increase in tropospheric "greenhouse gases" (GHG). Gases that absorb terrestrial longwave (LW) radiation in the atmosphere re-emit the energy at lower temperatures. This causes the so-called "greenhouse effect" (GHE), which results in a warming of the Earth's surface to keep the energy budget in balance. The main anthropogenic contribution to the concentration of greenhouse gases in the atmosphere stems from carbon dioxide (CO_2), which originates from the combustion of fossil fuel and burning of biomass. Other anthropogenic greenhouse gases are methane (CH_4), nitrous oxide (N_2O), chlorofluorocarbons (CFC), and tropospheric ozone (O_3). All of these have increased since the beginning of the industrialization in about 1750 (Fig. 6.1; *Myhre et al.*, 2001). In agreement with the expected warming due to the anthropogenic greenhouse effect, an increase in global mean surface temperature has been observed (Fig. 1.1; *Folland et al.*, 2001).

However, the observed temperature increase of 0.6 K for the period 1900 to 2000 is somewhat smaller than the warming expected due to the greenhouse effect (*Mitchell et al.*, 2001). This may be explained by important internal variability or the existence of another forcing of climate change. A negative forcing due to anthropogenic aerosols could be responsible for an offset of part of the warming GHE (*Wigley*, 1989; *Charlson et al.*, 1989; *Boucher and Anderson*, 1995). Since about two decades, the impact of anthropogenic aerosols has been studied. However, in the latest Intergovernmental Panel on Climate Change (IPCC) report, the level of scientific understanding of the impact of aerosols on the radiation balance has still been assessed as “low” or even “very low”. Nevertheless, it is commonly accepted that anthropogenic aerosols may have an impact strong enough to offset the warming by anthropogenic greenhouse gases at least to a significant fraction. The impact of aerosols on radiation is twofold. Firstly, a “direct” radiative effect exists, as aerosols scatter and absorb sunlight, thus generally enhancing the planetary albedo. Secondly, aerosols may act as cloud condensation nuclei thus changing cloud properties. These so-called “aerosol indirect effects” will be defined in Section 1.7. Besides these direct and indirect effects, absorbing aerosols may also cause a “semi-direct effect”. When radiation is absorbed by aerosols in the atmosphere, the surrounding air is heated and then evaporates clouds or hinders their formation. As a result it occurs a decrease in cloud water content or in cloudiness decreases the albedo, which generally causes a warming. This process has been modeled for conditions observed during the INDOEX experiment (*Ackerman et al.*, 2000a). Recent studies reveal that aerosols in large quantities, like dust, also have a non-negligible effect in the longwave spectrum (*Dufresne et al.*, 2002).

1.3. The role of clouds in the climate system

From a meteorological point of view, water is the most important tracer element of the atmosphere, in which water exists in all three thermodynamic states. The atmospheric source of water is evaporation over land and ocean surfaces. Water vapor is distributed throughout the troposphere and interacts with the energy balance. In the process of evaporation and condensation, latent heat is transported from the surface to the atmosphere. As a gas absorbing in the LW spectrum, water vapor causes an important greenhouse effect.

Water vapor eventually condensates to the liquid or solid phase thus forming clouds. In the Earth’s atmosphere, clouds exist at all layers of the troposphere, up to about 11 km. At temperatures above 0°C, they consist of liquid water, below about –35°C to –40°C, purely of ice, and in between, mixed-phase clouds are observed (*Houze*, 1993). On the global scale, the area cloud cover is about 60%. When water vapor condenses to form clouds, latent heat is released, and the respective layer of the atmosphere is thus heated. When cloud water re-evaporates, latent heat is uptaken from the environment. Clouds also interact with radiation. In the solar spectrum, clouds reflect sunlight. As the cloud albedo generally is larger than the albedo of the underlying surface, the occurrence of clouds enhances the planetary albedo. In the terrestrial spectrum, clouds absorb radiation and cause a greenhouse effect. These so-called “cloud radiative forcings” (CRF) in the SW and LW spectra are of opposite sign (*Kandel et al.*, 1998). The net effect is positive for high-level clouds and negative for low-level clouds. On a global scale, clouds have a net negative radiative forcing (*Kiehl and Trenberth*, 1997).

Precipitation is formed through cloud microphysical processes. Thus, clouds are at the origin of one of the socially, ecologically, and economically most important meteorological quantities. While condensation from water vapor is the source for cloud water, precipitation formation constitutes its final sink. The rain-forming processes thus influence the lifetime and water content of clouds.

1.4. Representation of cloud processes in large-scale models

In contrast to atmospheric motion, the condensation and cloud forming processes cannot be described by a fundamental equation in a GCM. They need to be represented as a function of the variables explicitly calculated in the model, a method known as parameterization. Among the first schemes applied in GCMs which parameterized clouds rather than simply imposing to the model an observed distribution was the one of *Sundqvist* (1978). He calculated cloud water as a prognostic variable in his model, and introduced a fractional cloudiness. While some GCM cloud schemes use a binary cloud fraction of zero or unity (e.g., *Fowler et al.* (1996)), most others use a similar approach to define in a grid box an entirely cloudy and a cloud-free fraction (e.g., *Slingo*, 1987; *Del Genio et al.*, 1996). However, in the vertical, at the exception of the schemes of *Del Genio et al.* (1996) and *Jakob and Klein* (1999), a cloud is considered to fill the model layer completely.

The fractional cloudiness is often calculated from the grid box mean relative humidity (RH) using a "critical value". For example, *Lohmann and Roeckner* (1996) use a vertically varying critical relative humidity which decreases from $\mathrm{RH}_{\mathrm{crit}}$=99% near the surface to $\mathrm{RH}_{\mathrm{crit}}$=60% in the free troposphere. Other schemes use a probability density function (PDF) of the total water mixing ratio in each grid box to define the saturated fraction of the grid cell (*Sommeria and Deardorff*, 1977). The form of the PDF can be considered for example of uniform (*Le Treut and Li*, 1991) or triangular (*Smith*, 1990) shape. However, schemes using such fixed PDFs do not differ substantially from parameterizations using a critical RH. As a first attempt to introduce a subgrid scale distribution of cloudiness based on physical processes, *Tompkins* (2002) defines a PDF of the total water mixing ratio using a Beta function. The scheme uses skewness and variance of the PDF as prognostic model variables, which are parameterized in terms of convection, turbulence, wind shear, and cloud microphysics.

The clouds defined in the cloudy fraction of a grid cell are generally considered homogeneous. This is called the assumption of plane parallel homogeneous (PPH) clouds. In several studies, it has already been shown that this assumption introduces large biases on the radiation transfer (e.g., *Pincus and Klein*, 2000; *Calahan*, 1994; *Carlin et al.*, 2002; *Stubenrauch et al.*, 1997), as well as on the precipitation formation (*Jakob and Klein*, 1999; *Wood et al.*, 2002)). Recent studies try also to deal with a possible introduction of statistical distributions in the vertical direction (*Di Giuseppe*, 2003). However, the treatment of the subgrid-scale variability is to a large extent beyond the scope of the present study and will be addressed in future work.

In the vertical, clouds are generally assumed to overlap either independently between each two layers (random overlap assumption), to overlap to the maximum possible extent (maximum overlap assumption), or to overlap in a maximum way in adjacent layers and randomly otherwise (maximum-random overlap assumption). Recently, *Hogan and Illingworth* (2000) derived from radar observations a parameterization based on the random-maximum assumption, but including an additional parameter taking into account the vertical separation of two cloudy layers. The knowledge of the overlap of clouds in different layers is necessary at least for the radiation transfer and may be used as well in the microphysics (see Chapter 9).

Most GCMs distinguish between convective and stratiform cloudiness. In a scheme parameterizing the deep convection, precipitation stemming from the convective events is diagnosed. A convective cloud cover may be derived using this quantity (*Trenberth*, 1995), while the so-called "stratiform" cloud cover is calculated using the different schemes described above. It is in this stratiform cloud parameterization that the cloud and precipitation microphysics is generally treated as well. Recent studies try to overcome the separation of stratiform and convective schemes (*Bony and Emanuel*, 2001).

1.5. The role of cloud microphysics

All those processes which act on the scale of individual cloud particles are known as "cloud microphysics". They include the formation of cloud droplets and ice crystals by the activation of hygroscopic aerosol particles, their growth by condensation deposition, and the processes which lead to precipitation formation and growth of precipitation particles.

Microphysical processes for warm (liquid water) and cold (ice) clouds may be distinguished.

1.5.1. Processes in liquid water clouds

Liquid cloud droplets can be considered spherical to a very good approximation. They are formed by deposition of water vapor on hydrophilic aerosol particles. Such aerosol particles are called *activated*, when their size exceeds a certain critical size. The number of droplets activated and subsequently the size of each droplet is determined by (*Twomey*, 1959)

1. The number concentration of hydrophilic aerosol
2. The supply of water vapor to condense, which in turn is given by the supersaturation of the ambient air.

The Köhler theory describes the supersaturation of the ambient air, S, in dependence of the size of a wetted aerosol and its chemical composition:

$$S = \left(1 - \frac{b}{r_d^3}\right) \exp\left(\frac{a}{r_d}\right) \tag{1.1}$$

where $\exp(a/r_d)$ is the "curvature term" which describes the decrease in necessary supersaturation for a droplet to be activated with increasing droplet radius, r_d, and $(1 - b/r_d^3)$ is the "solution term" which describes the dependence on the relative quantity of dissolved aerosol material and is dominant for small droplets. The variable a depends on temperature and density of the moist air, and b on the temperature and the chemical properties of the solution (*Pruppacher and Klett*, 1997). Recently, *Charlson et al.* (2001) proposed an important additional impact of soluble gases on the formation of clouds, which could render the process of activation more efficient.

Supersaturation in an air parcel is generated by cooling of wet air. This is generally the case in ascending air motion. The supersaturation in a parcel is dependent on the updraft speed. With this, the cloud droplet number concentration (CDNC) can be calculated as a function of aerosol number concentration and updraft speed, w:

$$N_d \propto f\,(N_a; w) \tag{1.2}$$

where N_d is the cloud droplet number concentration [m^{-3}], N_a the number concentration of hydrophilic aerosol [m^{-3}], and w, the updraft velocity [m s^{-1}].

Cloud droplets have a typical size of about 3 - 20 μm. Eventually, raindrops may form from cloud droplets by collision and coalescence (e.g., *Bartlett*, 1966)). For two spherical particles, the collision and coalescence is given by:

$$\rho_{air}\,\frac{\partial q}{\partial t} = \int \pi\, E(r,r')\ (r+r')^2\ |V(r) - V(r')|\ q(r')\ n(r')\ dr' \tag{1.3}$$

where q is the mixing ratio [kg kg^{-1}], ρ_{air} the air density [mg m^{-3}], r the particle radius [m], $E_{r,r'}$ is the collision efficiency, which also determines the collision cross section (e.g., *Hocking*, 1959), and $V(r)$ fall velocity of a particle of radius r. A distinction between cloud droplets and raindrops may be defined by their fall velocity. While cloud droplets have a very small terminal fall velocity, raindrops fall fast enough to leave the cloud. Typical raindrops are in the range of 100 μm to 1 mm. Comparing the sizes of cloud droplets and raindrops, 10^2 to 10^7 cloud droplets are needed to form a raindrop. If cloud droplets and raindrops are considered as two different species of water, two processes can be distinguished, by which rainwater is created from cloud water. The collision and coalescence of cloud droplets is known as autoconversion. This process is the initiation of rain. For this to be efficient, droplets need to have different fall velocities, which is determined by the size of the droplets. For an onset of autoconversion, thus, the droplet size spectrum has to be relatively broad. In addition, to form larger raindrops, colliding droplets have to be large enough. From observational studies it has been deduced that both conditions are given, when the particle radius exceeds a certain "critical" size (*Kessler*, 1969), which has been determined to be about 10 μm (*Pawlowska and Brenguier*, 2003). The second process is the collision and coalescence of raindrops and cloud droplets. While falling through a cloud, raindrops collect by this process plenty of cloud droplets, growing considerably.

1.5.2. Processes in ice clouds

Below the freezing point of 0°C, clouds may include ice crystals, and for temperatures below –40°C, all cloud water consists of ice. Ice crystals are formed by different nucleation processes.

Homogeneous nucleation : A wetted aerosol freezes, and grows by deposition of water vapor.

Heterogeneous nucleation : A supercooled wetted aerosol freezes by interaction with a "freezing nucleus". *Contact nucleation*, *deposition nucleation*, and *immersion nucleation* are distinguished (*Vali*, 1985), which refers to the collision of a supercooled droplet with an aerosol, the deposition of water vapor on a wetted aerosol, and the freezing by the activity of an insoluble aerosol inside a droplet, respectively.

The ability of different aerosol species to act as freezing nuclei is still very unclear and the subject of recent research (*DeMott et al.*, 2003).

In modeling studies, ice crystals are often considered to have spherical shape. This approximation is, however, generally not valid and may introduce large errors in some cases (*Doutriaux-Boucher et al.*, 2000).

Ice crystals may form snow flakes by collision and coalescence processes. The formation of snow from cloud ice has been studied much less intensively compared to the corresponding liquid water process. When assuming spherical particles, this process can be described by an equation similar to the one given earlier for liquid particles.

1.5.3. Processes in mixed clouds

When frozen and liquid particles collide, rimed particles are produced. When rime is formed, ice crystal splinters are produced. This so-called "secondary ice production" creates a large number of new ice crystals and has first been observed by *Hallett and Mossop* (1974). It is therefore also known as the Hallett-Mossop process. The saturation water vapor mixing ratio is lower when considering ice surfaces compared to liquid water surfaces. This implies that air may be supersaturated with respect to ice, even when its subsaturated w.r.t. liquid water. This has as a consequence the so-called Bergeron-Findeisen process by which in mixed-phase clouds, ice crystals grow at the expense of liquid cloud droplets (*Bergeron*, 1933). Further, while the atmosphere almost never is supersaturated w.r.t. liquid water at spatial scales larger than a few cubic meters, supersaturation w.r.t. ice is common and may reach as much as 70%. However, so far, almost no GCM is able to treat the ice supersaturation.

1.5.4. Impacts of microphysical processes on global climate

Microphysical processes are expected to react to or impact on global climate change. For example, aerosol indirect effects are commonly considered to be an anthropogenic perturbation of the climate. As cloud microphysics are complex processes and their impacts on global scale climate still are poorly understood, microphysical processes also serve to explain theories which try to link the observed climate change to natural phenomena or to show mechanisms inhibiting a profound climate change. For example, the so-called "Iris hypothesis" claims that with rising sea surface temperature (SST) due to greenhouse warming, cirrus cloudiness in the tropics would be reduced (*Lindzen et al.*, 2001). Enhancement of precipitation-forming microphysical processes due to increased cloud water content would be responsible for such a mechanism. Another study claims feedback of cloud microphysics to cosmic radiation variability to explain the observed climate change via the altering in aerosol particle charge (*Svensmark and Friis-Christensen*, 1997). These two theories remain largely controversial (e.g., *Lin et al.*, 2002; *Hartmann and Michelsen*, 2003; *Sun and Bradley*, 2002).

1.5.5. Representation of cloud microphysics in models

Several properties of the different water species and aerosols have to be considered to model cloud microphysical processes. These include the size distribution and chemical composition of aerosols, and the size distribution of cloud droplets, ice crystals, and precipitating particles. Some approaches exist to explicitly model cloud microphysical processes, with a particular focus on the rather complicated mechanism of activation of aerosol particles (e.g., *Wobrock et al.*, 2001).

Generally, two types of microphysical schemes may be distinguished, those resolving the size distributions of aerosol and water particles in size bins (e.g., *Young*, 1974a), and those which assume a fixed size distribution and partition the water into separate categories for cloud water and precipitation. The latter ones are called “bulk” schemes (e.g., *Kessler*, 1969). In the scope of the present study the latter type of parameterizations is rather of interest. Often, such more or less sophisticated parameterizations have been developed in the framework of cloud-resolving models (CRMs) or large-eddy simulation models (LES), which are able to resolve structures with a typical size of a few to several hundreds of meters. However, with such resolutions, microphysical processes still cannot explicitly be modeled. Even on such scales, they need to be parameterized. Schemes suitable to be used in CRMs have been adapted in the past several years for application in large-scale models for the sake of more physical realism in GCMs, and to be able to treat the influence of aerosols on clouds. By adapting CRM microphysical schemes, parameters often have to be adjusted for large-scale models to be able to simulate realistic cloud properties and precipitation distributions. An example is the “critical radius” in the autoconversion formulation, which is set to a lower value in GCMs compared to the value in CRMs or the measured values from observations (*Rotstayn*, 2000). The reason is, that at small scales, some droplets may exceed the critical value and onset precipitation, which then by accretion forms larger rain rates. At the coarse resolution of a GCM, however, the rather large critical radii very rarely are exceeded, or very large cloud water contents would have to be present on large scales.

1.6. Anthropogenic aerosols

In the context of general circulation modeling, five different species of aerosols are distinguished, which differ in chemical composition and origin. Of particular interest for their impact on climate are their hydrophilic or hydrophobic properties, which determine their ability to serve as cloud condensation nuclei (CCN), and the degree to which they absorb radiation. In the framework of anthropogenic climate change, and to quantify the contribution of anthropogenic aerosols to climate perturbations, it is important to distinguish natural and anthropogenic aerosol sources.

- Sulfate aerosols ($SO_4^=$) are typically of anthropogenic origin. Sources include the combustion of sulfur-containing fossil fuel and the burning of biomass. Sulfate particles are relatively small, and generally hydrophilic. When incorporated in cloud droplets and subsequently in rain drops, sulfate aerosols also cause the so-called “acid rain”, as they dissolve in water to form sulfuric acid.

- Organic carbon, which originates for example from the burning of biomass. Some organic aerosols have hydrophilic properties. Organic carbon aerosols are slightly absorbing in the SW spectrum.

- Black carbon (soot) is at least near its origin generally hydrophobic. Soot particles constitute the most absorbing aerosols.

- Sea salt, which is entirely of natural origin. However, possibly increasing wind speeds in an anthropogenically altered climate would increase the source strength for sea salt aerosols. Sea salt is hydrophilic. In remote oceanic regions, sea salt almost constitutes the only species of aerosol.

- Dust often contributes most to the total mass of aerosols. A main source for dust aerosols are deserts thus largely a natural origin. Land-use change or increase windspeed due to anthropogenic climate change, however, may constitute an anthropogenic source for dust aerosols. Generally, dust aerosols are hydrophobic. They may constitute ice nuclei (*DeMott et al.*, 2003). Dust is slightly absorbing.

Individual aerosol particles may be constituted of different chemical compositions. Different aerosol types may be mixed either "internally" or "externally", referring to aerosol particles consisting of several different chemical compounds, or an aerosol population where individual particles consist of pure chemical species.

It shall be noted that aerosols have a relatively short lifetime in the atmosphere. As tropospheric aerosol particles have a considerable mass, they are deposited after about a week at the surface. Hydrophilic aerosols which are included in cloud and subsequently precipitation particles can be deposited at the surface by washout. In consequence, aerosol concentration in the atmosphere is large particularly near the main source regions, and very low over remote maritime regions. Another consequence is that if the anthropogenic production of aerosol stops, any direct impact on climate will vanish as well after a couple of days or weeks.

1.7. Aerosol indirect effects

The impact of aerosols on clouds is known as aerosol "indirect" effect (AIE). The impact of aerosols on low-level liquid water clouds has been the first one to be studied. We will limit this section to those clouds as well.

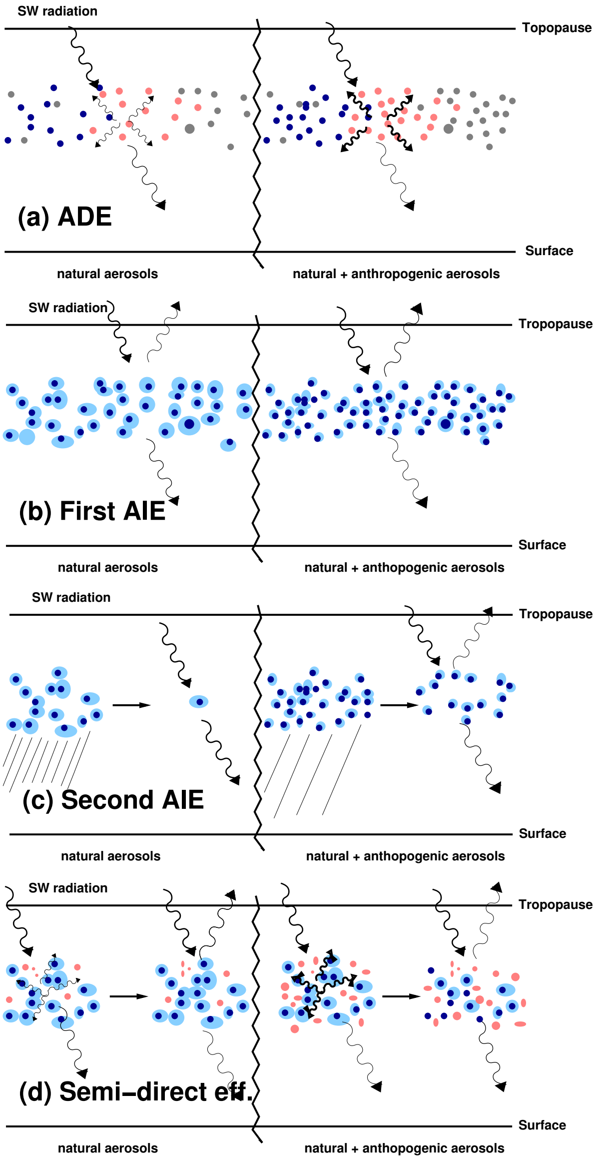

Figure 1.2.: Schematic description of (a) the aerosol direct effect, (b) the first indirect effect, (c) the second indirect effect, and (d) the semi-direct effect. Dots symbolize aerosols (absorbing aerosols are red and hydrophilic aerosols blue), light blue circles cloud droplets, wavy lines of different thickness indicate radiative transfer of different intensity, arrows (⟶) indicate a temporal evolution, and the more or less densely hatched area below the "cloud" indicates precipitation of different intensity.

However, aerosols may also have an impact on ice clouds (e.g., *Georgii*, 1959). It has been argued that aerosol from air traffic exhaust may contribute to the increase in cirrus cloudiness due to air traffic (*Boucher*, 1999). As in the IPCC definition and unless specified otherwise explicitly, the terms of aerosol direct and indirect effects refer here to the impacts of anthropogenic only aerosol.

1.7.1. Definition

Hydrophilic aerosols constitute cloud condensation nuclei (CCN). Generally, such particles are necessary for any cloud particle to form, as the spontaneous formation of liquid or solid particles from water vapor would need supersaturations of the order of several hundred percents, which never occurs in the atmosphere (*Houze*, 1993). An increase in aerosol number concentration makes more CCN available and more cloud particles may be formed. When the cloud liquid water content is constant the individual cloud droplets become smaller. This effect causes an increase in cloud albedo and is called alternatively the first AIE, cloud albedo effect, or Twomey effect (*Twomey*, 1974).

As mentioned earlier, autoconversion of cloud droplets to form rain drops depends on the size of the cloud droplets. For smaller droplets, the precipitation formation is less efficient or may even be suppressed. So, the lifetime of clouds is enhanced. For reflecting clouds the planetary albedo is increased. This is called second AIE or cloud lifetime effect (*Albrecht*, 1989).

1.7.2. Observational evidence

Field studies

A first estimate of the anthropogenic contribution to CCN is given by *Squires* (1966). From aircraft measurements, they deduce a source strength of anthropogenic CCN of the order of 14% of the natural CCN sources, when they extrapolate their measurements to the USA region, and of 5% for the entire northern hemisphere.

Brenguier et al. (2000b) measure several microphysical parameters in maritime stratocumulus clouds during the ACE-2 campaign. They find much larger CDNC (up to more than 400 cm^{-3}) in polluted compared to clean conditions (less than 100 cm^{-3}). Optical thickness of clouds, τ_c, is shown to depend strongly on cloud geometrical thickness, H. They find a relationship close to the the theoretical one derived for an adiabatically rising air parcel of $\tau_c \propto H^{\frac{5}{3}}$ for constant CDNC (*Brenguier*, 1991). *Pawlowska et al.* (1999) show the dependence of τ_c on CDNC, N_d, following the theoretical value of $\tau_c \propto N_d^{\frac{1}{3}}$ when scaling the optical thickness by $H^{\frac{5}{3}}$. *Brenguier et al.* (2003) analyze data of *Pawlowska and Brenguier* (2003) and *Schüller et al.* (2003), also from ACE-2 measurements. They relate cloud optical thickness, cloud droplet radius, and cloud droplet number concentration on a large scale (60x60 km^2) for several cases, from clean to heavily polluted conditions. Looking at clean to moderately polluted conditions, they find positive correlations between τ_c and N_d and r_e and N_d, respectively, with the behavior of $\tau_c \propto N_d^{\frac{1}{3}}$ and $r_e \propto N_d^{-\frac{1}{3}}$ expected from theory. However, when adding the strongly polluted cases, a different relationship is found. They attribute this finding to the differences in cloud geometrical thicknesses in the polluted compared to clean cases. Again using ACE-2 data, *Snider and Brenguier* (2000) show from a closure study that the Twomey equation (*Twomey*, 1959) of droplet activation was valid in the cases measured. The data derived from ACE-2 on the large scale are used in Chapters 4 and 9.

Hudson and Yum (2001) carry out an in situ study with aircrafts measuring CCN, CDNC, and drizzle water content above a coastal site in Florida. Distinguishing airmasses advected from the continent and the ocean, they show that clouds in continental airmasses generally contain more but smaller droplets and less drizzle. These two findings support the hypotheses for the first and second aerosol indirect effects, respectively.

Liepert and Lohmann (2001) compare observations of radiation fluxes at the surface measured from ground-based instruments to radiation fluxes calculated with two GCM simulations, one calculating aerosol indirect effects from natural and anthropogenic aerosols, and a second one using natural aerosols only. They find some features indicating that the anthropogenic aerosol indirect effect may be necessary to simulate realistically the observed radiation fluxes. However, their results remain ambiguous due to deficiencies in the simulated cloudiness.

Peng et al. (2002) examine data from liquid water cloud cases collected in the RACE and FIRE.ACE campaigns. They find cloud droplet effective radii (CDR) by 2 - 6 μm smaller in polluted compared to clean cases. In most cases, cloud optical depth and cloud albedo are found to be larger in polluted compared to clean cases. They establish a relationship between CDR and cloud albedo, which is found to be negative for clean cases (in agreement with the first aerosol indirect effect). For polluted cases, however, a positive relationship between cloud albedo and CDR is observed, which they attribute to the second indirect effect. Earlier investigation of similar relationships with their model confirms this finding (*Lohmann et al.*, 2000b).

Ramanathan et al. (2001a) report from the Indian Ocean Experiment (INDOEX) important indirect effects of aerosols originating from the Indo-Asian haze. In polluted compared to clean clouds, while liquid water content was approximately constant, much larger CDNC (315 cm^{-3} compared to 90 cm^{-3}) and smaller CDR ($\leq$ 6 μm compared to $\geq$ 7.5 μm) are observed, giving a radiative forcing due to the first aerosol indirect effect of –5 Wm^{-2} at the top of the atmosphere. *Ramanathan et al.* (2001a) show a logarithmic dependence of cloud optical thickness on aerosol optical thickness, with τ_c $\approx$14 for large aerosol optical thicknesses ($\tau_a \geq 0.5$). From a modeling study of the INDOEX campaign, an increase in low-level cloud lifetime results in an increase in low-level cloudiness of 2 % and a corresponding radiative impact due to the second aerosol indirect effect of –2 Wm $^{-2}$. The same study introduces the "semi-direct" effect of aerosols, which would evaporate cloud water or suppress the formation of clouds through heating of the atmosphere by absorbing aerosols. This effect is estimated to correspond to a radiative forcing of 4 Wm^{-2}. *Ramanathan et al.* (2001b) further interpret the INDOEX results in cloud-radiation models and analyze the impact of different aerosol species. For the global mean, they deduce a first AIE of –0.3 to –1 Wm^{-2} of sulfate aerosols and of –0.5 to –2 Wm^{-2} when adding carbonaceous aerosols.

Satellite data

Some of the first evidence for impacts on clouds by anthropogenic aerosols has been provided by analysis of ship tracks. Looking at TIROS satellite images. *Conover* (1966) find "anomalous cloud lines", linearly shaped lines of brighter clouds of up to 500 km length and a width of 25 km. They argue that the production of aerosols by ship exhaust was responsible for an altering of atmospheric concentration of CCN which could increase the cloud albedo by up to 20%.

Using two channels of the Advanced Very High Resolution Radiometer (AVHRR), *Coakley Jr. et al.* (1987) show the coincidence of smaller cloud particles and larger cloud albedo in ship tracks compared to the environment. More recently, *Taylor et al.* (2000) investigate ship tracks in the Monterey Area Ship Track (MAST) experiment. For relatively clean clouds, they find CDNC changes of up to a factor of 2 by comparing clouds affected by ship exhaust with those in the cleaner environment. In some cases, they find a suppression of drizzle and subsequently a considerable increase in LWP. A combination of both aerosol effects yields an increase in cloud radiative forcing at the top of the atmosphere of up to a factor of 4.

In a pioneering study *Han et al.* (1994) derive cloud top droplet radii for liquid water clouds from AVHRR satellite measurements over oceans on a global scale in the framework of the International Satellite Cloud Climatology Project (ISCCP). They show that CDR over continents are smaller by 2 - 3 μm than over oceans. Comparing maritime clouds in the southern and northern hemispheres, a difference of 1 μm, with the smaller droplets in the NH, is also found. *Han* *et al.* (1998) examine the relationship between CDR and cloud albedo. They show, that cloud albedo increases with decreasing CDR for most continental clouds and for optically thick clouds. However, for optically thin clouds over oceans, a decrease in cloud albedo is observed with increasing CDR. As a possible explanation, *Lohmann et al.* (2000b) deduce from a GCM modeling study that precipitating versus non-precipitating clouds would be responsible for this behavior. *Han et al.* (1998) also show a general positive correlation between cloud liquid water path (LWP) and CDR. *Han et al.* (2002) further investigate the dependence of LWP on CDNC. They find in only one third of the cases examined an increase in LWP with increasing CDNC as expected due to the second aerosol indirect effect. Another third of the cases shows approximately constant LWP, consistent with the Twomey hypothesis. Finally, a third of the cases shows a decrease in LWP with increasing CDNC, a process possibly related to boundary layer dynamics.

Kaufman and Nakajima (1993) evaluate AVHRR measurements of CDR over the Brazilian Amazon Basin and show that smoky (smoke optical depth of τ_s=2.0) compared to non-smoky ($\tau_s \leq 0.1$) reduce the CDR from 15 to 8 μm, where the smoke comes from forest fires and supplies efficient CCN. On the other hand, absorption by black carbon in the smoke reduces the reflectance. The net effect of smoke in this case is a reduction of the planetary albedo. *Kaufman and Fraser* (1997), however, again evaluating AVHRR data, show a decrease in CDR and an increase in cloud reflectance with increasing smoke optical depth at constant latitude. The relationship between smoke optical depth and cloud albedo and CDR, respectively, shows steeper slopes for larger integrated water vapor contents in the atmosphere (precipitable water, PW). They further show that a strong decrease in CDR with increasing smoke optical depth corresponds to a strong increase in cloud albedo. The radiative forcing caused by this impact of smoke on cloud albedo is evaluated to be –2 Wm^{-2}, which is a rather low value given that a region with high pollution is examined. *Feingold et al.* (2001), analyzing the same data, suggest a saturation effect for these very large aerosol concentrations. For the same experiment, *Reid et al.* (1999) measured in situ CDR using an aircraft. They find CDR values of 3 to 8 μm, thus much smaller than the ones derived from the satellite data.

Nakajima et al. (2001) relate several cloud microphysical quantities to aerosol number concentration from AVHRR data over oceans on a global scale. They show an increase in column-integrated CDNC and a decrease in CDR with increasing aerosol number concentration, in accordance with the first aerosol indirect effect. For large aerosol concentrations ($N_a > 10^{7.8} m^{-3}$), an increase in cloud optical thickness is also derived with increasing aerosol concentration. However, no correlation is found between N_a and cloud liquid water path. *Kawamoto and Nakajima* (2003) identify possible artifacts in the derivation of CDR from AVHRR data looking at a long time series of measurements (1985-1994). They also identify a slight decrease in CDR from 1985 to 1994, which they attribute to an increase in global mean aerosol concentration.

Wetzel and Stowe (1999) show a negative correlation between CDR and aerosol optical thickness, τ_a, derived from AVHRR data for low-level marine stratus clouds. Additionally, they show a seasonal and regional variability that compares well with variations in aerosol sources. They find a saturation effect in the CDR to aerosol burden relationship for $\tau_a > 0.12$. The interpretation of their results is somehow difficult as they look at largely averaged data. Thus, correlations may be due to other influences such as geographical ones. Other studies such as the one of *Nakajima et al.* (2001) may be criticized in a similar manner.

Schwartz et al. (2002) correlate AVHRR data of CDR and cloud albedo with sulfate aerosol concentrations simulated with a hemispheric chemistry transport model (CTM) for the North Atlantic ocean for two periods of several days in April 1987. They find a negative correlation between sulfate aerosol concentration and CDR, but no correlation of aerosols with cloud optical thickness or cloud albedo. They attribute this to the large variability in LWP which masks possible aerosol influences on cloud albedo.

Chameides et al. (2002) correlate ISCCP cloud optical thickness and column burdens of anthropogenic aerosol modeled with a coupled regional climate - chemistry transport model. For annually averaged data from 1990 - 1993 over the East Asian region, they find a correlation coefficient of $r^2 > 0.6$ between the two quantities, which corresponds to a confidence level of >99.99%, so that 60% of the variability in cloud optical thickness are explained by variation in aerosol burdens. However, they do not observe a consistent correlation between aerosol burden and cloud cover, indicating that either the second aerosol indirect effect does not play an important role or was offset by other processes such as the semi-direct effect.

Bréon et al. (2002) relate CDR and an aerosol index inferred from data of the POLarization and Directionality of the Earth's Reflectances (POLDER) instrument. They find a decrease in CDR with increasing aerosol index, which is steeper over oceans than over land. The data from *Bréon et al.* (2002) is used in Chapter 5.

Coakley, Jr. and Walsh (2002) analyze several hundred cases of ship tracks using AVHRR data. They find a statistically significant increase in cloud reflectance corresponding to a decrease in cloud droplet radius of 2 μm or more. Clouds with relatively small albedo and large droplet sizes are found to be the most susceptible. The change in cloud optical thickness found is not as large as expected for a given change in CDR. They argue that either the cloud LWP decreased in polluted compared to clean clouds, or that absorption by aerosols takes place, which would mask part of the cloud albedo increase. *Coakley, Jr. and Walsh* (2002) do not find a coherent variation in cloud top height in polluted versus clean environments, in contrast to other studies (e.g., *Brenguier et al.*, 2000b).

Rosenfeld and Lensky (1998) use multi-spectral AVHRR measurements to relate CDR to the temperature in convective clouds, the temperature being a measure for the height in the cloud. They identify large differences between continental and maritime clouds. In maritime clouds, CDR increase rapidly with height in a cloud due to coalescence up to a maximum size where precipitation onsets. This is not observed in continental clouds. They also find that glaciation onsets at much lower temperatures in continental compared to maritime clouds. They observe an important influence of pollution in biomass burning and urban regions. Using Tropical Rainfall Measuring Mission (TRMM) observations, *Rosenfeld* (1999) shows that clouds affected by smoke from forest fires do not form precipitation where similar clouds in the neighborhood do. With a similar approach, *Rosenfeld* (2000) shows for several different geographical locations that similarly, a suppression of precipitation in clouds can be inferred by urban and industrial pollution.

1.8. Concept of radiative forcing

At least in the framework of climate modeling, the concept of "radiative forcing" of an external perturbation of the climate system is very useful. A radiative forcing is defined as the difference in radiation flux at the tropopause between perturbed and unperturbed conditions. It is calculated for fixed tropospheric temperature and humidity profiles, letting the stratosphere adjust. With this definition, it has been shown (e.g., *Hansen et al.*, 1997), that the radiative forcing, ΔF, due to any small perturbation of the climate system is linearly related to a corresponding change in global mean surface temperature, ΔT_s

$$\Delta T_s = \lambda \, \Delta F \tag{1.4}$$

where λ is the so-called sensitivity parameter [K W^{-1} m^2], which depends on the model used, but is approximately constant for any perturbation for which the radiative forcing is calculated. The radiative forcing is especially useful to compare the magnitude of different perturbations of the climate system.

Concerning the radiative forcing of the aerosol indirect effects, the two different effects have to be distinguished. The first aerosol indirect effect is considered to change the cloud droplet size of low-level liquid water clouds. This change impacts directly on the cloud optical thickness, which in turn alters the cloud albedo. The impact on the LW radiative spectrum is small and is neglected here. Therefore the radiative forcing of the first aerosol indirect effect is generally calculated on-line in a model simulation, doing the radiation transfer calculation twice, a first time with a profile of the cloud optical thickness as it were in natural conditions, and a second time using the profile which is influenced by the additional anthropogenic aerosols. The radiative forcing of the first aerosol indirect effect is then given as the difference in the radiative fluxes calculated for the top of the atmosphere (TOA), as an adjustment of the stratosphere profiles can be neglected when looking at the SW spectrum (*Hansen et al.*, 1997). The radiative forcing due to the first aerosol indirect effect is estimated to be of the order of 0 to –2 Wm^{-2} (*Ramaswamy et al.*, 2001), with a considerable uncertainty (*Boucher and Haywood*, 2001; *Haywood and Boucher*, 2000).

For the second aerosol indirect effect, such a radiative forcing cannot be defined, as there are time-dependent processes involved. A cloud cover increase and subsequently an enhancement of cloud albedo as a reaction to an increase in aerosol concentration takes place only after some minutes to hours. To deal with this, *Rotstayn and Penner* (2001) define a "quasi-forcing" due to the second aerosol indirect effect. They carry out two model simulations which are identical except for aerosol concentration considered in the precipitation scheme of the model. In one of the simulations natural only aerosol concentrations are applied and natural plus anthropogenic aerosols in the second one. The difference in SW radiation flux at the top of the atmosphere (TOA) is taken as the quasi-forcing due to the second aerosol indirect effect. They find that with this definition, both aerosol indirect effects are of comparable magnitude. However, as shown in Chapter 6, this definition of a quasi-forcing may be too ambiguous to satisfactorily describe a radiative forcing due to the second aerosol indirect effect, as other cloud feedback processes may be active as well, e.g., concerning cirrus clouds. A slightly different approach has been proposed by *Kristjánsson* (2002), who calculate two cloud fields in a single model simulation, one of which includes the second aerosol indirect effect of anthropogenic aerosols, and the other one does not, the former one being used for the model integration, and the latter one stored for diagnostics.

1.9. The representation of cloud and precipitation microphysics and aerosol indirect effects in different GCMs: A review

Based on the cloud parameterizations in GCMs described earlier (Section 1.4), and with the aim of incorporating the aerosol indirect effects, several GCMs introduced comprehensive microphysical schemes. For an estimation of the first AIE, the parameterization of the link between aerosol concentration and CDNC is of main interest, as the choice of the aerosol species taken into account. The formulae which connect aerosol concentrations and CDNC can be divided into two categories, namely empirically based and physically based approaches. The former ones diagnose CDNC from aerosol mass or aerosol number concentration fitting a relationship to observations; the latter ones take into account model variables like the turbulent kinetic energy to incorporate some information about the updraft velocity in the clouds. Complexity in the aerosol concentrations considered ranges from prescribed fields of sulfate aerosols only to comprehensive cycles of different aerosol species calculated interactively in the GCM.

For the second aerosol indirect effect, the precipitation microphysics is of interest. GCMs that treat microphysics generally use bulk parameterizations. The most comprehensive schemes of precipitation microphysics include several different species of water like liquid and frozen cloud water, and rain, snow, hail or graupel as precipitation species. Multiple processes of conversion between the water species may be taken into account.

Lohmann and Roeckner (1996) introduce a microphysical scheme in the GCM of the Max Planck Institute for Meteorology, the European Centre for Medium Range Weather Forecasting - HAMburg GCM (ECHAM). In their parameterization, mixing ratios of water vapor, cloud liquid and ice water, and CDNC are prognostic variables. CDNC is linked to sulfate aerosol mass concentration following *Boucher and Lohmann* (1995). Autoconversion is parameterized as in *Beheng* (1994). The scheme has been extended to include a physically based activation scheme of droplets by *Lohmann et al.* (1999) and *Lohmann et al.* (2000a), which depends on aerosol number concentration and a subgrid-scale updraft velocity calculated from the turbulent kinetic energy. Sulfate and carbonaceous aerosols are considered. Using this model *Feichter et al.* (1997) evaluate the radiative forcing due to the first aerosol indirect effect by sulfate aerosols of –0.76 Wm^{-2}. *Lohmann* (2002b), *Lohmann and Kärcher* (2002) and *Kärcher and Lohmann* (2003) further introduce several processes of ice crystal nucleation in the ECHAM model.

Jones et al. (1994) introduce an empirical formula to diagnose CDNC from sulfate aerosol mass in the Hadley Centre GCM. This formula is fitted to observational data over various continental and maritime regions from *Martin et al.* (1994). The CDR is calculated from the liquid water content in stratiform clouds while holding the CDR in convective clouds fixed. *Jones et al.* (1994) calculate a radiative forcing due to the first AIE of –1.3 Wm^{-2}. *Jones and Slingo* (1996) examine several other empirical formulae of the aerosol to CDNC link, and find radiative forcings due to the first AIE in the range of –0.5 to –1.5 Wm^{-2}. *Wilson and Ballard* (1999) introduce a cloud microphysical scheme into the Hadley Centre model, which is based on the *Rutledge and Hobbs* (1983) parameterization. They use four different water species, vapor, liquid water, rain water, and "ice" which includes cloud ice and snow. An originality of their scheme is that condensation and evaporation is calculated for liquid water clouds only using the *Smith* (1990) scheme which applies a triangular PDF. Ice is formed by freezing of liquid cloud water, thus, no temperature-dependent parameterization of the partitioning between liquid and ice water is necessary. In their model, ice crystals are allowed to have non-spherical shape in the radiation parameterization following *Kristjánsson et al.* (1999). Autoconversion of liquid droplets to rain is calculated using the *Tripoli and Cotton* (1980) formula. A scheme parameterizing subgrid-scale saturation water vapor mixing ratio is introduced by *Cusack et al.* (1999), which they derive from simulations with their model in high resolution weather forecasting mode. *Jones et al.* (2001) use this microphysical scheme to evaluate the radiative impact of both aerosol indirect effects by comparing two simulations and found an impact of –1.9 Wm^{-2}. *Williams et al.* (2001) extend this study and find the first indirect effect in their model to be much larger than the second one. They give a global mean radiative impact of both AIE of –1.6 Wm^{-2}.

Rotstayn (1997) introduce a microphysical scheme in the Commonwealth Scientific and Industrial Research Organization (CSIRO) GCM. He use water vapor and cloud liquid and ice water as prognostic variables, diagnosing rain and snow as precipitation species. Convective clouds are diagnosed in a separate convection scheme. Clouds are considered to overlap randomly in their model. For ice clouds, rather than assuming spherical particles, the effective radius is calculated using an empirical parameterization of $r_e = 0.051\ q_i^{0.667}$. Condensation and evaporation is calculated using the scheme of *Smith* (1990). The autoconversion scheme is similar to the *Tripoli and Cotton* (1980) scheme and uses a critical liquid water mixing ratio, which depends on CDNC. Using this model and the empirical formula of *Boucher and Lohmann* (1995) to link sulfate aerosol mass to CDNC, *Rotstayn and Penner* (2001) evaluate the sum of both aerosol indirect effects to be –1.56 Wm^{-2}.

Del Genio et al. (1996) introduce a microphysical scheme in the Goddard Institute for Space Studies (GISS) GCM. They use water vapor, cloud water, and cloud ice as variables. Fractional cloudiness is allowed to occur in the vertical as well as in the horizontal dimensions by scaling vertically the cloud fraction, f, as $f' = f^{\frac{2}{3}}$, and the cloud optical thickness as $\tau_c' = f^{\frac{1}{3}}\ \tau_c$. In the radiation parameterization, a grid box is considered either cloudy or clear comparing the cloud fraction to a random number between zero and one, which in the temporal mean approaches the calculated cloud fraction. Similarly, clouds are considered either entirely liquid or frozen, comparing a random number to a calculated ice fraction which varies quadratically between zero at $-4°$C over ocean and $-10°$C over land to unity at $-40°$C. The Bergeron-Findeisen process is accounted for by calculating the possibility of glaciation in each cloud. *Menon et al.* (2002) introduce an empirical formula which links mass concentrations of sulfate and organic matter to CDNC into this model. Ice crystal number concentration is assumed to be constantly 0.06 cm^{-3} in their model. The microphysical scheme is extended to include the *Tripoli and Cotton* (1980) autoconversion scheme. *Menon et al.* (2002) evaluate the sum of both AIE to be –1.55 to –4.36 Wm^{-2}, depending on the choice of parameters in their microphysical scheme.

Ghan et al. (1997b) apply the cloud microphysics parameterization of the Colorado State University (CSU) Regional Atmospheric Modeling System (RAMS) (*Flatau et al.*, 1989) in the National Center for Atmospheric Research (NCAR) Community Climate Model (CCM). In this scheme, water vapor, cloud liquid and ice water, rain and snow as well as ice crystal number concentration are prognostic variables. Autoconversion is parameterized following *Ziegler* (1985). *Ghan et al.* (1997a) further apply a physically based link between aerosol number concentration, which depends on updraft velocity, aerosol number concentration, size distribution and chemical composition (*Abdul-Razzak et al.*, 1998). This scheme is further extended for multiple aerosol types by *Abdul-Razzak and Ghan* (1999). With this GCM, *Ghan et al.* (2001) quantify the aerosol indirect effects to be of –1.5 to –3.0 Wm^{-2}, depending on microphysical parameters and model resolution. Another microphysical scheme has been added to the NCAR CCM by *Rasch and Kristjánsson* (1998), based on the scheme of *Boucher et al.* (1995a). *Kristjánsson* (2002) use this scheme and introduce further a formula to predict CDNC from sulfate and black carbon. They find a radiative forcing of –1.8 Wm^{-2} for both aerosol indirect effects, where the first AIE is three times larger than the second. They confirm that the aerosol indirect effects caused by black carbon are negligible.

Takemura et al. (2000) describe a microphysical scheme in the Center for Climate System Research (CCSR) GCM. In their model, CDNC is linked to aerosol number concentration using an empirical formula. Precipitation formation is calculated from liquid water content using a characteristic time scale dependent on liquid water content and CDNC. With this model, the aerosol indirect effects are quantified to be –2.0 Wm^{-2}.

Smith and Randall (1992) and *Fowler et al.* (1996) introduce a comprehensive microphysical scheme in the Colorado State University (CSU) GCM. This scheme is adapted from the *Rutledge and Hobbs* (1983) parameterization and includes mixing ratios of water vapor, liquid and ice cloud water, rain and snow as prognostic variables. Autoconversion is parameterized following *Kessler* (1969). This model has not yet been used to investigate aerosol indirect effects.

1.10. Outline of the thesis

The thesis is subdivided into three partitions:

1. A comparison and evaluation of the GCM including the microphysical scheme of *Boucher et al.* (1995a) and the empirical link between sulfate aerosol mass and CDNC (*Boucher and Lohmann*, 1995) using satellite data and in situ measurements in order to study processes of the aerosol indirect effects,

2. An investigation of the climatic impacts of aerosol and greenhouse gas effects in GCM scenario simulations of the 20th century, and

3. A study of ice phase parameterizations, particularly including the development and evaluation

	Aerosols	Link CDNC-aerosols	Microphysics	Nudging
Chapter 2	Online SO_4, OM, BC, SS	BL95, sulfate	*Boucher et al.*	none
Chapter 3	Online SO_4, OM, BC, SS	BL95, sulfate	*Boucher et al.*	T, $\vec{v}$
Chapter 4	As observed	BL95 and modifications	*Boucher et al.*	T, $\vec{v}$
Chapter 5	Online SO_4, OM, BC, SS	BL95, maximum hydrophilic aer.	*Boucher et al.*	T, $\vec{v}$
Chapter 6	Monthly mean SO_4	BL95, sulfate	*Boucher et al.*	none
Chapter 7	Monthly mean SO_4	BL95, sulfate	*Boucher et al.*	none
Chapter 8	none	none	standard	none

Table 1.1.: Model versions used throughout the thesis. BL95 refers to *Boucher and Lohmann* (1995). In their formula, generally, sulfate aerosol mass concentrations are used except for Chapter 5, where we use the maximum of all hydrophilic aerosol mass concentrations instead.

of a comprehensive liquid and ice phase microphysical scheme.

The LMDZ GCM which is used in this study is presented in Chapter 2. Of particular interest is the warm cloud microphysical scheme of *Boucher et al.* (1995a), which has been implemented in the model. Table 1.1 summarizes differences in the model versions used throughout the thesis. These include the aerosol distributions applied (e.g., whether sulfate only or also other aerosols are used, calculated online in the model or precalculated monthly mean fields), the link between cloud droplet number concentration and aerosol distributions, the application or not of the microphysical scheme, and whether model variables are nudged to analysis data or not. Chapter 3 describes the satellite instrument POLDER, the data of which is widely used in the thesis. A direct comparison is done between model-calculated and POLDER-derived cloud and aerosol quantities. In Chapter 4, a single-column version of the LMDZ model is evaluated using data from the ACE-2 field campaign, and comparing its results to those of other models. This chapter cites the work of *Menon et al.* (2003), and adds some sensitivity studies with the LMDZ GCM. Using POLDER satellite observations and the LMDZ model, aerosol indirect effects are studied by establishing statistical relationships between aerosol index and cloud droplet radius and cloud liquid water path, respectively. This part, Chapter 5, is taken from *Quaas et al.* (2003a).

In the two following chapters, the relative impacts of aerosols and greenhouse gases on the climate of the 20th century are studied analyzing three fixed-SST atmospheric GCM ensemble simulations for the 1930 to 1989 period. In Chapter 6, we focus on the radiative impacts of the two anthropogenic perturbations, with a special interest in the response of clouds. Particularly, the second aerosol indirect effect is examined. Chapter 7 looks at trends in observed variables like surface temperature and diurnal temperature range and identifies different behavior of the model when forced with different perturbations. The results in these two chapters are taken from *Quaas et al.* (2003b) and *Quaas et al.* (2003c).

In the third part, the parameterization in the LMDZ GCM is evaluated with POLDER satellite data which treats the repartition of condensed water in liquid water and cloud ice (Chapter 8). The partitioning is parameterized as a function of the local temperature. This study is submitted as *Boucher and Quaas* (2003). A new cloud and precipitation microphysical scheme is developed for both, liquid and ice phases. The scheme is described and evaluated in Chapter 9. Four one-dimensional cases are examined, two cases of marine stratocumulus clouds observed in the ACE-2 campaign (see also Chapter 4), and two cases of thin cirrus clouds used in a model intercomparison project. A preliminary evaluation of the scheme in the global model using satellite observations is presented in Chapter 9 as well.

Chapter 10 summarizes the work and outlines promising approaches for future work.

1.11. Introduction : Résumé

Le système climatique et le changement climatique

Le changement climatique est considéré comme l'un des problèmes les plus urgents de l'humanité (*Nations Unies*, 1992 ; 2000). Gaz à effet de serre et aérosols modifient fortement le bilan radiatif du système climatique et provoquent ainsi des effets dangereux pour les équilibres sociaux, écologiques et économiques. Cela est l'une des raisons pourquoi la compréhension du système climatique est d'une importance particulière. Si de meilleures prévisions des réponses du système climatique aux perturbations anthropiques étaient disponibles, des décisions politiques contre les impacts négatifs pourraient être prises ou des adaptations de la société seraient possibles.

Les outils les plus importants pour la compréhension du système climatique global et pour la simulation du changement climatique sont les modèles du système terrestre (ESM en Anglais). Ce sont des modèles qui couplent plusieurs composantes, parmi lesquels des modèles de l'atmosphère, de l'océan, des surfaces continentales avec la végétation, des glaces de mer, de la biosphère et de la cryosphère. Cette étude sera concentrée sur la composante atmosphérique représentée par un modèle de circulation générale de l'atmosphère. Résolvant numériquement les équations qui gouvernent la dynamique de l'atmosphère et incorporant des processus adiabatiques, ces modèles sont capables de simuler une multitude de processus physiques. Pourtant, dû à la capacité limitée des ordinateurs et à la compréhension limitée des processus, les simulations actuelles du système atmosphérique restent irréalistes sous plusieurs aspects. La résolution et la complexité des modèles peuvent être augmentées par des meilleures méthodes numériques de modélisation (par example, *Quaas* , 2000) et des ordinateurs plus puissants. L'étude présente est quant à elle dédiée à l'amélioration de la compréhension des processus physiques et en particulier celle des effets indirects des aérosols.

Les impacts anthropiques sur le climat

Deux modifications majeures de la composition de l'atmosphère sont provoquées par l'humanité. La première et la plus importante est l'augmentation de la concentration troposphérique en gaz à effet de serre, qui absorbent le rayonnement terrestre et le ré-émettent à une température plus basse. Cela provoque l'effet de serre qui résulte en une augmentation de la température de la surface terrestre pour maintenir l'équilibre radiatif de la planète. Parmi ces gaz, le dioxyde de carbone, produit par la combustion des combustibles fossiles, est la composante la plus importante. Les autres principaux gaz à effet de serre anthropiques sont le méthane, le protoxyde d'azote, les chlorofluorocarbones et l'ozone troposphérique. La concentration de tous ces gaz a augmenté depuis le début de l'ère industrielle (Fig. 6.1 ; Myhre et al., 2001) et une augmentation de la température de la surface a été observée (Fig. 1.1 ; *Folland et al.*, 2001).

Pourtant, cette augmentation n'a pas été aussi forte qu'attendu à partir de simulations avec des modèles de circulation générale (MCG) incluant seulement l'effet de serre (par exemple , *Mitchell et al.*, 2001). Ce fait pourrait être dû à une importante variabilité interne du système ou à l'existence d'autres forçages. Un forçage négatif dû aux aérosols anthropiques pourrait avoir contrebalancé une partie du réchauffement par effet de serre (par exemple, *Wigley*, 1989 ; *Charlson et al.*, 1989 ; *Boucher et Anderson*, 1995). Depuis deux décennies, les différents effets radiatifs des aérosols ont été étudiés. Pourtant, dans le rapport récent du Groupe Intergouvernemental d'Experts sur le Changement Climatique (GIEC ou IPCC en anglais), le niveau de la compréhension scientifique des effets des aérosols a toujours été qualifié de ≪ bas≫ voire de ≪ très bas≫ . Pourtant, il est largement accepté que les aérosols jouent un rôle majeur sur le changement climatique. En ce qui concerne les impacts des aérosols sur le rayonnement, les effets ≪ directs≫ , par modification de l'albédo planétaire par diffusion et absorption, et ≪ indirects≫ par modification des propriétés des nuages, peuvent être distingués.

Les nuages dans le système climatique

D'un point de vue météorologique, l'eau est le traceur le plus important dans l'atmosphère, dans laquelle elle existe dans les trois phases thermodynamiques. La source principale de l'eau dans l'atmosphère est l'évaporation aux surfaces océaniques et continentales. La vapeur d'eau est ensuite distribuée partout dans l'atmosphère. Elle interagit avec le bilan énergétique. Par évaporation et condensation, la chaleur latente est distribuée dans l'atmosphère. Comme un gaz absorbant dans le spectre infrarouge du rayonnement, la vapeur d'eau provoque un effet de serre important.

La vapeur d'eau se condense en eau liquide et solide pour former des nuages. Des nuages existent dans toutes les couches de la troposphère jusqu'à environ 11 km de hauteur. A des températures supérieures à 0°C, les nuages sont composés d'eau liquide, pour des températures inférieures à –35 - –40°C, de glace, et entre ces deux températures, des nuages mixtes peuvent exister (par exemple, *Houze*, 1993). Les nuages couvrent le globe à hauteur de 60% environ à chaque instant. Par condensation et évaporation et donc en redistribuant de la chaleur latente, ils interagissent avec le bilan énergétique. Dans le spectre solaire, ils réfléchissent le rayonnement et augmentent l'albédo planétaire, car ils sont en général plus réfléchissants que la surface terrestre. Cela est un forçage négatif. Dans le spectre infrarouge, des nuages exercent un effet de serre et donc un forçage positif. L'effet net des nuages sur le rayonnement est négatif pour les nuages bas, et il est positif pour les nuages hauts. En moyenne globale, leur effet net est négatif (*Kiehl et Trenberth*, 1997).

Les précipitations se forment dans les nuages par des processus microphysiques. Les nuages sont donc à l'origine de cette quantité météorologique importante. La précipitation est le puits final de la vapeur d'eau atmosphérique et influence ainsi la durée de vie des nuages et leur contenu en eau.

Représentation des nuages dans des modèles de grande échelle

Contrairement aux mouvements atmosphériques d'échelle synoptique, les processus de condensation et de la formation des nuages ne peuvent pas être décrits explicitement dans les modèles de grande échelle. Ils doivent donc être représentés à partir des variables explicitement calculées dans le modèle, une méthode qu'on appelle ≪ paramétrisation≫ . Dans les premiers MCGs, les nuages étaient simplement prescrits en utilisant des observations. Depuis, une multitude de paramétrisations a été créée. Quelques modèles considèrent chaque maille comme étant remplie entièrement par un nuage ou pas du tout (par exemple, *Fowler et al.*, 1996), alors que d'autres introduisent une fraction nuageuse entre 0 et 100% (par exemple, *Slingo*, 1987 ; *Le Treut et Li*, 1991). A l'exception de peu de modèles (*Del Genio et al.*, 1996 ; *Jakob et Klein*, 1999), un nuage est considéré remplir une couche entièrement sur la verticale.

La fraction nuageuse peut être calculée en utilisant une ≪ valeur critique≫ de l'humidité relative (par exemple, *Sundqvist*, 1978 ; *Lohmann et Roeckner*, 1996). D'autres suivent l'approche de *Sommeria et Deardorff* (1977) qui ont proposé une distribution de l'eau totale dans chaque maille qui suit une fonction de probabilité de densité (PDF en anglais). Une telle PDF peut être considérée comme étant par exemple uniforme (*Le Treut et Li*, 1991) ou triangulaire (*Smith*, 1990). Des approches récentes introduisent une PDF pronostique qui prédit des propriétés de la fonction à partir des processus physiques simulés comme la turbulence, la microphysique des nuages, et la convection (*Tompkins*, 2002).

Des nuages sont considérés homogènes partout dans la fraction nuageuse de la maille, ce qu'on appelle l'hypothèse plan-parallèle homogène (PPH). Cette hypothèse peut introduire des erreurs systématiques dans l'estimation de l'impact radiatif des nuages, en particulier dans le spectre des ondes courtes (par exemple, *Pincus et Klein*, 2000 ; *Cahalan*, 1994 ; *Stubenrauch et al.*, 1997). Des approches récentes existent qui traitent cette problématique qui pourtant restera en dehors de cette étude.

Les nuages représentés par des couches discrètes se recouvrent sur la direction verticale. Pour calculer ce recouvrement, qui est d'importance pour l'estimation des flux radiatifs et de la précipitation, on peut faire les hypothèses différentes tel qu'un recouvrement aléatoire, maximal ou un mélange entre les deux. Récemment, *Hogan et Illingworth* (2000) ont proposé une nouvelle paramétrisation qu'ils ont créée à partir d'observations radar.

Des GCM distinguent souvent des nuages ≪ convectifs≫ des nuages ≪ stratiformes≫ . Les premiers sont diagnostiqués par le schéma de convection, le dernier par des schémas de nuages et de précipitation du type de ceux décrits ci-dessus. On peut estimer la couverture nuageuse et le contenu en eau des nuages convectifs en utilisant le taux de précipitation prédit par le schéma de convection.

La microphysique des nuages

L'ensemble de tous les processus liés aux nuages ou à la précipitation et qui jouent à l'échelle des particules individuelles est connu sous le terme de ≪ microphysique des nuages≫ . Ces processus englobent la formation des gouttelettes des nuages et des cristaux de glace par activation d'aérosols hydrophiles ou nucléation, leur croissance par condensation, les processus qui conduisent à la formation de la précipitation et la croissance des particules de précipitation, et les transformations entre les différentes espèces d'eau. On peut distinguer les processus de la phase liquide (parfois appelée phase chaude) et de phase glace (froide).

L'activation de nouvelles gouttelettes dépend de la concentration en aérosols hydrophiles, et de la sursaturation qui, elle, est déterminée par la vitesse verticale à l'échelle du nuage (par exemple, *Twomey*, 1959). Les gouttelettes formées grandissent ensuite par condensation de la vapeur d'eau sur les particules. Si les gouttelettes ont des tailles différentes et donc des vitesses de chute différentes, elles peuvent entrer en collision et former des gouttes plus grandes. On parle d'autoconversion des gouttelettes de nuages pour former des gouttes de pluie. On peut considérer qu'il y a précipitation lorsque la taille des gouttelettes excède un ≪ rayon critique≫ (*Kessler*, 1969). A partir des observations, ce rayon a été déterminé à 10 μm (*Pawlowska et Brenguier*, 2003). Une fois que les gouttes de pluie existent, elles tombent à travers des populations de gouttelettes qu'elles collectent par le processus d'accrétion. La taille typique d'une gouttelette de nuages est de l'ordre de 3 à 20 μm alors que les gouttes de pluie ont une taille typique de 100 μm à 1 mm. Il faut donc de 10^2 à 10^7 gouttelettes d'eau nuageuse pour former une goutte de pluie, si l'on considère ces particules sphériques, ce qui est effectivement une très bonne approximation.

Des cristaux de glace peuvent être formés par la nucléation homogène, où un aérosol humide croît par la déposition de la vapeur d'eau. La nucléation hétérogène est la congélation d'une petite gouttelette initialement d'eau liquide par interaction avec un aérosol qu'on appelle ≪ noyau de congélation≫ ou ≪ noyau glaçogène≫ . Par un processus similaire à l'autoconversion, les cristaux forment des flocons de neige quand ils atteignent une certaine taille. Les particules de glace sont souvent considérés comme étant sphériques dans des modèles de grande échelle, bien que ce ne soit probablement pas toujours une bonne approximation (par exemple, *Doutriaux-Boucher et al.*, 2000).

Dans les nuages de phase mixte, des particules givrées peuvent être formées quand des particules liquides et solides entrent en collision. Dans ce cas, des cristaux ≪ secondaires≫ sont formées par le processus de Hallett-Mossop (*Hallett et Mossop*, 1974). Comme le rapport de mélange de la vapeur d'eau de saturation est supérieur par rapport à l'eau liquide que par rapport à la glace, des cristaux de glace vont grandir au dépens des gouttelettes, un processus que l'on appelle processus de Bergeron-Findeisen (*Bergeron*, 1933).

Dans des modèles, on peut traiter la microphysique en résolvant la taille des particules en ≪ size bins≫ (par exemple, *Young*, 1974a), ou dans un schéma ≪ bulk≫ en distinguant différentes espèces d'eau telles que l'eau liquide des nuages, la pluie, etc. (par exemple, *Kessler*, 1969). Les paramétrisations considérées dans cette étude appartiennent à ce second type. De tels schémas ont souvent été conçus pour des modèles capables de résoudre des processus dans les nuages (cloud resolving models en anglais), puis adaptés pour les modèles à grande échelle. Parmi les modèles pour lesquels ont été développés des schémas de microphysique se trouvent ECHAM (*Lohmann et Roeckner*, 1996), le MCG du Hadley Centre (*Jones et al.*, 1994 ; *Wilson et Ballard*, 1999), celui du CSIRO (*Rotstayn*, 1997), du GISS (*Del Genio et al.*, 1996), le CCM du NCAR (*Ghan et al.*, 1997b ; *Rasch et Kristjànsson*, 1998), le MCG du CCSR (*Takemura et al.*, 2000), ou encore celui de CSU (*Fowler et al.*, 1996).

Aérosols anthropiques et effets indirects des aérosols

Dans le contexte de la modélisation à l'échelle globale, on distingue habituellement six espèces d'aérosols, les sulfates, les aérosols carbonés organiques, le carbone suie, les sels de mer, et les poussières. Leurs propriétés les plus importantes sont leur origine (naturelle ou anthropique), leur caractère hydrophile ou hydrophobe, leur distribution en taille et leur capacité à absorber le rayonnement solaire.

Une propriété importante des aérosols est leur taille qui fait qu'ils sont déposés à la surface plus ou moins facilement. Des aérosols hydrophiles peuvent aussi être incorporés dans les gouttes de pluie et déposés par la précipitation. Les forçages radiatifs dus aux aérosols sont donc concentrés spatialement à proximité des sources.

Les aérosols hydrophiles servent comme noyaux de condensation dans les nuages. Une augmentation de la concentration en nombre de ces aérosols peut ainsi provoquer une augmentation de la concentration en nombre des gouttelettes. Pour un contenu en eau liquide fixe, le nuage contient ainsi plus de gouttelettes qui sont plus petites, et l'albédo du nuage augmente (premier effet indirect ; *Twomey*, 1974). Le processus d'autoconversion est moins efficace pour des gouttelettes plus petites, comme il l'a été expliqué ci-dessus. Donc, l'eau d'un nuage contenant des gouttelettes plus petites est moins vite transformée en pluie, ce qui augmente sa durée de vie, et son contenu en eau liquide moyen (deuxième effet indirect ; *Albrecht*, 1989). Historiquement, les effets indirects des aérosols ont été étudiés pour les nuages d'eau liquide, et c'est également le cas dans cette étude. Pourtant, des études récentes posent la question d'un impact possible des aérosols sur les nuages de glace par exemple dû aux avions (*Boucher*, 1999) ou aux poussières désertiques (*De Mott et al.*, 2003).

Les deux effets indirects des aérosols ont été mis en évidence dans de nombreuses études. Parmi les principales campagnes de mesures, on peut citer le projet ACE-2 avec les données duquel le chapitre 2 travaille (*Brenguier et al.*, 2000b). D'autres études importantes sont basées sur la campagne INDOEX (*Ramanathan et al.*, 2001a). Plusieurs études satellitaires ont étudié le contraste terre-mer, entre les hémisphères du Nord et Sud (par exemple, *Han et al.*, 1994), entre les sillages de bateaux ($\ll$ ship tracks$\gg$ en anglais) et leur environnement (par exemple, *Conover*, 1966), ou entre conditions polluées et non-polluées (*Rosenfeld*, 2000). D'autres études établirent des relations statistiques entre aérosols et propriétés des nuages (*Kaufman et Fraser*, 1997 ; *Nakajima et al.*, 2001 ; *Bréon et al.*, 2002).

2. The LMDZ GCM

2.1. Introduction

The atmospheric general circulation model of the Laboratoire de Météorologie Dynamique has been developed since the late 1970s. The recent version, named LMDZ.3.3 (*Li*, 1999), is the result of a new conception primarily of the dynamics of the GCM since the late 1980s. It constitutes the atmospheric component of the Earth System Model of the Institut Pierre Simon Laplace (IPSL; see Fig. 2.1). Other components of this model include

- the oceanic GCM Océan Parallélisé (OPA; *Guilyardi and Madec*, 1997), which includes a model for sea ice;
- a model simulating continental surfaces and biospheric processes, ORCHIDEE (Organizing Carbon and Hydrology In Dynamic EcosystEms; *Maynard and Polcher*, 2002; *de Rosnay et al.*, 2002; *Verant et al.*, 2003);
- a comprehensive atmospheric chemistry model INCA (Interaction with Chemistry and Aerosols; *Hauglustaine et al.*, 2003), which includes 99 tracers and about 300 photochemical reactions as well as aerosol cycles for sulfate, mineral dust, black and organic carbon, and sea-salt aerosols;
- an aerosol module treating the cycles of sulfate (*Boucher et al.*, 2002), carbonaceous (*Reddy and Boucher*, 2003), dust and sea salt aerosols;
- a model for lakes (*Krinner*, 2003).

In this thesis, for practical reasons, the aerosol cycles of *Boucher et al.* (2002) and *Reddy and Boucher* (2003) for sulfate, black and organic carbon, sea salt, and dust, will be used instead of INCA.

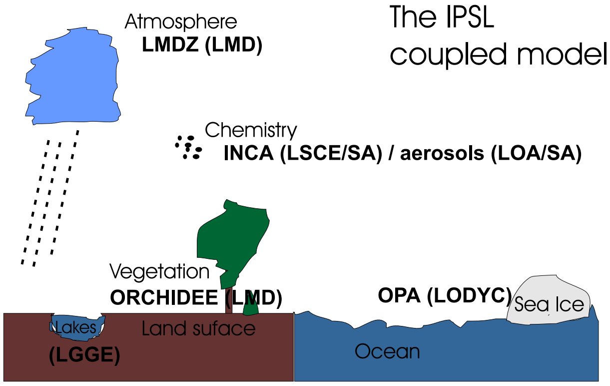

Figure 2.1.: Illustration of the Earth System Model of the IPSL.

The atmospheric model may be divided into a "dynamics" part which simulates the large-scale dynamical processes in the atmosphere, and a "physics" part, which describes the adiabatic processes. To a good approximation, the processes treated in the physics part at each point of the model grid can be considered independent from the surrounding cells, thus reducing the problem to one (the vertical) dimension.

2.1.1. Dynamics

The so-called "primitive equations", a set of nonlinear partial differential equations, describe the dynamics of the atmosphere. This set consists of the equations of motion which predict the horizontal winds, the thermodynamic equation which treats the time evolution of the temperature, the hydrostatic equation which links pressure to temperature, and the continuity equation which derives the vertical wind from the horizontal winds (e.g., *Trenberth*, 1995). The dynamical model variables are the horizontal winds, surface pressure, temperature, and total water content.

The primitive equations are solved numerically on a regular latitude-longitude grid. This grid, however, can be zoomed to increase the resolution to up to four times the standard resolution over any region of particular interest (*Le Van*, 1989). This technique is applied e.g. in Chapter 4. The variables of the model are evaluated using an Arakawa C grid. In the vertical, the equations are discretized using a hybrid sigma-pressure coordinate system. The timestep depends on the resolution and the choice of zooming or not the grid. In the studies presented, it is chosen as 180 s.

2.1.2. Physics

As mentioned earlier, the "physical" part of the model is assumed to be treatable independently in each grid column, using just the vertical dimension. The physics processes are simulated using a longer timestep compared to the dynamics part of 1800 s.

To a large extent, the physics of the Integrated Forecasting System (IFS) of the European Centre for Medium-Range Weather Forecasting (ECMWF) has been adapted in the LMDZ GCM (*White*, 2002). The planetary boundary layer turbulence is parameterized using an eddy-diffusivity approach, where the mixing coefficient is parameterized in terms of the Richardson number. The surface processes are evaluated in a bucket model, using the energy balance equation to diagnose the surface temperature. A review of this scheme is given in *Cheinet* (2002). A new approach to simulate convective boundary layers has been developed using a single column version of the LMDZ GCM (*Cheinet*, 2003; *Cheinet and Teixara*, 2003)), but is not yet implemented in the three-dimensional version.

For the deep convection parameterization, two approaches exist in the recent version of the LMDZ GCM, a scheme following *Tiedtke* (1989), and the parameterization of *Emanuel* (1991). Both of them are mass-flux schemes. As so far, the Emanuel scheme does not allow for the transport of tracers like aerosols in the model, the Tiedtke convection scheme is used in the present studies.

Radiative transfer is calculated in the model using a two-stream approximation, dividing the radiation in an upwelling and a downwelling flux. For the solar (SW) spectrum, a parameterization following *Fouquart and Bonnel* (1980) is used. This scheme takes into account two spectral bands of 0.25 to 0.68 μm and 0.68 to 4.0 μm. Cloud optical properties at each layer accounted for assuming a vertically random overlap of the fractional clouds. Cloud optical properties considered in the SW radiation scheme are cloud optical thickness, τ_c, single scattering albedo, ω_0, and cloud particle asymmetry parameter, g. The code also allows for scattering and absorption effects of aerosols in the SW radiation (aerosol direct effect). For the terrestrial (LW) spectrum, a code based on *Morcrette* (1991) is used in the GCM. This scheme considers six bands and calculates absorption and emission by molecules and clouds. Gases whose absorption is taken into account are water vapor, carbon dioxide, methane, nitrous oxide, and chlorofluorocarbons. The cloud radiative property of interest in the LW spectrum is its emissivity, ϵ. As radiation is computationally very expensive, it is applied only each 12th timestep of the physics, i.e., with a timestep of 6 hours.

2.2. Clouds and Precipitation

2.2.1. Standard model treatment

The GCM uses the total water content, q_t, as prognostic variable. In the model, all condensed water is re-evaporated before applying the physics parameterization. Following *Le Treut and Li* (1991), a "top-hat" probability density function (PDF) of the total water is assumed in each grid box (see Fig. 9.2), giving a uniform distribution between $(q_t\ (1-\Delta_{q_s}))$ and $(q_t\ (1+\Delta_{q_s}))$, where q_t is the grid box mean total water mixing ratio [kg kg^{-1}], and Δ_{q_s} is a parameter, which is considered to take vertically varying but otherwise constant values. Using this PDF, the horizontal fractional cloudiness in the grid box, f, is calculated as

$$f = \begin{cases} 0 & q_s > q_t\ (1+\Delta_{q_s} \\ \frac{q_t\ (1+\Delta_{q_s})-q_s}{2\ \Delta_{q_s}\ q_t} & q_s \in [q_t\ (1-\Delta_{q_s}), q_t\ (1+\Delta_{q_s})] \\ 1 & q_s < q_t\ (1-\Delta_{q_s} \end{cases} \tag{2.1}$$

where q_s is the saturation water vapor mixing ratio calculated in dependence of the temperature using the Tetens formula (*Tetens*, 1930). The total water content in the cloud covered fraction of the grid cell is determined as

$$q_t^{\mathrm{cc}} = \frac{q_s + \bar{q}_t + \Delta q}{2} \tag{2.2}$$

The total water content in the cloud-free part of the grid cell, q_t^{cf}, is calculated as the residual. The condensed water in the grid box is given by

$$q_c = f\ \left(q_t^{\mathrm{cc}} - q_s\right)\ \left(1 + \frac{L}{c_p}\frac{\partial q_s}{\partial T}\right)^{-1} \tag{2.3}$$

where the last term on the right-hand side takes into account the heating by latent heat release in the condensation process. The derivative $\partial q_s/\partial T$ is obtained from the Clausius-Clapeyron equation, and L is the latent heat taken as L_v, the latent heat of evaporation, for $T > 0°C$, and as L_s, the latent heat of sublimation, for $T < 0°C$.

When deep convection in a grid cell is simulated by the convection scheme, additional cloud water may be contributed by convective clouds. The cloud water from convective clouds is diagnosed using base and top of the convective cloud and convective rain rate calculated by the convection scheme. If the cloud water and cloud fraction calculated by this diagnostics exceed those of the stratiform scheme then they are used instead.

The condensed water is divided into liquid water and ice, depending on the local temperature, where the liquid fraction is given by

$$x_{\mathrm{liq}} = \begin{cases} 0 & T < T_{\mathrm{ice}} \\ \left(\frac{T-T_{\mathrm{ice}}}{T_0-T_{\mathrm{ice}}}\right)^{n_{\mathrm{x}}} & T \in [T_{\mathrm{ice}}, T_0] \\ 1 & T > T_0 \end{cases} \tag{2.4}$$

The parameters are taken as $T_0 = 0°\mathrm{C}$, $T_{\mathrm{ice}} = -15°C$, and $n_{\mathrm{x}} = 6$. In Chapter 8, this parameterization is evaluated using POLDER satellite data, and more realistic values of T_{ice} and n_{x} are derived.

Temperature is adjusted taking into account the latent heat of condensation or sublimation, respectively. The combination of the re-evaporation and the condensation scheme given above thus accounts for both, condensation of cloud water from water vapor and evaporation of cloud water.

Stratiform precipitation rate for liquid water clouds is calculated as

$$P_r = \frac{q_l}{\tau_p}\left[1 - \exp\left(-\left(\frac{q_l}{C_l}\right)^2\right)\right] \tag{2.5}$$

where q_l is the grid box mean liquid water mixing ratio given by $q_l = x_l\ q_c$, with x_l and q_c from the condensation scheme, τ_p a characteristic timescale for precipitation taken as 1800 s, and $C_l = 2 \times 10^{-4}\ kg\ kg^{-1}$ a precipitation threshold.

Snow formation in ice clouds is applied as a sedimentation term

$$P_s = \frac{q_i}{\Delta z}\ V_i \tag{2.6}$$

where q_i is the cloud ice mixing ratio ($q_i = (1-x_l)\ q_c$), Δz the layer thickness, and $V_i = 3.29\ (\rho_{air}\ q_i)^{0.16}$ the terminal fall-velocity of ice crystals (*Heymsfield and Donner*, 1990).

The evaporation of rain water is derived from a parameterization of *Kessler* (1969):

$$E_r = \alpha\left(1 - \frac{q_t}{q_s}\right)\sqrt{P_r}\ \Delta z \tag{2.7}$$

with a coefficient $\alpha = 2. \times 10^{-5} ms^{-1}$, and the precipitation flux, P_r and the layer thickness, Δz, taken without dimension. Both rain and snow are leaving the grid column in a single timestep. Whether it is rain or snow that reaches the surface is decided by the temperature of the lowest model layer being lower or larger than 0°C.

Concerning the cloud optical properties, the asymmetry parameter, g, is taken to be constant in the model, using $g = 0.865$ in the first and $g = 0.910$ in the second of the two spectral bands in the scheme of *Fouquart and Bonnel* (1980). Cloud optical thickness (COT) is defined as the vertical integral of the extinction, σ, of a cloud, which for spherical particles can be described as:

$$\begin{aligned}\tau_c &= \int_{z_{base}}^{z_{top}} \sigma dz = 2\pi \int_{z_{base}}^{z_{top}} \int_0^{\infty} r^2 \; n(r) dr dz \quad (2.8)\\ &= 2\pi \int_{z_{base}}^{z_{top}} \left(\int_0^{\infty} r^3 \; n(r) dr \right) \left(\frac{\int r^2 \; n(r) dr}{\int r^3 n(r) dr} \right) dz\end{aligned}$$

where $n(r)$ is the droplet size distribution, and z_{base} and z_{top} are cloud base and cloud top height, respectively. One can define an "effective radius", r_e, of the droplets as the ratio

$$r_e = \frac{\int r^3 \; n(r) dr}{\int r^2 n(r) dr} \qquad (2.9)$$

With the assumption of a constant r_e throughout the cloud and the definition of the liquid water path, W, the optical thickness may be parameterized as (*Stephens*, 1978)

$$\tau_c = \frac{3}{2} \frac{W}{\rho_{water} \; r_e} \qquad (2.10)$$

In the model, ice crystals are assumed to be of spherical shape with a constant effective radius of 35 μm, while the effective radius of liquid droplets is assumed to be 9 μm in the three lowest layers of the model and 13 μm otherwise.

The single scattering albedo of a cloud, ω, is parameterized in terms of COT:

$$\omega_0 = a_1 - a_2 \times 10^{a_3} \; \exp(-a_4 \; \tau_c) \qquad (2.11)$$

where the coefficients a_1-a_4 are slightly different in the two SW spectral bands. Finally, the emissivity of the clouds, ϵ, necessary in the LW radiative transfer is parameterized in terms of the liquid water path

$$\epsilon = 1 - \exp\left(-\alpha \; W\right) \qquad (2.12)$$

where the coefficient α is 0.13 for liquid and 0.09 for ice clouds.

2.2.2. The microphysical scheme of Boucher et al.

A refinement for studying aerosol effects compared to the standard scheme has been introduced by *Boucher and Lohmann* (1995), who diagnose the cloud droplet number concentration (CDNC, N_d) of liquid droplets from sulfate aerosol mass concentration, m_a, given in [μg sulfate m^{-3}] (formula "D"):

$$N_d = 10^{a_0 + a_1 \log{(m_a)}} \qquad (2.13)$$

where the empirical constants are $a_0 = 2.21$ and $a_1 = 0.41$, which were obtained from a fit to simultaneously measured sulfate aerosol masses and CDNC at various locations on the globe. Sulfate is used as a surrogate for all hydrophilic aerosols, bearing in mind that at least organic and sea salt aerosols constitute efficient CCN as well (*Novakov and Penner*, 1993). CDNC is given in m^{-3}. Assuming spherical particles, the volume-mean droplet radius, r_{dv} is calculated as

$$r_{dv} = \sqrt[3]{\frac{q_l \; \rho_{air}}{\frac{4\pi}{3} \; \rho_{water} \; N_d}} \qquad (2.14)$$

The effective radius of a droplet is linked to the volume-mean droplet as $r_e = 1.1 \; r_{dv}$ (*Pontikis and Hicks*, 1993).

The microphysics scheme of *Boucher et al.* (1995a) keeps the condensation/evaporation scheme and thus the determination of fractional cloudiness as well as the microphysical processes related to ice clouds, i.e., the snow formation. It introduces, however, microphysical processes of precipitation formation for liquid water clouds using autoconversion of cloud droplets to form rain and accretion of raindrops by collection of cloud droplets. The autoconversion rate, r_{ll}, is parameterized as

$$r_{ll} = c_1 \; H(r_e - r_0) \; q_l \; r_e^4 \; N_d \qquad (2.15)$$

where $H(x - x_0)$ is the Heaviside function. The "critical radius" r_0 is set to 8 μm in the model, a value slightly smaller than that observed from *Pawlowska and Brenguier* (2003). The parameter c_1 is the product of several constants and set to $c_1 = 0.1$ in the model. From Eqs. 2.14 and 2.15 it can be deduced that the autoconversion rate depends linearly on CDNC for $r_e > r_0$. The process of collision and coalescence of raindrops and cloud droplets is known as accretion, r_{rl}. This process is parameterized as

$$r_{rl} = c_2 \; q_l^{\mathrm{cc}} \; q_r \; \sqrt{\frac{\rho_{air}}{D_r}} \qquad (2.16)$$

where q_r is the rain water mixing ratio, and D_r the characteristic raindrop diameter of a Marshall-Palmer size distribution (*Marshall and Palmer*, 1948). The coefficient c_2 is the product of several constants, and is set to $c_2 = 0.7$ in the model. Evaporation of rain water is calculated following *Liu and Orville* (1969) as

$$E_r = -\frac{\alpha}{2}\left(\frac{q_t^{\mathrm{cf}}}{q_s} - 1\right)\frac{q_r}{\rho_{water}\ D_r^2} \qquad (2.17)$$

where ρ_{water} the density of liquid water. The coefficient $\alpha = 0.42 \times 10^{-5}\mathrm{km\ m^{-1}s^{-1}}$ is given by *Liu and Orville* (1969).

2.3. Comparison standard vs. Boucher scheme

The new scheme is compared with the standard model scheme and evaluated against observations in Figs. 2.2 to 2.5. For the total cloud cover, data from the International Satellite Cloud Climatology Project (ISCCP; *Rossow and Schiffer*, 1991) is averaged over 1984 to 1992. Cloud radiative forcings are taken from the Scanner of the Earth Radiation Budget (ScaRaB; *Kandel et al.*, 1998), for the March 1994 to February 1995 period, with the data for October 1994 missing. Precipitation over continents is used from the Global Precipitation Climatology Project (GPCP; *Huffman et al.*, 1997), for 1997. The model output is from a one year simulation forced with SST for 1997 from *Reynolds and Smith* (1995). We show zonal mean values for the annual global mean (in case of precipitation, over continents only), for northern hemisphere summer (June-July-August, JJA), for northern hemisphere winter (December-January-February, DJF), the annual mean over continents, and over oceans. Generally, the scheme of *Boucher et al.* simulates cloud and precipitation distributions which are rather similar to those simulated by the standard model scheme, and compares well with the observations. The scheme of *Boucher et al.* underestimates cloud cover in the annual mean by up to 5% in some regions of the northern hemisphere and up to 10% in some regions in the southern hemisphere, which is due to a too small cloud amount over land in the northern hemisphere and over oceans in the southern hemisphere. However, except maybe for a small region over land (around 20°N), it does generally a better job than the model's standard scheme.

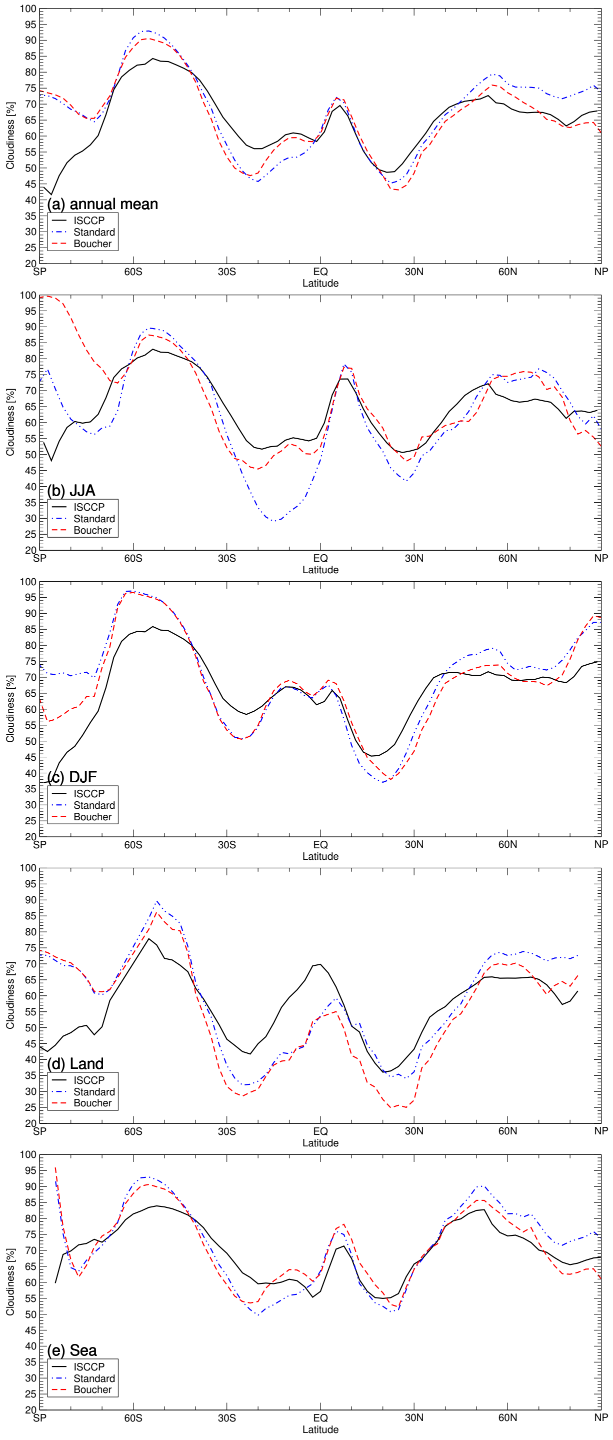

Figure 2.2.: Zonal mean cloudiness, from ISCCP observations (solid, black), for the standard scheme of the model (dot-dashed, blue), and for the scheme of *Boucher et al.* (dashed, red). For (a) annual global mean, (b) JJA global mean, (c) DJF global mean, (d) annual mean over continents, (e) over oceans.

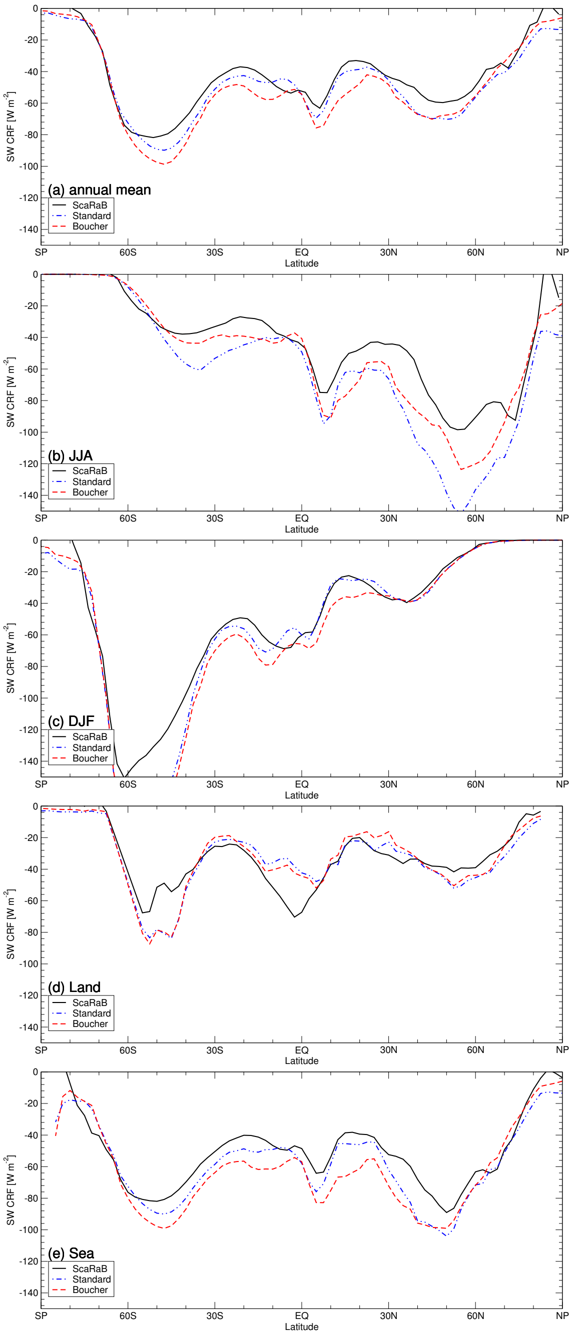

Figure 2.3.: Zonal mean SW cloud radiative forcing at the top of the atmosphere, from ScaRaB observations (solid, black), for the standard scheme of the model (dot-dashed, blue), and for the scheme of *Boucher et al.* (dashed, red). For (a) annual global mean, (b) JJA global mean, (c) DJF global mean, (d) annual mean over continents, (e) over oceans.

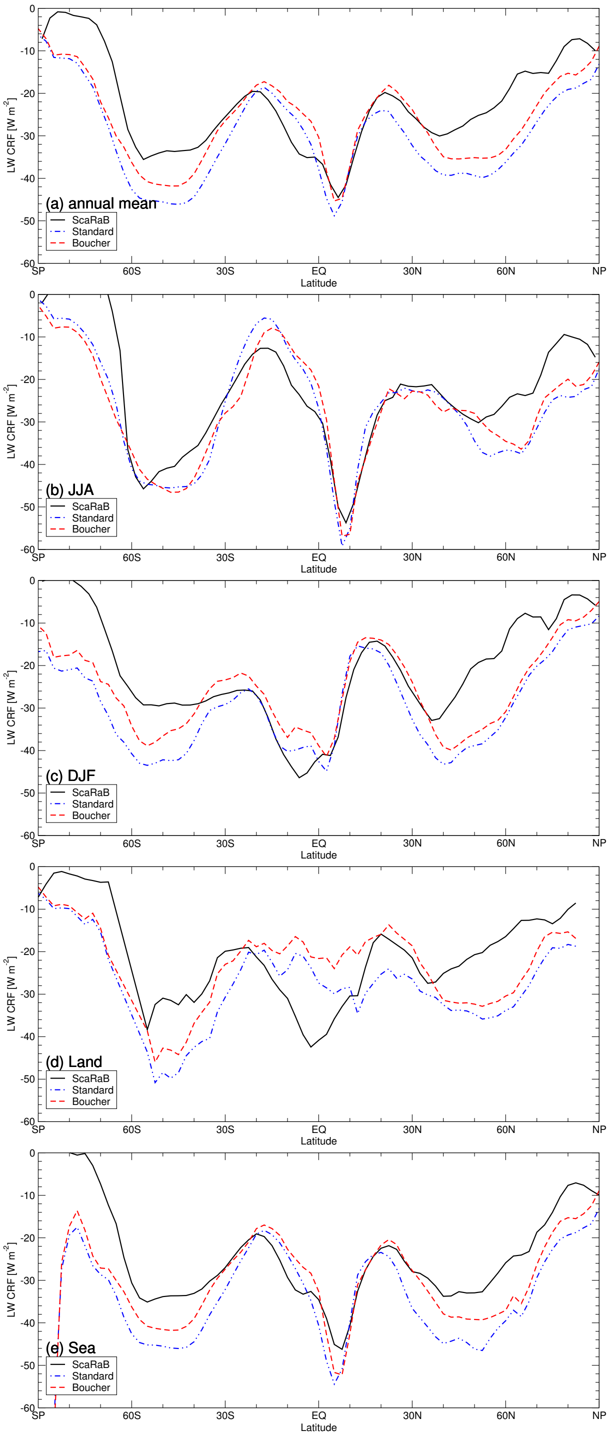

Figure 2.4.: As Fig. 2.3, but for LW cloud radiative forcing.

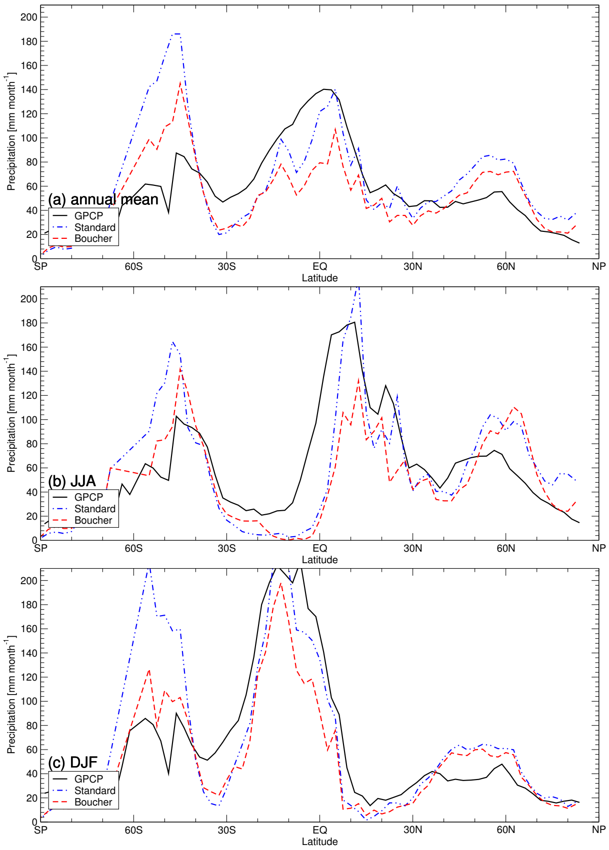

Figure 2.5.: Zonal mean precipitation [mm month^{-1}], from GPCP observations (solid, black), for the standard scheme of the model (dot-dashed, blue), and for the scheme of *Boucher et al.* (dashed, red). For (a) annual global mean, (b) JJA global mean, (c) DJF global mean.

Generally, the SW cloud radiative forcing simulated by the scheme of *Boucher et al.* is too strong, by several percent. This overestimation is better than for the standard scheme for JJA, but slightly worse for DJF and over also oceans for the annual mean. However, the LW CRF is much better using the scheme of *Boucher et al.* compared to the standard scheme even though both model versions show too strong LW cloud radiative forcing compared to the ScaRaB observations. Precipitation generally is simulated well by both schemes, with a slight underestimation of the rainfall at low latitudes by the scheme of *Boucher et al.*.

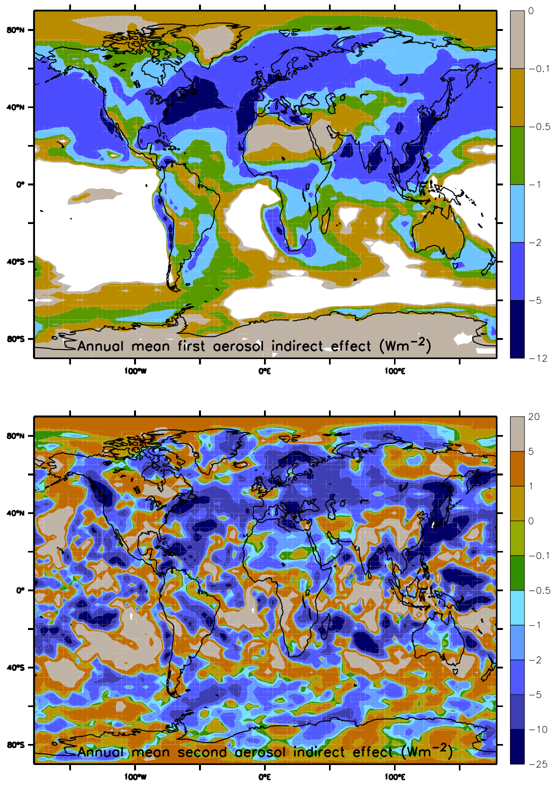

Figure 2.6.: Aerosol indirect effects by sulfate aerosols in the annual mean in the LMDZ using the scheme of *Boucher et al.* [Wm^{-2}]. (a) the first aerosol indirect radiative forcing and (b) the second aerosol indirect effect diagnosed as the "quasi-forcing".

For high and midlatitudes, however, the new microphysics scheme is closer to the observations, which is remarkable in particular for the southern hemisphere. It should be noted that some of the differences between the schemes and observations may be due to internal variability as a particular year has been simulated.

2.4. Conclusion: The aerosol indirect effects

Using the microphysical scheme of *Boucher et al.* and the empirical link between sulfate aerosol mass, the aerosol indirect effects have been evaluated in the model. Figure 2.6 shows the distributions of the

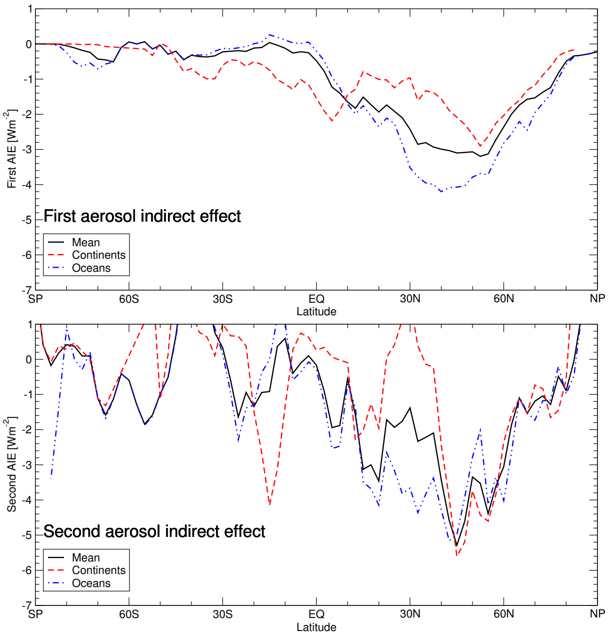

Figure 2.7.: Zonal mean aerosol indirect radiative (quasi-)forcings [Wm^{-2}], over land (red, dashed), over sea (blue, dash-dotted), and for the whole area (black, solid), for the annual mean (a) first aerosol indirect effect and (b) second aerosol indirect effect.

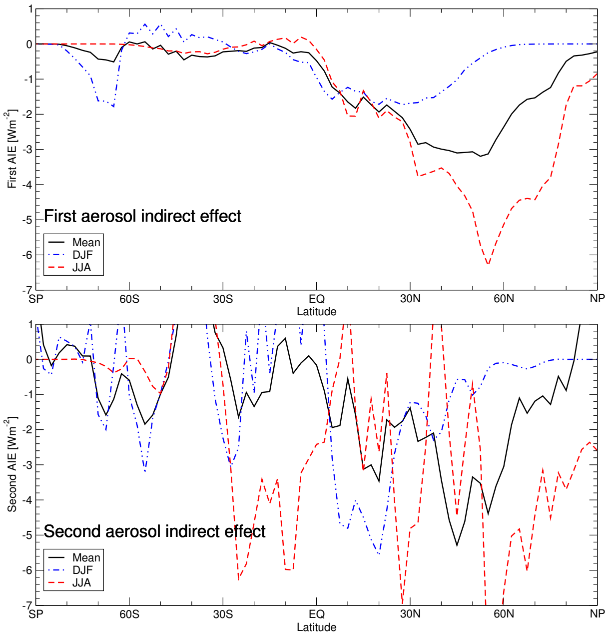

Figure 2.8.: Zonal mean aerosol indirect effects [Wm^{-2}], for June-July-August (red, dashed), for December-January-February (blue, dash-dotted), and for the annual mean (black, solid), for the annual mean (a) first aerosol indirect effect and (b) second aerosol indirect effect.

annual mean of both aerosol indirect effects, where the second indirect effect is estimated using the "quasi-forcing" definition of *Rotstayn and Penner* (2001). The first aerosol indirect effect is strongest in the northern hemisphere midlatitudes, where the main source regions for anthropogenic aerosols are located. In particular, marine clouds near the industrialized zones of North America, Western Europe, and East Asia are affected, showing an aerosol indirect effect of up to –12 Wm^{-2}. Over land, there is a belt of strong aerosol indirect forcing over the midlatitudes of the Eurasian continent. For the second indirect effect, much more scatter is observed. Due to the "quasi-forcing" definition, also cloud feedback processes other than the second aerosol indirect effect are included (see Chapter 6 for a discussion of this difficulty). Nevertheless, it can be identified that there are strong effects of aerosols particularly in the northern hemisphere, with quasi-forcing values of up to –25 Wm^{-2} over certain regions even in the annual mean.

Figure 2.7 shows the zonal annual mean of the aerosol indirect effects over land, oceans, and for the whole area. The first AIE clearly is stronger over oceans, as expected, as low-level marine stratocumulus clouds are the most affected. For the second AIE, a similar result can be found, although it is less pronounced. The second AIE is found to be of equal magnitude as the first AIE. Figure 2.8 shows the zonal mean of the aerosol indirect effects for northern hemisphere summertime (June-July-August, JJA) and wintertime (December-January-February, DJF), and for the annual mean. It is clearly found that both AIEs are stronger in summertime, as they are concentrated in the northern hemisphere and are active in the solar spectrum. For the global annual mean, the first aerosol indirect radiative forcing in our model is for sulfate aerosol concentrations at the end of the 20th century (≈ 1990) of –1.1 Wm^{-2}, and the quasi-forcing due to the second aerosol indirect effect of –1.2 Wm^{-2}.

2.5. Le modèle LMDZ : Résumé

Introduction

Le modèle de circulation générale atmosphérique du Laboratoire de Météorologie Dynamique est développé depuis les années 1970. Il représente la partie atmosphérique du modèle du système terrestre de l'Institut Pierre Simon Laplace (IPSL, voir Fig. 2.1). D'autres parties de ce modèle couplé sont le modèle de l'océan OPA (*Guilyardi et Madec*, 1997), un modèle de glace, le modèle de la surface continentale et de la végétation ORCHIDEE (*Maynard et Polcher*, 2002 ; *de Rosnay et al.*, 2002 ; *Verant et al.*, 2003), le modèle de la chimie atmosphérique INCA (*Hauglustaine et al.*, 2003) et un modèle de lacs (*Krinner*, 2003). Les cycles biogéochimiques des aérosols soufrés (*Boucher et al.*, 2002), carbonés (*Reddy and Boucher*, 2003), des sels de mer et des poussières ont également été développés pour LMDZ. Pour des raisons pratiques, c'est ce dernier module et non INCA qui sera utilisé dans cette thèse.

On peut diviser le modèle atmosphérique en une partie ≪ dynamique≫ qui traite les processus dynamiques à grande échelle, et une partie ≪ physique≫ qui décrit les processus adiabatiques. La dernière partie peut être traitée de manière unidimensionnelle en faisant l'hypothèse que chaque colonne de la maille horizontale est indépendante des autres.

Dans la partie dynamique, le jeu d'équations ≪ primitives≫ est résolu de manière numérique. Il contient les équations de mouvement pour les vents horizontaux, l'équation thermodynamique pour la température, l'équation hydrostatique qui lie la pression et la température, et l'équation de continuité pour calculer le vent vertical à partir des vents horizontaux (voir par exemple, *Trenberth*, 1995). La grille horizontale du modèle est une grille latitude - longitude qui peut être zoomée sur une région d'intérêt particulier où la résolution peut être augmentée jusqu'à un facteur 4. Dans la direction verticale, une coordonnée hybride de pression et niveaux sigma est utilisée.

La partie physique a été en partie adaptée du modèle IFS de l'ECMWF. La turbulence de la couche limite planétaire est paramétrée en utilisant l'approche dite de ≪ eddy-diffiusivity≫ et le coefficient de mélange est calculé en utilisant le nombre de Richardson. A la surface continentale, la température de la surface est diagnostiquée à partir de l'équation du bilan énergétique. Pour le traitement de la convection profonde dans le modèle, deux schémas de flux de masse peuvent être appliqués, celui de *Tiedtke* (1989) et celui d'*Emmanuel* (1991). Le premier est utilisé dans toutes les études de cette thèse.

Le transfert du rayonnement est paramétré avec l'approximation de deux courants ascendants et descendants, et deux bandes spectrales dans la partie solaire (ondes courtes, shortwave ou SW en anglais) et quatre dans la partie terrestre (ondes longues, longwave ou LW). Dans le spectre des ondes courtes, LMDZ utilise le schéma de *Fouquart et Bonnel* (1980) qui introduit deux bandes spectrales. L'épaisseur optique, τ_c, l'albédo de diffusion simple, ω_0, et le paramètre d'asymétrie, g, sont utilisés pour calculer le flux du rayonnement dans le ciel nuageux. Sur la verticale, la couverture nuageuse fractionnaire des différentes couches est supposée se recouvrir de manière aléatoire. Dans les ondes longues, le flux du rayonnement est calculé suivant la paramétrisation de *Morcrette* (1991), avec six bandes. Pour les nuages, l'émissivité, ϵ, est utilisée pour tenir compte de leur absorption et émission de rayonnement ondes longues dans l'atmosphère.

Nuages et précipitation

Le modèle utilise le rapport de mélange de l'eau totale comme variable pronostique. Toute l'eau condensée est ré-évaporée avant que le schéma de nuages et de précipitation ne soit appliqué. Suivant *Le Treut et Li* (1991), une fonction de densité de probabilité (PDF en Anglais) uniforme est considérée pour l'eau dans chaque maille. La partie de cette PDF qui dépasse le rapport de mélange de saturation donne la fraction nuageuse de la maille, et la partie d'eau qui se trouve dans cette partie et qui excède la saturation est condensée. Au cas où le modèle simule de la convection profonde, une fraction nuageuse et une quantité d'eau condensée sont calculées à partir de la précipitation prédite par le schéma de convection. Si ces valeurs dépassent celles qui sont calculées par le schéma ≪ stratiforme≫ décrit auparavant, celles-ci sont utilisées au lieu des dernières. L'eau condensée est partagée en eau liquide et en glace à partir de la température locale. Si celle-ci dépasse 0°C, toute l'eau est liquide, si elle est inférieure à –15°C, toute l'eau est glace, et entre les deux, une transition est considérée.

Dans la version standard du modèle, la précipitation est calculée de manière simple et dépend du contenu d'eau condensée dans la maille. Quand elle tombe à travers des couches claires, la précipitation peut s'évaporer. Concernant les propriétés optiques des nuages, l'épaisseur optique est liée au rapport entre la colonne d'eau condensée et le rayon effectif des particules dans la maille en considérant des particules sphériques de taille constante. L'albédo de diffusion simple est une fonction de l'épaisseur optique et le paramètre d'asymétrie est pris constant. Enfin, l'émissivité est calculée à partir de la colonne d'eau condensée.

Le schéma microphysique de *Boucher et al.*

Le changement principal entre le schéma microphysique des nuages présenté ici et le schéma standard est le fait que la concentration en nombre des gouttelettes (CDNC en anglais) est calculée et non plus implicitement diagnostiquée. Elle est liée à la concentration en masse des aérosols de sulfates suivant l'approche ≪ empirique≫ de *Boucher et Lohmann* (1995) qui ont examiné des mesures simultanées de CDNC et de masse de sulfates. La taille des particules, considérées comme étant sphériques, peut être calculée à partir du nombre de gouttelettes et de l'eau condensée. Cela ouvre la possibilité de calculer le premier effet indirect des aérosols. *Boucher et al.* (1995) ont également introduit des formules pour paramétriser la précipitation liquide en décrivant l'autoconversion des gouttelettes pour former des gouttes de pluie, la collision et la coalescence entre gouttelettes des nuages et gouttes de pluie qui aussi transforment gouttelettes en pluie. La paramétrisation des nuages de glace et de la neige n'a pourtant pas été changée.

Dans le chapitre 2 deux simulations avec LMDZ ont été comparées aux observations, dont une utilisait la version standard et l'autre incluait le schéma microphysique. Il a été montré que la couverture nuageuse ne change pas beaucoup entre les deux simulations et qu'elle est proche des observations (fig. 2.2). Le forçage radiatif des nuages dans les ondes courtes et dans les ondes longues est bien simulé dans les deux versions du modèle, et la version qui inclut la microphysique est même un peu meilleure dans les ondes longues (figs. 2.3 et 2.4). La précipitation sur les continents est bien simulée dans les deux versions du modèle (fig. 2.5).

Les deux effets indirects ont été estimés en utilisant le schéma de microphysique (fig. 2.6). Le premier effet indirect est concentré sur les moyennes latitudes de l'hémisphère nord où se trouvent les principales sources des aérosols. Il atteint –12 $\mathrm{Wm^{-2}}$ dans les régions des stratocumulus maritimes au large des côtes Est des continents de l'hémisphère nord. Le forçage est particulièrement fort dans les moyennes latitudes du continent eurasiatique. Le quasi-forçage par le deuxième effet indirect, ainsi qu'il a été défini par *Rotstayn et Penner* (2001), est beaucoup plus bruité. Il atteint jusqu'à –25 $\mathrm{Wm^{-2}}$ dans certains régions. Les deux effets indirects sont plus marqués sur océan que sur continent (fig. 2.7), et ils sont plus forts en été de l'hémisphère nord (juin-juillet-aot, JJA) qu'en hiver (décembre-janvier-février, DJF ; fig. 2.8). En moyenne globale et annuelle, on trouve un forçage de –1.1 $\mathrm{Wm^{-2}}$ pour le premier effet indirect et de –1.2 $\mathrm{Wm^{-2}}$ pour le second effet indirect pour des concentrations en aérosols de l'année 1990.

3. POLDER satellite observations

3.1. Introduction

Satellite instruments generally measure radiances at the top of the atmosphere. As the radiances depend on the state of the Earth surface and the atmosphere, information can be deduced about a variety of atmospheric and surface quantities. The radiances measured by satellite instruments in the shortwave spectrum consists of the part of the solar radiation reflected by the Earth's surface or by different components of the atmosphere. The longwave (LW) or terrestrial part of the spectrum refers to wavelengths of 4 to 25 μm, which corresponds to the radiation emitted by the Earth's surface or by molecules in the atmosphere. Common instruments measure the intensity of the radiation in different bands of wavelengths, also known as "channels" of the instrument. From the knowledge about scattering and absorption properties of different constituents of the atmosphere, some information about the distribution of these components can be deduced from the measured signal.

Satellites may be divided into two categories. Geostationary satellites are positioned above the Equator at the specific height at which their rotation speed is identical to that of the Earth. Thus, the same region of the Earth is always observed. The advantage is that in principle a continuous measurement is possible. A disadvantage is that only a part of the globe is observed and that in particular for high latitudes the measurement is not very reliable. Further on, their relatively high altitude makes the measured signal weaker. The second class of satellites are polar-orbiting platforms. Such satellites rotate at a fixed path, letting the Earth turn below them. Typically, each point of the Earths surface is passed about once a day for a swath of about 2500 km, where the high latitudes are measured several times a day and the low latitudes more sparsely. Instruments may be able to measure also along or across the track of the satellite.

3.2. The POLDER instrument

The POLarization and Directionality of the Earth's Reflectance (POLDER) instrument was developed by the Laboratoire d'Optique Atmosphérique (LOA) and the French Centre National d'Études Spatiales (CNES). It is the first satellite instrument to be able to measure spectral, directional and polarized characteristics of the reflected solar radiation simultaneously (*Deschamps et al.*, 1994). In particular the polarization of the radiation measured by the satellite instrument provides a new possibility to deduce properties of the constituents of the atmosphere.

The instrument uses 15 spectral bands between 0.44 and 0.91 μm. It measures in a range of ± 43° along the track of the satellite and ± 51° across the track, yielding a swath of 2400 km in width. The resolution at nadir is of 6 x 7 km^2. A "superpixel" in the data obtained consists of 9 image pixels giving a resolution of about 0.5°x0.5° at the Equator.

The POLDER-1 instrument was mounted on the Japanese ADEOS-1 platform. Data from November 1996 until June 1997 are available. Since December 2002, the POLDER-2 instrument is operating on the ADEOS-2 satellite.

3.3. Derived physical data

A multitude of physical information can be derived from the POLDER measurements, including land surface properties, ocean color, radiation budget measurements, and informations about clouds and aerosols. The latter two are of particular interest in the present study. Concerning the aerosols, the aerosol optical thickness, τ_a, is derived in the 865 nm channel over oceans (*Deuzé et al.*, 1999). Further on, the Ångström coefficient, α, which is a measure of the particle size, is derived over both oceans and continents using the polarized measurements in the 865 and 670 nm channels. A POLDER aerosol index (AI) is defined as the product of Ångström coefficient and aerosol optical thickness, $\alpha\tau_a$. This index is calculated over both land and ocean (*Deuzé et al.*, 2000; *Goloub and Arino*, 2000; *Deuzé et al.* 2001 *Tanré et al.*, 2001). All aerosol products are derived for cloud-free pixels according to the cloud screening algorithm of *Bréon and Colzy* (2000).

In this study the cloud optical thickness, cloud droplet effective radius, cloud top temperature, and cloud top thermodynamic phase will be used. In order to deduce the cloud top temperature, first, the cloud top Rayleigh pressure is first retrieved from the polarized signal at 443 nm (*Vanbauce et al.*, 1998). The temperature is then obtained by using the six-hourly ECMWF analysis data. The cloud thermodynamic phase retrieval is based on the angular and polarized signatures of cloud reflected radiances at scattering angles near 140° (*Goloub et al.*, 2000; *Riedi et al.*, 2000). Cloud optical thickness is derived in a manner similar to that used in the ISCCP (*Rossow and Schiffer*, 1991), assuming a homogeneous plane-parallel liquid water cloud with an effective radius of 10 μm (*Buriez et al.*, 1997; *Parol et al.*, 2000), using up to 14 viewing directions in the 670 nm channel. For liquid water clouds homogeneous at a large scale (150 x 150 km^2), *Bréon and Goloub* (1998) derive from the multi-directional polarized radiance measurements a cloud top droplet effective radius.

3.4. Comparison of LMDZ and POLDER data

In order to compare POLDER-derived physical quantities to those simulated by the LMDZ GCM, an integration of the model was carried out for the period of the observations from November 1996 to December 1997. To get realistic conditions of the dynamics, the sea surface temperature and sea ice extent were imposed from the *Reynolds and Smith* (1995) and the HADISST1.1 (*Rayner et al.*, 2003) datasets. Horizontal winds and temperature in the model were nudged to ECMWF reanalysis data using relaxation time constants of 0.1 day for the winds and 1 day for the temperature, respectively. The swath of the satellite is sampled in the model to give a daily coverage of the globe in the same way the POLDER instrument does it. Finally, for cloud droplet radius, cloud top temperature, and cloud top thermodynamic phase, the cloud top quantities are calculated for the top of the atmosphere using the random overlap assumption for the fractional cloudiness in the vertical. Figure 3.1 shows the comparison of the distributions obtained for model simulations and POLDER observations, averaged over the whole 8-month period. POLDER data is averaged to the coarser model grid.

For the aerosol index, the model simulates well the land-sea contrast in the aerosol burden. However, the aerosol burden diminishes too strongly away from the main source regions. Where the POLDER observations show relatively large aerosol burdens over almost all continental surfaces, the model shows rather low values for some regions of the South and North American continents and over Australia. Negative aerosol indices represent large aerosol particles. It is however rather difficult to interpret the differences in model and observations as in particular for small aerosol burdens the observations may not be very reliable either.

Cloud optical thickness generally is overestimated by the model, a problem common to GCMs, which is partly due to the coarse vertical resolution and the assumption of plane-parallel homogeneous clouds.

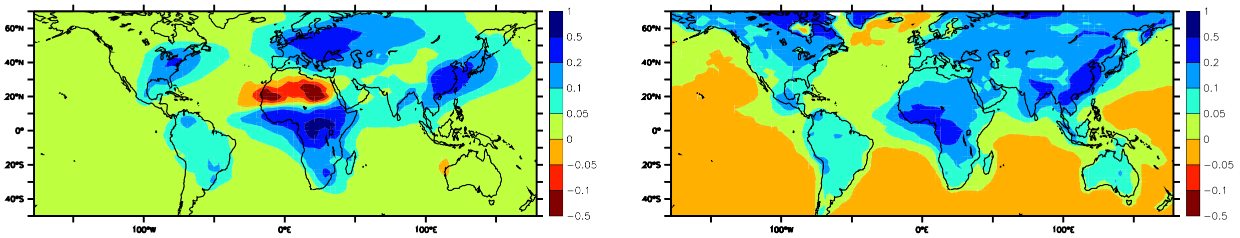

(a) Aerosol index, LMDZ (b) Aerosol index, POLDER

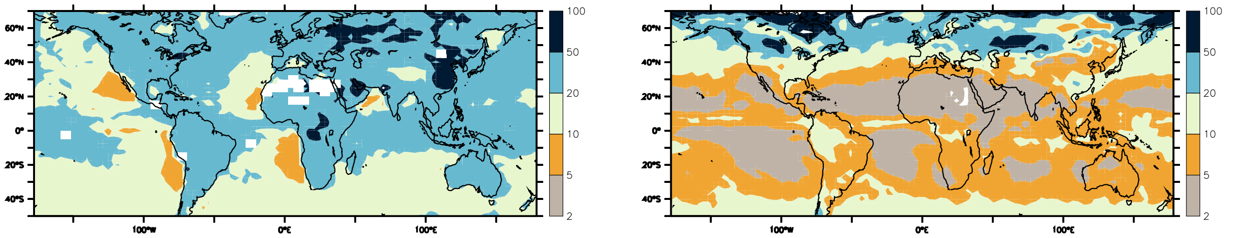

(e) Cloud opt. thickness, LMDZ (f) Cloud opt. thickness, POLDER

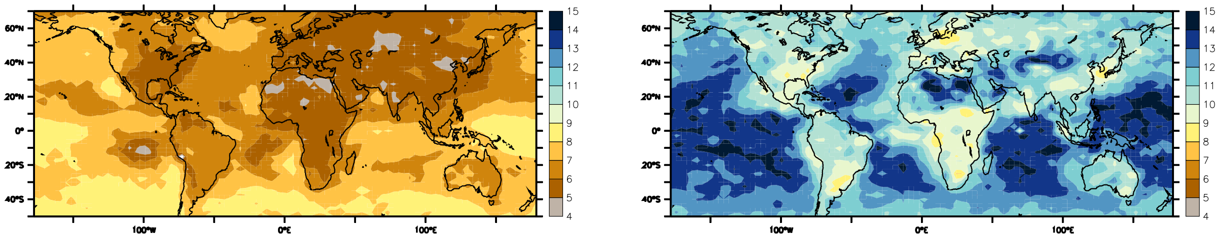

(c) CDR, LMDZ (d) CDR, POLDER

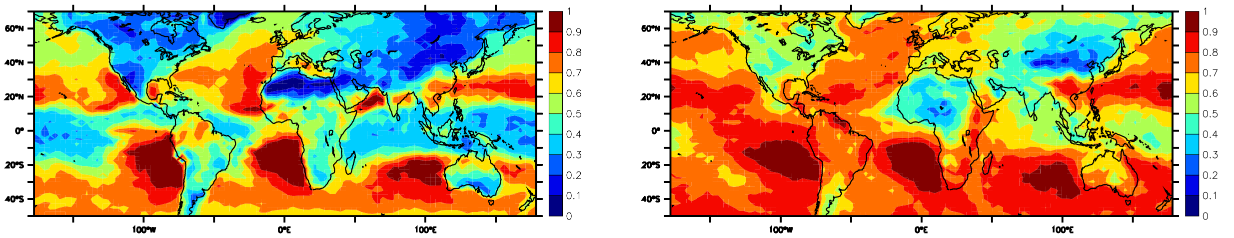

(g) Cloud top thdyn phase, LMDZ (h) Cloud top thdyn phase, POLDER

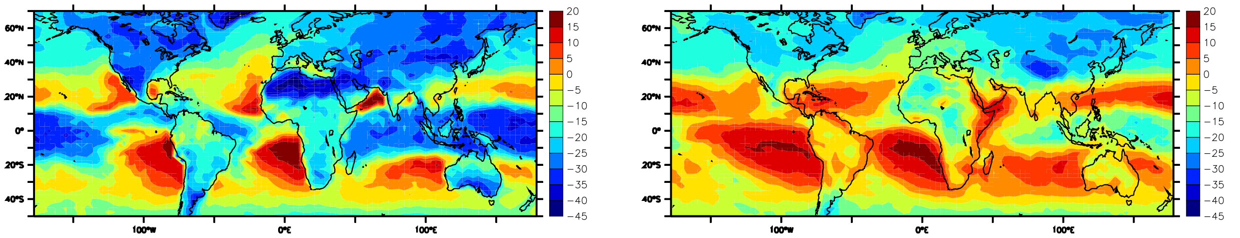

(i) Cloud top temperature, LMDZ (k) Cloud top temperature, POLDER

Figure 3.1.: Comparison of aerosol index for (a) the LMDZ model and (b) POLDER data, (c-d) cloud optical thickness, (e-f) cloud top droplet radius [μm], (g-h) cloud top thermodynamical phase, and (i-k) cloud top temperature [°C], for the period November 1996 to June 1997.

However, several features are well simulated. Optical thicknesses are larger in the northern hemisphere, and generally somewhat larger over land than over oceans. The larger optical thickness in the ITCZ region is well simulated.

The cloud droplet effective radius is estimated for large scale liquid water clouds in both model and observations and taken at the cloud top. The model shows generally too low CDR values, underestimating the size of the droplets by 2-3 μm on average. The contrast of larger droplets over oceans than over land is observed in both LMDZ model and POLDER data. Similarily, a contrast between both hemispheres is well simulated in the model. Particularly small radii over the industrialized regions of the northern hemisphere, the eastern part of North America, Europe, and East Asia, and off the east coasts of the North American and Asian continents is found in both, model and observations.

Concerning the cloud top thermodynamical phase, the model often simulates too many ice clouds (low values in Fig. 3.1). However, it is able to simulate more ice clouds over the continents than over oceans, as observed, and more ice clouds in the northern than in the southern hemisphere. The high level ice clouds in the ITCZ region are somewhat overestimated. The maritime stratocumulus regions off the west coasts of the continents with large liquid water fractions particularly in the southern hemisphere are very well captured by the model. The cloud top temperature is related to the thermodynamical phase (see also Chapter 8). Thus it is similarly found that clouds are higher over land than over ocean, and generally higher in the northern than in the southern hemisphere. However, the model generally places the clouds a little bit too high in the atmosphere.

3.5. Summary and conclusions

As the POLDER instrument is able to observe a variety of aerosol and cloud properties, the datasets are particularly useful to investigate cloud properties and aerosol-cloud interactions on a global scale. The approach to do this applied here is the evaluation of a global-scale model using the satellite observations, and to use the combination of model and observations to improve the understanding of the processes (see Chapters 8 and 5 for further results).

A comparison of a nudged simulation with the GCM and the satellite observations reveals some skills and some deficiencies of the model. Aerosol indices, cloud thermodynamical phase and cloud height are rather well captured by the model, showing very similar features compared to the POLDER observations, in particular when looking at hemispheric and land-sea contrasts. The latter ones are well captured for cloud optical thickness and cloud droplet size as well. However, systematic biases are found in these two quantities, with too small droplets, and too large cloud optical thicknesses.

Unfortunately, so far, only eight months of POLDER measurements are available. However, since December 2002, the POLDER-2 instrument is in space, and new data will be available soon.

3.6. Observations spatiales POLDER : Résumé

Introduction

Les instruments satellitaires de type radiomètre mesurent des luminances au sommet de l'atmosphère. Comme ces luminances dépendent de l'état de la surface terrestre et de l'atmosphère, de l'information peut être déduite sur une multitude de propriétés de la surface et de l'atmosphère. Les luminances mesurées par des instruments satellitaires dans la gamme des ondes courtes sont composées de la partie du rayonnement solaire qui est réfléchie par la surface terrestre ou par les différentes composantes de l'atmosphère. La partie ≪ terrestre≫ du spectre est celui des longueurs d'onde d'environ 4 à 25 μm, et est composée par le rayonnement émis par la surface, par certaines molécules dans l'atmosphère, les aérosols et les nuages. Des instruments typiques mesurent l'intensité du rayonnement dans différentes bandes de longueurs d'ondes, qu'on appelle aussi des canaux de l'instrument. si les propriétés de diffusion et d'absorption des composantes de l'atmosphère sont connues, des informations sur la distribution de ces composantes peuvent être déduites des signaux mesurés.

On distingue deux types de satellites. Les satellites géostationnaires sont positionnés au-dessus de l'équateur à une hauteur spécifique où leur vitesse de rotation est identique à celle de la terre. La même région de la surface de la terre est ainsi toujours observée. L'avantage de cette méthode est que des mesures continues sont en principe possibles. Par contre, seulement une partie du globe peut être observée, et en particulier les observations des hautes latitudes ne sont pas très fiables. De plus, l'altitude relativement élevée de ces satellites affaiblit le signal mesuré. La deuxième classe de satellites est celle des satellites défilants polaires qui tournent à une altitude donnée, la terre tournant au-dessous du satellite. Chaque point de la surface terrestre est ainsi survolé à peu près une fois par jour avec une fauchée au sol d'environ 2500 km, les hautes latitudes étant observées plusieurs fois par jour et les basses latitudes moins fréquemment. Des instruments peuvent également être capables de mesurer perpendiculairement et le long de la trace.

L'instrument ≪ POLarization and Directionality of the Earth's Reflectances≫ (POLDER) a été développé par le Laboratoire d'Optique Atmosphérique (LOA) et le Centre National de Études Spatiales (CNES). C'est le premier instrument capable de mesurer simultanément les caractéristiques muli-spectrales, multi-directionnelles et polarisées du rayonnement solaire réfléchi (*Deschamps et al.*, 1994). En particulier, la polarisation du rayonnement observée donne des nouvelles possibilités de déduire des propriétés des composantes de l'atmosphère.

L'instrument POLDER utilise 15 bandes spectrales entre 0.44 et 0.91 μm. Il mesure dans une zone de ± 43° le long de et ± 51° perpendiculairement à la trace du satellite, ce qui donne une fauchée au sol de 2400 km. La résolution au nadir est de 6×7 km^2. Un ≪ superpixel≫ des données dérivées est composé de neuf pixels de l'image donnant une résolution d'environ 0.5 × 0.5° à l'équateur.

L'instrument POLDER-1 a été monté à bord du satellite Japonais ADEOS-1 et a fourni des données de novembre 1996 à juin 1997. La deuxième version (POLDER-2) de l'instrument a volé sur le satellite ADEOS-2 de décembre 2002 à octobre 2003.

Données physiques

Une multitude d'informations physiques peut être déduite des mesures de POLDER comme des propriétés de la surface continentale, la couleur de l'océan, le bilan radiatif, et des informations sur des nuages et des aérosols. Ce sont les deux dernières qui sont d'intérêt particulier pour cette étude. Concernant les aérosols, l'épaisseur optique des aérosols, τ_a, est déduit des canaux à 670 et à 865 nm au-dessus des océans (*Deuzé et al.*, 1999). De plus le coefficient d'Ångström, α, qui est une mesure de la taille des particules, est également dérivé au-dessus des océans. Un indice des aérosols POLDER, AI, est défini comme le produit du coefficient Ångström et de l'épaisseur optique des aérosols, τ_a. Cet indice est calculé au-dessus des continents et des océans (*Deuzé* *et al.*, 2000 ; *Goloub et Arino*, 2000 ; *Deuzé et al.*, 2001 ; *Tanré et al.*, 2001). Dans cette étude, concernant les propriétés des nuages, l'épaisseur optique, le rayon effectif des gouttelettes, la température, et la phase thermodynamique au sommet des nuages seront utilisés. Afin de déduire la température au sommet des nuages, la pression ≪ Rayleigh≫ est d'abord déduite du signal polarisé à 443 nm (*Vanbauce et al.*, 1998). La température est ensuite dérivée en utilisant des analyses du Centre Européen des Prévisions Météorologiques à Moyen Terme (CEPMMT, ECMWF en anglais). La phase thermodynamique au sommet des nuages est estimé sur la base des luminances polarisées à des angles de diffusion autour de 140° (*Goloub et al.*, 2000 ; *Riedi et al.*, 2000). L'épaisseur optique des nuages est obtenu pareillement à la procédure d'ISCCP (*Rossow et Schiffer*, 1991), en supposant des nuages homogènes, d'eau liquide et composés de particules sphériques d'un rayon effectif de 10 μm, et en utilisant jusqu'à 14 directions de visée dans le canal à 670 nm (*Buriez et al.*, 1997 ; *Parol et al.*, 2000). Pour des nuages en eau liquide homogènes à une échelle de 150 × 150 km^2, *Bréon et Goloub* (1998) déduisent le rayon effectif des gouttelettes au sommet des nuages à partir de l'analyse du signal polarisé.

Comparaison données POLDER - modèle LMDZ

Afin de comparer les quantités physiques obtenues par l'instrument POLDER à celles simulées par le modèle de circulation générale LMDZ, une intégration du modèle a été effectuée pour la période des observations de novembre 1996 à juin 1997. Pour assurer des conditions réalistes de la partie dynamique du modèle, la température de la surface des océans et l'extension de la glace de mer ont été imposées au modèle à partir des observations (*Reynolds et Smith*, 1995 ; *Rayner et al.*, 2003). Les vents horizontaux et la température ont été guidés en utilisant des constantes de relaxation de 0.1 jour pour les vents et de 1 jour pour la température. La fauchée du satellite a été échantillonnée dans le modèle afin d'obtenir une vue du globe journalière de la même manière qu'elle se fait avec l'instrument spatial. Les quantités au sommet des nuages sont calculées en utilisant une hypothèse de recouvrement aléatoire des fractions nuageuses. Des distributions moyennées sur la période simulée de l'indice des aérosols, de l'épaisseur optique des nuages, du rayon effectif des gouttelettes, de la phase thermodynamique et de la température au sommet des nuages sont comparées aux quantités observées par POLDER (fig. 3.1).

Le modèle simule bien le contraste terre-mer dans le contenu en aérosols, même si les valeurs élevées sont trop concentrées autour des régions sources. L'épaisseur optique des nuages est surestimée en général par le modèle, ce qui est un problème commun à beaucoup de modèles et qui est en particulier d à la résolution verticale grossière des modèles ainsi qu'à l'hypothèse de l'homogénéité plan-parallèle des nuages. Pourtant, plusieurs caractéristiques sont bien simulées par le modèle. Les épaisseurs optiques sont plus grandes dans l'hémisphère nord, et en général plus grand au-dessus des continents qu'au dessus des océans. L'épaisseur optique élevée dans l'ITCZ est bien simulée.

Le modèle en général simule des rayons effectifs trop petits d'environ 2 à 3 μm en moyenne. Le contraste entre des gouttelettes plus grandes au-dessus des océans et plus petites au-dessus des continents est bien observé à la fois dans les données POLDER et dans LMDZ. Pareillement, le contraste entre les deux hémisphères est bien simulé dans le modèle. Des particules particulièrement petites au-dessus des régions industrialisées de l'hémisphère nord, la partie est de l'Amérique du Nord, Europe et l'Asie de l'Est, sont identifiées à la fois dans les observations et dans le modèle.

Concernant la phase thermodynamique au sommet des nuages, le modèle simule souvent trop de nuages de glace. Pourtant, il est capable de donner plus de nuages de glace au-dessus des continents qu'au-dessus des océans, comme c'est observé, et plus de nuages de glace dans l'hémisphère nord que dans l'hémisphère sud. Les nuages de glace dans l'ITCZ sont légèrement surestimés. Les régions de stratocumulus marins au large des côtes ouest des continents avec des fractions importantes des nuages d'eau liquide en particulier dans l'hémisphère sud sont bien simulées dans le modèle. Comme la phase thermodynamique est corrélée à la température, des résultats similaires sont trouvés pour la distribution de la température au sommet des nuages.

Part II.

Model evaluation and process studies

4. Evaluating parameterizations of cloud-aerosol processes with single column models and ACE-2 CLOUDYCOLUMN observations

4.1. Introduction

Contributions to the first aerosol indirect effect are considered to be largest for low-level stratiform clouds of moderate optical thickness. Low-level clouds with liquid water paths large enough to produce drizzle or rain in clean conditions would be most susceptible to the second AIE. Both conditions are fulfilled for marine stratocumulus clouds as observed particularly off the west coasts of the continents. Some of the first evidence for the aerosol indirect effects was provided by so-called ship tracks in marine stratocumulus clouds. The exhaust from ships results in brighter clouds along the track of a ship, observable in satellite observations (e.g., *Coakley Jr. et al.*, 2000; *Durkee et al.*, 2000; *Ackerman et al.*, 2000b). An explanation for this observation given in the references cited is an increase in cloud droplet number concentration due to the first AIE, and an increase in cloud liquid water content due to the second AIE.

An observational method well suited to provide evidence for and insight into cloud processes are field campaigns, in which in situ measurements of a multitude of different cloud and aerosol properties can be measured using aircraft.

The Second Aerosol Characterization Experiment (ACE-2) was dedicated to the measurement of aerosol effects in a marine stratocumulus cloud environment at midlatitudes. The ACE-2 campaign took place in the in June/July 1997, between Portugal and the Canary Islands. Five airplanes were measuring in situ aerosol and cloud properties along with radiation fluxes. In addition, aerosol measurements from the Punta del Hidalgo station on the Tenerife Island are available. In the CLOUDYCOLUMN project, several cloud microphysical properties have been measured in totally eight case studies (*Brenguier et al.*, 2000a). In the present study, data from two particular days are selected. On June 26th, a cyclone over western Europe advected pristine maritime airmasses from the North Atlantic Ocean to the ACE-2 region. The day of July 9th was the most polluted case, where a high pressure ridge carried polluted airmasses from the European continent to the region of measurements.

The study presented in this chapter was carried out in the framework of the European Project named Parameterization of the Aerosol indirect Climatic Effects (PACE). Six single-column model (SCM) versions of GCMs were used to study the behavior of the different parameterizations in the two ACE-2 CLOUDYCOLUMN cases, June 26th and July 9th, 1997. The results of this study are published in *Menon et al.* (2003). While the evaluation of the first AIE is rather simple, as just the influence of the aerosol concentration on cloud droplet number concentration (CDNC) has to be considered, both of which are observable quantities, the evaluation of the second AIE is much more complicated. The second AIE acts via the microphysical processes of precipitation formation, and it results in changes of cloud liquid water content, cloud lifetime, and precipita-

Date	m_a [μg m^{-3}]	N_a [cm^{-3}]	SO_4 [%]	ss [%]	OC [%]
June 26th	1.2	700	21	15	25
July 9th	5.8	4400	47	10	20

Table 4.1.: The aerosol mass concentration, m_a, number concentration, N_a, and the mass fractions of SO_4, seasalt (ss) and organic carbon (OC), for the clean (June 26th) and the polluted (July 9th) cases of the CLOUDYCOLUMN experiment (from *Guibert et al.*, 2003)

Date	N_d [cm^{-3}]	r_v [μm]	LWP [g m^{-2}]	H [m]	H_B [m]	τ_c	α_c
June 26th	52±16	7.77±3.64	18.5±17.8	202	1283	3.99±2.29	0.19±0.01
July 9th	256±38	4.73±1.67	11.0±10.8	167	817	4.23±2.54	0.27±0.02

Table 4.2.: Cloud droplet number concentrations, N_d, cloud droplet volume mean radius, r_v, cloud liquid water path, LWP, cloud geometrical thickness, H, the cloud base height, H_B, cloud optical thickness, τ_c, and cloud albedo, α_c, for the clean (June 26th) and polluted (July 9th) cases of the CLOUDYCOLUMN experiment. N_d, r_v, LWC, H, and H_B are deduced from in situ measurements (*Brenguier et al.*, 2003; *Pawlowska and Brenguier*, 2000). LWP is calculated from LWC using the maximum overlap assumption. τ_c and α_c are obtained from remote sensing data (*Schüller et al.*, 2003)

tion rate. Thus, a perfectly suited evaluation would require the knowledge of the distributions of these quantities, which in contrast to CDNC and aerosol concentration are highly variable both spatially and temporally. While we are aware of the problems due to the assumptions of homogeneity, we rather focus on the evaluation and comparison of different parameterizations of the autoconversion parameterization, which is the most important process for the onset and production of precipitation (The distinction between autoconversion between droplets to form raindrops and accretion of falling raindrops by the collection of droplets is different in large and small scale models. In small scale models, the accretion process is often of much more importance in the rain formation, a fact due to the higher resolution of these models).

4.2. Observational data

Guibert et al. (2003) report the aerosol concentrations and types for the different ACE-2 cases, measured at the Punto del Hidalgo ground station and using aircraft measurements. Table 4.1 summarizes the values given in their study. *Pawlowska and Brenguier* (2000) established a dataset of cloud parameters on a region of 60x60 km^2 covering the full track of the flights. They select the (almost) adiabatic cases from all available measurements and exclude cases where drizzle has been observed. The mean droplet number concentration and volume mean droplet radius are deduced from the mean droplet spectra. Similarly, *Brenguier et al.* (2003) give the mean values for cloud droplet radius, cloud droplet number concentration, and cloud liquid water content, for five sublayers of the stratocumulus cloud. Table 4.2 summarizes the characteristic values of the cloud quantities for the two clean and polluted cases. Together with measurements of the rainfall rate a complete cloud and precipitation microphysics and aerosol dataset is given at the scale of a GCM grid box for the two ACE-2 CLOUDYCOLUMN situations, a clear (June, 26th) and a polluted (July, 9th) one.

4.3. The SCMs

Six SCM versions of GCMs were used in the PACE project, named CSIRO, GISS, MetO, PNNL, ECHAM, and the LMDZ. Descriptions of the respective models are summarized in Table 4.3. As the situations of interest are non-convective, three

Set-up	CSIRO	GISS	MetO	PNNL	ECHAM	LMDZ
Investigator	J. Penner, X. Liu; Univ. Michigan	S. Menon, A. Del Genio; GISS	P. Davison, D. Roberts; Hadley Centre	S. Ghan; PNNL	U. Lohmann; Dalhousie Univ., J. Feichter; Max Planck Institute	J. Quaas; LMD/IPSL, O. Boucher; LOA
# levels (# below 720hPa)	18 (6)	31 (8)	30 (13)	24 (11)	19 (6)	19 (6)
Initialization time	0Z 25/06 and 0Z 08/07	0Z 25/06 and 0Z 08/07	0Z 26/06 and 0Z 09/07	0Z 26/06 and 0Z 09/07	April 1	0Z 26/06 and 0Z 09/07
Treatment of surface fluxes	Diagnosed by SCM from wind and temperature	Diagnosed by SCM from surface wind and temperature	Diagnosed by SCM	Diagnosed by SCM from wind and temperature	Standard GCM treatment	Diagnosed by SCM from wind and temperature
Nudging	Yes.	Yes.	No.	No.	Yes.	Yes.
Droplet nucleation	Physically based using updraft velocity, aerosol number and anthropogenic sulfate mass (*Chuang et al.*, 1997).	Empirically based in terms of mass of sulfate, organic and sea-salt aerosols and cloud turbulence (*Menon et al.*, 2002)	Empirically based (*Jones et al.*, 2001)	Physically based using updraft velocity, aerosol number concentration and distribution properties (*Abdul-Razzak and Ghan*, 1999)	Physically based, modified version of the *Ghan et al.* (1997a)-Scheme (*Lohmann*, 2002a)	Empirically based using sulfate aerosol mass (*Boucher and Lohmann*, 1995)
Subgrid q_l var. in autoconv.	Triangular PDF.	None.	None.	Triangular PDF.	None.	None.
References	*Rotstayn* (1997); *Rotstayn* (2000)	*Hansen et al.* (1997); *Del Genio et al.* (1996); *Menon et al.* (2002)	*Wilson and Ballard* (1999); *Jones et al.* (2001); *Lock et al.* (2000)	*Ghan et al.* (1997a); *Abdul-Razzak and Ghan* (1999)	*Lohmann et al.* (1999); *Lohmann* (2002a)	*Li* (1999); *Le Treut and Li* (1991); *Boucher et al.* (1995a)

Table 4.3.: Summarized description of the SCMs used in the PACE study.

parameterizations are more particularly of interest in the SCMs, namely the boundary layer, radiation, and microphysics schemes. The focus of the study is on the cloud droplet activation scheme, which contributes to the first AIE, and on the autoconversion scheme, which has the main influence on the second AIE in the model. Thus, we will address some differences and similarities of the SCMs in the microphysics parameterization in more detail.

Some of the set-up parameters of the one-day simulations are summarized in Table 4.3. The vertical resolution of all GCMs is rather coarse, varying from 18 to 31 layers, with roughly a third of them in the boundary layer (BL). The BL scheme in all SCMs diagnoses the latent heat fluxes at the ocean surface using the wind and temperature profiles. Radiation is parameterized in all SCMs using the two stream approximation with spectral bands in the solar and terrestrial spectra. The schemes are described in some more detail in *Menon et al.* (2003) and the references given therein.

4.4. Simulations

4.4.1. One-day SCM simulations: Method

One-day simulations with the six SCMs were carried out in the framework of the PACE project for each of the two ACE-2 CLOUDYCOLUMN cases. For the CSIRO, GISS, MetO and PNNL SCMs, the initial conditions were prescribed from ECMWF reanalysis data; the CSIRO and GISS models were also forced with ECMWF data. In contrast to this, the LMDZ SCM and the ECHAM SCM were initialized and forced with profiles from a nudged 3D-run of the GCM.

For the LMDZ model, daily mean SST values were imposed from the Reynolds SST dataset. Temperature and horizontal winds were nudged to ECMWF reanalysis data using relaxation time constants of 1 day and 0.1 day, respectively. The model grid was zoomed over the ACE-2 region with the center at 16.5°W and 29.5°N, obtaining a resolution of 140x90 km^2 in the zoom region. Values at the grid point (17.4°W/29.5°N) were taken to initialize and force the SCM. While winds, surface pressure and SST are imposed on the SCM, temperature and humidity are nudged using a relaxation constant deduced from wind speed and grid size (*Ghan et al.*, 1999).

4.4.2. One-day SCM simulations: Results

Figures 4.1 and 4.2 show the cloud amount and the cloud liquid water content simulated by the six SCMs. Along with this, Fig. 4.3 shows the cloud amount from ISCCP satellite measurements on a scale similar to the model resolution.

The results from the six models differ in various aspects. Three of the models (CSIRO, PNNL, LMD) tend to simulate continuously a cloud, which is in agreement with the observations. For the clean case (June 26th), MetO and ECHAM models simulate a continuous cloud as well. The daily mean cloud amount varies among the models between $< 50\%$ and $>80\%$ for June 26th, and shows even more scatter, between 10 and $>80\%$ on July 9th, the LMD model being at the upper end of this scale in both cases. ISCCP satellite observations give a cloud amounts of 80% and 82%, respectively. Comparing the two cases, CSIRO, PNNL, and LMD models simulate rather similar diurnal cycles of the cloud in both cases, PNNL placing the cloud lower in the polluted case. The diurnal cycle given by the LMD model is consistent with the ISCCP observations for June 26th, while on July 9th, the minimum at nighttime and early morning is not captured. For the clean case, it can be seen that the two models forcing the SCM with profiles from a nudged 3D-simulation (ECHAM and LMD models) simulate a similarly persistent cloud, so maybe the consistency in the 3D field enables the model to simulate a continuous cloud cover as observed. The two models that are able to resolve the vertical structure of the boundary layer clouds better than the other ones (MetO through a better resolution, and GISS through a vertical subgrid cloud fraction parameterization) simulate the smallest cloud amounts in both cases.

Similarly, it is in these two models, that the high-

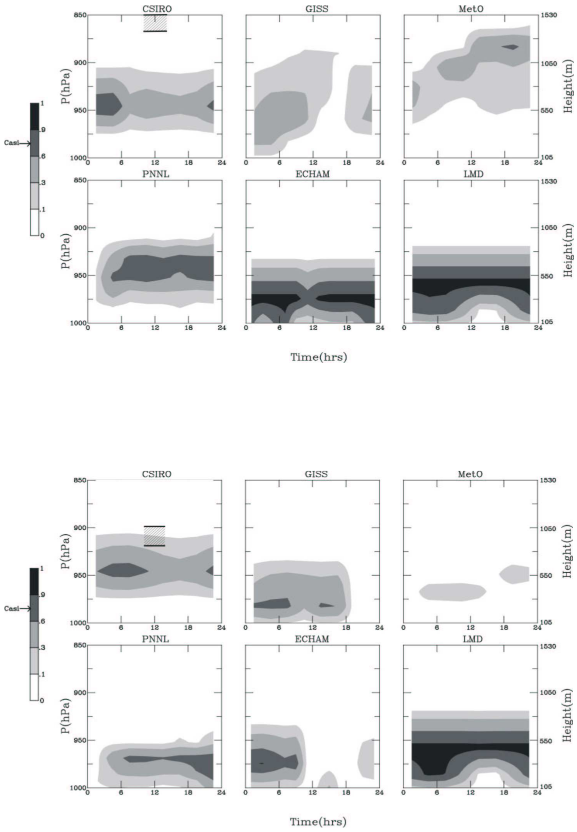

Figure 4.1.: Time-pressure plot of the predicted cloud fraction for (a) the clean (June 26) and (b) polluted (July 9) cases. Observed cloud base and top levels are reported in the upper left graph (CSIRO). Cloud fraction from observations with the casi radiometer are also indicated on the color bar.

est cloud bases are simulated (Figure 4.4), in better agreement with the observations. This feature is, however, more pronounced on June 26th than on July 9th. Again probably due to the coarse vertical resolution of the models, cloud geometrical thickness is overestimated by all models, the MetO and GISS models again being somewhat closer to the observations. It is remarkable that the simple vertical subgrid parameterization in the GISS model gives results very similar to the MetO model results which uses a considerably better resolution (13 against 8 layers in the boundary layer).

As shown in Fig. 4.5, all models strongly underestimate the measured rainfall rate at the surface. It can be noted, however, that the two models forced from a consistent 3D field (ECHAM and LMD) are able to produce a larger rain rate than the other models, in better agreement with the observations.

Concerning CDNC and CDR, all models successfully simulate more and smaller cloud droplets in the polluted compared to the clean case. SCM parameterizations differ primarily in the way of predicting N_d from aerosol concentrations, PNNL and ECHAM using physically based, the other models empirically based relationships. The PNNL model simulates too large CDNC in both cases, and ECHAM too low values in the polluted case. The empirical schemes are rather close to each other, showing, however,

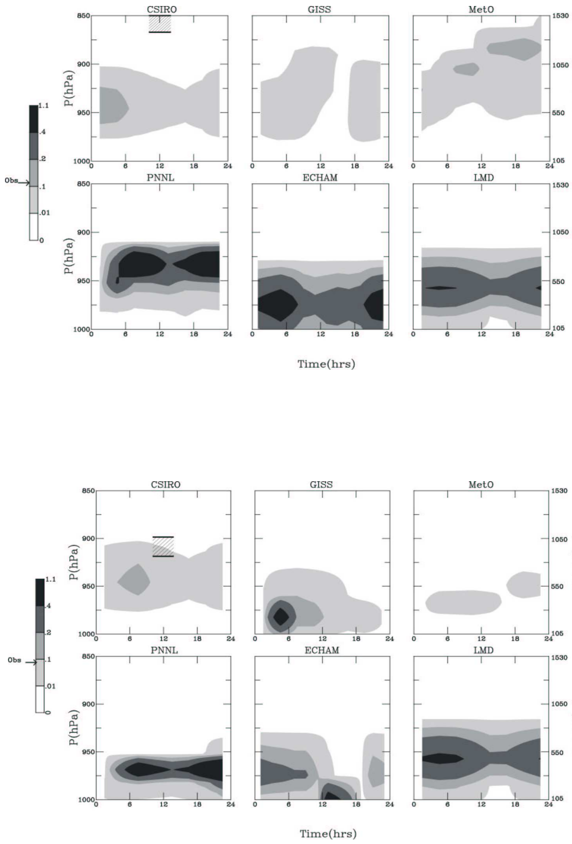

Figure 4.2.: As Fig. 4.1, but for cloud water mixing ratio [g kg^{-1}]. Observations from the casi radiometer are also indicated on the color bar.

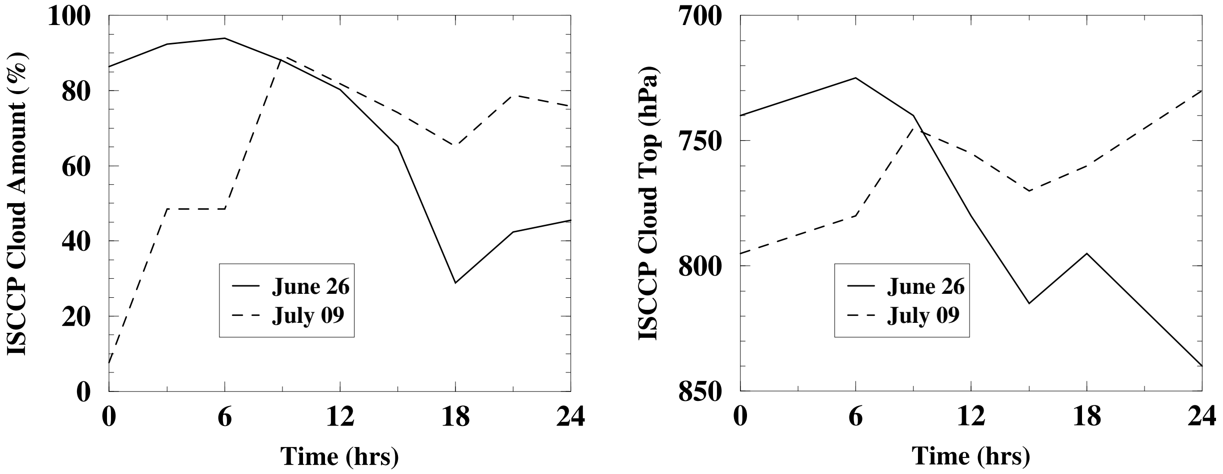

Figure 4.3.: ISCCP derived cloud amount and cloud top for the clean and polluted cases.

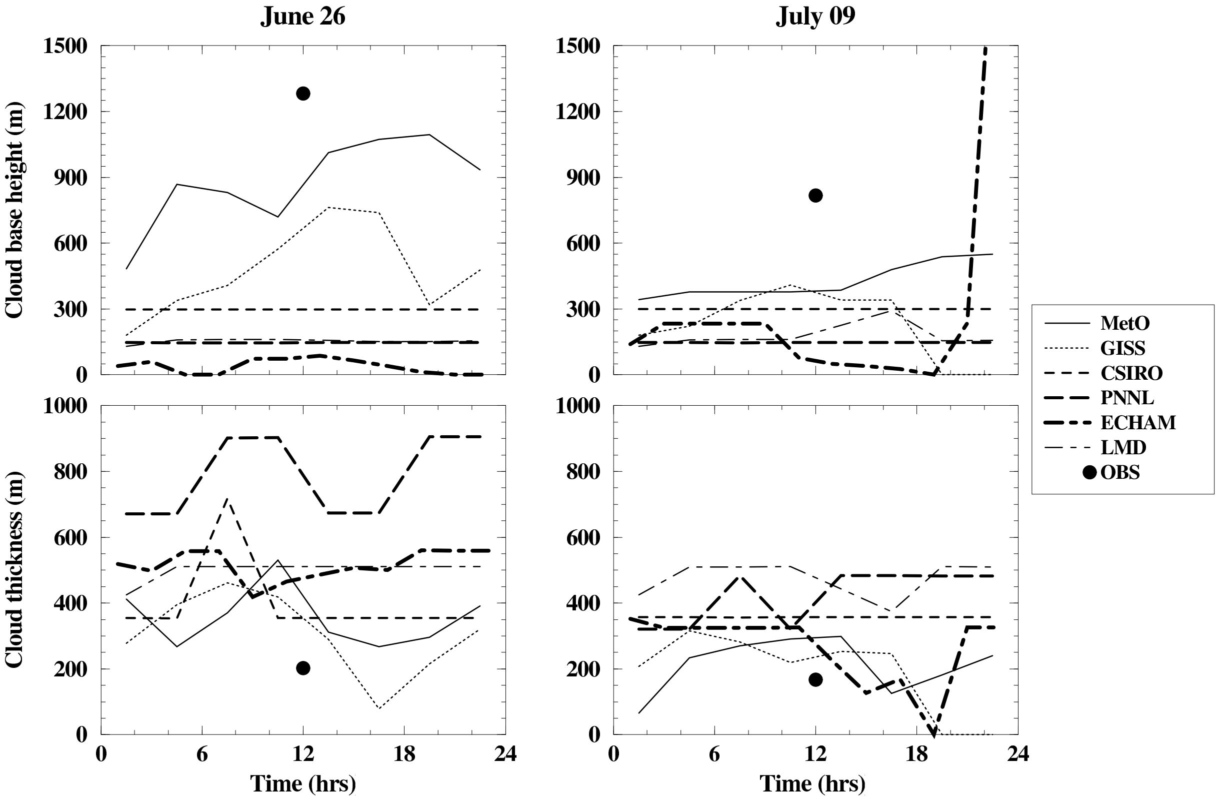

Figure 4.4.: Cloud base [m] and cloud geometrical thickness [m] simulated by the six SCMs. The observations are shown as a full circle.

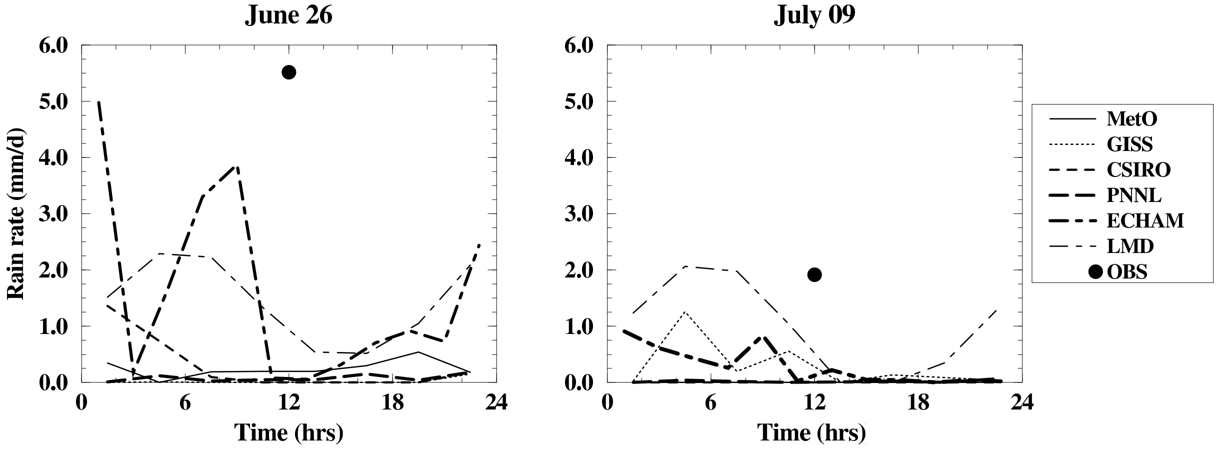

Figure 4.5.: Rain rate at the surface [mm day^{-1}].

different behaviors in response to the increase in aerosol burden from June 26th to July 9th. The LMD model has the smallest sensitivity to increased aerosol concentration, the GISS model the strongest one. Concerning the CDR, it is remarkable that all models rather overestimate the droplet size although several of them are within or close to the uncertainty range given for the observations. It should be noted that due to adaptation of the autoconversion schemes using a "critical radius" for the onset of precipitation, models tend to simulate too small CDR (*Rotstayn*, 2000). In the cases examined here, however, the CDR are well above this critical threshold value.

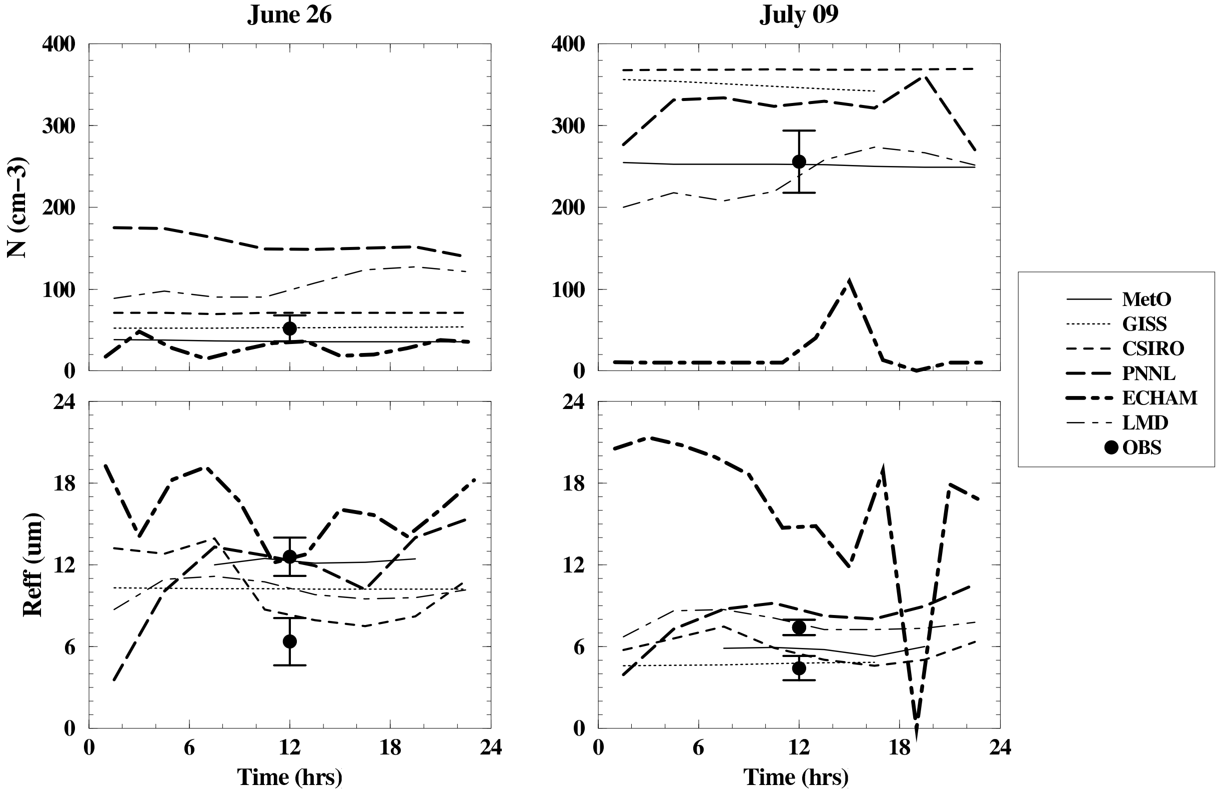

Figure 4.6.: Cloud droplet number concentrations ([cm^{-3}], upper panel) and cloud droplet effective radii ([μm], lower panel).

4.4.3. Single-step simulations: Method

Single-step simulations were carried out to test the microphysics parameterization alone. The models were initialized by the ECMWF temperature and humidity profiles for 12Z on June, 26th and July, 9th.

- EXP-N is the first experiment, in which the ability of the parameterizations is tested to predict the cloud droplet number concentration with given aerosol concentrations. In case of the LMDZ model, which uses the empirical formula of *Boucher and Lohmann* (1995), this is just a diagnosis of this formula given the aerosol mass concentration.
- In EXP-A simulations, the vertical resolution of the SCMs was increased to be able to resolve the five sub-layers of the clouds as in the observational data from *Brenguier et al.* (2003). Cloud droplet number concentration, Cloud liquid water content, and cloud geometry were prescribed. With these simulations, the degree of realism of the parameterization of cloud optical properties and radiation could be tested. At the same time, a comparison of rain rates at the base of the cloud and at the ground of models and observations allowed an evaluation of the autoconversion parameterizations.
- VERT was a third single-step parameterization, which was similar to EXP-A except that the standard vertical resolution of the SCMs was applied.

In addition to the results published in *Menon et al.* (2003), here, in EXP-N, different parameterizations for the link between CDNC and aerosol mass are tested with the LMDZ SCM: The formulae “(A)” and “(D)” from *Boucher and Lohmann* (1995), and two modifications of these two formulae: First, the sulfate aerosol mass is replaced by the maximum of the mass concentrations of three different species of hydrophilic aerosols (sulfate, organic matter, and sea salt), and second, the sum of the mass concentrations of hydrophilic aerosols is taken. The idea is that using the sum or the maximum of the masses of all hydrophilic aerosols instead of sulfate alone could help to overcome the difficulty of using sulfate as a surrogate for all aerosol types in regions where sulfate aerosols are sparse compared to other potential CCN.

4.4.4. Single-step simulations: Results and Discussion

For the EXP-N experiment (Table 4.4), all model parameterizations simulate larger CDNC concentrations for the polluted compared to the clean case. However, no clear distinction can be made between physically (PNNL and ECHAM) and empirically based schemes. While ECHAM overpredicts CDNC in the clean case, it matches the observations exactly in the polluted case. PNNL, however, matches the observations exactly in the clean case and largely underpredicts the CDNC in the polluted case. Among the other models, GISS uses a scheme partially derived from the ACE-2 data. This scheme, however, is nevertheless not able to reproduce the observed CDNC in both cases. For the LMD model, two different empirical formulae of *Boucher and Lohmann* (1995) were compared, and each of these was again modified to also take into account the non-sulfate aerosols. This was done in one study by using the maximum of the masses of sulfate, hydrophilic organic matter, and submicronic sea salt, and in a second one by using the sum of all these aerosol masses. Using the sum of all masses, the model seems to overpredict largely CDNC. Both formulae overpredict CDNC for the clean case for any of the aerosol mass concentrations tested. Formula “A” is better in predicting CDNC in the clean case, formula “D” better in the polluted case. It can be deduced that a formula which showed more sensitivity to aerosol concentration would be needed to simulate the differences between the two cases well.

Tables 4.6 and 4.7 give the results for the EXP-A simulations, for the model-simulated cloud optical thickness, τ_c, and the SW planetary albedo at TOA. For each of the two clear and polluted cases, four simulations were carried out: The first time, the liquid water content of the cloud was scaled to match the LWP observed by the FSSP instrument, and the second time, to match the OVID measurement of LWP. These two LWPs differ a lot. It is difficult to identify which estimate is better. On the one hand, as the OVID instrument infers LWP from radiation measurements, some uncertainty may be introduced. On the other hand, this method is able to capture a view of all LWP situations, where the FSSP in situ instrument can only collect samples. Therefore, the two different LWPs were used in the simulations. Then, these two simulations were done twice, at the resolution of the dataset, and at the lower standard model resolution.

Looking at the model-simulated cloud optical thickness, τ_c, mainly two parameterizations can be examined. The first is the way to derive the cloud optical thickness from (fixed) LWP, W, and CDR, r_e. This is done using the formula

$$\tau_c = \frac{3}{2}\frac{W}{\rho_w r_e} \tag{4.1}$$

from *Stephens* (1978), where ρ_w is the water density, for all models except the MetO model, which uses the parameterization from *Slingo* (1989)

$$\tau_c = W\left(a + \frac{b}{r_e}\right) \tag{4.2}$$

with two empirical constants a and b. However, in some of the models, τ_c is further scaled to consider subgrid-scale variability. In the GISS model, this factor is $f^{\frac{1}{3}}$ (where f is the cloud fraction), which is explained as a measure of possible vertical subgrid-scale variability (*Del Genio et al.*, 1996). For the PNNL, the scaling factor is $f^{\frac{3}{2}}$, and the ECHAM uses an “inhomogeneity factor” of $1. - 0.06\,W^{\frac{1}{3}}$ from *Tompkins* (2002). Further on, the CDR is calculated using the prescribed liquid water content and CDNC. Therefore, the volume-mean droplet radius, r_{dv}, is calculated assuming spherical particles. This is related to the effective radius by a factor k, which is (for the oceanic conditions) 1.077 in the CSIRO, MetO and ECHAM models, 1.1 in the PNNL and LMD models, and 1.28 in the GISS model, which are in the range of the observations (*Pontikis and Hicks*, 1993; *Martin et al.*, 1994). The second parameterization of interest is how the clouds are assumed to

Date	FSSP OBS	OVID OBS	CSIRO	GISS	MetO	PNNL	ECHAM
June 26th	52±16	46	68	51	34	52	84
July 9th	256±38	230	358	217	242	138	255
	SO_4, "D"	SO_4, "A"	max, "D"	max, "A"	sum, "D"	sum, "A"	
June 26th	92	59	99	64	142	99	
July 9th	245	186	245	186	300	235	

Table 4.4.: The predicted CDNC [cm^{-3}] from EXP-N (with observed aerosols prescribed), from FSSP and OVID observations and from the five SCMs (upper panel), and for six realizations with the LMDZ-GCM (lower panel, "A" and "D" indicate the two respective formulas of *Boucher and Lohmann* (1995), SO_4 means sulfate aerosols only, "max", the maximum of the mass concentrations of different hydrophilic aerosols is taken instead of sulfate mass, and "sum", the sum of their mass concentrations is taken).

	CSIRO	GISS	MetO	PNNL	ECHAM	LMD
Optical thickness	$\frac{3}{2}\frac{W}{\rho_w r_e}$	$\frac{3}{2}\frac{W}{\rho_w r_e}$	$W\left(a+\frac{b}{r_e}\right)$	$\frac{3}{2}\frac{W}{\rho_w r_e}$	$\frac{3}{2}\frac{W}{\rho_w r_e}$	$\frac{3}{2}\frac{W}{\rho_w r_e}$
Scaling of τ_c	none	$f^{\frac{1}{3}}$	none	$f^{\frac{3}{2}}$	$1-0.06W^{\frac{1}{3}}$	none
Factor in r_e-$r_{d,v}$ relation	1.077	1.28	1.077	1.1	1.077	1.1
Vertical overlap	random	none	max-rand	random	max-rand	random

Table 4.5.: Model parameterizations for the derivation of cloud optical thickness

overlap in the vertical, at least in the case of the high resolution, where multiple cloud layers exist. CSIRO, PNNL and LMD use a random overlap assumption, and MetO and ECHAM maximum-random overlap. In the GISS model, a layer is considered either entirely cloudy or clear in the radiation scheme, depending on a random number and the cloud fraction. Table 4.5 summarizes the differences in the parameterizations. For the cloud optical thickness, all models simulate the values within the uncertainty given for the FSSP observations. For the high resolution, PNNL shows the smallest optical thicknesses, which is due to the large scaling factor in τ_c. Similarly, the GISS model also simulates rather low values. The different formulation for cloud optical thickness used in the MetO gives values comparable to those obtained from the *Stephens* (1978) parameterization. This, however, may also be due to the fact that the MetO model uses a maximum-random vertical overlap assumption, which is different from the other models. The fact that the GISS model shows rather low values may also be due to the relatively large value of the scaling factor k. The LMD model simulates optical thicknesses within the range of the other SCMs, but generally somewhat larger values than the mean. When initialized with rather low liquid water contents, this is closer to the observations, while for relatively larger LWP, this is less realistic.

The models generally show larger optical thicknesses and albedos when coarsening the vertical resolution. For the coarse resolution, the ECHAM model shows rather low optical thicknesses which may be attributed to the use of the inhomogeneity factor for the scaling of τ_c.

Table 4.7 shows the SW planetary albedo. Here, the different radiation parameterizations can be evaluated against the other ones. Generally, the schemes are able to simulate slightly larger albedos for the polluted compared to the clean case, however, this increase is less in the models than in the OVID obser-

Date	Res.	LWP	OBS	CSIRO	GISS	MetO	PNNL	ECHAM	LMD
June 26th	O	F	3.99±2.29	3.63	3.34	3.26	3.21	-	3.50
	M	F		4.32	4.40	-	5.64	3.80	5.50
	O	O	5.09	7.59	8.19	6.44	7.05	-	7.30
	M	O		9.01	9.02	-	12.4	7.00	11.4
July 9th	O	F	4.23±2.54	4.23	3.49	3.66	3.20	-	4.00
	M	F		4.93	4.73	-	3.33	3.00	6.00
	O	O	4.99	8.85	7.77	7.64	7.20	-	8.50
	M	O		10.4	9.90	-	7.20	8.00	12.5

Table 4.6.: Cloud optical thicknesses simulated by the SCMs in EXP-A. Results for a vertical resolution (column "Res.") of the observations (O) and the model (M) are given. In one set of simulations, the liquid water path of the FSSP measurements was imposed to the models (column "LWP", F), and in another one, the LWP of the OVID measurements (O). FSSP deduced an optical thickness of 3.99±2.29 and 4.23±2.54 for June 26th and July 9th, respectively, and OVID 5.09 and 4.99, respectively.

Date	Res.	LWP	OBS	CSIRO	GISS	MetO	PNNL	ECHAM	LMD
June 26th	O	F	0.15±0.01	0.26	0.19	0.18	0.17	-	0.14
	M	F		0.27	0.23	-	0.27	0.21	0.18
	O	O		0.30	0.30	0.27	0.27	-	0.21
	M	O		0.32	0.35	-	0.41	0.27	0.28
July 9th	O	F	0.18±0.01	0.27	0.20	0.19	0.18	-	0.15
	M	F		0.27	0.24	-	0.18	0.19	0.19
	O	O		0.32	0.30	0.27	0.29	-	0.22
	M	O		0.33	0.37	-	0.29	0.30	0.28

Table 4.7.: As Table 4.6, but for TOA SW albedo.

vations. Models generally simulate too large albedos, except for some cases, as e.g. the LMD model when initialized with low LWPs and at high resolution. Coarsening the resolution results in the simulation of larger albedos, which is consistent with the increase in cloud optical thickness. Also due to the simulated differences in COT, the CSIRO model generally simulates rather large albedos, and the PNNL model rather low ones.

In Table 4.8, the rainfall rates simulated by the different autoconversion schemes are listed. It is astonishing that all models extremely underestimate the rainfall rates. A reason could be the inherent assumption of homogeneity. When increasing the vertical resolution from standard model resolution to the resolution of the observational dataset, somewhat more precipitation is simulated by some of the models, but still this precipitation is one to three orders of magnitude too small. The differences among the models that use an autoconversion scheme similar to the *Tripoli and Cotton* parameterization (GISS, MetO, CSIRO, LMD) can be used to examine the impact of the choice of parameters. However, as has been examined already in the analysis of the one-day simulations, the autoconversion threshold does not play a role, as the droplets are generally larger than the critical values of 7.5 or 8 μm used in the schemes. Testing the *Khairoutdinov and Kogan* (2000) autoconversion scheme in the ECHAM, which is similar

Date	OBS	Res.	CSIRO	GISS	MetO	PNNL	ECHAM	LMD
June 26th	25.5	O	0.43	0.01	3.33	0.05	-	0.41
		M	0.00	0.01	-	0.00	0.00	0.00
July 9th	2.22	O	0.00	0.00	0.83	0.01	-	0.00
		M	0.00	0.07	-	0.01	0.00	0.00

Table 4.8.: Rain water fluxes at cloud base [mg m^{-2} s^{-1}] from EXP-A for the clean and polluted cases, for the vertical resolution of the observations ("O") and of the models ("M").

to the *Tripoli and Cotton* (1980) parameterization but does not include a "critical value" reveals that this scheme is not able either to produce a realistic drizzle rate.

4.5. Summary and conclusion

Among single-column versions of six general circulation models, the LMDZ including the microphysical scheme of *Boucher et al.* (1995a) has been evaluated using in situ observations from two cases of the ACE-2 CLOUDYCOLUMN field study, a clean and a polluted one. The observational data is available averaged over a homogeneous maritime stratocumulus cloud on a scale of 60x60 km^2, which is a size comparable to the GCM resolution.

In all the quantities evaluated, the SCMs show a very large scatter. The stratocumulus clouds simulated by the different models in one day simulations vary in fractional cloudiness, liquid water content, CDNC, and cloud optical thickness. However, some results are very useful. Models applying a high resolution in the boundary layer or a vertical subgrid-scale parameterization are better able to simulate cloud base height and size. Models forced from a consistent three-dimensional field simulated cloud fractions better, indicating that the parameterizations might do a better job in the 3D than in the 1D version, possibly due to a canceling of errors.

All the models simulate larger CDNC and smaller droplet sizes in the polluted compared to the clean case. However, it is not possible to decide whether physically or empirically based schemes are preferable from their skill. Precipitation is extremely underestimated indicating some need for drizzle parameterization. The fact that none of the models is able to simulate drizzle of observed magnitude in neither the clean nor the polluted case indicates also that a second indirect effect cannot adequately be modeled with current GCMs. As expected, cloud optical properties were simulated much more realistically when increasing the vertical resolution. However, none of the individual parameterizations for cloud optical thickness, vertical cloud overlap, or effective radius can be distinguished to be preferable compared to the other ones.

4.6. Évaluation des paramétrisations de processus aérosols-nuages avec des modèles unicolonnes et des observations ACE-2 CLOUDYCOLUMN : Résumé

Introduction

Les contributions les plus importantes aux effets indirects des aérosols viennent des nuages stratiformes des niveaux bas et des épaisseurs optiques modérées. Des nuages bas avec des contenus en eau liquide assez élevés pour former de la bruine dans des conditions non-polluées sont les plus influenables par le deuxième effet indirect. Ces deux conditions sont remplies pour des stratocumulus marins comme on les observe au large des côtes ouest des continents. La campagne de mesures ACE-2 (Second Aerosol Characterization Experiment) a été dédiée aux mesures des effets des aérosols dans l'environnement des stratocumulus marins. Elle a eu lieu en juin/juillet 1997 entre le Portugal et les îles Canaries. Cinq avions ont mesuré in situ les propriétés des aérosols et des nuages. De plus, des mesures d'aérosols existent à la station Punto del Hidalgo sur l'île Tenerife. Dans le projet CLOUDYCOLUMN, des propriétés microphysiques des nuages ont été mesurées dans huit cas (*Brenguier et al.*, 2000a). Deux de ces cas ont été sélectionnés pour cette étude. Le 26 juin, un cyclone au-dessus de l'Europe de l'Ouest advectait des masses d'air propres sur la région d'ACE-2. Le 9 juillet, pour le cas CLOUDYCOLUMN le plus pollué, une zone de haute pression apportait des masses d'air pollué du continent européen vers la région de mesures.

L'étude présenté dans ce chapitre a été effectuée dans le cadre du projet Européen PACE (Parameterization of the Aerosol indirect Climatic Effects). Des versions unicolonnes de six différents MCGs ont été utilisées pour étudier les comportements des différentes paramétrisations dans les deux cas d'ACE-2. Les résultats de cette étude ont été publiés dans *Menon et al.* (2003). L'évaluation du premier effet indirect est relativement simple, c'est principalement l'influence de la concentration en aérosols sur la concentration en nombre des gouttelettes qui doit être considérée et ce sont tous les deux des quantités observées. L'évaluation du deuxième effet indirect est beaucoup plus compliquée. Le deuxième effet indirect modifie, via des processus microphysiques de la formation de la précipitation, le contenu en eau des nuages, leur durée de vie, et le taux de précipitation. Pour une évaluation parfaite la connaissance des distributions de toutes ces quantités, qui sont très variables temporellement et spatialement, serait donc nécessaire. Ici, on se focalise sur l'évaluation et comparaison de différentes paramétrisations de l'autoconversion, le processus le plus important pour la formation de la précipitation dans les modèles de grande échelle.

Données et méthode de simulations

Les propriétés des aérosols ont été mesurées à la station Punto del Hidalgo et avec des avions (*Guibert et al.*, 2003). En sélectionnant les cas adiabatiques et en excluant les cas dans lesquels de la bruine a été observée, *Pawlowska et Brenguier* (2003) ont établit à partir des vols d'avions un jeu de données valable pour une région de 60 × 60 km^2. De plus, *Brenguier et al.* (2003) déduisent un jeu de données pour cinq sous-couches du nuage, pour le rayon effectif, la concentration en nombre des gouttelettes, et le contenu en eau liquide. Des mesures par télédétection de l'albédo et de l'épaisseur optique des nuages viennent compléter le tableau (*Schüller et al.*, 2003).

Les six MCGs dont les versions unicolonnes ont été utilisées étaient ceux du CSIRO (*Rotstayn*, 1997 ; *Rotstayn*, 2000), du GISS (*Del Genio et al.*, 1996 ; *Menon et al.*, 2002), du Met Office (MetO ; *Wilson et Ballard*, 1999 ; *Jones et al.*, 2001), du PNNL (*Ghan et al.*, 1997a), ECHAM (*Lohmann et Roeckner*, 1996 ; *Lohmann et al.*, 1999) et LMDZ (*Li*, 1999 ; *Boucher et al.*, 1995).

Deux types de simulations ont été effectués. Des simulations d'une journée ont été faites pour les deux jours des 26 juin et 9 juillet 1997. Les conditions initiales étaient prescrites par des données du CEPMMT, et à l'exception de MetO et PNNL, les modèles unicolonnes étaient forcés par des données du CEPMMT (CSIRO et GISS) oú à partir des simulations 3D guidées avec des données du CEPMMT (ECHAM et LMDZ). Pour LMDZ, la simulation 3D qui a servi pour initialiser et forcer le modèle 1D a été effectuée en mode zoomé sur la région d'ACE-2. Un deuxième type de simulations consistait en simulations d'un seul pas de temps du modèle pour évaluer certaines paramétrisations individuellement. Les modèles ont été initialisés avec des profils de température et d'humidité du CEPMMT pour le 26 juin et le 9 juillet à 12h GMT. Dans l'expérience nommée ≪ EXP-N≫ , la concentration en nombre des gouttelettes est calculée à partir des aérosols donnés. Dans ≪ EXP-A≫ , la concentration des gouttelettes, le contenu en eau liquide, et la géométrie du nuage étaient prescrits. La paramétrisation des propriétés optiques des nuages, du rayonnement et de la précipitation pouvaient ainsi être évaluées. Dans cette expérience, la résolution verticale a été augmentée pour résoudre les observations données par Brenguier et al. (2003). ≪ VERT≫ consistait en la même étude, mais en utilisant la résolution verticale standard du modèle.

Résultats

Les résultats des six modèles varient sous plusieurs aspects (voir figs. 4.1 à 4.6). Trois des modèles (CSIRO, PNNL, LMDZ) simulent un nuage en continu, comme c'est le cas dans les observations. Dans le cas non-pollué (26 juin), MetO et ECHAM simulent un nuage également persistent. La nébulosité moyenne journalière varie entre moins de 50% et plus de 80% le 26 juin, et encore plus fortement, entre 10% et plus de 80%, le 9 juillet, LMDZ montrant des valeurs plutôt élevées dans les deux cas. Des données satellitaires ISCCP donnent des valeurs de 80% et 82% pour les cas propre et pollué. En comparant les deux situations, les modèles CSIRO, PNNL et LMDZ simulent des cycles diurnes des nuages assez similaires pour les deux cas, le nuage étant placé un peu plus bas dans le cas pollué dans le PNNL. Pour le 26 juin, le cycle diurne simulé par LMDZ est similaire à celui observé par ISCCP, alors que pour le 9 juillet, les minima pendant la nuit et le matin ne sont pas simulés. Dans le cas propre, dans les deux modèles qui sont forcés par des profils obtenus par des simulations 3D guidées (ECHAM et LMD), le nuage persistent qui a été observé est mieux simulé que par les autres modèles. Les deux modèles qui ont une résolution verticale plus élevée que les autres (MetO par une meilleure résolution, et GISS par une paramétrisation de la fraction nuageuse sous-maille verticale) simulent les fractions nuageuses les plus petites. Egalement dans ces deux modèles, les bases des nuages les plus hautes sont simulées, en meilleur accord avec les observations, et l'épaisseur géométrique des nuages est plus petite que dans les autres modèles, ce qui est aussi plus proche des observations. Il est remarquable que le schéma simple de paramétrisation sous-maille du modèle GISS donne des résultats similaires à ceux du modèle MetO qui utilise une résolution plus fine (avec 13 au lieu de 8 couches dans la couche limite).

Le taux de précipitation à la surface est fortement sous-estimé par tous les modèles. Les deux modèles forcés par un champ 3D d'une simulation (ECHAM et LMD) sont pourtant meilleurs que les autres.

Tous les modèles simulent plus de gouttelettes dans le cas pollué, et des gouttelettes plus petites dans le cas propre. Alors que PNNL et ECHAM utilisent des paramétrisations physiques pour le lien entre aérosols et nombre des gouttelettes, les autres appliquent des formules empiriques. Le modèle PNNL simule des concentrations trop larges dans les deux cas, et le ECHAM des valeurs trop petites dans le cas pollué. Les schémas empiriques sont relativement proches les uns des autres. Les rayons effectifs des gouttelettes sont plutôt surestimés par les modèles. Plusieurs modèles sont pourtant bien capables de simuler des valeurs aux incertitudes des observations près.

Dans les simulations à pas de temps uniques (tableaux 4.4 à 4.8), tous les modèles sont bien capables de simuler les concentrations de gouttelettes plus élevées dans le cas pollué en comparaison au cas propre. Pourtant, on ne peut pas distinguer clairement si ce sont les paramétrisations physiques ou empiriques qui sont les plus réalistes. Alors que ECHAM surestime la concentration dans le cas propre, il simule exactement la même concentration qu'observée dans l'autre cas. PNNL, de l'autre coté, donne la concentration exacte dans le cas propre et sous-estime largement la concentration dans le cas pollué. Parmi les paramétrisations empiriques, le GISS a été développé partiellement à partir des données d'ACE-2. Pourtant, il n'est pas capable de reproduire les concentrations observées dans les deux cas. Pour le LMD, plusieurs variations des formules de *Boucher et Lohmann* (1995) ont été testées, dont leurs formules ≪ A≫ et ≪ D≫ , en utilisant la masse des sulfates (comme proposé par les auteurs), puis le maximum des masses des différents types d'aérosols hydrophiles (sulfates, sels de mer submicroniques, aérosols carbonés hydrophiles), et enfin la somme de ces masses. Aucune de ces paramétrisations ne simule la variation de la concentration des gouttelettes entre les deux cas comme observée. Pour le cas propre, la concentration est surestimée par presque toutes les réalisations, et quand le résultat est proche des observations (avec les sulfates seulement dans la formule ≪ A≫ et maximum, formule ≪ A≫), la concentration est largement sous-estimée dans le cas pollué. Quand la concentration est bien simulée dans le cas pollué (sulfates, formule ≪ D≫ , maximum, formule ≪ D≫ , somme, formule ≪ A≫), elle est surestimée dans le cas propre. Donc, une autre paramétrisation qui serait plus sensible à la variation de la concentration des aérosols serait nécessaire.

Dans les études EXP-N, quelques particularités dans les différents paramétrisations pourraient être évaluées. Plusieurs modèles utilisent des facteurs pour ajuster leurs épaisseurs optiques. Ces modèles donnent des valeurs plus petites. Le modèle LMDZ, qui n'inclut pas un tel facteur, simule plutôt des valeurs élevées, ce qui est plus réaliste dans certains cas. Quand on utilise la résolution plus grossière du modèle (étude ≪ VERT≫), tous les modèles simulent des épaisseurs optiques et des albédos plus larges, ce qui est moins réaliste. La variation de l'albédo des nuages entre les cas propre et pollué est plus grand dans les observations que dans les modèles. Le taux de précipitation est fortement sous-estimé de plusieurs ordres de grandeur par tous les modèles. Évidemment, ils ne sont pas capables de simuler la bruine observée dans le cas des contenus en eau liquide relativement faible.

5. Aerosol indirect effects in POLDER satellite data and in the LMDZ GCM

5.1. Introduction

To understand the aerosol-cloud interactions on a global scale, the most promising approach is the combination of general circulation models (GCMs) and satellite measurements. GCMs include the treatment of a multitude of dynamical and physical processes and are able to simulate interactions between many climate parameters. Comparing the results of different simulations is a powerful method to understand climate processes. In contrast to observations, the impacts of single processes can be isolated. A disadvantage of GCMs is their coarse resolution. Observations with spaceborne instruments are the only measurements which cover the whole globe on long timescales. Satellite observations can therefore be used to evaluate GCM simulations. Current satellite instruments generally measure top-of-the-atmosphere radiances in the shortwave and longwave spectrum, thus providing a two-dimensional (latitude-longitude) view of cloud properties but with limited information on the vertical distribution.

Using AVHRR satellite observations, *Wetzel and Stowe* (1999) showed an inverse relationship between zonal and seasonal averages of aerosol optical depth and droplet size of stratus clouds over oceans. They also found an increase in seasonal and zonal mean cloud optical thicknesses with increasing aerosol optical thickness over oceans. *Schwartz et al.* (2002) used a combination of a hemispheric model and AVHRR satellite data to study the correlations between modeled aerosol data and satellite-derived cloud properties for a period of one week in April 1987 over the North Atlantic Ocean. They found a negative correlation between simulated sulfate aerosol concentration and observed cloud droplet radius, but no correlation between simulated sulfate and observed cloud optical depth. Again from AVHRR data, *Nakajima et al.* (2001) derived a negative correlation between cloud droplet effective radius and aerosol number concentration over oceans. However, their results do not show a correlation between aerosol concentration and cloud optical thickness or cloud liquid water path.

Bréon et al. (2002) used POLDER data to establish a relationship between quasi co-located aerosol properties and cloud droplet effective radii (CDR). They put in evidence the first aerosol indirect effect by identifying a decrease in cloud droplet effective radii with increasing aerosol concentrations. *Lohmann and Lesins* (2003a) compared these data with results from simulations with the ECHAM GCM to investigate the relative importance of the first and second AIE in their model. They found a too steep decrease in effective radius with increasing aerosol burden if the second indirect effect was excluded. *Lohmann and Lesins* (2003b) extended this study and further found an increase in LWP with increasing aerosol index in their model. They showed that, independently of the LWP, the CDR to aerosol index relationship is different in maritime compared to continental conditions.

In contrast to previous studies (with the exception of *Bréon et al.*, 2002), we do not average cloud and aerosol parameters over large regions and long timescales; rather we seek relationships between parameters derived from co-located (within a few degree resolution) and simultaneous measurements. A second difference from former studies is that we try to distinguish the aerosol impact on clouds for different cloud liquid water paths. *Han et al.* [1998, 2002] showed different behaviors of the relationship between cloud droplet column concentration and cloud optical thickness, τ_c, for small ($\tau < 15$) and large ($\tau > 15$) cloud optical thicknesses.

In this study, we exploit satellite data from the Polarization and Directionality of the Earth's Reflectances (POLDER) instrument and the Laboratoire de Météorologie Dynamique (LMD-Z) GCM. We establish statistical relationships in both satellite observations and results from model simulations to understand both the first and second AIE and to isolate the contribution of anthropogenic aerosols.

5.2. Observational data from POLDER

The POLDER-1 spaceborne radiometer on board the Japanese ADEOS satellite was able to measure various aerosol and cloud properties (*Deuzé et al.*, 1999; *Buriez et al.*, 1997) for the period from November 1996 until June 1997. Additionally *Bréon and Goloub* (1998) showed that in some cases multi-directional polarized radiance measurements can be inverted to estimate the CDR at cloud top. Their method unambiguously derives the size of spherical water droplets. This is an advantage compared to other methods to derive CDR which could be contaminated by aerosol layers above clouds (*Haywood and Osborne*, 2003). This retrieval was performed by *Bréon and Colzy* (2000) who derived cloud top droplet effective radii for the whole POLDER-1 period in cases of horizontally homogeneous liquid clouds on scales of at least 150x150 km^2.

We use the POLDER aerosol index (AI) derived over land and ocean (*Deuzé et al.*, 1999). The AI is estimated as the product of the aerosol optical depth, τ_a, and the Ångström coefficient, α, which is a measure of the particle size. It is therefore noted $\alpha\tau$ and may be interpreted as the load of submicronic aerosols. Recent studies have shown a high correlation between the AI and the column-integrated CCN concentration (*Nakajima et al.*, 2001). Regarding cloud properties, we use the cloud optical thickness, τ_c, derived over land and ocean (*Buriez et al.*, 1997) and the CDR described above.

We interpolate all observational data to the coarser GCM grid. In contrast to *Bréon et al.* (2002), where back-trajectories were used to relate a particular measurement of CDR to a clear-sky (upwind) measurement of aerosols, we correlate here the aerosol and cloud parameters in the same grid-box. This should be adequate, as the model grid-boxes are much larger than the POLDER pixels.

As there is no direct derivation of cloud liquid water path (LWP) from POLDER measurements, we estimate it from the cloud optical thickness, τ_c, and the CDR, r_e, by inverting the equation for τ_c (*Stephens*, 1978):

$$\tau_c = \frac{3}{2}\frac{\mathrm{LWP}}{r_e\ \rho_w} \tag{5.1}$$

where ρ_w is the density of liquid water. Thus, we get a measurement of LWP only over grid-boxes where a measurement of the CDR exists, i.e., for homogeneous liquid clouds. Note that POLDER estimates the cloud optical thickness from the reflectance measurements using a radiative transfer model.

5.3. Model description and derivation of a "satellite-like" model output

We use the Laboratoire de Météorologie Dynamique (LMD-Z) GCM (*Li*, 1999). Condensation of water vapor is calculated in the model using a "hat" probability density function for total water content to allow for fractional cloudiness (*Le Treut and Li*, 1991). We apply the microphysical scheme of *Boucher et al.* (1995a), which includes autoconversion and accretion for liquid water clouds and a fall-velocity dependent snow-formation equation for ice clouds. The CDNC (in cm^{-3}) is diagnosed from aerosol mass concentration, m_a (in μg m^{-3}), using the empirical formula of

Boucher and Lohmann (1995) (formula “D”):

$$N_d = 10^{a_0 + a_1 \log(m_a)} \tag{5.2}$$

where the empirical constants are $a_0 = 2.21$ and $a_1 = 0.41$. The LMDZ model includes a comprehensive on-line sulfur cycle model (*Boucher et al.*, 2002) as well as atmospheric cycles of sea-salt, organic matter, black carbon, and dust aerosols (*Reddy and Boucher*, 2003). In contrast to *Boucher and Lohmann* (1995) where the mass of sulfate aerosols was used as a surrogate for all aerosols, we use here instead the maximum of the masses of the three hydrophilic aerosol species considered in the model (sulfate, hydrophilic organic matter, and submicronic sea salt). This modification has an influence on cloud properties in biomass burning regions but a very small one in the northern hemisphere, where sulfate concentrations dominate. The volume-mean cloud droplet radius for liquid water clouds is calculated assuming spherical particles:

$$r_d = \sqrt[3]{\frac{q_l \, \rho_{air}}{\frac{4}{3} \, \pi \, \rho_w \, N_d}} \tag{5.3}$$

where q_l is the cloud liquid water mixing ratio, ρ_{air} the air density, ρ_w the density of liquid water, and N_d the CDNC. The volume-mean cloud droplet radius is related to the cloud droplet effective radius in our model as $r_e = 1.1 \; r_d$. While the first AIE causes the CDR to decrease, the second AIE results in an increase in cloud liquid water content, q_l. Both effects cause an increase in cloud optical thickness, which is parameterized as in Eq. 5.1.

We simulate the whole period of the POLDER-1 measurements (November 1, 1996 - June 29, 1997), starting two months before to allow for a spin-up of the aerosol concentrations. The SST and sea-ice are imposed using the SST dataset of *Reynolds and Smith* (1995) and the HADISST1.1 sea-ice data of the Hadley Centre (*Rayner et al.*, 2003). We nudge the model horizontal winds and temperature to ECMWF reanalysis data using relaxation times of 0.1 day for the winds and 1 day for the temperature in order to get realistic meteorological conditions. We simulate on-line in the model the POLDER swath to sample aerosols and clouds properties in the model in the same way the satellite does it. Therefore we do not expect any bias due to differences in sampling the diurnal cycle in the model and satellite data.

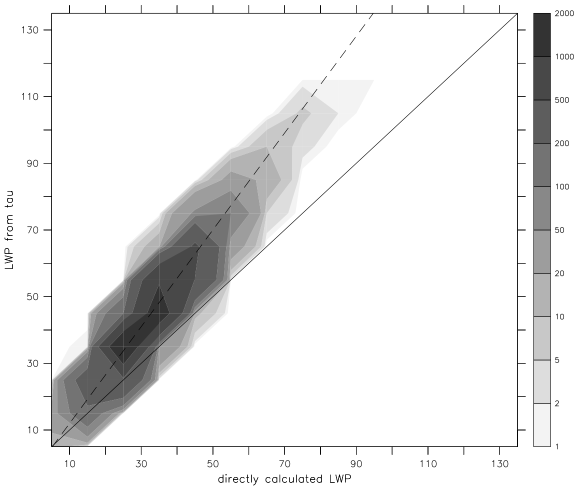

Figure 5.1.: Comparison of the LWP [g m^{-2}] calculated from cloud optical thickness and cloud droplet effective radius (y-axis) to the LWP directly calculated in the model. The correlation coefficient is 0.98 and the slope of the regression line is 1.45.

Cloud top quantities are estimated as seen by the satellite using the random cloud overlap assumption. By doing so we account for the contribution of each layer to the two-dimensional distribution seen at each gridpoint and time-step from above. For the effective radius only liquid water clouds which are not covered by clouds in layers above are considered. To match the POLDER criterion of horizontally homogeneous clouds at the 150x150 km^2 resolution, we only perform the estimation when at least a quarter of the grid-box is covered by a liquid cloud. As a model grid-box is 3.75 × 2.5° large, this matches approximately the resolution of the satellite data at least near the Equator. The optical thickness of liquid clouds is calculated using the ISCCP simulator (*Webb et al.*, 2001).

To be consistent with the derivation of LWP from the POLDER data, we also invert the LWP in the model from Eq. 5.1 using the above-derived optical thickness and cloud-top droplet radius of liquid clouds. This way of calculating the LWP is expected to give an upper bound to the LWP, as τ_c is an integrated value while r_e is the cloud-top droplet effective radius. As in general r_e increases with height in a cloud, the cloud-top value is expected to be largest. For the model output, the LWP calculated this way is compared to the LWP directly computed from the liquid water content, which is also sampled along the POLDER swath (Fig. 5.1). Despite the expected fact that the LWP calculated from τ_c and r_e gives larger values than the directly computed LWP, it is remarkable that there is a very good correlation between the two LWPs (with a correlation coefficient of 0.98). We can therefore use this retrieved LWP to compare with POLDER-estimated LWP and perform statistics at constant LWP (as done in the following section).

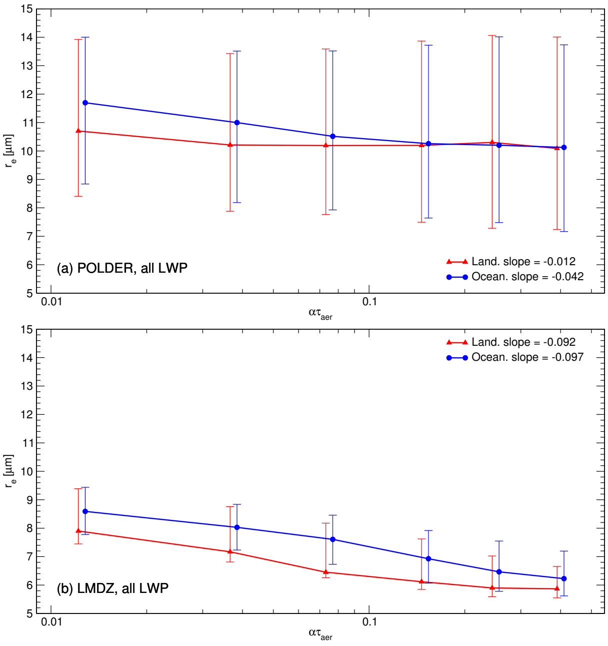

Figure 5.2.: Relationships between cloud droplet effective radius [μm] and aerosol index for the December 1996 to June 1997 period (for all LWP conditions) for POLDER observations (upper panel) and for LMDZ model outputs (lower panel). Continental (triangles, red) and maritime (circles, blue) conditions are separated. The analysis is restricted to the region 40°S–60° N, as POLDER observations of cloud optical thickness and thus LWP are not reliable at higher latitudes due to an influence of snow covered surfaces. Error bars show the mean deviation within each bin of aerosol index. Dotted lines indicate the number of points considered in each bin (right scale). The graphs are slightly shifted to the left for continental conditions and to the right for maritime conditions for the sake of better legibility.

5.4. Cloud droplet radius - aerosol index relationship

Fig. 5.2 shows the cloud droplet effective radius (CDR) to aerosol index (AI) relationships. The relationship is separated for continental and maritime conditions. For the POLDER data, a negative correlation is found over oceans. Over land, a negative correlation is found as well, but it is much less pronounced. For relatively large aerosol indices, almost no correlation between aerosol burden and CDR is observed. The slope of the relationship is calculated from the linear regression (aerosol indices from 0.0125 to 0.40) between the logarithms of r_e and $\alpha\tau$:

$$s = \frac{\partial \log r_e}{\partial \log \alpha\tau} \qquad (5.4)$$

We find s=–0.042 for maritime and s=–0.012 for continental conditions. Over oceans, *Bréon et al.* (2002) give a slope of s=–0.085, which is twice steeper than the one found in our study. This is due primarily to the averaging over a GCM gridbox, where different cloud and aerosol situations may be taken into account. Note that over land the aerosol index retrieval is not as reliable as over oceans.

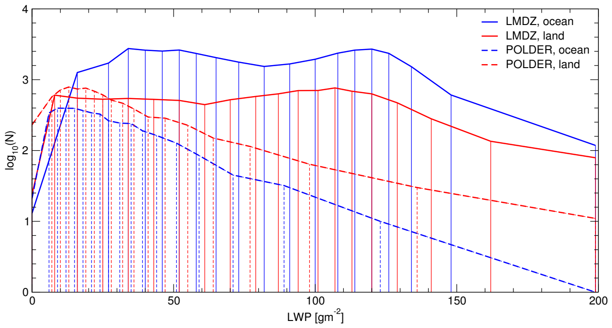

Figure 5.3.: Histogram of the LWP in model and observations. Vertical lines indicate the borders of the LWP bins.

In our model, a clear relationship exists, and the slope is s=–0.092 and –0.097 for continental and maritime conditions, respectively. A problem might arise because although we limit the analysis to homogeneous liquid water clouds, all LWP situations are taken into account. A correlation between CDR and AI might therefore be fortuitous if large aerosol burdens and low liquid water paths coincided because sources of fine-mode aerosols are located over land where the air is on average dryer. Strictly speaking the first AIE is defined as the CDR to AI correlation at constant cloud liquid water content (or equivalently constant LWP conditions). In order to examine the first AIE in this way, we classify all situations in model results and observations into 20 LWP bins, with LWPs ranging between 0 and 200 gm^{-2}, and the number of observations equally distributed between the bins. Fig. 5.3 shows a histogram of the LWP in model and observations. The size of the LWP bins used is also indicated on the figure. The CDR to AI relationship is established for each LWP bin and is shown on Fig. 5.4 for the POLDER data and the model results. In the observational data, the slopes become flatter with increasing LWP. Over land, s even becomes slightly positive for very large LWP values. A reason for the decrease in the negative slope of the CDR to AI relationship may be that for thick clouds the size of the droplets at cloud top may be controlled by the available water rather than by the aerosol concentration.

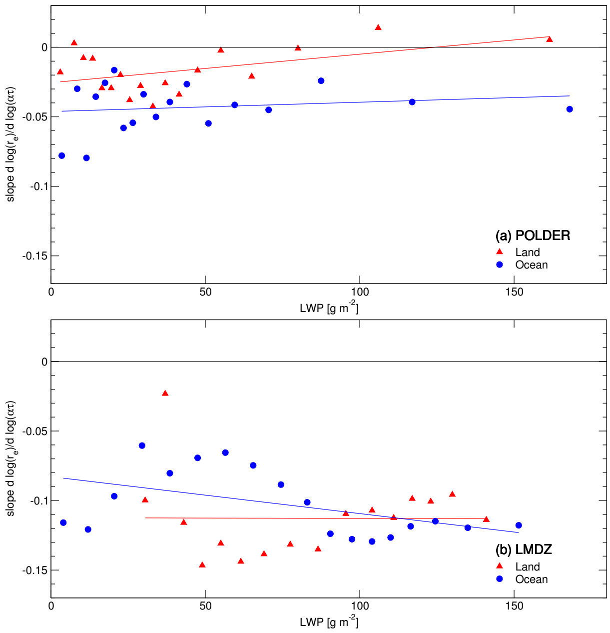

Figure 5.4.: Slope of the CDR to AI relationship, s, as a function of LWP, for a) the POLDER observations and b) the LMDZ model. Ocean and land regions are shown in blue (circles) and in red (triangles), respectively.

For the model there is no clear variation of the slope as a function of LWP. For small LWP (up to 60 gm^{-2}) over the ocean the slope becomes less negative. For LWPs between 60 and 100 gm^{-2} the slopes become steeper with increasing LWP and approach a rather constant value of –0.13 for LWP larger than 100 gm^{-2}. Over land a flattening of the slope is found for LWPs larger than 50 gm^{-2} and s approaches a value similar to that found over the ocean at very large LWPs.

In Fig. 5.5, we compare the slopes simulated by the model with the observed slopes for different situations. We calculate the slopes for the 20 LWP bins (for the whole period and for the whole globe) and the slopes for 24 regions of 15°x7.5° on the globe (for the whole period and for all LWP). In general, the model simulates too negative slopes for the CDR to AI relationship.

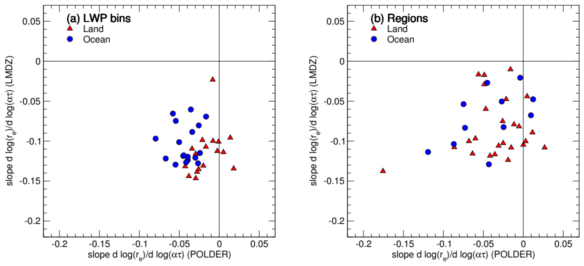

Figure 5.5.: Scatter plot of the slope s in the model and observations for a) the 20 LWP bins and b) the twenty-four 15°x7.5° regions in the globe. Blue circles and red triangles are for ocean and land regions, respectively.

The model always shows a negative correlation between CDR and AI, while in the POLDER observations, in particular over land, positive correlations may occur. There is a considerable scatter in Fig. 5.5, showing that the regional skills of the model are still limited.

The slopes are in a range of [–0.15,–0.02] for the model and [–0.08,+0.01] for the observations. Except for the positive values observed in POLDER data for continental conditions, our slopes are comparable to those given by *Feingold et al.* (2003), who used ground-based remote sensing measurements at different sites. In their study, values of [–0.16,–0.02] were observed. *Nakajima et al.* (2001) found a slope of –0.17 over oceans on a global scale, which is much larger than the mean values of –0.10 and –0.04 that we derived for the LMDZ model and POLDER data, respectively.

It is interesting to note that for the model the slope values s are of the order of one third (i.e., $\partial \log r_e / \partial \log N_d$) of the slope value implied by the constant $a_1 = 0.41$ in Eq. 5.2 between $\log N_d$ and $\log m_a$. This is because of the general linear relationship between m_a and $\alpha\tau$ in the model. A similar relationship has been proposed by *Nakajima et al.* (2001) between the aerosol column number concentration, N_a, and $\alpha\tau$.

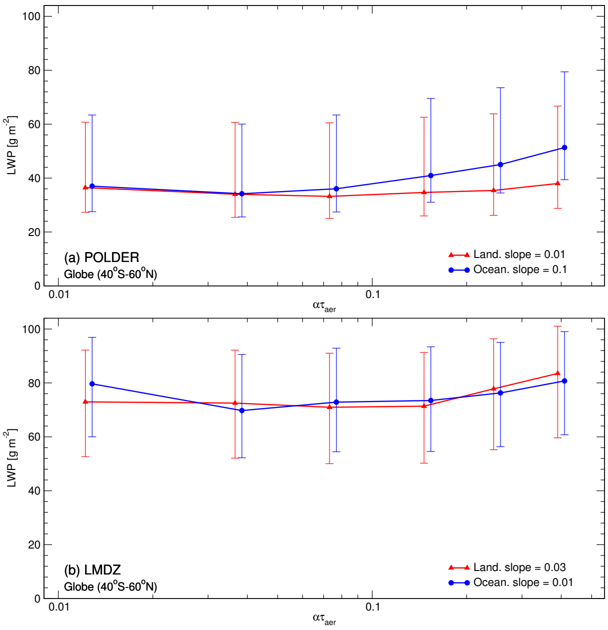

Figure 5.6.: Cloud liquid water path to aerosol index relationships over ocean (blue, circles) and land (red, triangles) for a) POLDER observations and b) LMDZ model calculations. The region is restricted to 40°S–60°N, and very large LWP values ($W > 150$ gm^{-2}) are excluded. The error bars indicate the mean absolute deviation within each bin.

5.5. Cloud liquid water path - aerosol index relationship

Examining the LWP to aerosol index relationship gives us some insight in the behavior of the second indirect effect. If the second aerosol indirect effect is real, larger LWP would be expected in regions with large aerosol concentrations. Although a correlation is not a proof of the second aerosol indirect effect, one would rather expect a negative correlation in the absence of second AIE because large AI in dry continental airmasses and low AI in humid maritime airmasses may be associated with thin and thick clouds, respectively.

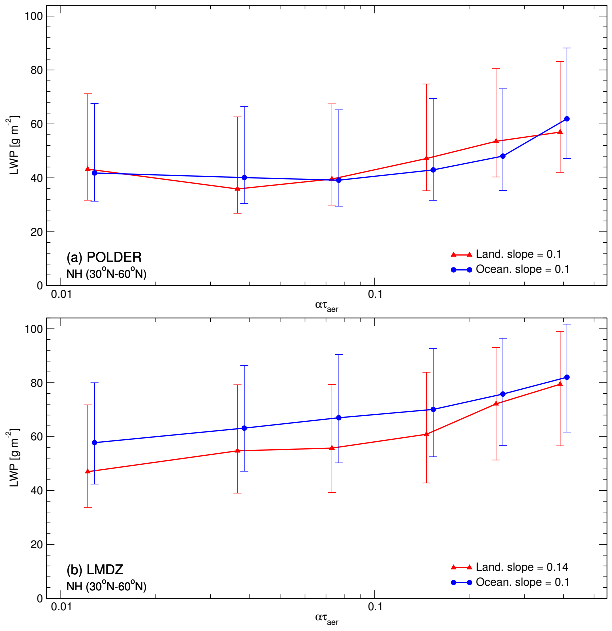

Figure 5.7.: As Fig. 5.6 but for midlatitudes of the northern hemisphere.

In Figs. 5.6 and 5.7, we plot the dependency of cloud liquid water path on aerosol index. For both the observations and the model, LWP is calculated by inverting Eq. 5.1, considering large-scale liquid water clouds only, for which a cloud droplet effective radius is defined. LWP values larger than 150 gm^{-2} are excluded from the analysis, because POLDER measurements of cloud optical thicknesses resulting in such large LWPs may be erroneous due to contamination by snow-covered surfaces (the LWP to AI relationship including all LWPs shows a very strong increase in LWP with increasing AI). While Fig. 5.6 shows the LWP to AI relationship for 40°S–60°N region, we restrict in Fig. 5.7 the analysis to northern hemisphere (NH) mid-latitudes (30°–60°N) where the AIE are expected to be very strong. Both the observations and the model show an increase in LWP as a function of aerosol index which is statistically significant at very high confidence levels (>95%) according to the Kendall rank correlation test (*Conover*, 1980).

For the 40°S-60°N region in POLDER observations, the relationship is much less steep for continental compared to maritime conditions for AI values larger than 0.1. Although an investigation of this process is beyond the scope of this study, one could argue that a semi-direct aerosol effect may play a role, which reduces cloudiness in regions with large concentrations of absorbing aerosols (*Ackerman et al.*, 2000a). A further analysis shows that the LWP to AI slope is the smallest in the region 0–30°N. Other influences may play a role as well. For example (*Feingold*, 2003) shows that the relationship between CDR and aerosol extinction becomes flatter with decreasing updraft velocity for large aerosol extinctions. It is also interesting to note, that in the POLDER data, and in some cases in the model simulations, the LWP to AI relationship shows slightly negative correlation at very small AI (for the first two $\alpha\tau$ bins). This could be due to the coincidence of low aerosol concentrations and large LWP values, for example in remote maritime areas.

The positive correlation is even more pronounced when looking at NH mid-latitudes only (Fig. 5.7). The slopes of the LWP to AI relationship in model and observations are of the same magnitude. However the positive slope occurs for $\alpha\tau > 0.1$ in the observations whereas it is observed throughout the range of AI in the model.

5.6. Indirect effects of anthropogenic aerosols

We performed two more experiments to further test the influence of anthropogenic aerosols. The control simulation is referred to as PD/PD (“present-day/present-day”), indicating that the present-day aerosol concentrations are taken in both the radiation and precipitation schemes. Anthropogenic aerosols act on the first and second AIE through these two parameterizations, respectively. In the PD/PI experiment anthropogenic aerosols influence only the radiation parameterization while a pre-calculated monthly mean pre-industrial aerosol distribution is used for the precipitation scheme. In the PI/PI experiment anthropogenic sources were switched off in the aerosol model and “pre-industrial” aerosol contributions are used for the first and second AIE. Fig. 5.8 compares the PD/PD and PD/PI experiments.

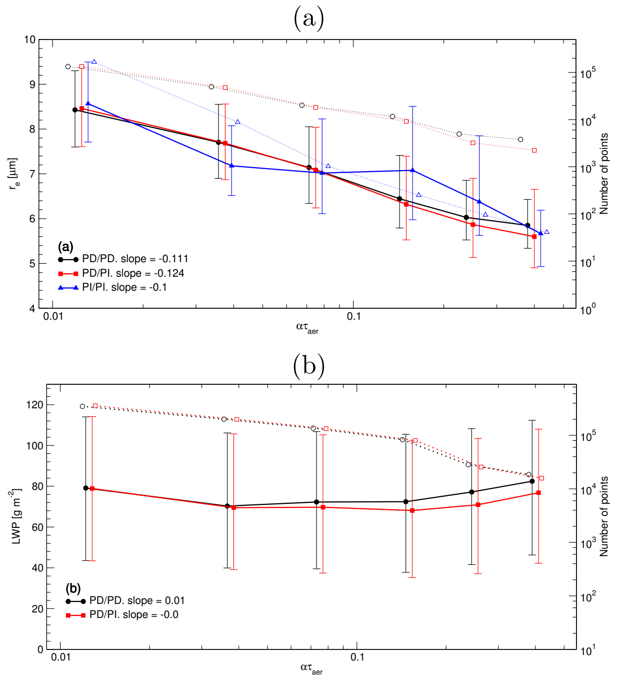

Figure 5.8.: (a) Relationships between CDR and AI for the PD/PD control (black), PD/PI (red), and PI/PI (blue) experiments. (b) Relationships between LWP and AI for the PD/PD (black) and PD/PI (red) experiments. The error bars indicate the mean absolute deviation within each bin and the dotted lines the number of points within each AI bin (right scale). No constraint on LWP is applied.

The impact of the second AIE on the CDR to $\alpha\tau$ relationship is relatively small – the slope is steepened only from –0.11 to –0.12. As shown in the previous section, LWP increase with increasing $\alpha\tau$ is largest for $\alpha\tau$ values larger than 0.1. Accordingly, we observe an impact of the second AIE on the CDR to $\alpha\tau$ relationship only at very large $\alpha\tau$ values. This finding is in contrast to the conclusion of *Lohmann and Lesins* (2003a) who found that the slope of the CDR to $\alpha\tau$ relationship in their model is strongly reduced by the impact of the second indirect effect. However they calculate the impact of the second AIE in a different manner, which prevents a more in-depth analysis of the differences between the two models.

Fig. 5.8a also shows the CDR to AI relationship in the PI/PI simulation using the pre-industrial AI value on the x-axis. The PI/PI curve shows that one should also expect a correlation between CDR and AI in pre-industrial conditions. The slope of the relationship is comparable to those obtained when using present-day aerosol conditions. The existence of a positive slope is therefore by itself not a proof of an anthropogenic impact; it has to be combined by an increase in aerosol index as well.

Finally Fig. 5.8 shows the LWP to AI relationships. Here, an impact of the second aerosol indirect effect caused by anthropogenic aerosols can clearly be identified by looking at the difference between the PD/PD and PD/PI curves. While there is no additional impact of anthropogenic aerosols on the second AIE for small aerosol indices, there is a strong anthropogenic contribution at AI larger than 0.1.

5.7. Summary and conclusions

Using satellite-derived data from the POLDER instrument and model simulations with the LMDZ GCM, we investigated the first and second AIE. We established relationships between aerosol index and cloud-top CDR for homogeneous liquid water clouds. In both observations and model, a decrease in CDR with increasing AI is found. In the observations, this decrease is less pronounced at large AI values. When establishing the CDR to AI relationship at fixed cloud liquid water path (LWP) a similar relationship is found. However, with fixed LWP, the decrease in CDR is also found in the observations at large AI. This difference to the relationship in the case of all LWP conditions is an indication of the impact of the second AIE on the CDR to AI relationship. The slopes of the relationship are –0.01 and –0.04 for the observations over land and ocean, respectively, and –0.09 and –0.10 for the model over land and ocean, respectively.

The slope of the CDR to AI relationship is found to become flatter with increasing LWP in the observations, while it approaches an almost constant value of about –0.13 for the model. In general, the model simulates too steep slopes compared to the POLDER data. The slopes found for different regions, LWPs, and periods are, however, comparable to those given by other authors.

To investigate the second AIE, we established a LWP to AI relationship. An increase in LWP with increasing AI is found for both model and observations. This increase is significant in particular for large AI ($\alpha\tau > 0.1$). A decrease in LWP with increasing AI is found at very small AI, which could be attributed to a geographical coincidence of low aerosol burden and thick clouds in remote regions. When limiting the region to northern hemisphere mid-latitudes, the LWP to AI relationship becomes much more pronounced. The slope of the LWP to AI relationship in the model matches well the observations.

In order to investigate the anthropogenic contribution to the aerosol indirect effects, additional experiments were carried out with the model, in which a pre-industrial aerosol distribution was used for the calculation of the first and second indirect effect, respectively. We find a small impact of the anthropogenic contribution to the second AIE on the CDR to AI relationship, which is restricted to large AI values. Anthropogenic aerosols causes the CDR to decrease by 0.5 μm on average in the CDR to AI relationship. The slope however is hardly changed. Similarly, a small impact of anthropogenic aerosols on the LWP to AI relationship is found at large AI values. The comparison between model and observations provides insight in some skills and deficiencies of the model. Two shortcomings have already been widely noticed and are common to many GCMs – the CDR simulated are in general too small compared to observations by up to 3-4 μm and the LWP is too large by 10-20 gm^{-2}. The model simulates too steep slopes for the CDR to AI relationship, in particular at large AI values. In regions with large aerosol burden (the northern hemisphere mid-latitudes), a slightly too steep dependence between LWP and AI is simulated at low AI values. However, the general shapes of the CDR to AI and the LWP to AI relationships are well simulated. The slopes of the LWP to AI relationships match rather well the observations.

5.8. Les effets indirects des aérosols dans les données satellitaires POLDER et dans le modèle LMDZ : Résumé

Introduction

Une des approches les plus prometteuses pour la compréhension des processus climatiques à l'échelle globale est la combinaison de modèles à grande échelle et d'observations satellitaires. Les MCGs traitent une multitude de processus dynamiques et physiques, et ils peuvent simuler les interactions entre plusieurs paramètres du climat. La comparaison entre différentes simulations est une méthode importante pour l'investigation des processus climatiques. En contraste aux observations, l'influence d'un paramètre particulier peut être isolé. Les observations avec les instruments spatiaux sont les seules mesures qui couvrent tout le globe avec de longues séries temporelles. A partir des mesures de luminances, des instruments satellitaires peuvent reconstituer des distributions à deux dimensions, qui sont valables pour le sommet des nuages dans le cas des propriétés des nuages.

En se focalisant sur les effets des aérosols sur les nuages, *Han et al.* (1994, 2002), *Wetzel et Stowe* (1999), *Nakajima et al.* (2001) et *Schwartz et al.* (2002) ont examiné les données AVHRR (Advanced Very High Resolution Radiometer) et ont montré des différences entre continent et océan, entre les deux hémisphères, et des relations statistiques entre les aérosols et les propriétés des nuages comme le rayon effectif des gouttelettes afin de mettre en évidence les effets indirects des aérosols. *Breon et al.* (2002) ont montré une corrélation négative entre l'indice en aérosols et la taille des gouttelettes. *Lohmann et Lesins* (2002, 2003) ont utilisé ces observations pour analyser les effets indirects dans leur modèle de grande échelle. Ils ont trouvé des relations différentes au-dessus des continents et des océans et ils ont montré l'importance du deuxième effet indirect pour reproduire la relation observée entre aérosols et rayon effectif des gouttelettes.

Méthodes

Dans cette étude, on utilise les données satellitaires dérivées de l'instrument POLDER. Pour les aérosols, l'indice en aérosols ($\alpha\tau$; *Deuzé et al.*, 1999) est utilisé, et pour les nuages, l'épaisseur optique (τ_c ; *Buriez et al.*, 1997) et le rayon effectif (r_e ; *Bréon et Colzy*, 2000) sont utilisés. Les données des observations sont interpolées sur la grille plus grossière du modèle.

Pour le lien entre aérosols de sulfates et concentration en gouttelettes dans notre modèle, nous utilisons la formule $\ll$ D$\gg$ de *Boucher et Lohmann* (1995) (Eq. 5.2). Ici, on considère la masse maximale des trois espèces d'aérosols hydrophiles utilisés dans le modèle au lieu de la seule masse des sulfates afin de mieux représenter les régions de combustion de la biomasse. Le rayon effectif des gouttelettes au sommet des nuages est calculé en faisant l'hypothèse de recouvrement aléatoire des nuages, et il n'est calculé que pour les nuages en eau liquide qui couvrent au moins un quart d'une maille pour reprendre les même conditions que dans les observations. L'épaisseur optique des nuages est calculée en utilisant le simulateur ISCCP (*Webb et al.*, 2001). Toutes les sorties du modèle sont échantillonnées en simulant la fauchée du satellite dans le modèle afin de constituer une distribution globale journalière de la même manière que pour l'instrument.

Aucune mesure de la colonne d'eau liquide (liquid water path, LWP en anglais) n'existe pour les données POLDER. Le LWP alors est calculé à partir des mesures de l'épaisseur optique et du rayon effectif des gouttelettes, ce qui donne une certaine surestimation du LWP. Pourtant, une comparaison entre le LWP directement calculé dans le modèle et le LWP calculé de cette manière à partir des données du modèle montre que ces deux quantités sont très fortement corrélées et qu'une analyse des LWP ainsi dérivés des observations est bien raisonnable (fig. 5.1).

Relation entre le rayon des gouttelettes et l'indice des aérosols

La relation entre le rayon effectif au sommet des nuages en eau liquide (cloud droplet radius, CDR en anglais) et l'indice des aérosols (aerosol index, AI en anglais) a été établie et pour les observations POLDER et pour le modèle LMDZ, séparément pour les régions continentales et maritimes (fig. 5.2). Premièrement, il est important de noter que le modèle sous-estime le rayon effectif d'environ 3 μm, ce qui est lié à la paramétrisation de l'autoconversion dans le schéma de précipitation et une erreur bien connue pour plusieurs modèles à grande échelle (*Rotstayn*, 2000). A la fois dans le modèle et dans les observations, le rayon effectif est plus grand au-dessus des océans qu'au-dessus des continents. La pente de la relation entre rayon effectif et indice des aérosols peut être calculée comme $s = \partial \log(r_e)/\partial \log(\alpha\tau)$. Pour les observations, on obtient une pente de –0.012 au-dessus des continents et de –0.042 au-dessus des océans. Pour les conditions maritimes, *Bréon et al.* (2002) donnent une pente de –0.085. La différence est due au fait que nous interpolons ici les donnés à la grille plus grossière du modèle. Les sorties du LMDZ donnent des pentes de –0.092 dans les conditions continentales et de –0.097 dans les conditions maritimes. Le fait que ces pentes sont supérieures à celles des observations est d'abord dû à une forte anticorrélation dans le modèle pour des indices en aérosols élevés, ce qui n'est pas le cas dans les observations.

Le premier effet indirect des aérosols a été défini par *Twomey* (1974) à LWP constant, ce qui exclut un impact du deuxième effet indirect sur la relation CDR-AI. De plus, une corrélation entre ces deux quantités peut être fortuite, si par exemple des concentrations en aérosols faibles se trouvent aux mêmes endroits que des nuages avec des contenus en eau liquide élevés comme dans des régions éloignées des océans. Pour examiner le premier effet indirect à LWP constants, nous classons les situations en 20 classes de LWP entre 0 et 200 gm^{-2} avec un nombre de cas distribué uniformément entre les classes (fig. 5.3). La relation CDR-AI est établie dans chacune des classes. Dans les observations, la relation devient plus raide, et en particulier pour des AI élevés, l'anticorrelation est plus marquée. L'impact de fixer le LWP est moins clair pour le modèle. La relation devient plus raide au-dessus des continents, mais un peu plus plate au-dessus des océans. Le choix du nombre des classes n'a pas d'influence importante sur ces résultats. L'analyse de la pente des relations en fonction du LWP montre que les relations CDR-AI deviennent plus plates pour de grands AI dans les observations (fig. 5.4). Au-dessus des continents, les pentes peuvent même devenir positives. Pour le modèle, un tel comportement ne peut pas être trouvé.

En comparant les pentes simulées par le modèle dans différentes régions du globe, et pour différents LWP à celles données par les observations dans les mêmes conditions, on observe que le modèle simule en général des pentes trop fortes, et toujours négatives, alors que dans les observations, on trouve parfois des pentes positives (fig. 5.5).

Les valeurs pour les pentes trouvées dans le modèle et les observations sont respectivement dans les intervalles de [–0.15,–0.02] et de [–0.08,+0.01]. A l'exception des valeurs positives dans les données de POLDER dans les conditions continentales, ces pentes sont comparables à celles trouvées par *Feingold et al.* (2003) qui utilisaient des observations de télédétection à partir du sol à différentes stations et trouvaient des valeurs de [–0.16,–0.02]. Au-dessus des océans en moyenne annuelle globale, *Nakajima et al.* (2001) donnent une valeur de –0.17, ce qui est grand comparé aux pentes trouvées ici.

Pour le modèle, les valeurs trouvées sont proches d'une valeur de 1/3 ($= \partial \log r_e/\partial \log N_d$) de la constante a_1=0.41 de l'équation 5.2 qui reflète la relation entre la concentration en nombre des gouttelettes et m_a.

Relation entre la colonne d'eau liquide et l'indice des aérosols

Une corrélation positive entre la colonne d'eau liquide et la concentration en aérosols pourrait être une indication du deuxième effet indirect. Nous regardons les relations LWP-AI pour tout le globe et pour la région des moyennes latitudes de l'hémisphère nord (figs. 5.6 et 5.7). A la fois dans les observations et dans le modèle, on trouve une corrélation positive entre le LWP et l'indice en aérosols qui est statistiquement fiable à des niveaux très élevés suivant le test de corrélation de Kendall (*Conover*, 1980). Pourtant, cette corrélation ne se trouve dans les observations que pour des AI relativement élevés quand on regarde tout le globe, alors que dans le modèle, on le trouve aussi pour des petits indices d'aérosols. Quand on se focalise sur les moyennes latitudes de l'hémisphère nord, la corrélation positive est plus prononcée. Les pentes des relations sont bien similaires dans les observations et dans le modèle.

Nous avons fait deux simulations de plus avec le modèle pour étudier les impacts des aérosols anthropiques. Les aérosols peuvent exercer le premier effet indirect dans le modèle via la paramétrisation du transfert radiatif, et le deuxième effet indirect via la paramétrisation de la précipitation. Dans la première des simulations additionnelles, nommée PD/PI, des concentrations actuelles (≪ present-day≫ , PD en anglais) ont été utilisées dans le schéma du rayonnement et des concentrations pré-calculées pour la situation pré-industielle (PI) dans la paramétrisation de la précipitation. Dans la deuxième simulation, nommée PI/PI des concentrations pré-industrielles ont été utilisées à la fois dans le rayonnement et dans la précipitation. La simulation de contrôle, où les aérosols actuels sont utilisés dans les deux paramétrisations est nommée PD/PD. La relation CDR-AI ne change pas beaucoup entre les différentes simulations, parce que la physique derrière la relation ne change pas (fig. 5.8). Pourtant, on peut identifier que la relation est légèrement plus plate pour des indices en aérosols élevés dans le cas où le deuxième effet indirect des aérosols anthropiques est inclus (PD/PD) comparé au cas où il ne l'est pas (PD/PI), ce qui montre une (faible) influence du deuxième effet indirect des aérosols anthropiques sur cette relation. Similairement, on trouve une corrélation plus forte entre LWP et indice en aérosols au cas où le deuxième effet indirect des aérosols anthropiques est inclus.

Part III.

Impacts of aerosol forcings on climate change

6. Impacts of greenhouse gases and aerosol direct and indirect effects on clouds and radiation in atmospheric GCM simulations of the 1930 - 1989 period

6.1. Introduction

Looking back at the twentieth century the observed warming on the global scale has been less than expected from the anthropogenic greenhouse effect alone (*Mitchell et al.*, 2001). Particularly for the period of 1940 to 1980, an almost constant temperature has been observed. We thus choose a slightly longer period from 1930 to 1989 to investigate possible reasons for this behavoir. Since serveral years, an additional anthropogenic forcing by sulfate aerosols has been proposed as a negative forcing which counterbalanced the warming effect of greenhouse gases (*Wigley*, 1989; *Charlson et al.*, 1989). In this study, we analyze the impact of greenhouse gases and aerosols on the Earth's radiation budget, with focus on indirect or feedback effects by modification of cloud properties.

Anthropogenic greenhouse gases consist of carbon dioxide from fossil fuel combustion and biomass burning, and other gases like methane, nitrous dioxide, chlorofluorocarbons, and tropospheric ozone. These gases are responsible for a warming of the Earth's surface because of enhanced atmospheric absorption and emission at lower temperatures of longwave (LW) radiation in the troposphere. The combustion of (sulfur-containing) fossil fuel is also a major source for sulfate aerosols. Aerosols scatter sunlight and enhance the planetary shortwave (SW) albedo, an effect known as the "aerosol direct effect" (ADE). In addition, by their ability to act as cloud condensation nuclei, (hydrophilic) aerosols change cloud properties, producing essentially an increase in cloud albedo. These processes are called "aerosol indirect effects" (AIE). As it has been shown by field studies (e.g., *Brenguier et al.*, 2000a) and satellite observations (e.g., *Bréon et al.*, 2002), the cloud droplet effective radius, r_e, decreases with increasing aerosol concentration. For a constant liquid water content, this results in a larger cloud albedo (this effect is called the first AIE, *Twomey*, 1974). Smaller droplets are also less likely to collide, therefore delaying or suppressing rain-forming microphysical processes. This results in a longer cloud lifetime and thus a larger cloud liquid water content, which again results in a larger cloud albedo (called the second AIE, *Albrecht*, 1989). Such an effect has been observed by *Rosenfeld* (2000) using satellite observations of clouds in various polluted and unpolluted conditions.

It is useful at least in the framework of modeling of external influences on the climate to introduce the concept of *radiative forcing* provoked by an external perturbation. The radiative forcing, ΔF, is defined as the difference in radiation flux at the tropopause in perturbed and unperturbed conditions, while the temperature and humidity profiles in the troposphere are fixed. In this definition, e.g., used by the IPCC (2001), any "small" global mean radiative forcing in a GCM is directly related to a change in global mean surface temperature at equilibrium through a model-dependent sensitivity parameter λ:

$$\Delta T_s = \lambda \, \Delta F \tag{6.1}$$

The largest anthropogenic radiative forcing is due to the greenhouse effect, with a positive annual global mean of the order of 2.4 Wm^{-2} for greenhouse gas (ghg) concentrations at the end of the 20th century compared to pre-industrial conditions (e.g., *Ramaswamy et al.*, 2001). The annual global mean radiative forcing by the sulfate aerosol direct effect is estimated to be about of –0.5 Wm^{-2}, the forcing by the first AIE to be of the order of –1.0 Wm^{-2}, although both are very uncertain (*Boucher and Haywood*, 2001).

The suitable tools to understand and possibly predict the impact of anthropogenic climate perturbations are general circulation models (GCMs) which simulate the dynamical and physical processes on a global scale. Using an atmospheric GCM, we try to understand the role greenhouse gases and aerosol effects have played in the evolution of the climate of the last century. We focus on changes in radiation fluxes throughout our simulation period of 1930 - 1989. The radiative forcing due to greenhouse gases and the aerosol direct and first indirect effects are computed. The second indirect effect, however, cannot be diagnosed instantaneously as it is related to a time-evolving process. There has been come controversy whether it should be considered as a forcing or a feedback mechanism. *Rotstayn and Penner* (2001) define a "quasi-forcing" for the second AIE as the difference in radiation flux between two model integrations with *fixed* SST, which are identical except for a change in the aerosol concentration in the precipitation parameterization. They showed that, at least for the first AIE, the quasi-forcing was a good estimate of the actual radiative forcing compiled for fixed profiles of temperature and humidity.

In analogy to this, we introduce the "radiative impact" of an anthropogenic perturbation. This is defined as the difference in radiative fluxes between two simulations with *evolving* SSTs, with and without the perturbation, but otherwise identical. We compute the radiative impact due to greenhouse gases and the total aerosol radiative impacts, including the aerosol direct and both indirect effects. Thus, the *radiative forcings* due to greenhouse gases and aerosol direct and first indirect effects can be compared to the *radiative impacts* of greenhouse gases and aerosols, which include feedback processes.

6.2. Model description

6.2.1. The atmospheric model

The model used is the atmospheric general circulation model (GCM) of the Laboratoire de Météorologie Dynamique (LMD). It is a grid-point model which we ran in a resolution of 96x73 points on a regular longitude-latitude horizontal grid with 19 hybrid sigma-pressure coordinate levels. The timestep is 6 min for the dynamical part of the model and 30 min for the physics. Prognostic variables are temperature, horizontal winds, surface pressure, and total water content.

The physics of the model has formerly been described e.g. in *Li* (1999) and is reported briefly. Radiative transfer is calculated in the model using an advanced version of the scheme of *Fouquart and Bonnel* (1980) for the solar spectrum and an updated version of the code of *Morcrette* (1991) for the terrestrial part. In difference from former studies (e.g., *Le Treut et al.*, 1998), the diurnal cycle is included. Convection is parameterized in the model using the Tiedtke scheme (*Tiedtke*, 1989). The land surface processes are parameterized through a bucket model, and the surface temperature is evaluated in the boundary layer scheme using the surface energy balance equation.
Condensation of water vapor is calculated using a "hat" probability density function for total water content to allow for fractional cloudiness (*Le Treut and Li*, 1991). We apply the cloud microphysics scheme of *Boucher et al.* (1995a), which includes autoconversion and accretion for liquid water clouds and a simple snow-formation equation for ice clouds.

6.2.2. Parameterization of the aerosol indirect effects

The cloud droplet number concentration (N_d, in cm^{-3}) is diagnosed from the sulfate aerosol mass concentration, m_{SO_4} (μg sulfate m^{-3}) using an empirical formula (*Boucher and Lohmann*, 1995, , formula "D"):

$$N_d = 10^{2.21+0.41\ \log_{10}(m_{\mathrm{SO}_4})} \tag{6.2}$$

The volume-mean cloud droplet radius for liquid water clouds assuming spherical particles is

$$r_d = \sqrt[3]{\frac{q_l\ \rho_{\mathrm{air}}}{\frac{3}{4}\ \pi\ \rho_{\mathrm{water}}\ N_d}} \tag{6.3}$$

where q_l is the liquid water mixing ratio, ρ_{air} and ρ_{water} the densities of air and water, respectively. From the combination of Eq. 6.2 and 6.3 it can be deduced that an increase in sulfate aerosol mass concentration directly results in a decrease in the cloud droplet radius for constant liquid water content.

The cloud property relevant to the radiation transfer in the solar spectrum is the cloud optical thickness, τ_c. This quantity relates aerosols, clouds, and radiation in our model. Cloud optical thickness is parameterized in terms of r_e and the cloud liquid water path, W (*Stephens*, 1978):

$$\tau_c = \frac{3}{2}\frac{W}{r_{\mathrm{e}\ \rho_w}} \tag{6.4}$$

The autoconversion, R_{ll}, of liquid water droplets to raindrops in the scheme of *Boucher et al.* depends on the cloud droplet radius

$$R_{ll} \propto E_{ll}\ q_l\ r_d^4\ N_d \tag{6.5}$$

where E_{ll} is the collision efficiency, which is considered to be 0 for droplet radii less than a "critical radius", r_{crit}, and 1 for larger droplets. For constant cloud liquid water content, $r_d \propto N_d^{-1/3}$ and thus $R_{ll} \propto r_d$ for $r_d > r_{\mathrm{crit}}$. The conversion of cloud to rain water is thus less efficient for smaller droplets.

The cloud optical thickness and thus the cloud albedo are increased by the first AIE by decreasing r_e and by the second AIE by increasing W.

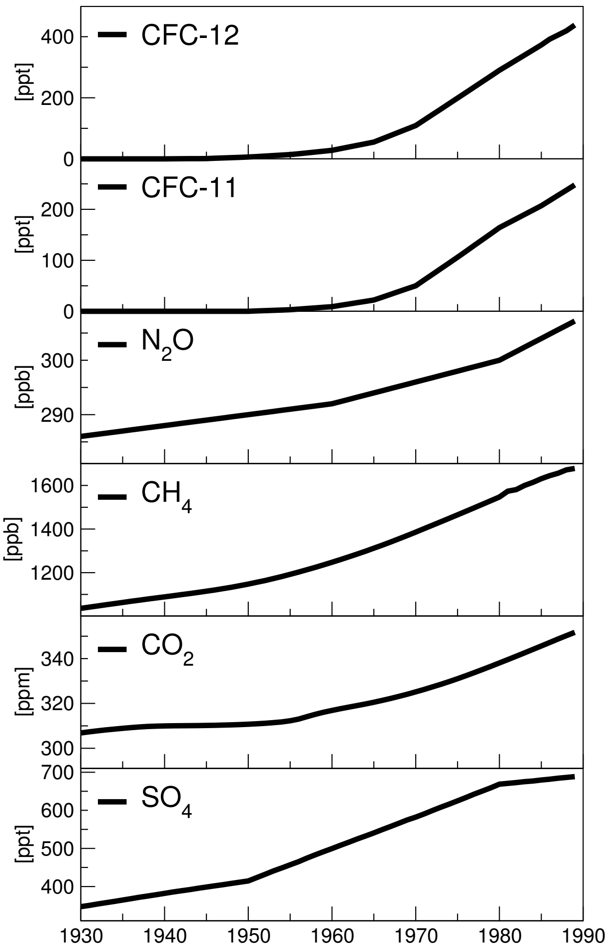

Figure 6.1.: The evolution of the sulfate aerosol at 850 hPa (*Boucher and Pham*, 2002) and greenhouse gas concentrations (*Myhre et al.*, 2001). Global and annual means are shown.

6.2.3. Experiment setup

The simulations were done using time-varying observed sea surface temperature (SST) and sea-ice extent distributions from Hadley-Centre analyses (HADISST1.1, *Rayner et al.*, 2003)) for the period 1930 - 1989. The monthly mean distributions are smoothed out in time.

Monthly mean sulfate aerosol distributions were computed every 10 years of the simulation using historical emission data and applying a comprehensive sulfur cycle model (*Boucher et al.*, 2002; *Boucher and Pham*, 2002). The monthly distributions are also smoothed out in time. Fig. 6.1 shows the global

	GHG+AER	GHG	CTL
Greenhouse gases	time-varying	time-varying	pre-industrial
Aerosols	time-varying	pre-industrial	pre-industrial

Table 6.1.: Summary of the forcings in the three ensembles. Throughout the paper, we will use upper case abbreviations to name the simulations, and lower case, if the forcing itself is meant.

and annual mean sulfate aerosol mixing ratio at 850 hPa.

Greenhouse gases are considered well mixed throughout the troposphere in our model. We use yearly mean averages of CO_2, CH_4, N_2O, CFC-11 and CFC-12 from *Myhre et al.* (2001) as displayed in Fig. 6.1.

We carried out three ensembles of simulations, each consisting of three members for which the initial conditions for 1st January 1930 were slightly perturbed. In the first, named GHG+AER, greenhouse gases as well as sulfate aerosol concentrations were varying as described above. In the second, named GHG, sulfate aerosols were fixed to the calculated pre-industrial distribution, while the greenhouse gas concentrations increased during the simulation. Finally, we did a control simulation CTL, in which both sulfate aerosols and greenhouse gas concentrations were fixed to their pre-industrial concentrations. A summary of the ensembles is given in Tab. 6.1. Throughout this paper, the abbreviations GHG and AER in capitals will refer to the scenarios, whereas ghg (“greenhouse gases”) and aer (“aerosols”) in lower case refer to the perturbations of the atmospheric concentrations themselves.

6.2.4. Radiation diagnostics

The influence of greenhouse gases and aerosols on the radiative fluxes in our model is examined using two different approaches. Firstly, we calculate the *radiative forcings*, as defined in the introduction. Secondly, we define a *radiative impact*, a new quantity which includes feedback processes of the climate system. The shortwave and longwave spectra are treated separately, as are the perturbations by greenhouse effect and different aerosol effects.

Radiative forcings

For greenhouse effect, the radiative forcing is calculated off-line using the temperature and humidity profiles and the cloud and surface properties for each month of the simulations. The difference in longwave radiative flux at the tropopause between current and pre-industrial greenhouse gas concentrations is computed after adjustment of the stratosphere profiles (*Cess et al.*, 1993, *Hansen et al.*, 1997).

Concerning the aerosol effects, the shortwave radiative forcings due to the aerosol direct and first aerosol indirect effect are calculated on-line in the simulation. The radiation scheme is applied twice, with the aerosol and cloud optical properties for current and pre-industrial aerosol distributions, and the difference in SW radiative fluxes at the top of the atmosphere (TOA) is taken as the radiative forcing. This implicitly neglects the adjustment of the stratosphere, which is a valid assumption for the SW spectrum (*Hansen et al.*, 1997). The radiative fluxes computed with the current aerosol concentrations are used in the integration, while the fluxes calculated with pre-industrial values are just stored for the analysis.

Radiative impacts

In order to include the impact of changing cloud properties and (other) feedback processes in our analysis, we define a new quantity, the “radiative impact” of a given perturbation ($I_{\text{perturbation}}$). We define this radiative impact as the difference in radiative fluxes, F, at the top of the atmosphere between two scenarios, in which all but one parameter of the simulation are fixed and the internal variability of the model is removed by averaging over an ensemble of simulations.

According to this definition, the total sulfate aerosol

$$
\begin{array}{lclcl}
\hline
I_{\mathrm{SW}}|_{\mathrm{aer}} & = & < F_{\mathrm{SW}}|_{\mathrm{GHG+AER}} > & - & < F_{\mathrm{SW}}|_{\mathrm{GHG}} > \\
I_{\mathrm{SW}}|_{\mathrm{ghg}} & = & < F_{\mathrm{SW}}|_{\mathrm{GHG}} > & - & < F_{\mathrm{SW}}|_{\mathrm{CTL}} > \\
\hline
I_{\mathrm{LW}}|_{\mathrm{aer}} & = & < \mathrm{GHE}|_{\mathrm{GHG+AER}} > & - & < \mathrm{GHE}|_{\mathrm{GHG}} > \\
I_{\mathrm{LW}}|_{\mathrm{ghg}} & = & < \mathrm{GHE}|_{\mathrm{GHG}} > & - & < \mathrm{GHE}|_{\mathrm{CTL}} > \\
\hline
\end{array}
$$

Table 6.2.: Definition of the SW radiative impacts of aerosols and greenhouse gases. The total greenhouse effect (GHE) is defined in the text. The brackets indicate ensemble averaging.

radiative impact, I_{aer}, is the difference in radiative fluxes between the GHG+AER and GHG simulations. The radiative impact of aerosols is composed of the aerosol direct effect as well as the first and second aerosol indirect effects, which possibly includes further feedback processes due to aerosols. Similarly, we define the radiative impact of greenhouse gases, I_{ghg} (see Table 6.2 for a summary).

In the shortwave spectrum, we compare the net radiative fluxes at the top of the atmosphere in two ensembles. This is, however, not possible in the longwave spectrum. While over land the surface temperature adjusts to bring the radiative budget at TOA to equilibrium, this is not the case over the oceans, where the SST is fixed. We therefore introduce a new quantity, termed the total greenhouse effect (GHE). This is defined as the difference in the upward LW radiative fluxes at the surface and TOA. The upward LW flux at the surface is the sum of the thermal emission of the surface and the reflected fraction of the atmospheric thermal emission reaching the surface. The GHE can therefore be written as

$$\mathrm{GHE} = \left[\epsilon\sigma T^4 + (1-\epsilon)\, F_{\mathrm{sfc}} \downarrow \right] - F_{\mathrm{TOA}} \uparrow$$

where ϵ is the surface emissivity, σ the Stefan-Boltzmann constant, and T the surface temperature. The GHE can be seen as the amount of energy in the LW spectrum responsible for a greenhouse effect at the surface.

Using this radiation quantity, the radiative impact in the LW spectrum can be defined as the difference in GHE between the ensemble means of two scenarios (Table 6.2).

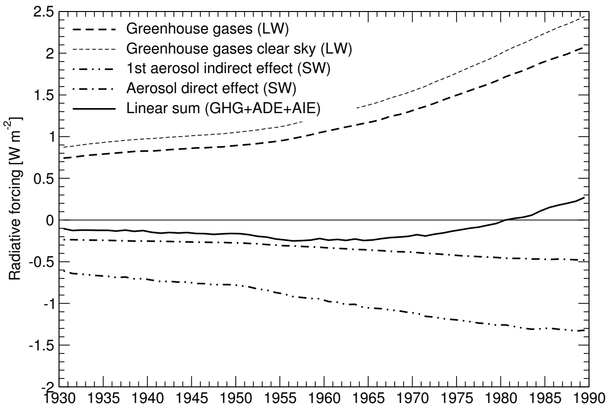

Figure 6.2.: Annual global mean radiative forcings [Wm^{-2}] as diagnosed in the ensemble mean of the GHG+AER simulations: greenhouse gas forcing (LW spectrum, dashed line), aerosol direct forcing (SW spectrum, dot-dashed), and first aerosol indirect forcing (SW, dot-dot-dashed). The solid line corresponds to the sum of the three diagnosed radiative forcings.

6.3. Results

6.3.1. Radiative forcings

Figure 6.2 shows the radiative forcings in the scenario simulation GHG+AER. The greenhouse gas forcing in the model is positive and ranges from 0.74 Wm^{-2} in 1930 to 2.07 Wm^{-2} in 1989, which is consistent with the value of 2.43 Wm^{-2} given by the IPCC (*Ramaswamy et al.*, 2001) for all greenhouse gases in year 2000. The direct forcing by sulfate aerosols decreases from –0.2 to –0.5 Wm^{-2} and the first aerosol indirect forcing from –0.6 to –1.3 Wm^{-2}. This is also in the range of results compiled by *Ramaswamy et al.* (2001) (–0.2 to –0.8 Wm^{-2} for the ADE and –0.3 to –1.8 Wm^{-2} for the first AIE).

If the three forcings add up linearly, the net forcing would be slightly negative for the period 1930 to 1980 (with a minimum of –0.25 Wm^{-2} in 1956), and positive afterwards (up to 0.27 Wm^{-2} in 1989).

Figure 6.2 also shows the greenhouse gas LW radiative forcing, restricted to cloud free conditions. This quantity is about 0.1 to 0.2 Wm^{-2} larger than its all-sky counterpart. The explanation is that (high-level) clouds themselves cause a greenhouse effect and thus mask part of the greenhouse effect due to anthropogenic greenhouse gases.

6.3.2. Radiative impacts

The longwave spectrum

In Fig. 6.3, the LW radiative impacts of greenhouse gases and aerosols are shown. The LW radiative impact of the aerosols is negligible. A trend of about 0.2 W m^{-2} decade^{-1} is simulated for the radiative impact of greenhouse gases with very similar values for all-sky and cloudy-sky conditions. The radiative impact in cloud free conditions, $I^{\mathrm{cf}}_{\mathrm{ghg}}$, is about 0.2 to 0.5 Wm^{-2} larger. We now seek an explanation as for why the radiative impact in cloudy sky, $I^{\mathrm{cc}}_{\mathrm{ghg}}$, and in all sky, $I^{\mathrm{a}}_{\mathrm{ghg}}$, show the same evolution, which involves the role of cloud feedbacks.

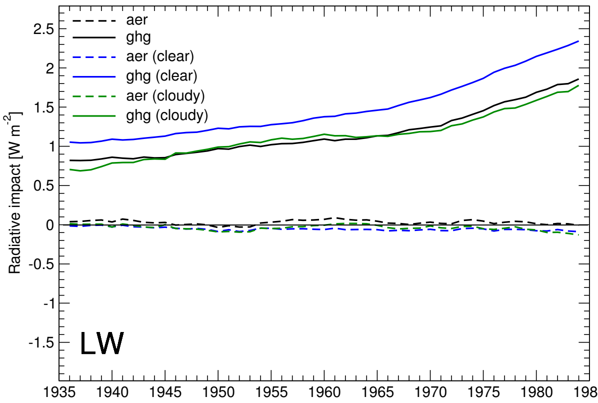

Figure 6.3.: Global annual means of the longwave radiative impact [Wm^{-2}], as defined in Section 6.2.4, for aerosols and greenhouse gases for all-sky (black), cloud free (blue) and cloudy (green) conditions. An 11-year running mean is applied.

The all-sky GHE is composed by the GHE in the cloudy, GHE$^{\mathrm{cc}}$, and in cloud free regions, GHG$^{\mathrm{cf}}$, where each of the contributions is weighted by the respective cloudy and cloud free fractions of the grid cell, f and (1–f), respectively:

$$\mathrm{GHE}^{\mathrm{a}} = f\ \mathrm{GHE}^{\mathrm{cc}} + (1-f)\ \mathrm{GHE}^{\mathrm{cf}} \tag{6.6}$$

The all-sky radiative impact of greenhouse gases (see Section 6.2.4), is thus influenced by the difference in GHE in cloudy and cloud free conditions, and by the change in the cloud cover, $\Delta f = f_{\mathrm{GHG}} - f_{\mathrm{CTL}}$:

$$\begin{aligned} I^{\mathrm{a}}_{\mathrm{ghg}} &= I^{\mathrm{cf}}_{\mathrm{ghg}}\ (1-f_{\mathrm{GHG}}) + I^{\mathrm{cc}}_{\mathrm{ghg}}\ f_{\mathrm{GHG}} + \\ & \quad \Delta f\ (\ \mathrm{GHE}^{\mathrm{cc}}_{\mathrm{CTL}} - \mathrm{GHE}^{\mathrm{cf}}_{\mathrm{CTL}}) \end{aligned} \tag{6.7}$$

The fact that the all-sky radiative impact of greenhouse gases follows its cloudy-sky counterpart means that the third term on the right hand side of Eq. 6.7 compensates for the observed increase in cloud free radiative impact. Since $\mathrm{GHE}^{\mathrm{cc}}_{\mathrm{CTL}} - \mathrm{GHE}^{\mathrm{cf}}_{\mathrm{CTL}}$ is a positive quantity, there must be a decrease in the cloud cover (see Section 6.4).We can summarize the following results:

- The radiative impact of greenhouse gases is larger in clear-sky conditions compared to all-sky conditions.

- The increase in all-sky radiative impact results from an increase in clear-sky GHE, an increase in cloudy-sky GHE, and a decrease in cloud cover.

The radiative impact of the greenhouse gases varies from 0.81 Wm^{-2} in 1930 to 2.09 Wm^{-2}, which is close to the corresponding diagnosed radiative forcing. Since the radiative impact includes some feedbacks, the two quantities being equal means that the net radiative impact of these feedback processes is small in the context of these experiments with fixed SST.

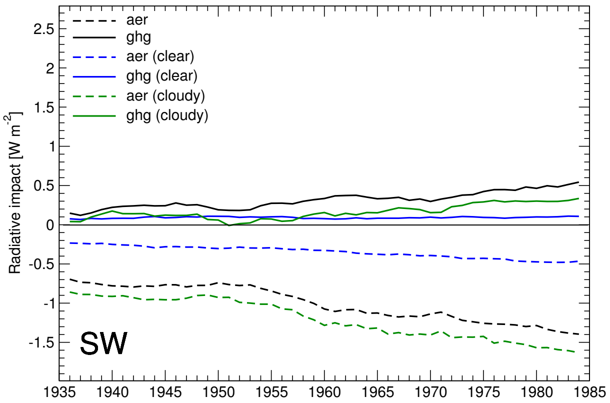

Figure 6.4.: Global annual means of the shortwave radiative impacts [Wm^{-2}], as defined in section 6.2.4, for aerosols and greenhouse gases. An 11-year running mean is applied.

Looking at cloud free conditions however the radiative impact of greenhouse gases is larger than the corresponding radiative forcing. This small difference can be explained by the existence of a positive feedback related to an increase in water vapor concentration due to a warmer atmosphere.

The shortwave spectrum

Figure 6.4 shows the radiative impact in the SW spectrum. A small radiative impact is simulated concerning the greenhouse gases. We attribute this to a snow cover feedback (melting of snow due to the warmer surface temperature in the simulation including anthropogenic greenhouse gases), which is of the order of 0.1 Wm^{-2} and exhibits a gentle trend of 0.002 Wm^{-2} decade $^{-1}$. In cloudy conditions, greenhouse gases cause an increase in radiative impact, which is somewhat smaller than the increase in all-sky conditions. We conclude that

1. The increase in SW flux in cloud covered conditions corresponds to less reflecting clouds.
2. As the all-sky radiative impact is larger than for both the clear and cloudy-sky radiative impact the cloud cover must be reduced by greenhouse gases.

These findings will be discussed in the following section.

For the aerosols a decrease in the clear-sky radiative impact is simulated from –0.2 to –0.5 Wm^{-2}. This is almost exactly the evolution diagnosed for the aerosol direct radiative forcing. It can be concluded that there is almost no net radiative impact due to feedback processes in cloud free conditions and for fixed SST. In cloudy conditions, the radiative impact is strongly negative and decreases from –0.8 to –1.6 Wm^{-2}. The all-sky radiative impact lies in between the two, ranging from –0.7 to –1.4 Wm^{-2}. This is only a little bit more than the radiative forcing diagnosed for the first AIE alone and thus much smaller than the sum of first AIE and ADE forcings. We investigate in Section 6.4.2 the feedback processes that introduce some positive radiative impact due to aerosols.

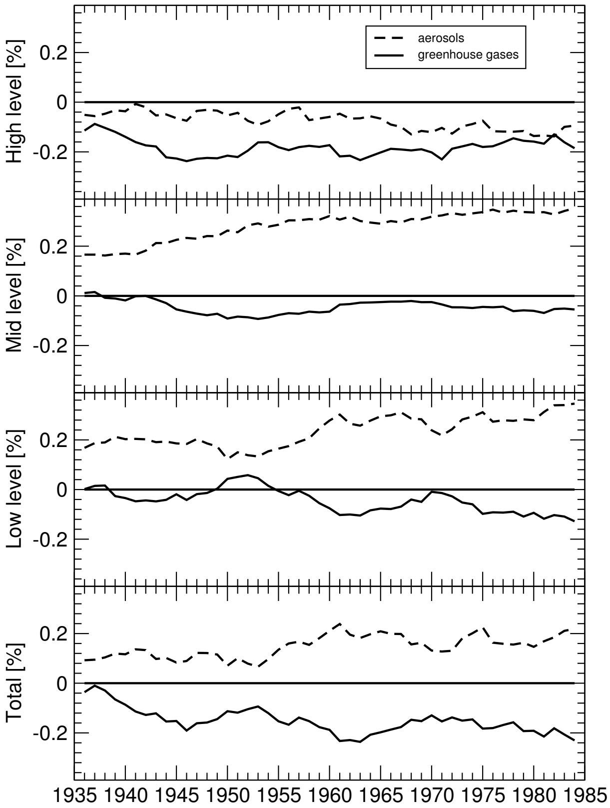

Figure 6.5.: Temporal evolution of the differences in annual and global mean cloudiness between ensemble means. The evolution for high-level (above 450 hPa), mid-level (between 800 hPa and 450 hPa), and low-level clouds (below 800 hPa), and the total cloudiness is shown. An 11-year running mean is applied.

6.4. Discussion

6.4.1. Trends in cloudiness

Figure 6.5 shows the simulated evolution of the change in global annual mean cloud cover. The changes in total, low-level (below 800 hPa), mid-level (between 800 and 450 hPa) and high-level (above 450 hPa) cloud cover are shown. As already noted in the analysis of the radiative impacts in the previous section, the anthopogenic greenhouse gases result in a decrease in cloud cover. This reduction is found for clouds at all three levels, and it is strongest for high-level clouds. There is an increase in water vapor content in the atmosphere, q_v, in the GHG compared to the CTL experiments, while the saturation water wapor mixing ratio, q_{sat}, increases as well. The net effect is a decrease in cloudiness. As already shown, clouds also contain less water and have thus a smaller albedo.

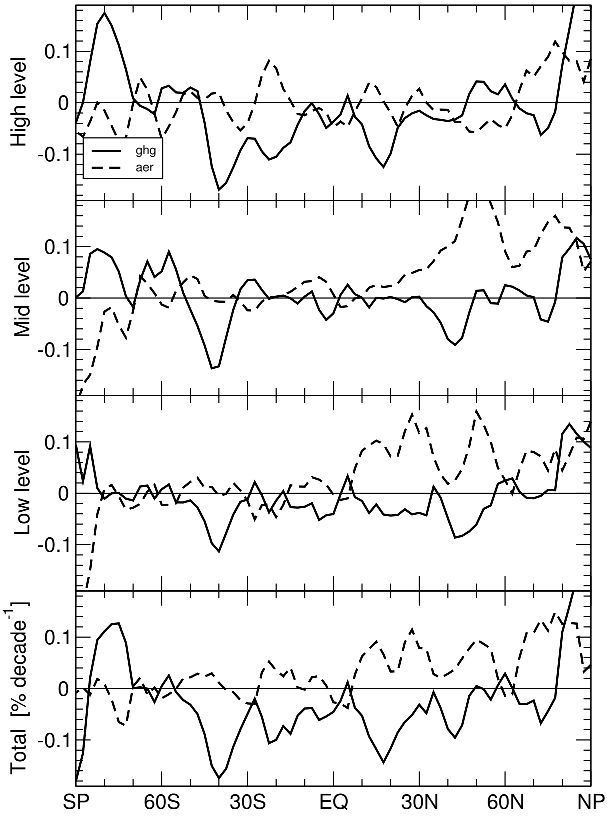

Figure 6.6.: Zonal mean of the linear trends in the annual mean high-, mid-, and low-level, and total cloudiness. The differences between ensemble means are shown, as in Fig. 6.5.

Figure 6.6 shows the zonal average of the linear trends in the high, middle, and low-level, and total cloudiness. It shall be noted that in the global mean, these trends have the slope of the curves in Fig. 6.5. For the aerosol impact on cloudiness, different behaviors can be noted for clouds at different levels. High-level cloudiness decreases, which is a result of the cooling of the upper troposphere due to the aerosol radiative effects. The reduction in high-level cloudiness due to aerosols does not show a uniform distribution over the globe. While sometimes even an increase can be observed (e.g., at 20 °S and in the northern hemisphere high latitudes), at most latitudes, the tendency is negative. Aerosols seem always to have an opposite effect of the greenhouse gases.

For low and mid-level clouds, greenhouse gases cause a slightly decreasing trend at low and mid latitudes, and an increase at high latitudes. The impact of aerosols on low and mid-level clouds is different in both hemispheres. In the southern hemisphere, except at very high latitudes, almost no trends in low and mid-level cloudiness are observed. This is expected, as the anthropogenic aerosol concentration in the SH is rather low. In the northern hemisphere, however, low and mid-level cloudiness increases under the influence of aerosols. A reason for this could be the second AIE. This question will be addressed in the following Section.

The minima in the trend in low-level cloudiness observed at 40 and 60°N correspond to a decrease in cloudiness in limited regions (over Himalaya, Greenland, and Alaska), counterbalancing the general increase.

6.4.2. Influence of clouds on the SW radiative impact

As stated in Section 6.3.2, greenhouse gases have a positive radiative impact in the SW spectrum due to the reduction in cloudiness, in particular at low-levels.

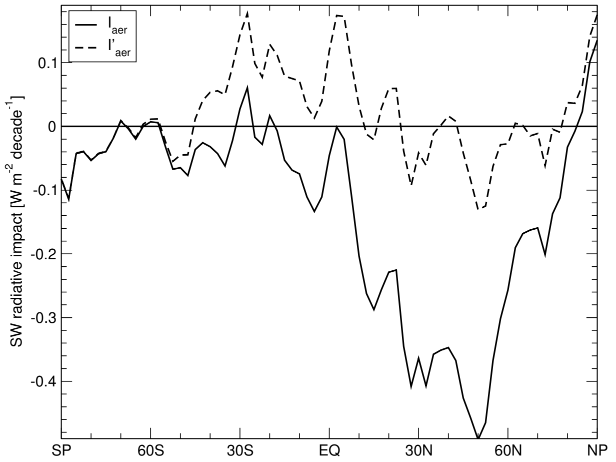

Figure 6.7.: Zonal mean linear trends in the annual mean SW radiative impact of the aerosols as defined in section 6.2.4 (I_{aer}, solid line) together with the radiative impact of second AIE and cloud feedbacks ((I'_{aer}, dashed line).

Due to the impact of the aerosols, on the other hand, the amount of low- and mid-level clouds increases, especially in northern hemisphere midlatitudes, while high-level cloud cover slightly decreases. To isolate the effect of aerosols on the cloudiness (or cloud water content) from the other aerosol effects acting in the SW spectrum (i.e., the ADE and the first AIE), we introduce a new quantity, I'_{aer}, defined as the radiative impact of aerosols minus the diagnosed radiative forcing due to the first AIE and the ADE:

$$I'_{\mathrm{aer}} = I_{\mathrm{aer}} - \Delta F_{\mathrm{1st\ AIE}} - \Delta F_{\mathrm{ADE}} \qquad (6.8)$$

This quantity I'_{aer} is a measure of the second aerosol indirect effect and all cloud feedbacks associated to aerosol effects. It is positive, increasing from 0.2 to 0.4 Wm^{-2} in 1989. Since the radiative impact in clear-sky not explained by the direct radiative forcing of aerosols ($I^{\mathrm{cf}}_{\mathrm{aer}} - \Delta F_{\mathrm{ADE}}$) is very close to zero and limited to high latitudes, we infer that there are no major feedbacks involved except processes involving clouds.

Figure 6.7 shows the zonal mean of the linear trends 1930 to 1989 of the I_{aer} and $I_{\mathrm{aer}'}$. The total aerosol radiative impact (I_{aer})is negative almost everywhere, with the lowest values in the northern hemisphere midlatitudes.

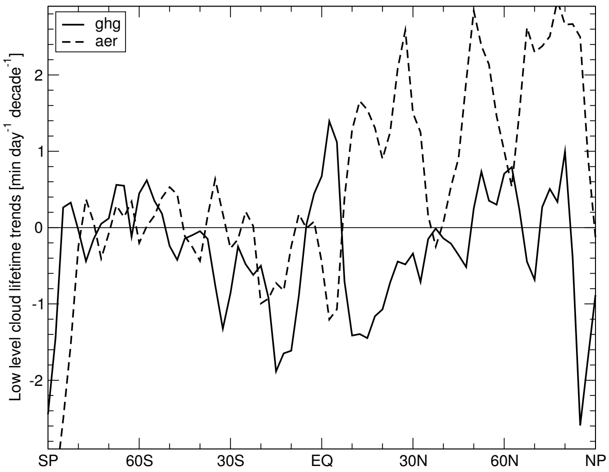

Figure 6.8.: Zonal mean linear trends of the annual mean diurnal lifetime of low-level clouds [min day^{-1} decade^{-1}]. Differences between scenarios are shown as before.

The radiative impact of second AIE and cloud feedbacks (I'_{aer}) is negative in northern hemisphere midlatitudes, while it is positive in the region 40°S - 20°N. Analysis shows that high cloud cover and I'_{aer} trends are anticorrelated (correlation coefficient –0.38 for the globe, and –0.46 for the region mentioned). The increase in I'_{aer} therefore seems to be linked to the decrease in high-level cloud cover.

I'_{aer} is negative in northern hemisphere midlatitudes despite the reduction in high-level cloudiness. This is due to the increase in low-level cloudiness which we interpret as the second aerosol indirect effect.

6.4.3. The impact of the second aerosol indirect effect

There are two possibilities how a time-average cloud cover increase can be generated at a given grid box. Either there is an increase in cloud extent at each given time, or there is a longer persistence of a given cloud amount. The temporal extent of clouds, or their lifetime is controlled by the microphysical processes that convert cloud water into precipitation. The second indirect effect causes these processes to be slower for liquid water clouds, and thus will increase the persistence of clouds. We calculated the cloud lifetime in both scenarios, with and without anthropogenic aerosols. Cloud lifetime is defined here as the time per day, in which a grid box is covered with fractional cloudiness above a threshold of 1% (to exclude an impact of possible spurious persistent cloud cover). Cloud lifetime is thus expressed in minutes per day.

We show in Fig. 6.8 the zonal mean of the 1930 to 1989 linear trends in low-level cloud lifetime. The differences between the scenarios are shown to isolate the impact of the respective perturbations. Greenhouse gases decrease the cloud lifetime at low latitudes. This may be due either to an increase in cloud liquid water, thus an increase in cloud droplet size and an increase in the efficiency of rain-forming microphysical processes, or to an intensification of convection, which would cause the convective rain formation to become more efficient.

Except at two latitude bands (40°N and 60°N, again due to regionally limited effects of opposite sign over Himalaya, and Greenland and Alaska, respectively), cloud lifetime increases strongly due to aerosols all over the northern hemisphere. The increase in low-level cloud cover is well correlated to the increase in cloud lifetime (correlation coefficient of 0.86), which suggests that the increase in low-level cloud cover is due to an increase in the duration of clouds rather than an increase in their fractional coverage when they are present.

6.5. Conclusion

We investigated the radiative impacts of greenhouse gases and aerosols in a simulation of the 20$^{\text{th}}$ century. Using the LMDZ GCM in a version forced by observed SST and sea ice distributions, we carried out three ensembles of simulations: a first ensemble where both greenhouse gases and sulfate aerosols were increasing according to historical values, a second ensemble, where the aerosol distribution was fixed to pre-industrial values, and finally, a control ensemble, where the greenhouse gas concentrations were fixed to pre-industrial values as well.

Both greenhouse gases and aerosols impact strongly the longwave and shortwave radiative fluxes. While the increase in the greenhouse effect due to the greenhouse gases and the decrease in the SW radiative impact due to the aerosol direct effect are straightforward understandable, the impact on radiation via the change of cloudiness is more complicated. The change in clouds in different atmospheric layers has a strong impact in both solar and terrestrial components. The radiative impact of aerosols on the SW radiation is strongly negative and the radiative impact beyond the direct radiative forcing of aerosols and the first AIE is positive. It results from the second aerosol indirect effect that leads to an increase in cloud water in low-level clouds, particularly in the northern hemisphere but a decrease in high-level cloudiness, resulting in a reduction of cloud albedo and thus a positive radiative impact. The latter finding may be due to our parameterization which does not take into account the impact of aerosols on ice clouds. A simulation with a future complex microphysics scheme, treating both liquid water and ice clouds, will be needed to confirm this finding.

Our results, although obtained in transient simulations, therefore suggest that it may not be appropriate to diagnose the second AIE as the difference between two simulations at fixed SST, as complex feedbacks involving high-level cloudiness are also at stake.

6.6. Impacts des gaz à effet de serre et des effets directs et indirects des aèrosols sur les nuages et le rayonnement dans des simulations de la période 1930 à 1989 avec un MCG atmosphérique : Résumé

Introduction

En regardant l'évolution du climat pendant le 20ième siècle, le réchauffement global n'a pas été aussi fort qu'attendu dû à l'effet de serre anthropique seul (*Mitchell et al.*, 2001). En particulier dans la période 1940 à 1970, une température moyenne annuelle globale presque constante a été observée. La période 1930 à 1989 est alors choisie pour examiner les raisons possibles à ce comportement. Depuis quelques années, un forçage radiatif supplémentaire dû aux aérosols de sulfates anthropiques a été proposé comme un forçage négatif qui pourrait contrebalancer une partie de l'effet réchauffant dûs aux gaz à effet de serre (*Wigley*, 1989 ; *Charlson et al.*, 1989).

Méthodes

Trois ensembles de simulations ont été effectuées avec LMDZ en imposant la température de la surface de la mer (sea surface temperature, SST en anglais), et l'extension de la glace de mer à partir des distributions mensuelles du Hadley-Centre (HADISST1.1, *Rayner et al.*, 2003). Des distributions mensuelles des aérosols soufrés ont été calculées chaque décennie de la simulation en utilisant des données historiques des émissions et en appliquant un modèle complet du cycle de soufre (*Boucher et al.*, 2002 ; *Boucher et Pham*, 2002). Les gaz à effet de serre sont considérés comme étant bien mélangés partout dans l'atmosphère. Les moyennes annuelles des cinq espèces (CO_2, CH_4, N_2O, CFC-11 et CFC-12) de gaz à effet de serre anthropiques de *Myhre et al.* (2001) sont utilisées. Chaque ensemble de simulations consiste de trois membres. Dans le premier scénario, nommé GHG+AER, les gaz à effet de serre et les sulfates ont été utilisés comme décrit auparavant. Dans un deuxième scénario, la concentration en aérosols a été fixée à une distribution pré-industrielle (nommé GHG). Dans le troisième scénario, celui de contrôle (CTL), les concentrations des gaz à effet de serre ont été fixées à des valeurs pré-industrielles aussi.

Dans l'ensemble GHG+AER, le forçage radiatif par les gaz à effet de serre a été calculé hors-ligne en utilisant les profils de température et d'humidité dans la troposphère et les conditions de la surface terrestre. Le forçage radiatif est calculé comme la différence dans le flux du rayonnement à la tropopause entre des situations actuelles et pré-industrielles pour les gaz à effet de serre après ajustement des profils dans la stratosphère (*Cess et al.*, 1993 ; *Hansen et al.*, 1997). Pour les aérosols, les forçages par l'effet direct et par le premier effet indirect ont été calculés en ligne dans la simulation GHG+AER dans le spectre des ondes courtes. Le schéma du rayonnement est appliqué deux fois, une fois en utilisant la concentration en aérosols actuels (c'est ce flux de rayonnement qui était utilisé pour l'intégration du modèle), et une deuxième fois en utilisant la concentration pré-industrielle. Les deux paramètres qui changent sont les propriétés optiques des aérosols et l'épaisseur optique des nuages, qui est diagnostiquée avec les deux concentrations en nombre de gouttelettes différentes. L'ajustement de la stratosphère peut être négligé dans le spectre des ondes courtes.

Afin d'inclure aussi d'autres effets sur les nuages dans l'analyse, et en particulier le deuxième effet indirect, nous introduisons comme nouvelle quantité ≪ l'impact radiatif≫ d'une perturbation donnée. Cet impact radiatif est défini comme la différence du flux de rayonnement au sommet de l'atmosphère entre deux scénarios, dans lesquels tous sauf un des paramètres sont fixes, et dont la variabilité interne a été enlevée en moyennant sur l'ensemble. Selon cette définition, l'impact radiatif des aérosols dans le spectre des ondes courtes est la différence des flux radiatifs entre les scénarios GHG+AER et GHG (tableau 6.1). Pour le spectre des ondes longues, il faut pourtant encore modifier un peu cette définition afin de l'appliquer à nos scénarios, car au-dessus des océans, la température de la surface, qui a été fixée, ne peut pas s'ajuster pour établir l'équilibre radiatif. Au lieu du flux de rayonnement au sommet de l'atmosphère, nous utilisons donc l'effet de serre total (greenhouse effet, GHE en anglais), qui est défini comme la différence entre le flux net ondes longues à la surface terrestre et le flux ondes longues sortant au sommet de l'atmosphère. La différence en GHE entre deux moyennes d'ensembles est ainsi l'impact radiatif dans le spectre des ondes longues.

Résultats

Le forçage radiatif calculé pour les gaz à effet de serre est positif et augmente de 0.74 à 2.07 $\mathrm{Wm^{-2}}$ de 1930 à 1989, ce qui est similaire aux valeurs données par le GIEC (*Ramaswamy et al.*, 2001) pour les gaz à effet de serre bien mélangés en 1990. Le forçage direct par les sulfates décroît de –0.2 à –0.5 $\mathrm{Wm^{-2}}$, et le forçage par le premier effet indirect de –0.6 à –1.3 $\mathrm{Wm^{-2}}$, ce qui est aussi dans la marge des valeurs cités par *Ramaswamy et al.* (2001) de –0.2 à –0.8 $\mathrm{Wm^{-2}}$ pour l'effet direct et de –0.3 à –1.8 $\mathrm{Wm^{-2}}$ pour le premier effet indirect (fig. 6.2).

En regardant les impacts radiatifs sur le spectre des ondes longues, des impacts négligeables sont trouvés pour les aérosols (fig. 6.3). Pour les gaz à effet de serre, une tendance d'environ 0.2 $\mathrm{Wm^{-2}}$ $\mathrm{decade^{-1}}$ est observée. On peut séparer les impacts radiatifs pour les conditions claires et nuageuses, et on trouve alors que l'impact radiatif des gaz à effet de serre est presque aussi grand en ciel nuageux qu'en ciel total, mais qu'en ciel clair il est d'environ 0.2 à 0.5 $\mathrm{Wm^{-2}}$ plus grand. Les gaz à effet de serre augmentent ainsi l'effet de serre à la fois dans les conditions claires et dans les conditions nuageuses, mais la couverture nuageuse diminue. Comme l'effet de serre total est plus grand en ciel nuageux qu'en ciel clair, cela explique la concidence trouvée entre l'impact radiatif en ciel nuageux et en ciel total. On peut comparer le forçage radiatif calculé avant avec l'impact radiatif. La différence entre ces deux quantités est que l'une contient les rétroactions, et l'autre non. En ciel clair, on trouve que l'impact radiatif est légèrement plus grand que le forçage radiatif. On peut attribuer cela à la rétroaction de la vapeur d'eau, qui pourtant est limitée aux continents car la température de la surface océanique est la même dans les deux scénarios qui sont comparés ici.

Dans le spectre des ondes courtes, on trouve un faible impact des gaz à effet de serre pour des ciels clairs, qui est dû à une rétroaction de la couverture de neige dans les hautes latitudes (fig. 6.4). En ciel nuageux, on trouve un impact positif d'environ 0.1 à 0.3 $\mathrm{Wm^{-2}}$ (1930 à 1989), qui correspond à une diminution de l'albédo des nuages dû à une diminution de la couverture nuageuse. Les aérosols ont un impact négatif en ciel clair qui est très similaire à l'effet direct des aérosols qui a été diagnostiqué. En ciel nuageux, ils ont un effet qui est légèrement plus grand que le premier effet indirect.

Discussion

Les rétroactions des nuages sont d'un intérêt particulier (figs. 6.5 et 6.6). On trouve à partir des différences entre des ensembles de simulations que les gaz à effet de serre font diminuer la couverture nuageuse à tous les niveaux, dans les basses et moyennes latitudes jusqu'à 0.2 % $\mathrm{décennie^{-1}}$. Les aérosols, de l'autre côté ont des impacts différents à différents niveaux. Alors que la couverture nuageuse haute est légèrement diminuée, la couverture nuageuse dans les niveaux bas et moyens augmente jusqu'à 0.2 % $\mathrm{décennie^{-1}}$, avec des tendances beaucoup plus fortes dans l'hémisphère nord que dans l'hémisphère sud. En isolant l'impact radiatif des processus de rétroactions des nuages, et en excluant donc les impacts radiatifs de l'effet direct des aérosols et du premier effet indirect, nous avons montré la contribution du deuxième effet indirect à l'impact radiatif (fig. 6.7). L'impact radiatif des processus de rétroaction des nuages combine deux effets. La légère réduction de la couverture haute exerce un impact positif dû à la réduction de l'albédo des cirrus. L'augmentation de la couverture nuageuse dans les niveaux bas et moyen augmente pourtant l'albédo des nuages, avec un effet net légèrement positif en moyenne globale. L'augmentation de la couverture basse est liée à une augmentation de la durée de vie des nuages plutôt qu'à une augmentation de la couverture nuageuse spatiale à chaque instant donné. C'est donc bien le deuxième effet indirect qui est responsable de cette rétroaction. Le deuxième effet indirect des aérosols est beaucoup plus marqué dans les moyennes latitudes de l'hémisphère nord qu'ailleurs dans le globe. L'impact radiatif des rétroactions des nuages total y est négatif alors qu'il est positif dans l'hémisphère sud.

7. Relative importance of greenhouse gas and aerosol forcings for climate trends of the 1950 - 1989 period in atmospheric GCM simulations.

7.1. Introduction

Analysis of the evolution of the Earth's climate during the 20th century indicates an anthropogenic impact on several meteorological quantities. One of the observed features is a trend of up to 0.1 K decade^{-1} for the annual global mean surface temperature (e.g., *Folland et al.*, 2001). Trends have been observed as well in precipitation, cloud cover, and diurnal temperature range (*Folland et al.*, 2001), some on global scales and some only on regional scales. One of the challenging tasks of climate research is the detection and attribution of a possible impact of human activities on the Earth's climate. Two main anthropogenic sources of perturbations to the Earth's atmosphere have been identified in the last decades, both of them mainly due to energy production, namely greenhouse gases and aerosols.

Using an atmospheric GCM forced with transient observed SST and sea-ice extent distributions, we try to understand the role the effects of greenhouse gases and aerosols played in the evolution of the climate of the last century. Recently, similar simulations have been carried out with the Hadley Centre GCM (*Sexton et al.*, 2003), which identified the impact of several anthropogenic forcings on land surface air temperatures. Here, we look at concrete impacts of aerosols and greenhouse gases on measurable, and measured, climate parameters. As the imposed SST in our simulation drives the temperature and precipitation evolution to a large extent, we focus on parameters more sensitive to aerosols such as the cloud cover and the diurnal temperature range.

7.2. Model simulations

The ensemble simulations analyzed in this chapter have been described in Section 6.2 and are briefly summarized in Table 7.1. In Fig. 7.1 we show the temporal evolution of the surface temperature in the three ensembles. Because the changes in radiative forcing are relative to pre-industrial situations (Tab. 7.1), the three ensembles start with different conditions in 1950. Warming by the greenhouse effect causes the simulation with increasing greenhouse gas concentrations to be the warmest and the CTL simulations, where greenhouse gas concentrations are fixed to pre-industrial values, to be the coolest. The GHG+AER simulation is in between as the cooling by aerosol effects partially offsets the warming by the greenhouse effect. Two major findings can be deduced from Fig. 7.1. Firstly, the time evolution of the temperature is largely dominated by the imposed evolving SST, which is the same in all three sets of simulations. Secondly, the number of three members for each ensemble seems to be sufficient as there are clear differences in the ranges of results corresponding to the three ensembles.

	GHG+AER	GHG	CTL
Greenhouse-gas concentration	current	current	1750
Sulfate aerosol concentration	current	natural sources only	natural sources only

Table 7.1.: Characterization of the three ensembles.

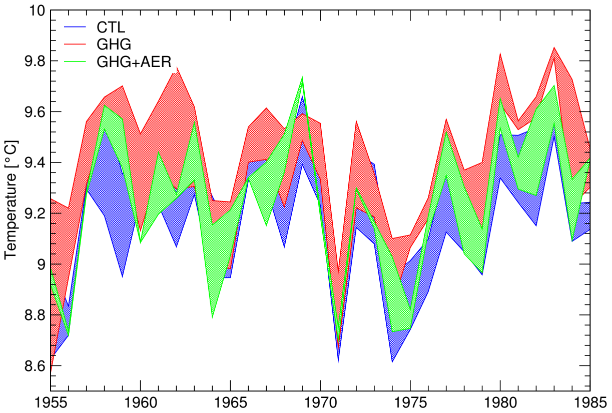

Figure 7.1.: Evolution of the annual and global (60°S - 80°N) mean surface temperature over land in the three ensembles [°C]. An 11-year running mean is applied. The shaded area corresponds to the range covered by the members of each ensemble. In green, the GHG+AER simulation, in red, the GHG simulation, and in blue, the CTL simulation.

7.3. Observations

Folland et al. (2001) summarize the identified observed trends in climate parameters since the beginning of the industrialization. On a global scale, the most important change observed is the general increase in surface temperature (*Jones and Moberg*, 2003; *Peterson et al.*, 1998). This increase is due mainly to an increase in nighttime temperatures. The daily minimum temperature has risen almost twice as much as the maximum temperature during the 20th century. Thus, the diurnal temperature range (DTR), defined as the difference between monthly mean daily maximum and minimum temperatures, has decreased (e.g., *Karl et al.*, 1993; *Easterling et al.*, 1997; *Hansen et al.*, 1995). Other climate parameters show trends as well, but we will limit the present study to these two features which are considered to be well proven on a global scale. However, while studying the trends in DTR, it should be noticed, that at least for several regions an increase in cloud cover has been observed and that over some regions precipitation has increased (*Easterling et al.*, 1997).

7.4. Results

7.4.1. Land surface temperature

In Fig. 7.2 we show the evolution of the global annual mean land surface temperature in the three ensembles and the HadCRUT2 observations dataset (*Jones and Moberg*, 2003). As already shown in Fig. 7.1, to a large degree, the evolution in the model scenarios is dominated by the imposed SST. Generally, the model captures well the interannual variability as well as the overall trend. The ensemble means and the observations are correlated with correlation coefficients of 0.81, 0.80 and 0.78 for GHG+AER, GHG, and CTL scenarios, respectively. The linear trend in temperature over the whole period (1950 - 1989) is 0.29 °C decade^{-1} in the observations, and 0.74, 0.84, and 0.70 °C decade^{-1} for the GHG+AER, GHG, and CTL experiments, respectively. To identify the different impacts on climate parameters introduced by the forcings by greenhouse gases and aerosols, respectively, we now look at the geographical distributions.

In the observations and the model output, we calculate the linear trend at each grid point as the slope of the linear regression of the time series. We isolate the regions where the trend is significant above the 90% confidence level according to the rank correlation test of Kendall (*Conover*, 1980, pp. 256f.).

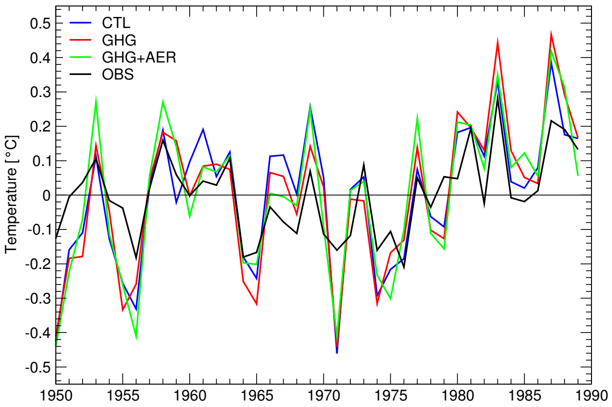

Figure 7.2.: The evolution of the departure of the annual global (60°S-80°N) mean land surface temperature from the 1950 to 1989 mean, in the GHG+AER (green line), GHG (red), and CTL (blue) simulations, and in the HadCRUT2 observations (black).

These trends are plotted in Fig. 7.3 for the period 1950 - 89 for the northern hemisphere summertime (June-July-August, JJA). In JJA, aerosol radiative effects are most marked, because they are concentrated in the northern hemisphere and impact on the SW radiation. Figure 7.3 shows the trends in JJA surface temperature over land in the three ensembles and observations. For many parts of the globe, the trends in surface temperature are controlled by the impact of the imposed SST on the continents via dynamical teleconnections. For most parts of the southern hemisphere, the three simulations do not differ much. Some differences in the geographical distributions of the temperature increase over Australia can be noted. The CTL scenario shows a cooling over South America, which is not the case for the two other ensembles. Also the high latitudes of the northern hemisphere (north of 60°N) show a similar pattern of increasing temperature. This is due to a decreasing trend in the imposed sea ice extent, which is the same in all three simulations. In North Africa and the midlatitudes of the Eurasian and North American continents, however, some differences between the three scenarios can be identified.

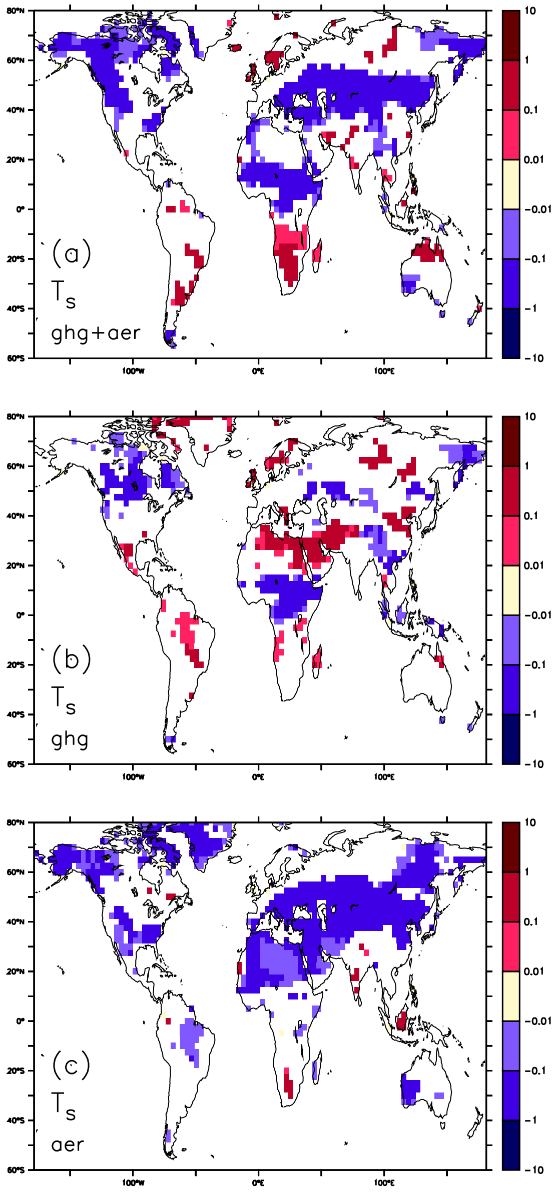

Figure 7.4.: Differences in the linear trend (1950 - 1989) in JJA surface temperature over the continents [K decade^{-1}] between the simulations. (a), the impact of both greenhouse gases and aerosols (difference GHG+AER–CTL), (b), the impact of greenhouse gases (GHG–CTL), and (c), the impact of the aerosols (GHG+AER–GHG). Only regions with trends statistically significant above the 90% confidence level are shown.

The deceasing SST of the North Atlantic causes

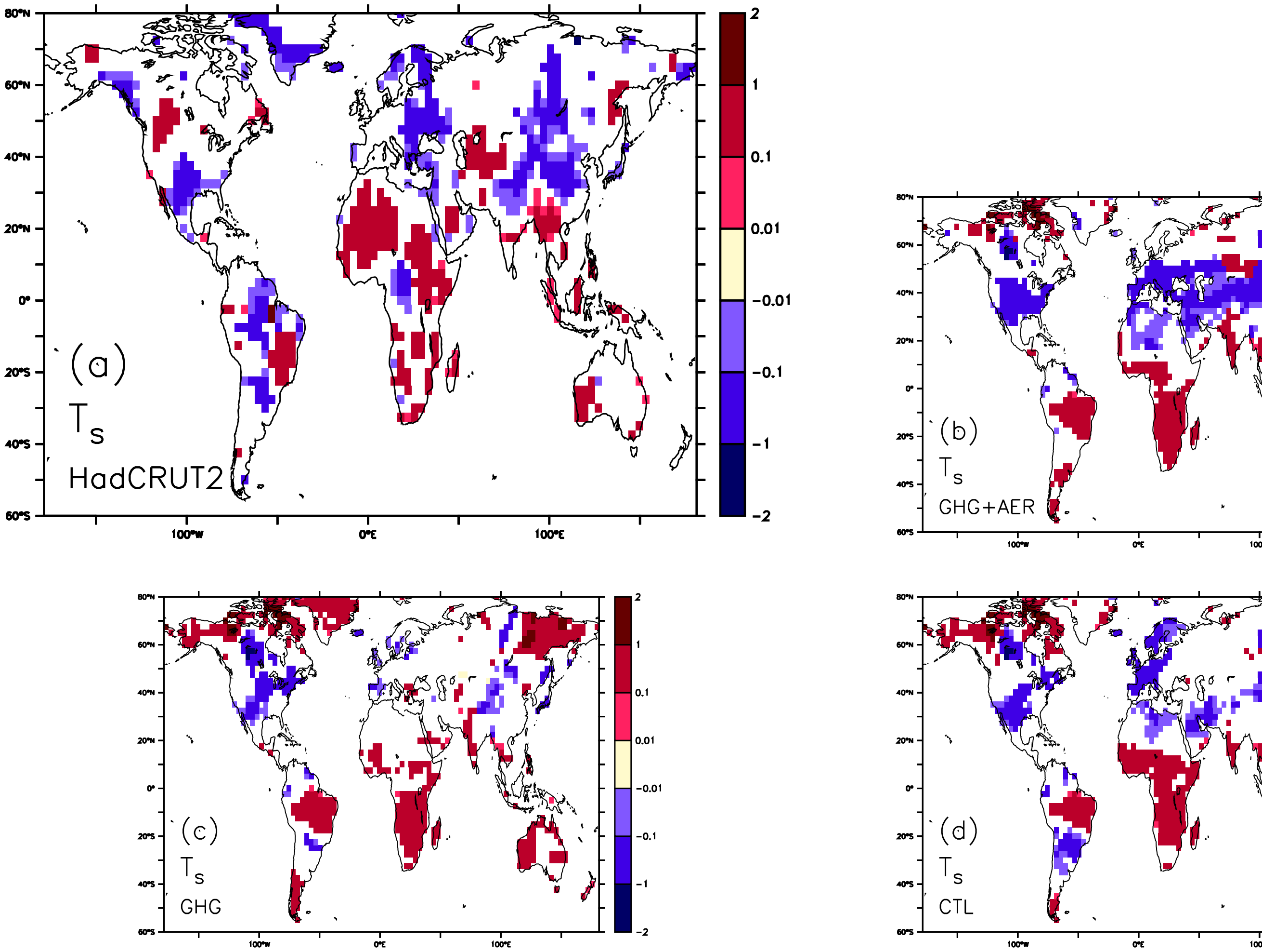

Figure 7.3.: The linear trend (1950 - 1989) in JJA surface temperature over land [K decade^{-1}] as simulated by the LMDZ GCM. (a) for HadCRUT2 observations, (b) the GHG+AER simulation, (c) the GHG simulation, and (d) the CTL simulation. Only regions with trends statistically significant above the 90% confidence level are shown.

$$
\begin{array}{lclcl}
\hline
\Delta\frac{\partial T_{\mathrm{sfc}}}{\partial t}|_{\mathrm{ghg+aer}} & = & <\frac{\partial T_{\mathrm{sfc}}}{\partial t}|_{\mathrm{GHG+AER}}> & - & <\frac{\partial T_{\mathrm{sfc}}}{\partial t}|_{\mathrm{CTL}}> \\
\Delta\frac{\partial T_{\mathrm{sfc}}}{\partial t}|_{\mathrm{ghg}} & = & <\frac{\partial T_{\mathrm{sfc}}}{\partial t}|_{\mathrm{GHG}}> & - & <\frac{\partial T_{\mathrm{sfc}}}{\partial t}|_{\mathrm{CTL}}> \\
\Delta\frac{\partial T_{\mathrm{sfc}}}{\partial t}|_{\mathrm{aer}} & = & <\frac{\partial T_{\mathrm{sfc}}}{\partial t}|_{\mathrm{GHG+AER}}> & - & <\frac{\partial T_{\mathrm{sfc}}}{\partial t}|_{\mathrm{GHG}}> \\
\hline
\end{array}
$$

Table 7.2.: Definition of the impacts of greenhouse gases (“ghg”), aerosols (“aer”) and the combination of both (“ghg+aer”) on the trends in surface temperature (T_{sfc}). The brackets indicate ensemble averaging.

the surface temperature to decrease in the simulation without other imposed forcings CTL in Western Europe. This decrease is offset by warming due to increased GHE in the GHG simulation. In the GHG+AER simulation, the same tendency can be observed for the northern part of western Europe, while the southern part shows a strong cooling. The GHG+AER simulation shows a persistent cooling in the midlatitudes (20 - 50°N), which is not observed in the other two simulations. This cooling is stronger than in the two other ensembles also for the midlatitudes of the North American continent.

Comparing observations and the three ensembles, it seems difficult to identify one of the scenarios which would unambiguously simulate more realistic results that the other ones, mainly due to the strong impact of the imposed SST. However, when looking at the Eurasian continent, the GHG scenario is not able to simulate the observed cooling trend. The CTL ensemble shows some cooling but the geographical distribution over Europe and over East Asia are rather different from the observed patterns. On average, the cooling simulated by the CTL scenario is not as strong as in the HadCRUT2 observations. Particularly, a strong cooling trend is observed in the measurements and in the GHG+AER scenario over regions with increasingly high aerosol burdens in the period of interest, i.e., over East Europe and East Asia. Generally, the order of magnitude of the trends in surface temperature is the same in both, model simulation and observations. Figure 7.4 shows the differences in the surface temperature trends between the three simulations. The impact of aerosols on surface temperature is defined as the difference in the trends between the GHG+AER and the GHG ensembles. The impacts of greenhouse gases and the combination of greenhouse gases and aerosols are defined accordingly (see Table 7.2 for a summary). The decreasing temperature trend observed in the GHG+AER simulation in the NH midlatitudes is due to the aerosol forcing. Via dynamical effects, aerosols cause a warming in South Africa. This warming is amplified when both forcings, greenhouse gases and aerosols, are combined. This warming trend is also shown by the observations.

7.4.2. Diurnal temperature range

As pointed out by several authors (e.g., *Karl et al.*, 1993; *Easterling et al.*, 1997; *Hansen et al.*, 1995), the diurnal temperature range (DTR) (defined as the difference between monthly mean daily maximum and minimum temperatures at a given location) has decreased in the second half of the 20th century over large parts of the continents. The minimum nighttime temperatures have risen much faster than the daytime maximum temperatures. *Easterling et al.* (1997) shows decreasing trends for most continental regions for the 1950 to 1993 period. In the midlatitudes of the North American continent, a consistent decrease by –0.1 to –0.3°C decade^{-1} is given. For Europe the trend is not clear including an increase in DTR in central Europe, slight decreases over the British Islands and the Mediterranean region, and a decrease over Eastern Europe.

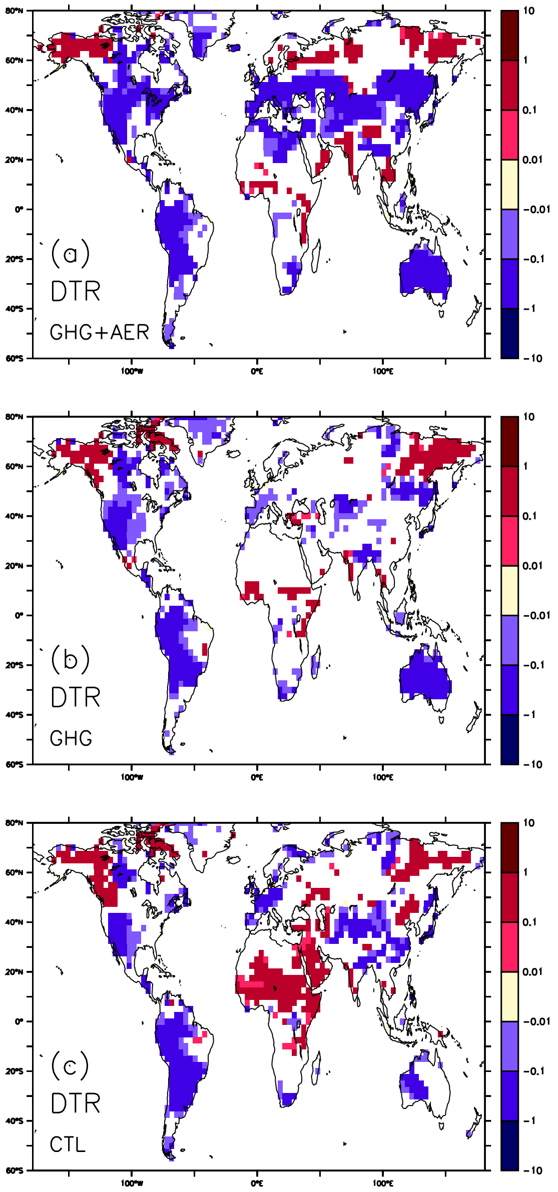

Figure 7.5.: As for Fig. 7.3, but for the diurnal temperature range over land [K decade^{-1}].

Over Asia, although at some locations a slight increase in DTR is observed, generally the DTR has decreased by –0.1 to –0.3°C decade^{-1}. Similarily, over Australia most regions show a decrease, and over South America and Africa, also a rather strong decrease of up to –05 °C is found. Recently, it has also been shown on a regional scale for the case of France that a clear increasing trend can be detected for summer nighttime minimum temperatures which is not obvious in daytime maximum temperatures (*Spagnoli et al.*, 2002). This behavior in the region of France has been attributed to variations in evapotranspiration using a modeling study (*Planton and Spagnoli*, 2003). Figure 7.5 shows the distributions of the linear trends in DTR in the three scenarios for northern hemisphere summertime (June-July-August; JJA). For South and North America, all three simulations show similar results - a reduction of the DTR of the order of –0.1 to –1 K decade^{-1}. Particularly, this reduction is concentrated over the western half of the continents. Over Alaska, however, an increase in DTR is observed. These findings are in good agreement with the observational data shown by *Folland et al.* (2001). Over Australia, both scenarios show a stronger reduction in DTR than the control ensemble. For Africa and the Eurasian continent, both perturbations, greenhouse gases and aerosols, lead to a decrease in DTR. The GHG+AER scenario is the only one which reproduces a reduction in DTR of the same order of magnitude as observed. Figure 7.6 shows the differences between the ensembles to identify the impacts of the two forcings. Clearly, aerosols are needed to explain the strong reduction of the DTR over the Eurasian continent. In particular, aerosols are responsible for the reduction in DTR over Europe and over Southeast Asia.

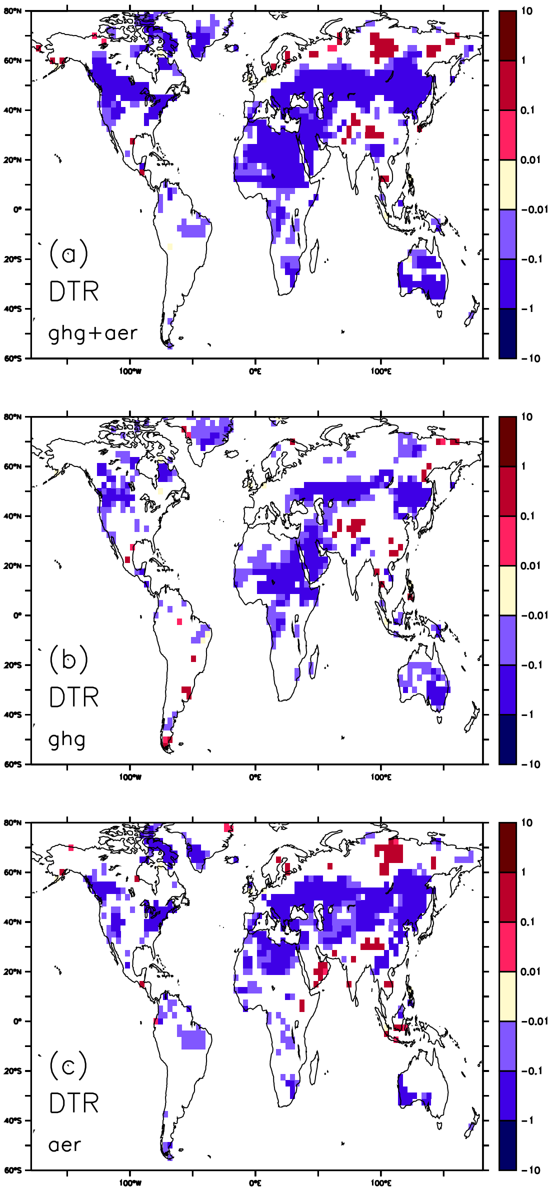

Figure 7.6.: As for Fig. 7.4, but for the diurnal temperature range over land [K decade^{-1}].

7.5. Discussion

A reduction in DTR might be due to a negative radiative forcing in the solar spectrum such as expected from aerosol direct and indirect effects. While a forcing in the terrestrial spectrum as the greenhouse effect is active both night and day, an increase in SW albedo has a cooling effect on the Earth's surface only at daytime (solar heating during the daytime is reduced). This would reduce the daily maximum temperature. The warming effect due to the greenhouse gases increases the nighttime temperature, but the daytime temperature as well, and therefore would not directly reduce the DTR. However, a possible increase in cloud cover as a feedback to the increased greenhouse effect would increase the SW albedo and might thus explain the decrease in DTR.

Other explanations for the reduction in DTR exist. For example, the increase in air-traffic induced contrail coverage of the globe may be responsible for the reduction in DTR (*Travis et al.*, 2002; *Meerkötter*

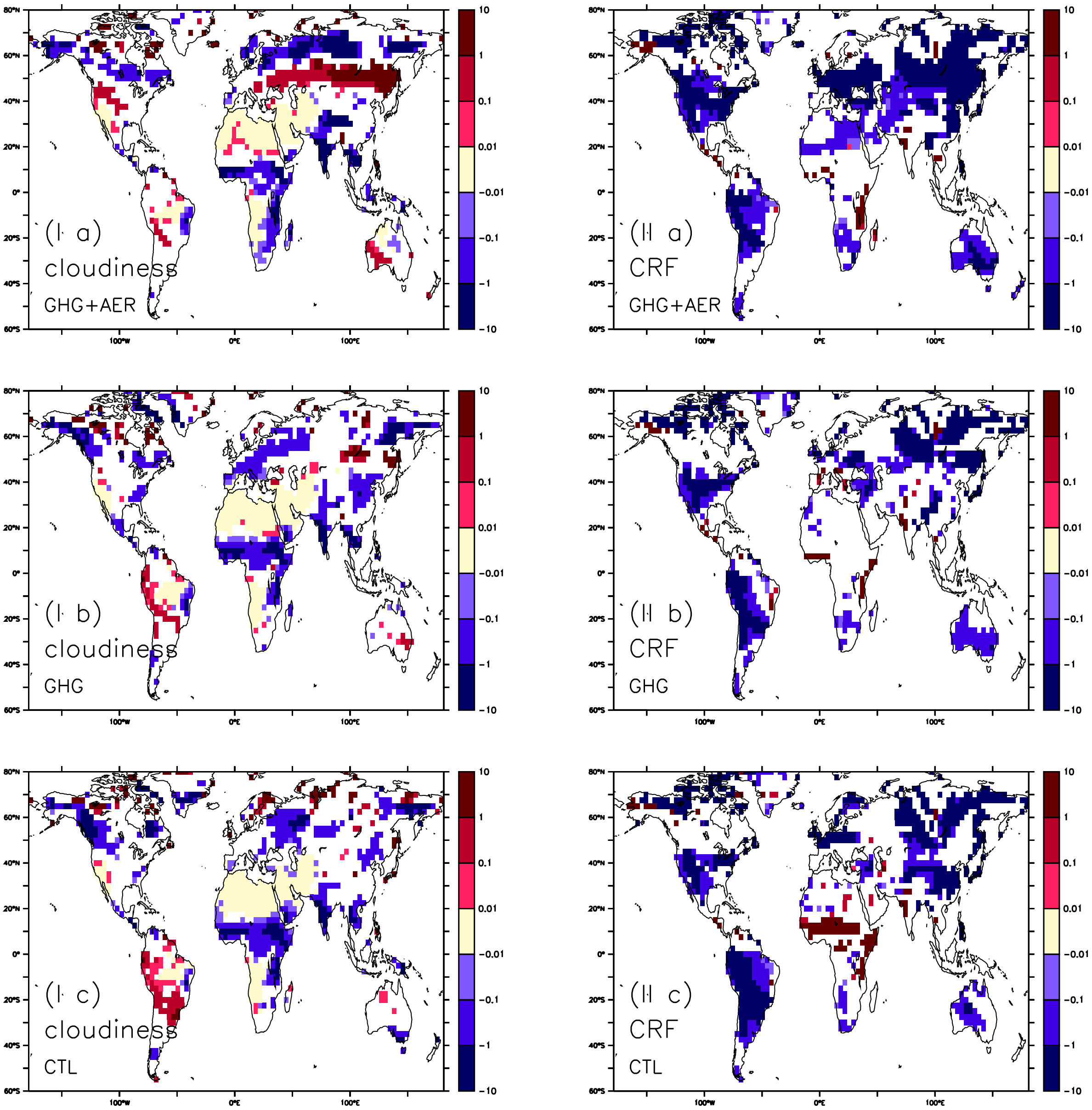

Figure 7.7.: Linear trends (1950 - 1989) in JJA cloud cover (I) and SW cloud radiative forcing (CRF, II), (a) for GHG+AER, (b) for GHG, and (c), for CTL scenarios [Wm^{-2} decade^{-1}].

et al., 1999). *Dai et al.* (1997) show a negative correlation between precipitation increase and DTR decrease in timeseries for several regions. They argue that precipitation increase is correlated with an increase in cumulonimbus and nimbostratus cloudiness. They explain that assuming the existence of the second aerosol indirect effect, a forcing different from aerosol forcing would be responsible for this increase in precipitation, as the second AIE rather would tend to decrease the precipitation. Soil moisture variation may have an important influence on DTR changes. Increased evaporation due to larger soil moisture would lead to a lowering of temperatures during daytime with less stable boundary layers, while during nighttime with stable boundary layers, this effect would be much smaller (*Dai et al.*, 1997; *Dai et al.*, 1999; *Stone and Weaver*, 2003).

Dai et al. (2001) and *Stone and Weaver* (2003) studied the trends in DTR in the twentieth and twenty-first century in simulations performed with two different GCMs. Both studies argue that it is an increase in low-level cloud albedo and in soil moisture that causes the decrease in DTR. They do not find an influence of aerosol direct effects. However, they did not examine the aerosol indirect effects.

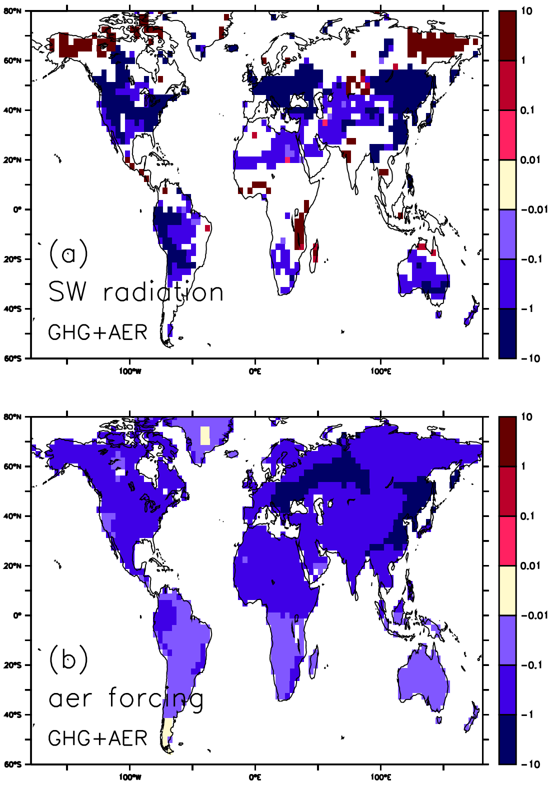

Figure 7.8.: Linear trends (1950 - 1989) in JJA TOA (a) net SW flux, and (b) SW forcing by the first aerosol indirect effect and the aerosol direct effect [Wm^{-2} $decade^{-1}$].

Folland et al. (2001) show a correlation between the decrease in DTR and the increase in cloud cover. *Hansen et al.* (1995) deduct from a modeling study, that a combination of aerosol and cloud cover increase particularly over land causes the decrease in DTR, which they attribute to an aerosol indirect effect.

In Fig. 7.7, we show the linear trends in cloudiness and in SW cloud radiative forcing (CRF). Comparing the GHG and CTL scenarios, a largely similar pattern of change in cloudiness and CRF is observed. The slight differences include a smaller increase in cloud cover and CRF over the South and North American continents in the GHG compared to the CTL ensemble. The GHG scenario does not show the increase in CRF as observed in the CTL ensemble over the equatorial region over Africa.

Some interesting differences are found comparing the GHG+AER scenario to the two others. A strong increase in cloud cover is observed over the mid latitudes of the northern hemisphere, and accordingly a stronger decrease in (negative) CRF than in the GHG and CTL ensembles. This is observed as well over the Eurasian as over the North American continents. Figure 7.8 shows in addition the trends in net SW radiation flux at the top of the atmosphere (TOA) and the diagnosed forcing by the aerosol direct and first indirect effects in the GHG+AER scenario. Trends in SW radiation are largely corresponding to the trends in CRF, except for the high latitudes of the northern hemisphere, where the surface albedo changes due to snow cover feedbacks play an important role. Comparing the patterns of diagnosed forcings by aerosols to the geographical distribution of the trends in SW radiation flux, it can be noted that the strongly negative trends in the NH midlatitudes are corresponding to strongly negative forcing trends due to aerosols. In Fig. 7.9 we show the JJA linear trends of surface evaporation in the three scenarios. For some regions, the anticorrelation between evaporation and DTR trends postulated by *Dai et al.* (1997) and *Planton and Spagnoli* (2003) can be observed, e.g. for central Africa and, in the GHG simulation, over Australia. However, as these regions are rather limited, the correlation may be fortuitous. Similarily, the trends in surface humidity and DTR are not found to be correlated (not shown).

7.6. Conclusions

We showed results of three ensemble simulations with an atmospheric GCM (the LMD-Z) using imposed observed SST distributions. In one of these scenarios GHG+AER, anthropogenic greenhouse gas and sulfate aerosol perturbations were imposed according to historical evolutions. In a second one (GHG), only greenhouse gases were used, and in the third one (CTL), greenhouse gases and aerosols were fixed to pre-industrial conditions.

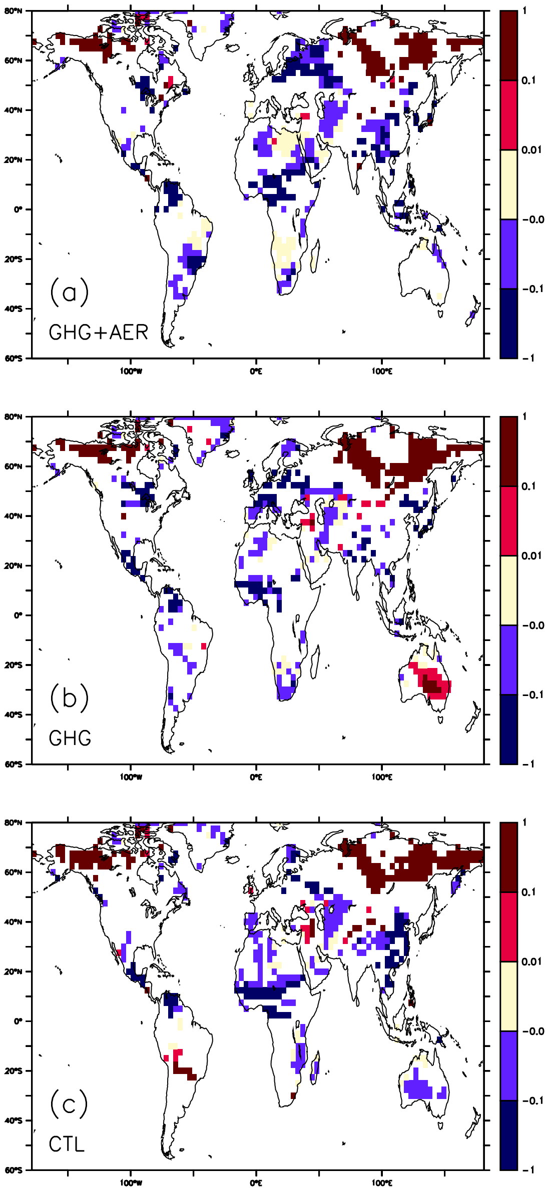

Figure 7.9.: The linear trend in JJA surface evaporation [mm day^{-1} $decade^{-2}$]. For (a) GHG+AER, (b) GHG and (C) CTL scenarios. Only statistically significant trends are shown.

The forcing by the imposed SST controls the evolution of temperature also over continental surfaces to a large extent. Interesting impacts of the two anthropogenic forcings are observed. Looking at patterns of linear trends in surface temperature, it can be noted that the scenario including both forcings is closest to observations (HadCRUT2 dataset, *Jones and Moberg*, 2003).

	90°S-90°N	40°S-55°N	40°N-55°N
DTR-CRF	0.24	0.68	0.70
DTR-F^{SW}	0.83	0.73	0.82
DTR-E	0.50	–0.08	–0.02
T_s-CRF	–0.37	0.46	0.11
T_s-F^{SW}	0.87	0.66	0.57
T_s-E	0.73	–0.22	–0.11

Table 7.3.: Correlation between trends in cloud radiative forcing (CRF), SW radiation flux (F^{SW}), and surface evaporation (E), and trends in diurnal temperature range (DTR) and surface temperature (T_s), for different latitude belts.

In particular over the Eurasian continent, a cooling trend has been observed, which can only be simulated with the model when aerosol forcings are included. Similarly, while all three ensembles simulate comparable patterns of decreasing diurnal temperature range (DTR) for most parts of the globe (South and North America, Australia), the scenario including the aerosol forcing is the only one that is able to reproduce the reduction in DTR in the magnitude observed in the northern hemisphere. We analyzed trends in cloudiness and SW cloud radiative forcing (CRF) in the three scenarios. CRF changes largely control trends in SW radiation flux at the top of the atmosphere, except for NH high latitudes, where surface albedo changes due to snow cover feedbacks play a role. Aerosol forcings contribute strongly to stronger CRF and thus SW forcings particularly in NH midlatitudes. Table 7.3 lists the correlation coefficients between trends in CRF and SW radiation flux and surface temperature and DTR, respectively, for the GHG+AER ensemble.

The correlation coefficients in the two other ensembles are similar to the ones given for this scenario. Trends in surface temperature are correlated to changes in SW forcing, but only slightly connected to trends in CRF. However, the DTR changes are strongly correlated to both the changes in CRF and SW radiation flux. We do not find a consistent anticorrelation between evaporation and DTR trends as was the case in previous studies.

The overall conclusion is that in our model study, DTR decreases as observed particularly over continental surfaces of the northern hemisphere are strongly correlated to changes in SW cloud radiative forcing. Among the three ensembles, the only one which is able to simulate the observed magnitude and geographical distribution of the decrease in DTR is the scenario including the two forcings.

For the trends in surface temperature, the results are more ambiguous. However, the reduction in continental surface temperature over the Eurasian continent is resulting in the model study only in the scenario including both anthropogenic forcings, greenhouse gases and aerosols, where aerosols are the forcing responsible for the cooling trends.

7.7. Importance relative des gaz à effet de serre et des forages d'aérosols pour des tendances climatiques de la période 1950 à 1989 à partir des simulations de MCG atmosphériques : Résumé

Introduction

Outre l'augmentation de la température moyenne annuelle globale de 0.1 K décennie^{-1} (*Folland et al.*, 2001), des tendances ont été observées pour la précipitation, la couverture nuageuse, et l'écart journalier de la température (diurnal temperature range, DTR en anglais), quelques-unes à l'échelle globale, d'autres à l'échelle régionale (*Folland et al.*, 2001).

Nous utilisons les simulations présentées dans le dernier chapitre pour examiner les impacts relatifs des gaz à effet de serre et des différents forages par les aérosols sur les tendances de température de la surface continentale et sur le DTR. Nous limitons cette étude à la période 1950 à 1989 car c'est dans cette période que les tendances observées ont été les plus claires.

Résultats

Les trois ensembles de simulations sont capables de reproduire l'évolution observée de la température de la surface continentale, même si des différences entre les scénarios existent (fig. 7.1). Pourtant, le scénario qui inclut les deux forages anthropiques reproduit les observations de manière légèrement meilleure que les deux autres (coefficient de corrélation de 0.81 comparé à 0.80 et 0.78 pour les ensembles GHG et CTL).

Nous regardons les distributions géographiques des tendances linéaires de quantités physiques, qui sont définies comme la pente de la régression linéaire de la série temporelle à chaque point de la grille horizontale. L'impact des aérosols est le plus fort dans l'été de l'hémisphère nord, parce que les forages des aérosols sont actifs dans le spectre solaire et les aérosols anthropiques sont concentrés dans l'hémisphère nord. Nous nous focalisons alors sur la saison juin-juillet-aot (JJA). De plus, seulement des tendances qui sont statistiquement fiables à des niveaux supérieurs à 90% sont considérées.

Pour plusieurs parties du globe, les tedances de la température sont contrôlées par la SST imposée, et ce même au-dessus des continents (fig. 7.3). Dans la plupart de l'hémisphère sud ainsi qu'aux hautes latitudes de l'hémisphère nord, les trois ensembles ne diffèrent donc que peu. C'est en particulier dans les moyennes latitudes de l'hémisphère nord et en Afrique du Nord que se trouvent les différences entre les trois scénarios. La SST décroissante de l'Atlantique du Nord fait diminuer la température dans la simulation CTL au-dessus de l'Europe de l'Ouest. Cet effet est contrebalancé par le réchauffement par l'effet de serre dans l'ensemble GHG. Dans les simulations GHG+AER, on trouve le même effet pour la partie nord de l'Europe de l'Ouest, alors que la partie sud montre un fort refroidissement. Le scénario GHG+AER donne un refroidissement persistent dans les moyennes latitudes de l'Amérique du Nord et au-dessus du continent eurasiatique qu'on ne trouve pas dans les deux autres. Il est difficile d'identifier lequel des ensembles est le plus proche des observations, en particulier à cause de l'impact fort de la SST imposée. Pourtant, en regardant le continent eurasiatique, l'ensemble GHG ne simule pas la tendance de refroidissement observée. Le scénario CTL montre des régions de refroidissement, mais la distribution spatiale au-dessus de l'Europe et de l'Asie de l'Est est différente de celle observée. De plus, le refroidissement n'est pas assez fort en moyenne. Ce n'est donc que le scénario GHG+AER qui montre l'amplitude et la distribution des tendances de refroidissement comme dans les observations. En établissant les différences entre les moyennes d'ensembles, on peut isoler les impacts respectifs des deux forages anthropiques. Cette analyse montre que c'est le forage par les aérosols qui est responsable tendances de refroidissement dans la simulation GHG+AER. Comme il l'a été montré par plusieurs auteurs (par exemple, *Karl et al.*, 1993 ; *Easterling et al.*, 1997 ; *Hansen et al.*, 1995) la température minimale de nuit a augmenté beaucoup plus rapidement que la température maximale de jour, et donc l'écart journalier de la température a diminué pendant la deuxième moitié du 20ième siècle. Dans nos simulations, des tendances très similaires ont été trouvées dans le DTR pour la plupart de l'hémisphère sud, et pour les hautes latitudes de l'hémisphère nord (fig. 7.5). Pour les basses et moyennes latitudes de l'hémisphère nord, pourtant, des différences entre les scénarios peuvent être identifiées. La réduction du DTR est plus fort dans l'ensemble GHG comparé à CTL, et encore beaucoup plus fort dans l'ensemble GHG+AER. Les deux forages anthropiques, les gaz à effet de serre ainsi que les forages par les aérosols, augmentent donc la tendance négative du DTR. C'est pourtant seulement le scénario GHG+AER qui inclut les deux forages qui est capable de simuler cette réduction et en amplitude et en distribution.

La réduction du DTR observée peut être expliquée par plusieurs processus différents. L'une des possibilités serait un forage négatif actif dans le spectre solaire qui agit donc seulement pendant la journée. Un tel forage pourrait venir des effets directs ou indirects des aérosols (*Hansen et al.*, 1997), ou encore d'une augmentation de l'albédo des nuages bas, d soit à une augmentation de la couverture nuageuse soit à une augmentation de leur contenu en eau liquide (*Easterling et al.*, 1997). D'autres études montrent une corrélation entre une augmentation du taux de précipitation et la réduction du DTR (*Dai et al.*, 1997) où de l'évapotranspiration de la surface et le DTR (*Planton et Spagnoli*, 2003).

Dans notre étude, nous trouvons une corrélation des tendances du DTR avec les tendances du flux du rayonnement solaire au sommet de l'atmosphère (coefficient de corrélation de l'ordre de 0.8), avec le forage radiatif des nuages (coefficients de corrélation entre 0.24 et 0.70), mais pas avec l'évaporation au sol (coefficients de corrélation entre –0.1et 0.50 ; tableau 7.3).

Part IV.

Parameterization of ice phase processes

8. Evaluation of the cloud thermodynamic phase parameterization in the LMDZ GCM by using POLDER satellite data

8.1. Introduction

Clouds cover the Earth's surface by about 60% to 70% and have a very strong effect on the radiation balance in both the terrestrial and the solar spectrum. Unfortunately, the representation of clouds in climate models is still unsatisfying. As most cloud properties cannot be resolved by global-scale models, they have to be parameterized in terms of the model variables. Cloud parameterizations are complicated by the fact that clouds cover a large range of scales (from microphysics to mesoscale systems). Moreover they must treat the liquid and ice phases separately. Liquid and ice clouds have quite different effects on the Earth radiation balance. Precipitation-forming microphysical processes in ice and mixed-phase clouds are different from those in liquid water clouds. In the absence of explicit liquid and ice cloud microphysics there is no simple parameterization for the partitioning of condensed water into liquid and ice phase. The local temperature is therefore often used to define the liquid and ice fractions.

Giraud et al. (2001) used combined data from POLDER-1 and ATSR-2 satellite instruments to establish a relationship between cloud top brightness temperature and cloud top thermodynamic phase for a day in June, 1997. They found a clear relationship between the two quantities. A sharp transition between ice and liquid clouds in the temperature range of 240 to 260 K was observed.

Satellites observe clouds with a global coverage at approximately the spatial scale of GCMs. Thus, satellite observations are well suited for the evaluation of GCM parameterizations. Here, we use the data from the POLDER-1 instrument in order to infer a statistical relationship between cloud top temperature and cloud phase and to test the partitioning between liquid and ice water as a function of the local temperature in the atmospheric General Circulation Model (GCM) of the Laboratoire de Météorologie Dynamique (LMDZ).

8.2. Tools and methodology

8.2.1. POLDER-1 satellite observations

POLDER (POLarization and Directionality of the Earth's Reflectances) is a radiometer which was on board the Japanese polar orbiting ADEOS-1 platform from August 1996 until June 1997. POLDER is a wide field-of-view camera (with a swath of 2400x1800 km^2 and a resolution of 6x7 km^2) which observes the Earth's surface and atmosphere through 15 filters and polarizers in the visible and near infrared. It was the first space instrument to simultaneously observe the polarization and the multi-spectral and directional signatures of the reflected radiation (*Deschamps et al.*, 1994). We use cloud top thermodynamic phase and cloud top temperature retrieved from POLDER data (*Buriez et al.*, 1997). The cloud top Rayleigh pressure is retrieved from the polarized signal at 443 nm based on molecular scattering by the atmosphere above the cloud (*Vanbauce et al.*, 1998). Using the corresponding interpolated temperature profile from 6-hourly ECMWF meteorological analyses we convert the cloud top pressure into a cloud top temperature. The cloud thermodynamic phase is also retrieved from POLDER data as described in *Goloub et al.* (2000) and *Riedi et al.* (2000). The retrieval is based on the angular and polarized signatures of cloud reflected radiances at scattering angles near 140°. These cloud parameters are extracted at the pixel resolution. The POLDER level-2 products are then computed at the scale of a "super-pixel" composed of 9x9 POLDER level-1 pixels (about 0.5°x0.5° at the Equator). In POLDER the level-2 cloud phase parameter can take three different values: *liquid* if all cloud pixels are liquid, *ice* if all cloud pixels are ice, and *mixed* if both liquid and ice pixels coexist within a super-pixel. The satellite is used at its original resolution of 9x9 pixels as well as at the GCM resolution after an appropriate regridding.

8.2.2. The LMD GCM

We use here the Laboratoire de Météorologie Dynamique (LMD) GCM. The resolution considered is 96 points evenly spaced in longitude and 72 points in latitude. The model is vertically discretized on 19 hybrid σ-pressure levels ($\sigma = p/p_s$ where p and p_s are the atmospheric and surface pressures). An important characteristic of the LMD GCM version used in this study is the definition of the cloud and precipitation parameterizations. Cloud water is predicted in the model by a budget equation where the ice and liquid phases are considered jointly. The condensation scheme uses a "hat" probability density function for total water in a grid box, which allows for fractional cloudiness (*Le Treut and Li*, 1991). Depending on the local temperature, the total condensed water is partitioned between liquid water and ice. Clouds are composed entirely of ice crystals or liquid droplets if the local temperature is lower than T_{ice} or larger than T_0, respectively. In between T_0 and T_{ice}, the fraction of liquid water is given by

$$x_{\text{liq}} = \begin{cases} 0 & T < T_{\text{ice}} \\ \left(\frac{T - T_{\text{ice}}}{T_0 - T_{\text{ice}}}\right)^{n_x} & T \in [T_{\text{ice}}, T_0] \\ 1 & T > T_0 \end{cases} \tag{8.1}$$

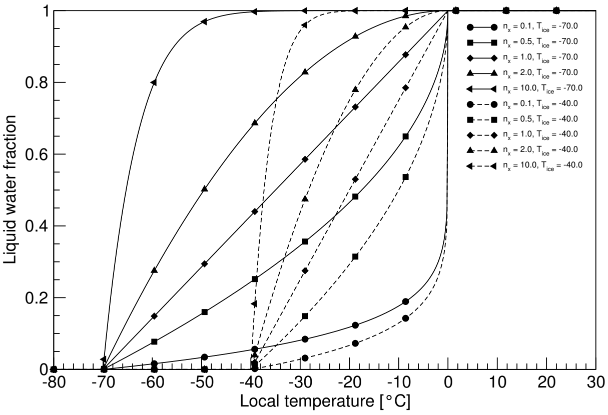

Figure 8.1.: Liquid water fraction as a function of the local temperature for $T_{\text{ice}} = -70°\text{C}$ and $T_{\text{ice}} = -40°\text{C}$, with values for $n_{\text{x}} \in [0.1, 0.2, 1, 2, 10]$.

In the standard version of the model, $T_{\text{ice}} = -15°\text{C}$, $T_0 = 0°\text{C}$, and $n_x = 6$. The choice of $T_0 = 0°\text{C}$ is rather straightforward as ice crystals in the atmosphere melt rapidly above the melting point. The two other parameters, however, are more difficult to define. Observations suggest T_{ice} to be in the range of –35°C to –40°C (*Houze*, 1993). Values for T_{ice} in GCMs include –40°C (*Del Genio et al.*, 1996), –35° (*Lohmann and Roeckner*, 1996), –20° (*Fowler et al.*, 1996), –15°C (*Smith*, 1990). Schemes using the a formula similar to Eq. 8.1 use $n_{\text{x}} = 2$ (*Del Genio et al.* (1996); *Smith* (1990)). The impact of T_{ice} and n_{x} on the x_{liq} to T relationship is illustrated in Fig. 8.1. We will examine the sensitivity of the model results to these parameters and compare them to the satellite observations.

The period simulated is that of POLDER-1 from November 1996 to June 1997. Reynolds sea surface temperature (SST) and HadISST1.0 sea-ice extent are imposed (*Rayner et al.*, 2003). Winds and temperature are nudged to ECMWF reanalyses in order to get realistic meteorological conditions.

8.2.3. Simulation of satellite observations from the model results

In order to compare the model results with the satellite parameters, we produce a 2D "satellite-like" field from the 3D model results. For this study, we assume that clouds are opaque for the quantities we are interested in and we use a random overlap assumption. The column cloud fraction, f, can be expressed as:

$$f = 1 - \prod_{i=1}^{n}(1 - f_i)$$

where f_i is the cloud fraction at model layer i and n is the uppermost layer. Under the same assumption the cloudy-sky mean of a variable x (cloud-top temperature, fraction of liquid clouds, ...) as seen from the top of atmosphere can be computed as:

$$x_{\text{cloudy}} = \frac{\sum_{i=1}^{n} x_i f_i \prod_{k=i}^{n}(1 - f_{k+1})}{f} \tag{8.2}$$

using the convention $f_{n+1} = 0$.

For each cloudy layer we approximate the Rayleigh temperature as the temperature of the interface between the highest cloudy layer and the clear layer above it. We then derive the cloud Rayleigh temperature at the top of the atmosphere (TOA) from Eq. 8.2. In the same way a TOA cloud liquid fraction is computed from the cloud liquid fractions at the different levels. Finally the GCM output is sampled along the satellite overpass which is calculated on-line in the model. Because the physical timestep is 30 minutes in our model, the sampled cloud fields are within ±15 minutes of the actual satellite observations. Therefore we do not expect any bias in the GCM due to the diurnal cycle.

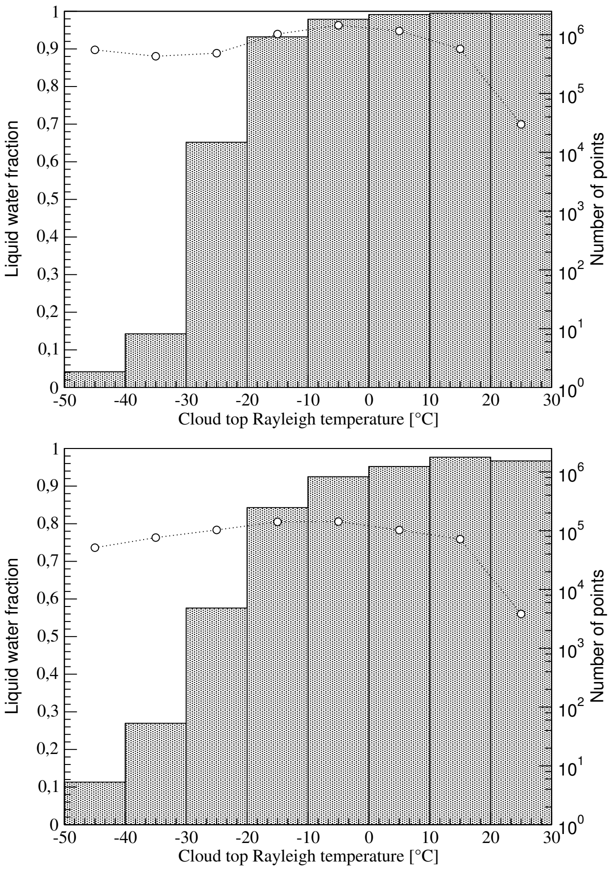

Figure 8.2.: Fraction of liquid phase at cloud top as a function of the cloud Rayleigh temperature in the POLDER observations at (a) the POLDER resolution and (b) at the GCM resolution. The dashed line shows the number of points in each bin (right scale).

8.3. Results

8.3.1. Cloud phase to cloud temperature relationship in the satellite observations

We estimate the average liquid cloud fraction for each 10 K bin of cloud Rayleigh temperature in the POLDER retrievals. Fig. 8.2 shows the phase to temperature relationships for the 8-month POLDER period. Looking at shorter periods or particular regions gives rather similar results.

It is noteworthy, however, that the relationship is much less smooth if POLDER data are not regridded to the GCM resolution due to the larger heterogeneity in the cloud properties. It is therefore important to first decrease the resolution of satellite data before comparing with the GCM results. It is due to the cloud sampling that even for temperatures above the melting point small fractions of ice clouds exist. This would be the case e.g. in tropical regions with deep convection where a cumulonimbus may exist along with low level trade cumuli. Our results differ slightly from those of *Giraud et al.* (2001), who found less ice clouds at temperatures close to 0°C.

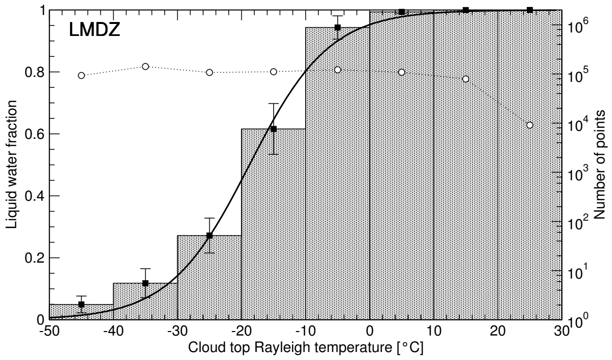

Figure 8.3.: Same as Fig. 8.2 but for standard LMDZ model results.

8.3.2. Model relationships

Fig. 8.3 shows the same relationships but for model-simulated quantities. An obvious deficiency is the too steep transition between 0% and 100% liquid water fraction in a temperature range of only about 50°C. The simulated phase to temperature relationship is very robust and does not vary much when looking at different regions or periods. Particularly, the result of a short simulation of a few days is not different from that from a 8-month simulation.

8.3.3. Parameter fit

Keeping the parameterization for the repartition of condensed water into liquid water and ice (Eq. 8.1), we try to find the values of the two parameters T_{ice} and n_{x} which match best the POLDER observations. The upper bound of 0°C is kept as larger values for the melting point would not be physically reasonable. We vary T_{ice} between -70°C and 0°C and n_{x} between 0.1 and 10. We carry out three-day simulations for the period of June 10-12, 1997 for each pair of parameters. The resulting phase to temperature relationships can well be fitted with an hyperbolic tangent function of the form:

$$x_{\text{liq}} = (1 + \tanh(a_1 T + a_2))/2 \qquad (8.3)$$

with a_1 and a_2 as fitting parameters determining the degree of flatness of the curve and a shift to lower temperatures, respectively. The fitted hyperbolic tangent functions for the POLDER observations and the standard model parameterization are superimposed to Figs. 8.2 and 8.3.

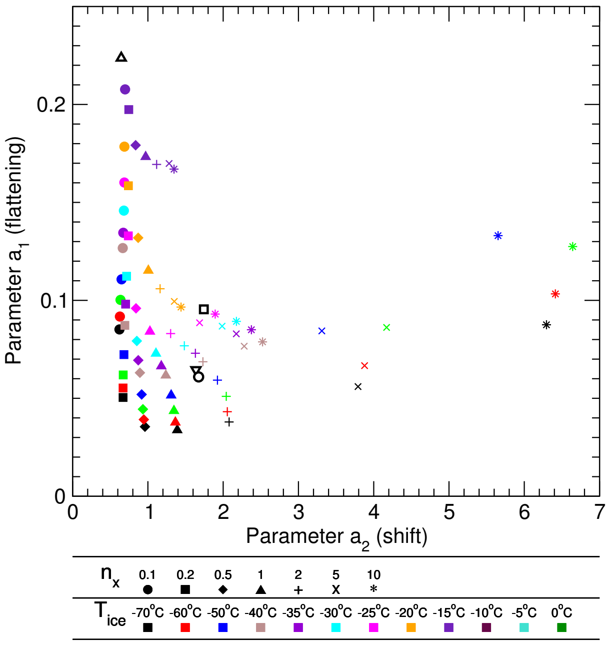

Figure 8.4.: Scatter plot of the a_1 and a_2 parameters fitting the top-of-atmosphere cloud liquid fraction to temperature relationships. space. On the x-axis, parameter a_2, and on the y-axis, parameter. The open circle is for the POLDER observations while the other symbols depict the relationships obtained in the GCM simulations with varying T_{ice} and n_{x}.

Fig. 8.4 shows the results of the different simulations in the parameter space of a_1 and a_2. Firstly, a temperature below which all cloud water is ice of rather low value is needed. The fit corresponds to a temperature of $T_{\text{ice}} = -32$°C. It is interesting that in Fig. 8.2 considerable liquid fractions are shown for temperatures below –35°C, which is due to the sampling at the model grid resolution. The freezing temperature found is slightly larger but rather close to the values found by observational studies (*Sassen and Dodd*, 1988) or used in high resolution models (*Spice et al.*, 1999). Secondly, a concave function has to be chosen to match the observations, but the exponent is smaller than so far used in the model.

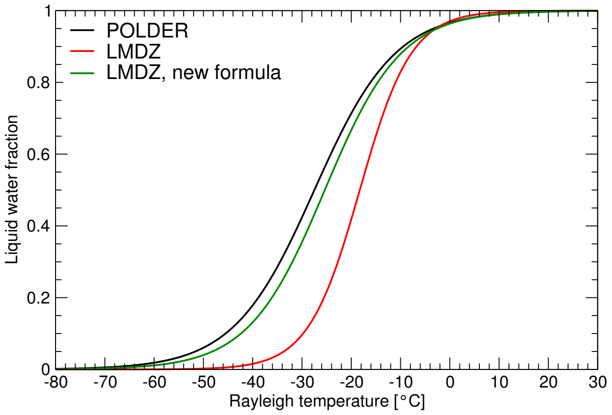

Figure 8.5.: Regressions of the phase to temperature relationship as from Figs. 8.2 (black curve) and 8.3 (red) for the 8-month POLDER period, and for a simulation using the new pair of parameters (green)

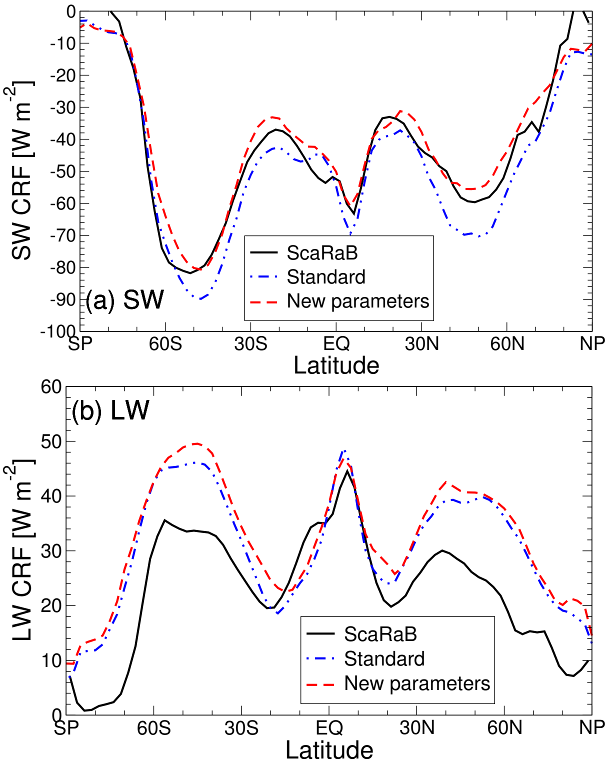

Figure 8.6.: Annual cloud radiative forcing [Wm^{-2}]. (a) Long-wave and (b) Short-wave for ScaRaB observations (black, solid), the Standard model scheme (blue, dash-dotted), and the new pair of parameters (red, dashed).

8.4. Conclusions

Using data derived from the spaceborne instrument POLDER-1, we establish a relationship between cloud top temperature and cloud top thermodynamical phase. We simulate the same period with the LMDZ GCM by nudging the winds and temperature to ECMWF reanalysis data. The model's parameterization for the thermodynamical phase of condensed water, a distribution according to local temperature, is tested. We carried out multiple simulations varying two parameters and identified the best fit of model to POLDER data. The standard parameterization for the liquid and ice fraction clearly is too steep and can not capture the fraction of liquid water clouds observed even at very low temperatures. The curve resulting from the "best fit" to the observational data obtained from short simulations using different parameters is able to reproduce well the observations (Fig. 8.5). The temperature where all cloud water consists of ice is found to be $T_{\mathrm{ice}} = -32°\mathrm{C}$, which is close to observed values. The exponent of the transition function is determined as n_{x}=1.9. These two values are different from those arbitrarily chosen in the standard model parameterization of the LMDZ, but are rather close to values used in other GCMs. We carried out simulations of one year for both, the old and new pairs of parameters (T_{ice} and n_{x}). Fig. 8.6 shows the zonal annual mean cloud radiative forcings (CRF) in the shortwave and longwave spectra, comparing the two model versions with ScaRaB satellite measurements for March 1994 to February 1995 (*Kandel et al.*, 1998). While in the SW spectrum, the new parameterization simulates a cloud radiative forcing closer to the observations except for southern hemisphere midlatitudes, a general bias of the model to simulate too strong CRF in the longwave spectrum is slightly enhanced at midlatitudes when using the new parameters.

8.5. Évaluation de la paramétrisation de la phase thermodynamique dans le MCG LMDZ en utilisant des données satellitaires POLDER : Résumé

Introduction

Les processus de nuages et de précipitation sont assez différents suivant la phase thermodynamique dans lesquels ils ont lieu. De plus, le transfert radiatif est influencé différemment dans les nuages de glace et dans les nuages d'eau liquide. Parmi d'autres, l'étude présentée dans les derniers deux chapitres a de nouveau montré les réactions différentes des nuages de glace et d'eau liquide aux forçages externes.

Ce sont là quelques-unes des raisons pour lesquelles la paramétrisation de la phase thermodynamique dans des modèles de grande échelle est d'une importance particulière. En absence d'une représentation explicite de la distribution de l'eau condensée en eau liquide et glace, l'indicateur le plus important pour la phase thermodynamique de l'eau condensée est la température locale. La paramétrisation la plus simple consiste à fixer une température au-dessus de laquelle l'eau est liquide et au-dessous de laquelle elle est solide. Pourtant, des observations montrent que toute l'eau est bien liquide au-delà de 0°C, alors que de l'eau liquide peut être trouvée à des températures aussi froides que –40°C (*Houze*, 1993). Beaucoup de modèles à grande échelle définissent donc une température, au-dessus de laquelle toute l'eau est liquide (dans la plupart des cas, 0°C), une température T_{ice}, au-dessous de laquelle toute l'eau est congelée, et ils partagent l'eau condensée dans la maille de la grille entre eau liquide et glace en suivant une formule exponentielle entre ces deux températures. Dans cette étude, nous cherchons à fixer les deux paramètres de cette paramétrisation, qui sont T_{ice} et l'exposant de la fonction de transition.

Méthode

Nous utilisons pour cela des observations spatiales de l'instrument POLDER de la température et la phase thermodynamique au sommet des nuages (voir chapitre 3). Dans une étude similaire avec des données combinées de la phase thermodynamique dérivée par POLDER et la température de brillance donnée par l'instrument ATSR-2, *Giraud et al.* (2001) ont montré une forte corrélation entre la température au sommet des nuages et la phase thermodynamique comme elle est dérivée par POLDER. Nous simulons avec le modèle LMDZ la période de mesures de POLDER (Novembre 1996 à Juin 1997) en mode guidé et avec des SST observées imposées. La température et la phase thermodynamique au sommet des nuages sont échantillonnées en utilisant l'hypothèse de recouvrement aléatoire sur la fauchée du satellite. La relation statistique entre la température et la phase thermodynamique au sommet des nuages est établie à la fois dans les sorties du modèle et dans les observations POLDER. Nous ajustons ensuite une tangente hyperbolique à deux paramètres à cette relation. Comme nous l'avons montré, cette relation est très stable dans le modèle, et elle est très similaire que l'on l'établisse à partir des sorties de quelques jours, plusieurs jours, ou toute la période. Nous effectuons alors plusieurs simulations courtes en variant les deux paramètres de la paramétrisation de la phase thermodynamique en fonction de la température locale dans le modèle et déduisons les deux paramètres de la tangente hyperbolique ajustée.

Résultat

Avec cette méthode, nous trouvons un très bon accord entre modèle et les observations pour le choix de –32°C comme T_{ice} et une transition suivant une fonction exponentielle avec un exposant de 1.7. Ces deux valeurs sont différentes de celles choisies par hasard dans la formule standard du LMDZ (–15°C et 6), mais sont proches des paramètres utilisés dans d'autres modèles ($T_{\text{ice}} = -35$°C ; *Del Genio et al.*, 1996 ; *Lohmann et Roeckner* , 1996 ; n_{x}=2, *Smith et al.*, 1990). Nous avons effectué deux simulations en imposant la SST, une avec le jeu de paramètres ≪ standard≫ , l'autre avec les deux nouveaux paramètres. Comme nous avons pu le montrer en comparant les sorties du modèle aux observations de ScaRaB (*Kandel et al.*, 1998), le forçage radiatif des nuages est beaucoup mieux représenté dans le spectre des ondes courtes en utilisant les nouveaux paramètres, mais il reste très similaire dans le spectre des ondes longues (fig. 8.6).

9. A new liquid- and ice phase microphysical scheme for the LMDZ GCM: Description and preliminary results

9.1. Introduction

The term "microphysics" in the global atmospheric modeling context refers to the physical processes connected with clouds and precipitation, beginning from nucleation of cloud particles and condensation, to formation of different forms of precipitation, to the fall and possible evaporation of precipitation. For all these processes, individual particles have to be considered, having a typical size scale of some micrometers. Nevertheless, it is by these processes that all clouds and precipitation appear, evolve, and disappear.

Clouds play a fundamental role in the atmospheric energy balance. They increase the shortwave planetary albedo, a cooling effect, and on the other hand, they increase the longwave greenhouse effect, warming the surface. In addition, they distribute latent heat in the atmosphere. The different representation of clouds is a major source of uncertainty in climate change scenario simulations with different general circulation models (*Cess et al.*, 1990; *Le Treut and McAvaney*, 2002).

Precipitation is one of the main climate variables. Nevertheless, climate models are so far not able to coherently simulate the response of precipitation to anthropogenic climate change. This, however, would be one of the most important predictions to provide to the public.

One of the reasons for these shortcomings may be the insufficient parameterization of microphysics in the models. There has been some experience in modeling of liquid water microphysics in GCMs with simple formulations for ice-phase microphysics (e.g., *Boucher et al.*, 1995a; *Del Genio et al.*, 1996). Some global models also contain microphysical formulations for ice- and mixed-phase clouds (*Lohmann and Roeckner*, 1996; *Fowler et al.*, 1996; *Rotstayn*, 1997; *Ghan et al.*, 1997a; *Wilson and Ballard*, 1999). In this study, we develop a comprehensive liquid- and ice-phase cloud microphysical scheme and apply it in the Laboratoire de Météorologie Dynamique (LMD-Z) GCM. We replace thus the former microphysical scheme of *Boucher et al.* (1995a), which consisted of formulations for autoconversion and accretion of liquid clouds, and a simple fall-velocity dependent snow formation equation. Liquid water droplet number concentration so far was linked to sulfate aerosol mass using an empiric equation (*Boucher and Lohmann*, 1995).

The new scheme is described in Section 9.2. Finally, in Section 9.3, we show results from simulations using the new scheme compared to the former one.

9.2. Description of the scheme

In the new microphysical scheme, water is divided into categories of vapor, cloud water, and precipitating water. Cloud water is further split in liquid water and ice. For precipitating water, liquid water (rain), slowly-falling (snow) and fast-falling (graupel) ice water are separated. The mixing ratios of these six water species are treated prognostically in the model. For cloud water, in addition, the number concentrations of liquid droplets and ice crystals are treated as

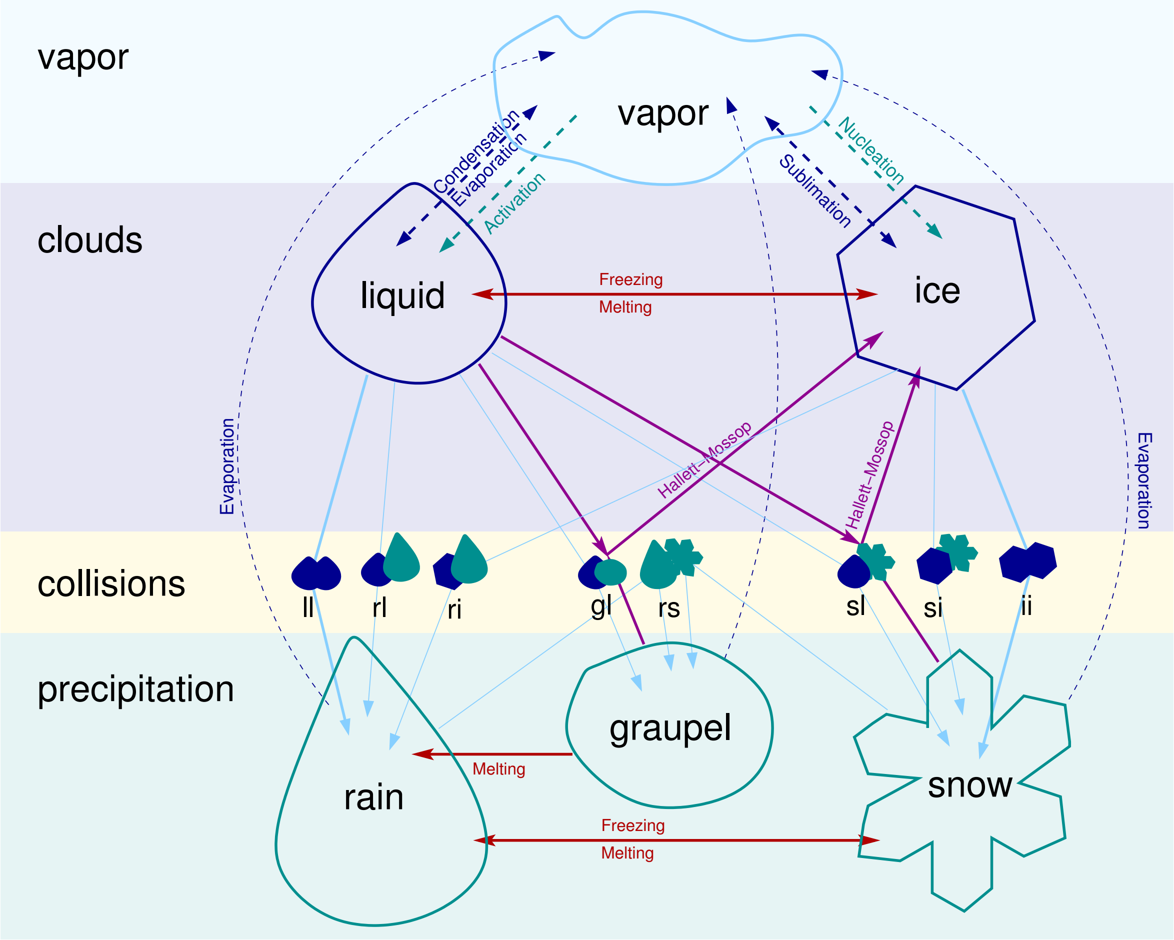

Figure 9.1.: The six water categories of the model and transition processes between them.

q_l	Cloud liquid water mixing ratio	[kg kg^{-1}]
q_i	Cloud ice mixing ratio	[kg kg^{-1}]
q_r	Rain water mixing ratio	[kg kg^{-1}]
q_s	Snow mixing ratio	[kg kg^{-1}]
q_g	Graupel mixing ratio	[kg kg^{-1}]
N_l	Cloud droplet number concentration	[m^{-3}]
N_i	Ice crystal number concentration	[m^{-3}]

Table 9.1.: Prognostic variables for water species in the model.

prognostic variables. Precipitating water, however, is assumed to follow a Marshall-Palmer distribution (*Marshall and Palmer*, 1948; *Gunn and Marshall*, 1957). While water vapor and cloud water are transported by the large scale dynamics, precipitation is considered to remain in the grid column of its origin. This is a valid assumption because the time for precipitation (fall speed times height) is small compared to the time for advection to an adjacent grid box (horizontal wind speed times horizontal resolution). In future studies, however, a possible impact of transportation of precipitating water shall be examined. Table 9.1 summarizes the prognostic variables of the model.

Process	Description	Variables concerned
Condensation / Evaporation / Sublimation	Transformation of water vapor to liquid water and ice and vice versa	q_v, q_l, q_i, N_l, N_i.
Activation/Nucleation	Creation of new droplets and new crystals	N_l, N_i, q_v, q_l, q_i
Collisions/Coalescence	Transformations between liquid water, ice, and precipitating species	q_l, q_i, q_r, q_s, q_g, N_l, N_i
Freezing / Melting	Conversions between liquid water and ice and between rain and snow	q_l, q_i, q_r, q_s, N_l, N_i
Evaporation of precipitation	Conversion of precipitating species to water vapor	q_v, q_r, q_s, q_g

Table 9.2.: Processes in the new microphysical scheme.

The scheme treats five types of processes. Condensation and evaporation are the transitions between water vapor and cloud liquid water, and sublimation the transition between water vapor and cloud ice. New cloud particles may form via activation of aerosols or nucleation for liquid droplets and ice crystals. Cloud and precipitation particles may collide with each other and coalesce, which yields a transition to another water category. When rime is produced, new ice splinter are created by the secondary ice production mechanism. Finally, precipitation particles may fall, and when falling through sub-saturated air masses, they may evaporate. Table 9.2 lists the five processes in the order they are treated in the model, and Fig. 9.1 schematically visualizes the processes connecting the different water categories. The microphysical processes are described in more detail in the following section.

9.2.1. Condensation/Evaporation

To calculate condensation and evaporation of cloud liquid water and cloud ice, a scheme based on *Le Treut and Li* (1991) is applied. The scheme applies a probability density function (PDF) to the total water content (i.e., cloud liquid and ice water are re-evaporated before applying the PDF). The saturation water vapor mixing ratio is calculated using the Tetens-Formula (*Tetens*, 1930):

$$q_{sat} = \frac{\frac{R_d}{R_v}\ e_{sat}(T)}{p - \left(1 - \frac{R_d}{R_v}\right)\ e_{sat}(T)} \tag{9.1}$$

where

$$e_{sat}(T) = a_1\ \exp\left[a_3\left(\frac{T - T_0}{T - a_4}\right)\right] \tag{9.2}$$

with the empirical constants a_3 and a_4 being different for $T < T_0$ and $T > T_0$. A parameter, Δ_{q_s}, determines the width of the PDF of the total water mixing ratio distribution. This parameter varies vertically in the range [0.4-0.99], but is constant horizontally and temporally. Figure 9.2 shows schematically the PDF in a grid box. The cloud fraction of the grid box is calculated as

$$f = \frac{q_t(1 + \Delta_{q_s}) - q_s}{2\ \Delta_{q_s}\ q_t} \tag{9.3}$$

and is restricted to $f \in [0, 1]$. The total water mixing ratio in the cloudy part of the grid box is

$$q_{t,cloud} = \frac{q_t(1 + \Delta_{q_s}) + q_s}{2} \tag{9.4}$$

The fraction of q_t that exceeds the saturation water vapor mixing ration in the cloudy part, is condensed. The grid-box mean condensed water is thus:

$$q_{cond} = (q_{t,cloud} - q_s)\frac{1}{1 + \frac{L_v}{c_p}\frac{\partial q_{sat}}{\partial T}}\ f \tag{9.5}$$

$$= \frac{(q_t(1 + \Delta_{q_s}) - q_s)^2}{4\ \Delta_{q_s}\ q_t}\frac{1}{1 + \frac{L_v}{c_p}\frac{\partial q_{sat}}{\partial T}} \tag{9.6}$$

where the last factor on the right hand side of this equation accounts for the latent heating in the condensation process. The derivative of saturation water vapor mixing ration w.r.t. temperature is calculated

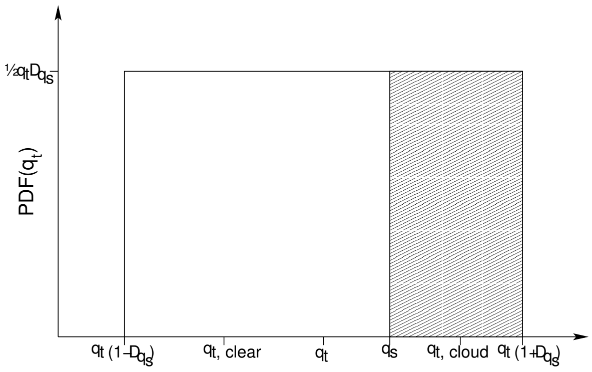

Figure 9.2.: The PDF of total water mixing ratio.

from the Clausius-Clapeyron equation. L_v is replaced by L_s for $T < T_0$ and q_{cond} is restricted to values between 0 and q_t. The condensed water is divided into cloud liquid water and cloud ice depending on the local temperature. The ice fraction is defined as

$$x_{\text{liq}} = \begin{cases} \left(\frac{T-T_{\text{ice}}}{T_0-T_{\text{ice}}}\right)^{n_{\text{x}}} & T \in [T_{\text{ice}}, T_0] \\ 0 & T < T_{\text{ice}} \\ 1 & T > T_0 \end{cases} \tag{9.7}$$

where T_{ice} and n_{x} are parameters. Their values recently have been fixed using POLDER satellite data to $T_{\text{ice}} = -32°C$ and $n_{\text{x}} = 1.7$ (*Boucher and Quaas*, 2003, see Chapter 8).

9.2.2. Activation of droplets

The formulation of cloud droplet activation from aerosol is of major importance to simulate the aerosol indirect effects, i.e., the impact of aerosols on clouds. We use the *Twomey* (1959) formula

$$\left.\frac{dN_l}{dt}\right|_{act} = c^{\frac{2}{2+k}} \left(\frac{1.63 \times 10^{-3}\ w^{1.5}}{k\ B\left(\frac{3}{2}, \frac{k}{2}\right)}\right)^{\frac{k}{k+2}} \tag{9.8}$$

where $B(x_1, x_2)$ is the Beta-function, k the Twomey constant, and c is the concentration of aerosols activated at 1% supersaturation. We set c to 90% of the hydrophilic aerosol number concentration. Taking a constant value is a valid limitation, according to *Junge and McLaren* (1971) and *Fitzgerald* (1973). The parameter k is chosen to be $k = 0.2$, which is somewhat smaller than the values given by *Twomey* (1959). However, he looked at convective clouds with rather strong updraft velocities, so a smaller value is supposed to be valid for the large scale. New cloud droplets are activated in the part of the grid cell which is supersaturated, i.e., the cloudy fraction as defined earlier (Section 9.2.1). The grid-box mean vertical wind, $\bar{w}$, generally is close to zero and often slightly negative. Thus, the subgrid scale vertical wind in the cloud has to be evaluated. To do this, we assume subsidence to take place in the cloud-free fraction of the grid cell. When $\bar{w}$ is negative, the subsidence in the cloud free part, $w\downarrow^{\text{cf}}$, is calculated from the mean velocity by multiplying it with a random number between 1 and 2 – an approach similar to that of *Donner et al.* (1997). When the mean vertical velocity is very slightly negative or positive, the clear-sky subsidence is assumed to be $w\downarrow^{\text{cf}}_{\text{min}} = -1.2$ cm s^{-1} (which is a typical value for subsidence according to *Suhre et al.*, 2000):

$$w\downarrow = min(\bar{w} \times (1+r), w\downarrow_{\text{min}}) \tag{9.9}$$

where r is a random number between 0 and 1. The updraft in the cloudy part of the grid cell is determined as the residual:

$$w^{\text{cc}}\uparrow = \frac{\bar{w} - (1-f)w^{\text{cf}}\downarrow}{f} \tag{9.10}$$

where indices “cf” and “cc” refer to the “cloud-free” and “cloud-covered” parts of the grid cell, respectively.

9.2.3. Nucleation of ice crystals

Little is known about the process of nucleation of ice crystals from aerosol. In general, two different ways are distinguished (*Young*, 1974b; *Vali*, 1985)):

- *Homogeneous nucleation*, which is the freezing of supercooled liquid water droplets. Homogeneous nucleation occurs at temperatures below –35°C (*Sassen and Dodd*, 1988; *Spice et al.*, 1999).

- *Heterogeneous nucleation*, including the action of a solid aerosol. Three modes of functioning exist:
  - *Contact nucleation*, a collision between a supercooled drop and an aerosol particle.
  - *Deposition nucleation*, where water vapor deposits on a dry or wetted aerosol.

- *Immersion nucleation*, the freezing of a droplet including an aerosol with an insoluble component.

The nucleation processes where ice crystals form by freezing of liquid droplets are treated in the freezing part of the scheme. From the nucleation processes given above, the nucleation by deposition nucleation is the only one explicitly treated by the nucleation scheme in the parameterization presented here. According to *Meyers et al.* (1992), ice crystal number concentration can be described in dependence on the supersaturation:

$$N_{ID} = \exp\left(a + b\ S_i\right) \tag{9.11}$$

where S_i is the supersaturation over ice in %, and $a = -0.639$ and $b = 0.1296$ are constants. The supersaturation of the cloudy part of the grid is used, calculated from the grid-box mean supersaturation and an assumed sub-saturation in the clear part of the grid box, which varies between a minimum value and twice the grid-box mean value. Similarity to the subgrid updraft velocity calculated for the droplet activation scheme, the supersaturation in the cloudy part of the grid box is thus given as

$$S_i^{cc} = \frac{\bar{S}_i - (1-f)S_i^{cf}}{f} \tag{9.12}$$

9.2.4. Collisions/Coalescence

Particles may collide and potentially coalesce. Assuming a constant size distribution for all particles, the number of particles that collide per volume and time is

$$r_{pq} = E_{pq}\ N_p\ N_q\ \frac{\pi}{4}\left(D_p + D_q\right)^2\ \left|V_p - V_q\right| \tag{9.13}$$

where all quantities are averaged over the size distribution, and p and q refer to the particle species (liquid water, ice, rain, snow, or graupel), and E_{pq} are the collision efficiencies (see Table 9.4; the efficiencies are taken from *Rutledge and Hobbs* (1983) except for the autoconversion cases E_{ll} and E_{ii}). The terminal fall velocities V of the different species are listed in Section 9.2.6. While number concentrations N are calculated prognostically for droplets and ice crystals, the precipitation species are assumed to follow the Marshall-Palmer distribution, so their number concentration can be estimated from the precipitating water mixing ratio. As mentioned above, droplets, raindrops, and graupel are considered to be spherical, and thus the effective diameter is determined from the mixing ratio with the fixed density of the particles, while ice crystals and snow flakes are considered as plates (*Rutledge and Hobbs*, 1983), with a diameter [m] of

$$D_p = 16.3\ \sqrt{\frac{\rho_{air}\ q_p}{N_p}} \tag{9.14}$$

Similarly to other schemes, Eq. 9.13 is changed for p=q (i.e., for autoconversion of droplets and crystals) to become

$$r_{pp} = H(D_p - D_{p0})\ N_p^2\ \frac{\pi}{4} D_p^2\ V_p \tag{9.15}$$

In this particular case, the collision efficiency is a Heaviside function, which is 0 below a threshold “critical diameter” and 1 above. The critical diameter is chosen as 14 μm for liquid droplets and 70 μm for ice crystals. Secondary ice particle production is accounted for (*Hallett and Mossop*, 1974; *Mossop*, 1985). When rime is formed, i.e., when coalescence between graupel and liquid droplets, or between rain and snow takes place, a new ice crystal of initial mass of $m_{i0} = 10^{-12}$ kg is produced per kg of new rime.

9.2.5. Freezing/Melting

Where the temperature exceeds 0°C, ice crystals and snow flakes melt to form droplets and raindrops, respectively.

For temperatures below 0°C, we treat the heterogeneous freezing by relaxing the ice crystal number concentration to the empirically temperature-dependent value from *Meyers et al.* (1992):

$$N_{IC} = \exp\left(a - b\ T\right) \tag{9.16}$$

where T is the temperature in °C, and $a = -2.80$ and $b = 0.262$ are empirical constants. On the expense of droplets and raindrops, the number concentration of ice crystals and snowflakes, respectively, is then relaxed towards the maximum concentration possible given by the freezing nuclei. For temperatures below –35°C, liquid droplets and rain particles freeze immediately.

	droplet	crystal	raindrop	snowflake	graupel
droplet	raindrop	N/A	raindrop	snowflake	graupel
crystal	-	snowflake	graupel	snowflake	N/A
raindrop	-	-	N/A	graupel	N/A

Table 9.3.: Particles that may collide. Coalescence for a particle in a row with the one in the column gives a particle of the form mentioned. “N/A” indicates that a collision between the two particles cannot occur in the model.

	droplet	crystal	raindrop	snowflake	graupel
droplet	$H(r - r_{l,0})$	N/A	1.	1.	1.
crystal	-	$H(D - D_{i,0})$	1.	0.1	N/A
raindrop	-	-	N/A	1.	N/A

Table 9.4.: Coalescence efficiencies for the collisions considered. “$H(x - x_0)$” is the Heaviside function, which is 0 for $x < x_0$ and 1 otherwise. Values are from *Rutledge and Hobbs* (1983) except for the two autoconversion cases.

9.2.6. Falling of precipitation

Different from cloud droplets and ice crystals, the three precipitation species may fall. The terminal fall velocity of raindrops is calculated as

$$V_r = C_2\ r - C_3 \tag{9.17}$$

where C_2=86.2 and C_3=0.155 $\mathrm{ms^{-1}}$ are constants and r is the raindrop radius (valid for 35.9μm$< r <$ 300μm, *Johnson* (1982). For snowflakes considered as “sideplanes”, *Locatelli and Hobbs* (1974) give the fall-speed

$$V_s = a\ (D \times 10^3)^b \tag{9.18}$$

with the empirical constants a=0.82 $\mathrm{ms^{-1}}$ and b=0.12. Finally, graupel falls at a speed of

$$V_g = a\ (D \times 10^3)^b \tag{9.19}$$

with the constants a=1.2 $\mathrm{ms^{-1}}$ and b=0.65 (“Cone-shaped graupel”; *Locatelli and Hobbs*, 1974). All quantities are given in SI units. For the explicit fall scheme to be numerically correct, a sub-timestep is introduced for the microphysical scheme. The timestep in this scheme is 90 s.

9.2.7. Precipitation fractions

To somehow take into account the subgrid-scale variability, the given fractional cloudiness is exploited to calculate a precipitation fraction for each of the precipitation species. When precipitation originates from autoconversion of droplets or ice crystals, this precipitation is assumed to be homogeneously distributed throughout the cloud. The precipitation fraction changes when new rain is formed in a layer, when the respective precipitation species is totally evaporated, or when due to a conversion between two different precipitation species one of them is entirely consumed. When rain falls, random overlap between the precipitation and cloud fractions is assumed consistently with the cloud overlap assumption in the model.

9.2.8. Evaporation

The evaporation scheme is adapted from *Boucher et al.* (1995a):

$$E_p = -\frac{\alpha}{2}\left(\frac{q_t^{cf}}{q_s} - 1\right)\ \frac{q_p}{\rho_{water}\ r_p^2} \tag{9.20}$$

where the index p refers to the respective precipitation species (rain, snow, or graupel), and $\alpha = 0.5$ as in *Boucher et al.* (1995a). In contrast to their scheme, however, the size of precipitation particles is calculated using the Marshall-Palmer distribution.

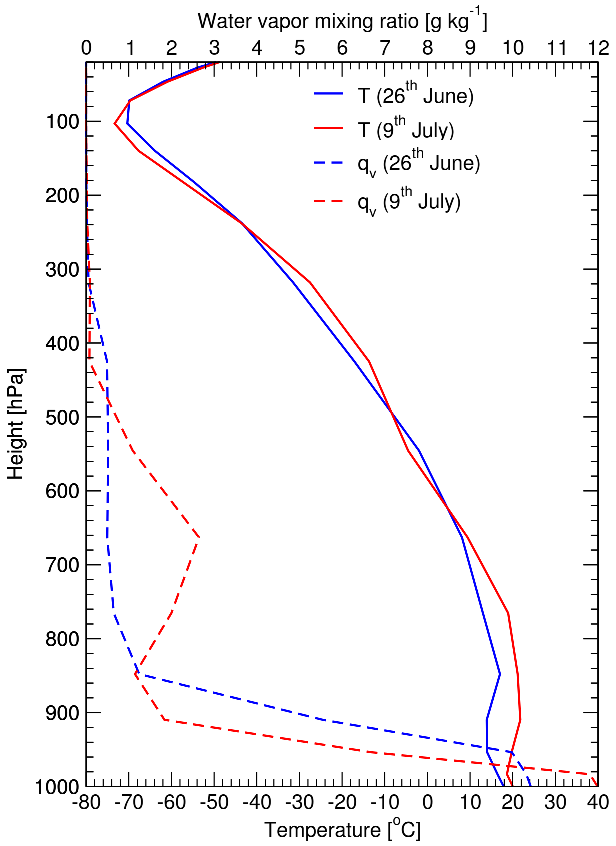

Figure 9.3.: Initial profiles of temperature and water vapor mixing ratio for the two ACE-2 cases (blue, June 26th; red, July 9th).

9.3. Results of 1D case studies

We test this new parameterization in two test cases using a single column model (SCM) version of the LMDZ GCM. This approach has formerly been used in Chapter 4.

9.3.1. Test cases for stratocumulus clouds: ACE-2

To test the liquid water part of the new microphysical scheme, the ACE-2 CLOUDYCOLUMN cases are chosen (*Brenguier et al.*, 2000a). Two of the ACE-2 cases have formerly been used to test the parameterization of the aerosol-cloud interactions in SCM versions of several GCMs (Chapter 4; *Menon et al.*, 2003).

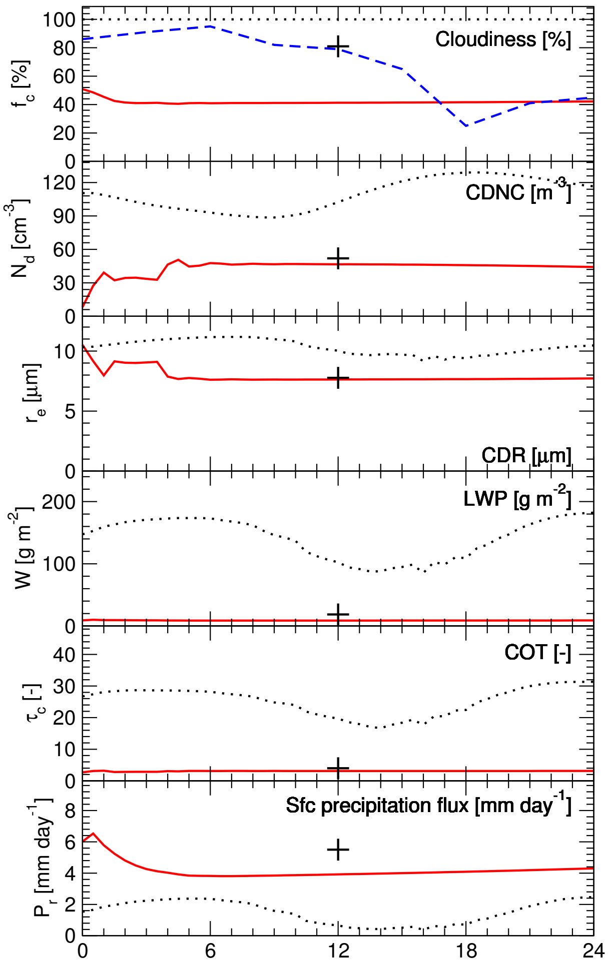

Figure 9.4.: Results of a SCM simulation for the clean ACE-2 case (June 26th, 1997) using the new microphysical scheme (red solid line), and using the microphysical parameterization of *Boucher et al.* (black, dotted line). Superimposed crosses show the observations. For cloudiness, ISCCP satellite observations are shown as blue dashed line.

Aerosol properties have been measured along with cloud microphysical properties and radiation (*Brenguier et al.*, 2000b). Observational values for the aerosols are summarized in Table 4.1 (*Guibert et al.*, 2003), and for microphysical cloud properties in Table 4.2. Figures 4.1 to 4.6 summarize the results from the single column versions of six different GCMs, including the LMDZ GCM with the microphysical scheme (*Boucher et al.*, 1995a) and the empirical formula to link CDNC to sulfate aerosol mass (*Boucher and Lohmann*, 1995).

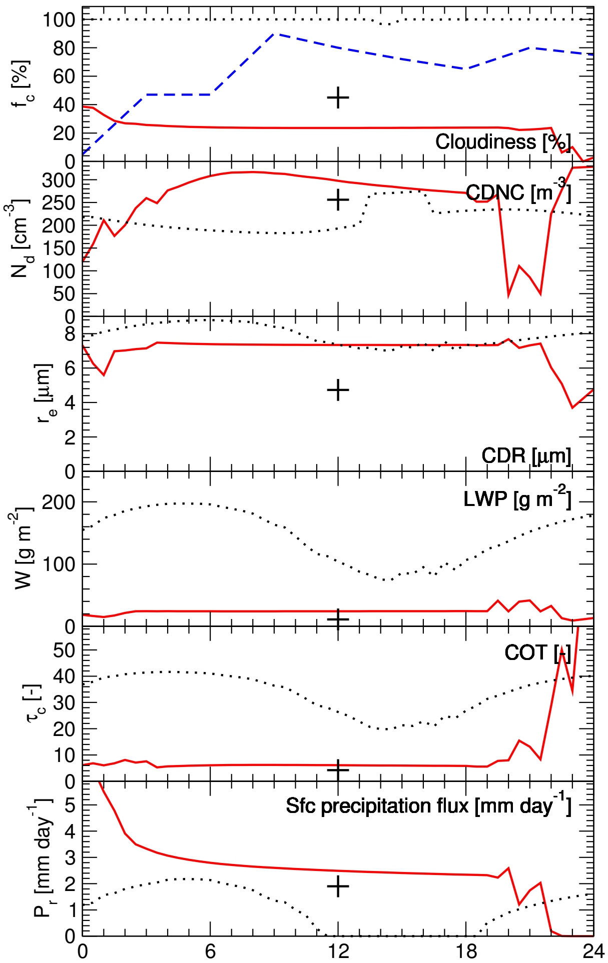

Figure 9.5.: As Fig. 9.4, but for the polluted ACE2 case (July 9th, 1997).

Figures 9.4 and 9.5 show the results of the LMDZ GCM in its single column version including the new microphysical scheme for the ACE-2 CLOUDYCOLUMN clear (June 26th, 1997), and polluted cases (July 9th, 1997), respectively. As aerosol data in Eq. 9.8, the total number concentration of sulfate, organic carbon, and sea salt is taken. The observations of the ACE-2 field study are shown as crosses, and for the cloud amount, also ISCCP cloud cover is displayed (*Rossow and Schiffer*, 1991). Along with these data, we show the results of the LMDZ SCM using the microphysical scheme of *Boucher et al.* as in Chapter 4. The results are very encouraging, as several of the deficiencies of the old microphysical scheme and of schemes of other GCMs identified in the study reported in Chapter 4 seem to be improved by the new parameterization.

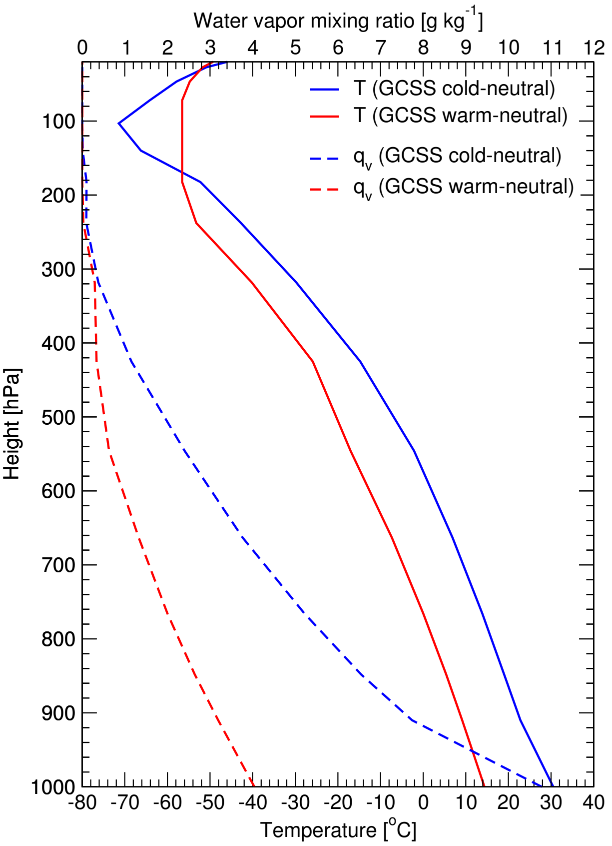

Figure 9.6.: Initial profiles of temperature and water vapor mixing ratio for the two GCSS working group II cases (blue, warm-neutral; red, cold-neutral).

The new parameterization is very well able to capture the differences between the clean and polluted cases. Cloud droplet number concentration is a factor of 5 larger in the polluted compared to the clean case, and the simulated CDNC is in close agreement with the observations in both cases, where the old scheme overestimated CDNC in the clean case and underestimated it in the polluted case. The droplet size is very well simulated in the clean case and somewhat overestimated in the polluted case. However, the scheme still simulates slightly smaller droplets in the polluted compared to the clean case. Cloud liquid water path and subsequently cloud optical thickness is much better simulated by the new scheme than by the former one, which overestimated both quantities by almost an order of magnitude. Now, the LWP is even underestimated in the clean case, and slightly overestimated in the polluted case.

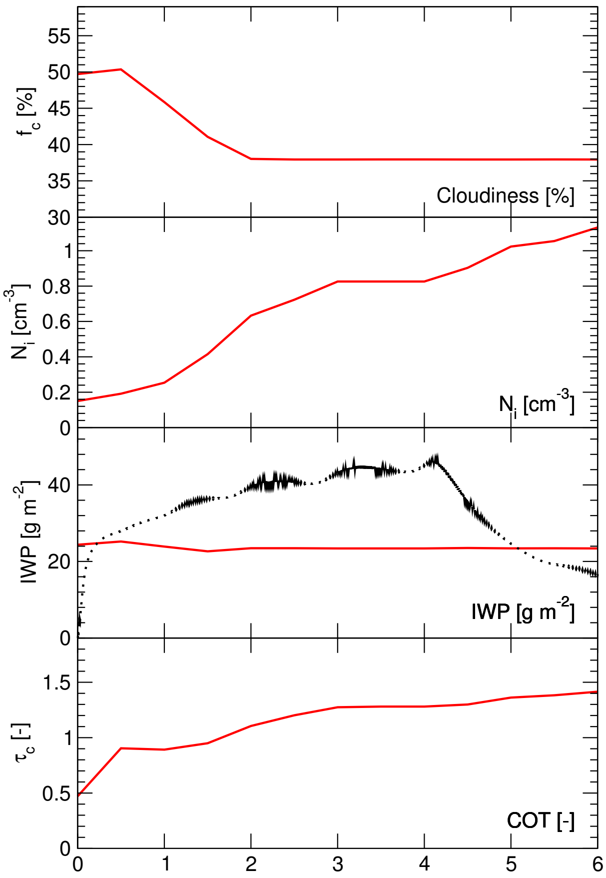

Figure 9.7.: Results of a SCM simulation for the "warm-neutral" GCSS WG2 case for cloudiness, ice crystal number concentration, ice water path, and cloud optical thickness. In red, the LMDZ GCM, and for the ice water content, in black, the Meso-NH model.

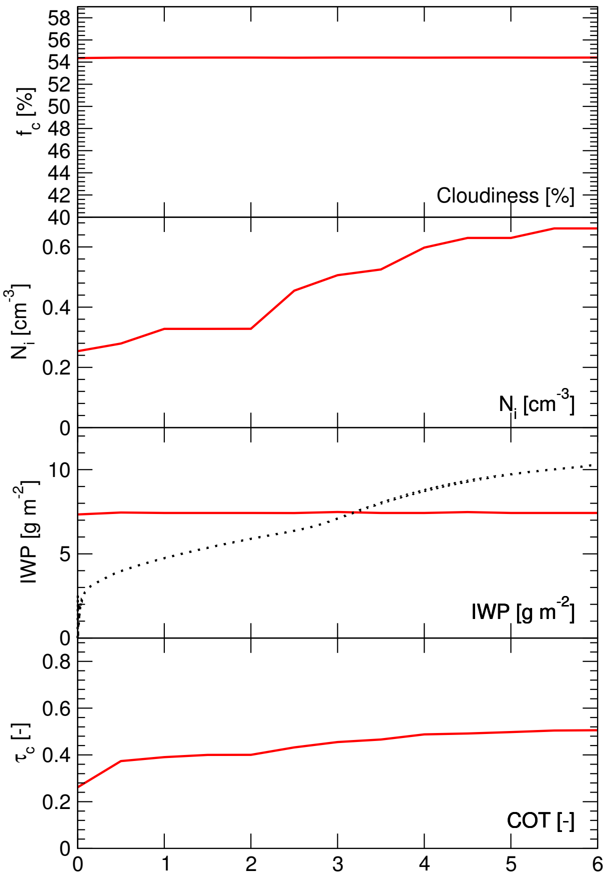

Figure 9.8.: As Fig. 9.7, but for the "cold-neutral" GCSS WG2 case.

Cloud optical thickness is very well simulated by the scheme in both cases. An important improvement of the new parameterization is its ability to simulate the drizzle precipitation observed. Consistently with the observations, the model simulates a slightly lower precipitation rate in the polluted than in the clean case.

9.3.2. Test cases for cirrus clouds: GCSS WG2

In the framework of the Global Energy and Water Cycle Experiment (GEWEX) Cloud System Studies (GCSS), one of the working groups (working group 2, WG2) investigates cirrus cloud systems. Within this group, a model intercomparison project is undertaken. A range of models covering parcel models to general circulation models are compared against each other. Results have been published for the parcel models by *Lin et al.* (2002). It should be noted that even such small-scale models show a very large scatter in results, often covering several orders of magnitude. Among the meso-scale models, Meso-NH has been evaluated using the GCSS WG2 cases. Meso-NH includes a comprehensive cirrus clouds microphysical scheme (*Thouron*, 2003). The two GSCC WG2 cases consist of a "warm-neutral" and a "cold-neutral" test case. In the intercomparison, a constant aerosol concentration of 200 cm^{-3} is considered, and for the first four of six hours of integration, a vertical ascending motion of 3 cm s^{-1} is applied. No radiation is used in the single-column test integration. Figure 9.6 shows the initial profiles of temperature and humidity.

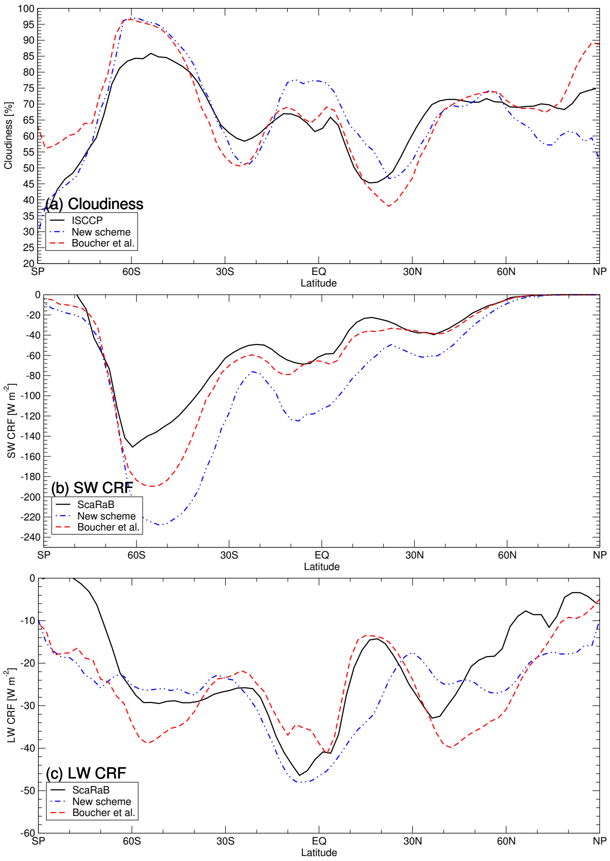

Figure 9.9.: DJF zonal mean (a) cloudiness [%], (b) SW and (c) LW cloud radiative forcing [Wm^{-2}]. Model results with the scheme of *Boucher et al.* (dashed, red) and the new scheme (blue, dotted), and observations (solid, black; (a) ISCCP, and (b-c) ScaRaB.

Figures 9.7 and 9.8 show the main results for the warm-neutral and cold-neutral cases, respectively. Along with the results from the LMDZ model using the new microphysical scheme, results of an integration of Meso-NH are shown for ice water path. The GCM simulated a thin cirrus in both cases, with rather small optical thickness. Ice water content is very well simulated when comparing the GCM to the mesoscale model.

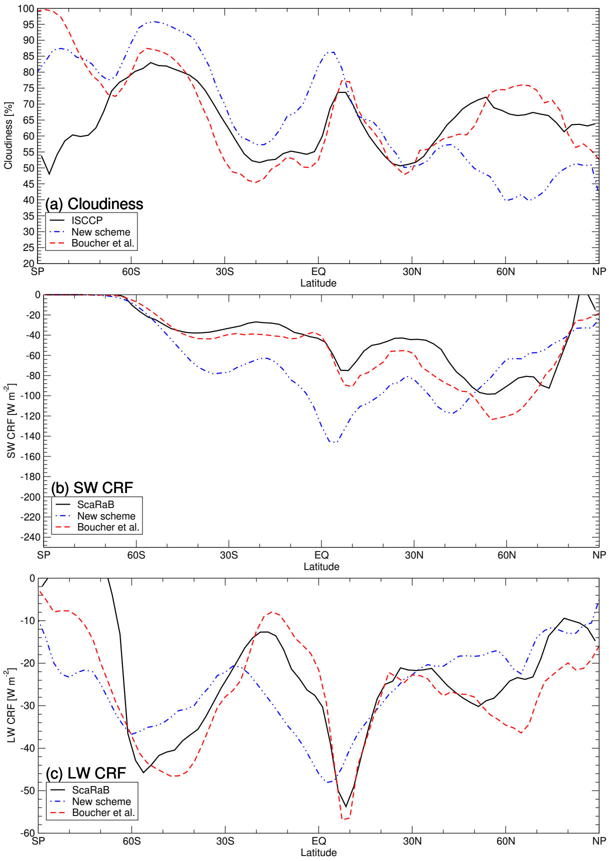

Figure 9.10.: As Fig. 9.9, but for JJA.

9.4. Preliminary 3D results

Using the new parameterization applying the same set of parameters as in the one dimensional simulations shown in the previous section, we carried out three-dimensional model simulations with the atmospheric GCM, forced with observed SST for 1997 (*Reynolds and Smith*, 1995) and using aerosol source data for ≈ 1990.

In Figs. 9.9 and 9.10 we show the zonal means for northern hemisphere summertime (June-July-August, JJA) and wintertime (December-January-February, DJF) for cloudiness and cloud radiative forcing in the SW and LW spectra. Observational data from the International Satellite Cloud Climatology Project (ISCCP; *Rossow and Schiffer*, 1991), averaged over the 1984 to 1992 period is shown for cloudiness and from the Scanner of the Earth Radiation Budget (ScaRaB; *Kandel et al.*, 1998) for 1994 and 1995 for cloud radiative forcings. The simulation using the new scheme is compared to a simulation with the scheme of *Boucher et al.* (1995a). The results are encouraging, even though of course several deficiencies still exist. Cloudiness is well simulated at most latitudes, slightly overestimating the cloud cover in the southern hemisphere and in the tropics, and underestimating it in the northern hemisphere. This behavior is related to a generally too small low level cloudiness over land and a slightly too large low level cloud cover over oceans. Shortwave cloud radiative forcing is overestimated with the new scheme, probably due to the too large low level cloud cover over the oceans. LW cloud radiative forcing however, is captured quite well, and in some cases the new scheme already does a better job than the old microphysical scheme of the model (e.g., at midlatitudes in the JJA case). The main deficiency of the new scheme so far is the strong underestimation of precipitation (not shown). As the observations are available only over land, only for continental cases the precipitation is evaluated here. Over oceans, the precipitation simulated by the new scheme is also somewhat smaller than the one given by the old scheme, but this is much less pronounced than over land (not shown). Probably, the underestimation in precipitation is linked to the underestimation in continental low level cloud cover.

9.5. Summary and discussion

The new scheme has been tested on the ACE-2 CLOUDYCOLUMN clean and polluted cases, and compared to observations and to the scheme of *Boucher et al.*. The new scheme successfully predicts larger CDNC, smaller CDR, and larger cloud optical thickness in the polluted compared to the clean case, consistently with the two aerosol indirect effects. However, due to the much larger LWC in the polluted case, it does not capture well the observed and expected decrease in precipitation.

To evaluate the parameterizations in the ice phase, two test cases of the GCSS working group 2 have been used. The new scheme has been evaluated using a single-column version of the GCM and comparing the results to a simulation with the meso-scale model Meso-NH. The new scheme underpredicts the ice water content in the cirrus in both cases by an order of magnitude. Ice crystal number concentration is underestimated in the warm case, and overestimated in the cold case. The results are strongly sensitive to several model parameters as well as to the initial temperature profile.

A preliminary study of the new scheme in the global model has been presented. Although some deficiencies of the new parameterization still exist, the results are encouraging. Precipitation is strongly underestimated by the scheme, and shortwave cloud radiative forcing is overestimated. However, the cloud cover is simulated rather well, and longwave cloud radiative forcing is sometimes already better simulated with the new scheme compared to the previous one. This is a particularly interesting result as it suggests that the ice phase is simulated well, and that major deficiencies still present may rather be linked to liquid phase processes.

Certainly, the degree of evaluation for the new scheme so far is not sufficient. The introduction of this new scheme opens a variety of possibilities to evaluate the model thoroughly. Quantities to be evaluated include the column droplet number concentration, ice crystal number concentration and size, and different precipitation species besides the quantities which could already be investigated in the old scheme (as presented in Chapter 2). Such evaluation and development is planned for the near future, in particular using a long time series of a comprehensive set of ground-based remote sensing measurements from the Site Instrumental de Recherche par Télédétection Atmosphérique (SIRTA) near Paris in France as well as using satellite data, particularly for the ice phase from a new TIROS-N Vertical Sounder (TOVS) dataset (see also Chapter 10).

9.6. Un nouveau schéma de microphysique de phase liquide et de glace pour le MCG LMDZ : Description et résultats préliminaires: Résumé

Introduction

Comme nous l'avons expliqué dans les derniers chapitres, ainsi que dans l'introduction de la thèse, la phase glace joue un rôle essentiel dans les processus microphysiques des nuages. Il est important de représenter ces processus de manière réaliste dans un modèle à grande échelle. De plus, des processus jusque-là peu connus comme des impacts possibles des aérosols sur les nuages en glace pourraient être étudiés une fois qu'une représentation de la phase glace dans un schéma de microphysique existe. La précipitation devrait être simulée de manière plus réaliste, car les processus microphysiques de formation de la précipitation dans les nuages de glace et de phase mixte sont importants pour le taux de précipitation.

Description du schéma

Dans le nouveau schéma, l'eau est partagée entre les classes de vapeur d'eau, d'eau nuageuse, et d'eau de précipitation. L'eau des nuages est de plus divisée en eau liquide et glace, et l'eau précipitante est divisée en eau liquide (de la pluie) et eau solide tombant à vitesse lente (de la neige) et rapide (des grêlons). Les rapports de mélange sont traités de manière pronostique dans le modèle. Pour l'eau nuageuse, les concentrations en nombre des gouttelettes et des cristaux sont de plus traitées de manière pronostique. L'eau précipitante est supposée suivre la distribution de Marshall-Palmer (*Marshall et Palmer*, 1948 ; *Gunn et Marshall*, 1957). Alors que la vapeur d'eau et l'eau nuageuse sont transportées par la dynamique à grande échelle, la précipitation est considérée rester dans la colonne de la grille où elle est créée.

Cinq types de processus sont pris en compte dans le schéma. La condensation/évaporation ainsi que la sublimation sont pris en compte en gardant le schéma de *Le Treut et Li* (1991). Des nouvelles particules peuvent être formées par les processus d'activation d'aérosols en gouttelettes, et de la nucléation pour les cristaux. Des particules peuvent tomber en collision et coalescer. Cela forme de la précipitation par autoconversion et peut causer des transformations entre les différentes espèces d'eau nuageuse et de précipitation. Si des particules givrées sont formées, de nouveaux cristaux sont produits par la formation secondaire de cristaux (*Hallett et Mossop*, 1974). La précipitation tombe et elle peut s'évaporer quand elle tombe à travers de l'air sous-saturé.

Comme mentionné, la condensation/évaporation est traitée suivant *Le Treut et Li* (1991). L'activation des gouttelettes à partir des particules d'aérosols se fait avec la formule de *Twomey* (1959) qui dépend de la concentration en nombre des aérosols en faisant une hypothèse sur la fraction d'aérosols activée à 1% de sursaturation, et de la vitesse du vent vertical. La dernière doit être prise en compte à l'échelle du nuage. Dans le schéma, nous partageons la vitesse verticale en une subsidence dans la partie claire de la maille, et un panache ascendant dans la partie nuageuse, en considérant une subsidence minimale, et en multipliant le vent ascendant par un facteur entre 1 et 2 suivant un chiffre aléatoire. Cette approche est similaire à celle de *Donner et al.* (1997). La nucléation hétérogène des cristaux est prise en compte suivant *Meyers et al.* (1992), et au-dessous des températures locales de moins de –35°C, toutes les gouttelettes gèlent de manière homogène dans le modèle.

Le taux de collision entre deux particules dépend de la différence des vitesses de chute des deux particules, du carré de la somme des diamètres et des concentrations en nombre des deux espèces. La probabilité de coalescence est prise en compte avec un facteur d'efficacité suivant *Rutledge et Hobbs* (1993), et pour l'autoconversion de gouttelettes et des cristaux, la dispersion de la distribution en taille des particules est prise en compte en mettant la vitesse de chute d'une des particules en collision à zéro et en modifiant le facteur d'efficacité en une fonction Heaviside. Pour les particules liquides et les grêlons, on considère des sphères, alors que les cristaux de glace et les flocons de neige sont considérés comme étant hexagonaux. Des particules solides fondent immédiatement quand la température dépasse 0°C. La congélation d'une particule liquide dépend de la présence des noyaux de congélation au-dessus de –32°C, dont la concentration dépend de la température suivant *Meyers et al.* (1992).

L'évaporation de la précipitation est paramétrisée suivant *Boucher et al.*, 1995. Pour prendre en compte l'information sous-maille qui vient de la fraction nuageuse à l'origine de la précipitation, nous estimons une fraction sous-maille de chaque espèce de précipitation qui est modifiée quand de la nouvelle précipitation est formée, quand toute la précipitation est évaporée où transformée ou quand elle tombe.

Résultats

Comme tests unidimensionnels, deux cas de stratocumulus marins et deux cas de cirrus ont été choisis, dont les premiers étaient les cas d'ACE-2 déjà décrits dans le chapitre 4, et les dernières étaient des cas de cirrus du groupe de travail 2 du GCSS, un cas chaud-neutre, et un cas froid-neutre. Pour les cas liquides, le nouveau schéma améliore beaucoup le modèle (figs. 9.4 et 9.4). Le schéma est bien capable de simuler les différences entre le cas pollué et le cas propre. La concentration en nombre des gouttelettes est plus large d'un facteur 5 dans le cas pollué comparé au cas propre, les deux étant en bon accord avec les observations, alors que l'ancien schéma surestimait la concentration dans le cas pollué et la sous-estimait dans le cas propre. La taille des gouttelettes est bien simulée dans le cas propre et un peu surestimée dans le cas pollué où le rayon est quand-même plus petit que dans le cas propre. La colonne d'eau liquide et donc l'épaisseur optique du nuage sont beaucoup mieux simulées par le nouveau schéma que dans l'ancien, qui surestimait les deux quantités de presqu'un ordre de grandeur. Une amélioration importante est la capacité du nouveau schéma de simuler la bruine observée. En accord avec les observations, le schéma simule moins de taux de précipitation dans le cas pollué que dans le cas propre.

Concernant les cas de cirrus, nous avons pu comparer les colonnes de glace simulées par le nouveau schéma à celles simulées par un modèle méso-échelle, Méso-NH, qui contient un schéma complet de microphysique des phases liquide et glace (*Thouron*, 2003). Dans les deux cas, le nouveau schéma du MCG est en bon accord avec le modèle à haute résolution (figs. 9.7 et 9.8).

Des résultats très préliminaires ont été montrés pour le cas 3D (figs. 9.9 et 9.10). La couverture nuageuse est bien simulée en comparaison avec l'ancien schéma et comparé aux observations ISCCP à l'exception d'une surestimation dans l'hémisphère sud et dans les tropiques, et une sous-estimation dans l'hémisphère nord, ce qui est dû à une couverture nuageuse basse trop faible au-dessus des continents. Le forçage radiatif des nuages est surestimé dans le spectre des ondes courtes, alors qu'il est bien simulé dans le spectre des ondes longues. Le taux de précipitation est largement sous-estimé, en particulier au-dessus des continents.

10. Conclusions and perspectives

10.1. Summary and conclusions

A study of the indirect effects of aerosols on radiation through an altering of cloud properties was presented. The main tool used in the study is the general circulation model of the Laboratoire de Météorologie Dynamique (LMDZ GCM). A large part of the study concerned the evaluation of parameterizations in this model using in situ measurements and satellite observations. New parameterizations have been developed and evaluated.

The microphysical scheme of *Boucher et al.* (1995a) along with the empirical link between sulfate aerosol mass and cloud droplet number concentration following *Boucher and Lohmann* (1995) has been implemented in the recent version of the LMDZ model. Comparison with the standard model scheme of clouds and precipitation and an evaluation with satellite data shows the skills of the new scheme in realistic simulation of cloud and precipitation fields.

An intercomparison project, which analyzed results of single-column versions of six different GCMs focused on the evaluation of different parameterizations for the aerosol indirect effects, thereby considering also parameterizations of cloud schemes, microphysics, and radiation. The results of the SCMs were compared to observations from the ACE-2 CLOUDYCOLUMN field study. Concerning the LMDZ SCM, it was noted that the scheme compares well with the other models. Major deficiencies common to the models and evident also for the LMDZ scheme are too large cloud geometrical thicknesses, liquid water paths, and optical thicknesses. From the model intercomparison, it could be concluded that it is probably the too coarse vertical resolution which is responsible for this deficiency. A model with a simple parameterization of vertical subgrid fractional cloudiness gives results somewhat closer to the observations, which suggests that such an approach might be promising. Thus, the development and evaluation of a more comprehensive and realistic scheme for the parameterization of subgrid variability of water is a major part of planned future work. All models severely underestimate the drizzle precipitation by several orders of magnitude. Thus, a microphysics scheme able to simulate drizzle at low liquid water contents would be of importance. The models not being able to realistically simulate the drizzle in neither polluted nor clean cases may imply that the second aerosol indirect effect cannot be well captured by current GCMs. Several sensitivity experiments with the LMDZ scheme reveal the inability of the examined *Boucher and Lohmann* formulae to simulate realistic CDNC for both cases, mainly because it is not sensitive enough to changes in aerosol mass. However, none of the other GCM schemes can unambiguously be identified to be more skillful either, and in particular, even the most comprehensive physically based approaches do not give more realistic results than the rather simple *Boucher and Lohmann* formulae.

A centerpiece of the study was the evaluation of aerosol indirect effects in satellite observations of the POLDER instrument and in the LMDZ GCM. Statistical relationships between the POLDER aerosol index (AI) and effective droplet radius at the top of homogeneous liquid water clouds (CDR) have been established in both model and observations. While there is a systematic underestimation of CDR in the model, the CDR to AI relationship in model and observations compare well. However, a saturation effect at large AI values is found in the observations but not in the model. The relationship has been established for several different fixed liquid water path (LWP) conditions. While the observations show flatter CDR to AI relationships for larger LWPs, the model does not show a coherent dependence of this relationship on LWP. Although some correlation can be found for model-simulated and observed slopes of the CDR to AI relationship for different LWPs and over different geographical regions, the model is not yet too skillful. In a second part of the study a relationship between AI and LWP was established. LWP is found to increase with increasing AI in both model and observations, which is an indication of the existence of the second AIE. This relationship is more pronounced when looking at the northern hemisphere midlatitudes only. Major shortcomings of the model include a too steep increase in LWP for large AI over land, which might be an overestimate of the second AIE or be due to the fact that the model does not include a semi-direct effect of aerosols. The model shows a too steep increase in LWP with increasing AI for small AI values when looking at NH midlatitudes, which might indicate that the autoconversion scheme is too sensitive to changes in CDNC. A modeling study further reveals that the general behaviors of the CDR to AI and LWP to AI relationships are very similar for pre-industrial and present-day conditions. However, the influence of the second AIE is somewhat stronger under present-day conditions.

Having thus validated to a certain degree the modeling of the aerosol indirect effects using the microphysical scheme, the question arises of the impact of aerosol forcings on climate change. A main result of early modeling studies of anthropogenic climate change due to greenhouse gas forcing was that simulated warming was much stronger than observed in the 20th century. In particular, for a period of about 30 years from 1940 to 1970, the global mean surface temperature has been constant rather than increasing. Scientists proposed direct forcing by sulfate aerosols and indirect forcing as an additional anthropogenic forcing counterbalancing part of the greenhouse gas warming. In this study, an analysis of the impacts of both greenhouse gases and sulfate aerosols on the climate of the 1930-1989 period is presented. Three different ensemble simulations were carried out with the LMDZ GCM in a mode forced with observed SST. The first ensemble includes both, greenhouse gas and aerosol forcing, the second, greenhouse gas forcing only, and the third, a control experiment using just the time-varying SST without additional anthropogenic impacts. The impact of greenhouse gases and aerosols on radiation is analyzed, including the indirect impacts via altering of cloud properties. It has been shown that the results for the radiative forcings compare well with results of other modeling studies. We defined in addition to the radiative forcing a "radiative impact" of greenhouse gases and aerosols which we calculate as the difference in radiation fluxes between two scenarios. With this quantity, we analyze the radiative impacts of greenhouse gases and aerosols in the solar and terrestrial spectra, and in clear and cloudy sky conditions. The radiative impact of aerosols is found to be of almost equal magnitude compared to the greenhouse gas radiative impact. However, while the greenhouse gas radiative impact is stronger in cloud free conditions, aerosols have a much larger radiative impact in cloudy conditions. For greenhouse gases, it is found that the LW radiative impact is composed of an increase in greenhouse effect in both, clear and cloudy sky, but a decrease in high-level cloudiness reduces the radiative impact in cloudy conditions. Aerosols have a negligible radiative impact in the LW spectrum. In the solar spectrum, greenhouse gases exert a slightly positive radiative impact due to a reduction in cloudiness. Aerosols cause a largely negative radiative impact in clear sky conditions due to the aerosol direct effect, and in cloudy sky conditions due to the first aerosol indirect effect. Additionally, cloud feedback processes are active, as well as the second aerosol indirect effect. The sum of these two mechanisms is evaluated to be positive in the global mean because of a reduction in high-level cloudiness due to a cloud feedback. For low-level clouds, however, in particular in northern hemisphere midlatitudes, clearly a second aerosol indirect effect can be identified. An increase in low-level cloud lifetime of up to 2 min day^{-1} decade^{-1} can be observed in the zonal mean for the northern hemisphere.

Impacts of greenhouse gases and aerosols on observed trends are evaluated for the different scenarios. Comparing the evolution of global mean land surface temperatures of the three simulations with observations we find a rather good agreement for the trend and variability. Looking at distributions of the linear trends for the 1950 to 1989 period, we find that the scenario including both forcings agrees best with the observations. In particular for the midlatitudes of the Eurasian continent, a cooling is observed, which is not simulated except for the scenario where aerosols are present. A clear trend has been observed for the diurnal temperature range (DTR), which is defined as the difference between daily maximum and minimum temperatures. It has formerly been argued that this may be due to a negative forcing active in the SW spectrum, which thus limits the greenhouse gas warming on daytime but is not active at night. From the scenarios, we find that both greenhouse gases and aerosols result in a decrease in DTR, but that only the simulation including aerosols is able to simulate a DTR decrease of the distribution and magnitude indicated by observations. Further analysis shows that the DTR trend is explained to a large degree by increasing cloudiness due to both forcings, and that for the ensemble simulation including the aerosols, the aerosol direct and indirect effects play an important role as well at least in the midlatitudes of the northern hemisphere. A general conclusion of this study is that aerosols played an important role during the 1930 to 1989 period, having a radiative impact of comparable magnitude as the greenhouse gases. Climate trends in the model are altered by aerosol forcings, being in better agreement with the observations.

The important impacts of both greenhouse gas and aerosol forcings on high-level cloudiness and the resulting implications for climate change identified in the ensemble simulations of the last century highlight once more the importance of a realistic representation of ice cloud processes in GCMs. Further more, recent research indicates that aerosol impacts on cirrus clouds may be important. Finally, the predominant role of ice and mixed-phase clouds clouds for the formation of precipitation is another hint for the importance of ice cloud parameterizations. This makes the determination of the cloud thermodynamic phase a particularly important parameterization of the model. Like most GCMs, LMDZ diagnoses whether condensed water consists of liquid water or ice by local temperature, which is in principle a physically reasonable approach. The scheme uses two parameters, the temperature T_{ice}, below which all cloud water immediately freezes, and the shape of the transition between entirely liquid and ice phases for the range in between T_{ice} and the melting temperature. Observations of cloud phase and cloud top temperature from POLDER satellite data have been averaged to the coarser model grid. In the model, "satellite-like" cloud top properties were calculated using nudged simulations, sampling the POLDER swath, and estimating cloud top properties using a random overlap of fractional clouds in the vertical. Statistical relationships between thermodynamical phase and cloud top temperature have been established in both model and observations. From a multitude of model simulations, the pair of parameters is found for which the phase to temperature relationship matches best the observations. The values found differ from those used previously in LMDZ, but are similar to values in use in other GCMs. Testing the cloud radiative forcing using both the new and old parameterizations, reveals that the cloud fields agree better with the observations for the new parameters than for the arbitrarily chosen values used before.

A microphysical scheme has been developed in the present study which consistently treats microphysical processes of liquid and ice clouds. The scheme uses mixing ratios of water vapor, liquid and ice cloud water, and three different precipitation categories as model variables. For liquid cloud droplets and ice crystals, the number concentrations are used as prognostic variables as well. For the activation of liquid droplets from aerosols, a physically based scheme has been adapted, which uses number concentrations of sulfate, hydrophilic organic carbon, and submicronic sea salt aerosols and the vertical wind speed using some assumptions on the subgrid variability to determine the cloud droplet number concentration (CDNC). For ice clouds, heterogeneous nucleation of crystals is calculated using an empirical supersaturation-dependent formulation. Collection and coalescence processes forming liquid and solid precipitation, and collection and accretion processes causing increase of precipitation particles and transitions between different precipitation categories are treated. Secondary ice production by the Hallett-Mossop process is included by a simple parameterization. Precipitation falls and may evaporate when falling through clear air. The new scheme is evaluated for one-dimensional cases for marine stratocumulus clouds (using the ACE-2 data) and for cirrus clouds (using the GCSS WG2 cases). Very encouragingly, the new scheme improves several shortcomings that were identified for the previous scheme in the study reported in Chapter 4. Cloud droplet number concentration is very well simulated in both cases. Cloud liquid water path and cloud optical thickness are much better simulated by the new scheme, being now in close agreement with the observations. Perhaps most important is the ability of the new scheme to simulate the drizzle observed in the ACE-2 cases. The parameterization simulates very well the difference between the clean and polluted cases, with much more droplets in the polluted case of slightly smaller size, and producing less drizzle. For the cirrus cases, we could compare the ice water path with results from the mesoscale model Meso-NH. It is very well simulated in both cases. Preliminary results of a global scale simulation reveal that still several shortcomings of the new parameterization exist. However, cloudiness already is well simulated at most latitudes, showing not enough cloud cover for northern hemisphere mid and high latitudes, which is due to the too small low level cloud cover over land. Precipitation over continents is strongly underestimated compared to GPCP observations and to a simulation using the microphysical scheme of *Boucher et al.*. Shortwave cloud radiative forcing is overestimated by the new scheme. Longwave cloud radiative forcing, on the other hand, is already very well simulated. This is particularly interesting as it is controlled by the high level ice clouds, which were of main interest by the introduction of the new scheme.

10.2. Perspectives

While some progress has been made since the earliest attempts to quantify the aerosol indirect effects in the mid 1990s, plenty of uncertainties remain. In its latest report, the IPCC (2001) still assesses the level of scientific understanding of the aerosol indirect effects as “very low”, giving a range in the estimate of the global mean radiative forcing due to the first aerosol indirect effect as large as 0 to –2 $\mathrm{Wm^{-2}}$, without fixing a best estimate. For the second aerosol indirect effect, no radiative impact is given at all. Aerosol climate impacts are still very poorly taken into account in climate change simulations (*Anderson et al.*, 2003). The studies of Chapter 4 reveals large uncertainties in aerosol indirect effect modeling in GCMs.

Current research work on the issue of aerosol indirect effects is done using observations and modeling approaches and investigating processes ranging from the microscale to global extension. A large part of this range has been addressed in the present study, while the interest was centered on the large scale and focused on the modeling part. Satellite data from a variety of instruments with a large contribution of data from the innovative POLDER instrument have been used to evaluate the model (Chapters 2, 3 and 8) and to analyze processes related to aerosol indirect effects (Chapter 5). Data from a field study has been used to study the cloud and aerosol processes for a specific case (Chapter 4). Large scale historical observations have been used to investigate the climate change during the 20th century (Chapter 7). The development of the new microphysical parameterization included the interaction with mesoscale models for both adaptation of parameterizations existent in those models and validation of the GCM scheme (Chapter 9).

In future work, the approach which consists of using a variety of observational data, particularly of satellite instruments, and smaller-scale models will be continued.

Short term: Improvement of the new scheme

A long timeseries of ground-based remote sensing radar, lidar, and radiometer measurements of aerosol, cloud and precipitation properties is readily available from the Site Instrumental de Recherche par Télédétection Atmosphérique (SIRTA) near Paris in France. The data will be used to evaluate and improve the new microphysical scheme presented in this study. This will be done firstly by establishing statistical distributions in the observations to be able to compare the one dimensional measurements to the large scale model. Secondly, the mesoscale model Meso-NH which includes a comprehensive liquid and ice microphysical scheme will be used as an intermediate tool to translate the measurements to the scale of a GCM grid box. The focus of this part of the evaluation and development studies will be to evaluate the simulated physical quantities related to the microphysical processes as cloud water, particle concentrations, and sizes. The mesoscale model will also be used to evaluate particular microphysical processes.

A new, comprehensive, and so far unique dataset for cirrus cloud observations from TIROS-N Vertical Sounder (TOVS) satellite measurements has recently been established (*Stubenrauch et al.*, 2003; *Rädel et al.*, 2003). These data will be used to evaluate the ice cloud part of the new microphysical scheme. Particularly, radiative properties will be evaluated using this satellite data, and new approaches for the parameterization of radiative properties of ice clouds will be tested.

Mid-term: A new subgrid-scale scheme using PDFs, use of new satellite data

The development of a new, very promising approach to improve microphysics parameterizations is planned. *Tompkins* (2002) introduced the concept of a prognostic probability density distribution of total water content, with width and skewness treated as prognostic variables in the model and predicted based on turbulence, convection, and microphysics. The use of such a knowledge of subgrid scale distribution of water in the microphysical scheme should largely improve the skill of the parameterizations. Again, the use of mesoscale models and satellite data will be a central tool to develop this new approach, and to evaluate the new parameterizations.

Future work implies as an important component the use of upcoming new satellite measurements. New data are now available for aerosol and cloud properties from the POLDER-2, MODIS, and ENVISAT satellite instruments. More complete data covering larger timescales will soon be available. The data from the first spaceborne lidar and radar instruments on the CALIPSO and CLOUDSAT satellites are also very promising. For the first time global three-dimensional data will be available. A multitude of simultaneous measurements of vertical distributions of aerosol and cloud properties will be available. This is a very promising approach to evaluate and improve the parameterizations of cloud processes and aerosol indirect effects in global scale models.

Long term: Climate change studies

The goal of improvements of global scale modeling is a better understanding of the climate system and a prediction of climate change. Many shortcomings still exist due to which simulations of climate change still give somewhat ambiguous results (see also Chapters 6 and 7). However, the approach of a comprehensive description of cloud microphysics including ice and mixed-phase processes and aerosol indirect effects as developed in the present study and improved by the methods outlined above is promising to reduce the uncertainties related to these processes. Further on, it is expected that the performance of computing hardware will improve. Simulations with a fully coupled Earth System Model including the comprehensive microphysical scheme can thus be carried out. A better resolution of the GCM in both horizontal and vertical directions will further improve the results. Regional scale predictions of climate change become possible, which is of particular importance for the study of aerosol indirect forcings as they are concentrated near the source regions. Aerosol impacts on the hydrological cycle imply feedback processes with other components of the Earth System as vegetation and oceans. Such processes will be studied in simulations of future climate change.

10.3. Conclusions et perspectives : Résumé

Résumé et conclusions

Nous avons présenté une étude des effets indirects des aérosols dans le modèle de grande échelle LMDZ et dans les observations satellitaires. L'outil principal utilisé dans cette étude est le modèle de circulation générale du Laboratoire de Météorologie Dynamique (MCG LMDZ). Le schéma de microphysique de *Boucher et al.* (1995) a été implémenté dans ce modèle, et une comparaison avec la version standard et avec des observations satellitaires montre des très bons résultats pour cette paramétrisation.

Dans un projet de comparaison entre des versions unidimensionnelles de différents modèles de grande échelle et d'évaluation avec des données in-situ de la campagne de mesures ACE-2, le modèle LMDZ avec le schéma de microphysique de *Boucher et al.* donne d'assez bons résultats. Des problèmes majeurs communs à tous les modèles et évidents aussi pour LMDZ sont les épaisseurs géométriques et optiques et la colonne d'eau liquide trop grande. Une des raisons pour cette insuffisance est la résolution verticale trop grossière. Deux modèles avec une meilleure résolution verticale, soit par une paramétrisation sous-maille, soit par un nombre plus élevé de couches, donnent des meilleurs résultats comparés aux autres modèles. Ceci implique que l'approche d'introduire une représentation sous-maille de la variabilité verticale des nuages serait prometteuse pour améliorer le modèle. Un tel travail fait partie des plans pour le futur. Tous les modèles montrent une incapacité à simuler la bruine pour les contenus en eau liquide observés. Ceci peut impliquer que les modèles sont incapables de simuler adéquatement le deuxième effet indirect qui est considéré être le plus fort justement sur les nuages bas qui produisent de la bruine en masses d'air pur, et non plus dans des conditions polluées. Pour l'activation des gouttelettes, on a montré qu'aucun des modèles ni des différentes variantes des formules de *Boucher et Lohmann* (1995) peuvent bien simuler simultanément les deux cas. En particulier, parmi les paramétrisations testées, les schémas physiques n'étaient pas meilleurs que les schémas empiriques.

Une étude centrale de la thèse était l'évaluation des effets indirects à partir des relations statistiques entre propriétés des nuages et aérosols dans les observations satellitales de POLDER et dans le modèle LMDZ. La relation entre le rayon effectif des gouttelettes (CDR en anglais) au sommet des nuages et l'indice des aérosols (AI) est une indication du premier effet indirect. La taille des gouttelettes est systématiquement sous-estimée dans le modèle. Pourtant, la relation CDR-AI dans le modèle est similaire à celle des observations, à l'exception du fait que dans les observations, on trouve une corrélation moins forte pour les AI élevés que pour les petits AI, alors que dans le modèle, la relation reste la même pour tous les AI. En séparant les situations de colonne d'eau liquide (LWP en anglais) à peu près fixes, nous avons pu nous rapprocher plus strictement la définition de l'effet indirect des aérosols par Twomey (1974). Pourtant, la relation calculée en moyennant sur des différents relations à LWP fixe n'est pas très différente comparée à celle qui considère toutes les situations. En corrélant la pente de la relation CDR-AI au LWP pour lequel elle a été établie, on trouve dans les observations des relations plus fortes pour les petits LWP. Au-dessus des continents, des pentes légèrement positives sont mêmes trouvées pour des LWP élevés. Dans le modèle, une telle dépendance n'est pourtant pas identifiable. Les pentes de la relation CDR-AI et dans les observations POLDER et dans le modèle pour des différents LWP et pour des différentes régions sont dans la gamme des valeurs données par d'autres auteurs. Dans une deuxième partie, la relation entre la colonne en eau liquide et l'indice des aérosols a été établie. A la fois dans les observations et dans le modèle, une corrélation positive a été trouvée, qui est pourtant plus marquée au-dessus des moyennes latitudes de l'hémisphère nord qu'en considérant tout le globe. La pente de la relation est un peu trop forte dans le modèle, ce qui pourrait indiquer une surestimation du deuxième effet indirect ou être dû au fait que le modèle n'inclut pas l'effet semi-direct des aérosols. Les relations CDR-AI et LWP-AI sont très similaires dans des conditions pré-industrielles et dans les conditions actuelles dans le modèle, ce qui montre la persistance des principes physiques sous jacentes. Pourtant, on trouve un faible effet du deuxième effet indirect additionnel dû aux aérosols anthropiques.

Avec un modèle comprenant le schéma de microphysique et le lien entre aérosols et nuages ainsi validé, on est capable d'examiner les impacts des aérosols sur le changement climatique. Nous avons effectué des simulations pour la période historique de 1930 à 1989, pour laquelle des observations du changement climatique suggèrent un impact probable des forçages par les aérosols anthropiques. Nous avons fait trois ensembles de simulations dont chacun contenait trois membres. Tous les simulations étaient forcés par des températures de la surface de la mer (SST en anglais) et extension de la glace de mer observées. Le premier scénario, nommé GHG+AER, contenait des gaz à effet de serre et des distributions des aérosols de sulfates changeants selon des émissions historiques. Dans le deuxième, GHG, les aérosols étaient fixés à une distribution pré-industrielle, et dans le troisième, CTL, les gaz à effet de serre étaient fixés à des valeurs pré-industrielles aussi. L'impact radiatif des gaz à effet de serre est trouvé être plus fort dans les conditions de ciel clair que de ciel nuageux. Une réduction de la couverture nuageuse due à l'effet de serre anthropique est observée, qui implique une réduction du forçage dans le spectre des ondes longues, et un impact radiatif positif dans le spectre solaire. L'impact radiatif des aérosols est aussi fort que celui par les gaz à effet de serre, mais de signe opposé. L'impact des aérosols est pourtant plus fort en ciel nuageux qu'en ciel clair, où seulement l'effet direct des aérosols est actif, et il joue sur le spectre solaire seulement. En ciel nuageux, outre le premier effet indirect, le deuxième effet indirect est un forçage négatif important. Pourtant, dans l'hémisphère sud et dans les tropiques, il est contrebalancé par une rétroaction des nuages qui consiste en une réduction de la couverture nuageuse haute qui implique un forçage positif dans le spectre solaire due à une réduction de l'albédo des nuages hauts. Pour la période 1950 à 1990, nous avons comparé les impacts des différents forçages sur les tendances de la température des surfaces continentales et sur l'écart journalier de la température (DTR en anglais) au-dessus des continents pour l'été de l'hémisphère nord où les impacts des aérosols anthropiques sont estimées être les plus forts. Alors que pour la plupart des régions du globe, les tendances de températures et du DTR sont contrôlées par la SST imposée, on trouve que les tendances négatives de température au-dessus des moyennes latitudes du continent eurasiatique ne peuvent être expliquées par le modèle que dans le scénario qui contient les forçages anthropiques des gaz à effet de serre et des aérosols. Pareillement, les tendances de DTR diffèrent le plus parmi les scénarios au-dessus des moyennes latitudes de l'hémisphère nord, où aussi c'est le forçage par les deux, gaz à effet de serre et aérosols sulfates anthropiques combinés, qui explique le mieux les tendances observéss. En corrélant les tendances des différentes quantités dans les sorties du modèle, on a pu montrer que dans le modèle, la diminution du DTR est expliquée par les tendances dans le flux du rayonnement dans le spectre des ondes courtes, qui sont largement contrôlés par les tendances dans le forçage radiatif des nuages et par les forçages des aérosols au cas où ils sont inclus (scénario GHG+AER). Contrairement à d'autres études, l'évaporation ne semble pas jouer pas un rôle déterminant dans notre modèle pour la réduction du DTR.

Comme il a été montré par ces études, et comme il est suggéré par d'autres raisons comme le réalisme physique, la représentation de la phase glace dans un modèle de grande échelle est d'une grande importance. Nous avons étudié la paramétrisation qui distribue l'eau condensée dans le modèle en eau liquide et en glace à partir de la température locale en utilisant des observations satellitaires de POLDER. Dans ce but, nous avons établi des relations statistiques entre la température et la phase thermodynamique au sommet des nuages dans la même manière dans les observations et dans plusieurs simulations avec le modèle en variant les deux paramètres qui contrôlent la température au-dessous de laquelle l'eau liquide n'existe plus ($T_{\rm ice}$) et l'exposant de la fonction de transition entre cette température et celle, au-dessus de laquelle toute l'eau est fondue. Les deux paramètres trouvés sont de –32°C et 1.7. Ils diffèrent de ceux utilisés dans la version standard du modèle, mais sont proches des valeurs utilisées dans d'autres modèles. Le forçage radiatif des nuages n'est pas changé dans le spectre des ondes longues en choisissant le nouveau jeu de paramètres au lieu de l'ancien, et il est beaucoup amélioré dans le spectre des ondes courtes.

Un nouveau schéma microphysique a été développé qui traite les phases liquides et glace de manière consistante. Il utilise les rapports de mélange de la vapeur d'eau, de l'eau liquide et glace des nuages ainsi que de trois différentes espèces de précipitation, et les concentrations en nombre des gouttelettes et des cristaux de glace comme des variables du modèle. Pour l'activation des gouttelettes à partir des aérosols, une paramétrisation physique a été introduite. Le nouveau schéma donne des résultats encourageants dans des tests sur les cas unidimensionnels. Pour les cas de stratocumulus marins d'ACE-2, il simule beaucoup mieux les concentrations des gouttelettes, les épaisseurs optiques des nuages et la bruine observés que l'ancien schéma. Il est ainsi sous beaucoup d'aspects meilleurs que les autres paramétrisations testées et présentées dans le chapitre 4. Dans le cas de cirrus, le nouveau schéma est capable de simuler le contenu intégréen glace des nuages aussi bien qu'un modèle de méso-échelle avec un schéma complet de microphysique. Des résultats préliminaires tridimensionnels relèvent pourtant encore des déficiences. Alors que la couverture nuageuse et le forçage radiatif des nuages dans le spectre des ondes longues sont assez bien simulés, il y a encore des problèmes avec le forçage radiatif dans le spectre des ondes courtes et dans la précipitation.

Perspectives

Alors qu'il y a eu des avancées scientifiques depuis les premiers essais de quantifier les forçages indirects des aérosols dans les années 1990, une multitude d'incertitudes persistent. Dans son dernier rapport, le GIEC (IPCC en anglais) jugent toujours le niveau de la compréhension scientifique des effets indirects des aérosols d'être ≪ bas≫ ou même ≪ très bas≫ . Pour le premier effet indirect, des valeurs sont données dans un écart aussi grand que 0 à –2 Wm^{-2}, alors que pour le deuxième effet indirect aucune valeur n'est donnée du tout.

Le travail de recherche récent dans le domaine des effets indirects des aérosols se fait en s'appuyant sur des approches de modélisation et d'observations, étudiant des processus de la micro-échelle jusqu'à des extensions globales. Une grande partie de ce domaine a été traitée dans cette thèse, alors que l'intérêt était centré sur la modélisation et sur la grande échelle. Des données satellitaires de plusieurs instruments avec une importante contribution de l'instrument POLDER ont été utilisées pour l'évaluation du modèle et pour des études de processus. Des données de campagnes de mesures ont été utilisées pour évaluer des processus de nuages et d'aérosols dans des cas spécifiques. Des observations historiques à grande échelle ont été utilisées pour étudier le changement climatique pendant le 20ième siècle. Le développement d'une nouvelle paramétrisation de la microphysique des nuages a impliqué l'interaction avec des modèles de méso-échelle afin d'adapter des paramétrisations existantes dans de tels modèles et pour l'évaluation du MCG.

Cette approche d'utiliser une variété de données d'observations, en particulier des instruments satellitaires, ainsi que des modèles de plus petite échelle, doit être poursuivie dans les travaux futurs.

A court terme, le nouveau schéma doit être évalué et amélioré en utilisant des données de télédétection à partir du sol ainsi que des données satellitaires. Le Site Instrumental de Recherche par Télédétection Atmosphérique (SIRTA) à Palaiseau à proximité de Paris fournit des données d'instruments radar, lidar, et radiomètres desquels des quantités physiques d'aérosols, nuages et précipitation peuvent être déduites. Des distributions statistiques des quantités vont être établies pour utiliser les données unidimensionnelles pour l'évaluation du modèle à grande échelle, et puis un modèle intermédiaire à méso-échelle va être introduit pour pouvoir utiliser les données du SIRTA. Cette étude sera focalisée sur l'évaluation et le développement des quantités physiques simulées liées aux processus microphysiques comme le contenu en eau des nuages ou la concentration et la taille de particules. Le modèle à méso-échelle sera également utilisé pour évaluer les processus microphysiques.

Un nouveau, complet, et jusqu'à présent unique jeu de données d'observations de cirrus de TOVS a été récemment établi. Ces données pourront être utilisées afin d'évaluer la partie glace du nouveau schéma. En particulier, les propriétés radiatives peuvent être évaluées, et des nouvelles approches pour leur paramétrisation seront examinées.

A moyen terme, une paramétrisation de la variabilité sous-maille de l'eau doit être développée en poursuivant l'approche de *Tompkins* (2002) qui a introduit une fonction de probabilité de densité, dont la variance et l'inclinaison sont prédites en fonction de la turbulence, de la convection et de la microphysique. La connaissance de la variabilité sous-maille de la distribution de l'eau pourrait largement améliorer le degré de réalisme des processus microphysiques. Pour le développement et l'amélioration d'un tel schéma, de nouveau, des observations satellitaires ainsi que des modèles à méso-échelle vont être utilisés.

Concernant les données satellitaires, des nouveaux instruments vont fournir des jeux de données plus complets et pour une période plus longue, comme MODIS et les instruments d'ENVISAT. De plus d'ici quelque temps, les observations d'un radar sur CLOUDSAT et d'un lidar sur CALIPSO vont pouvoir fournir en quelque sorte des données tridimensionnelles, ce qui va largement améliorer les possibilités d'évaluation et de développement des modèles à grande échelle.

A long terme enfin, un modèle avec des paramétrisations des nuages, de la précipitation et des interactions aérosols - nuages ainsi améliorées accompagné d'un développement de la puissance des ordinateurs et des techniques de calcul, permettront des études plus poussées du changement climatique. Avec un modèle du système terrestre comprenant la dynamique de l'océan et des surfaces continentales comme il est développé à l'IPSL, des simulations de scénarios pour le changement climatique des 20ièmes et 21ièmes siècles vont pouvoir être effectuées. Les résultats vont être examinés en se focalisant sur les aspects régionaux du changement climatique pour lesquels les forçages par les aérosols jouent un rôle important, ainsi que sur le cycle hydrologique. Le dernier point implique une étude du couplage entre les différents sous-systèmes du système climatique, dont l'atmosphère mais aussi l'océan, les surfaces continentales et la végétation sont des composantes importantes.

A. Abbreviation and notation list

A.1. Abbreviations

ACE Aerosol Characterization Experiment

ADE Aerosol Direct Effect

ADEOS ADvanced Earth Observation Satellite

AIE Aerosol Indirect Effect

AOT Aerosol Optical Thickness

AVHRR Advanced Very High Resolution Radiometer

BL Planetary Boundary Layer

CCM Community Climate Model

CCN Cloud Condensation Nuclei

CCSR Center for Climate System Research

CDNC Cloud Droplet Number Concentration

CDR Cloud Droplet Radius

CGT Cloud Geometrical Thickness

CNES Centre National d'Études Spatiales

C.N.R.S. Centre National de Recherche Scientifique

COT Cloud Optical Thickness

CRM Cloud Resolving Model

CSIRO Commonwealth Scientific and Industrial Research Organization

CSU Colorado State University

CTM Chemistry Transport Model

DJF December-January-February

ECHAM ↑ECMWF-HAMburg ↑GCM

ECMWF European Centre for Medium-Range Weather Forecasting

ERBE Earth Radiation Budget Experiment

ESM Earth System Model

FIRE.ACE First ↑ISCCP Regional Experiment - Arctic Cloud Experiment

GCM General Circulation Model

GCSS ↑GEWEX Cloud System Study

GEWEX Global Energy and Water Cycle Experiment

GHE GreenHouse Effect

GHG GreenHouse Gases

GISS Goddard Institute for Space Studies

IDRIS Institut de Développement et des Resources en Informatique Scientifique

IFS Integrated Forecasting System

INCA INteraction with Chemistry and Aerosols

INDOEX Indian Ocean Experiment

IPCC Intergovernmental Panel on Climate Change

IPSL Institut Pierre Simon Laplace

ISCCP International Satellite Cloud Climatology Project

ITCZ Inner Tropical Convergence Zone

JJA June-July-August

LES Large Eddy Simulation model

LGGE Laboratoire de Glaciologie et Géophysique de l'Environnement

LMD Laboratoire de Météorologie Dynamique

LMDZ ↑LMD-Zoom ↑GCM

LOA Laboratoire d'Optique Atmosphérique

LODyC Laboratoire d'Océanographie Dynamique et du Climatologie

LSCE Laboratoire des Sciences du Climat et de l'Environnement

LW Longwave

LWP Liquid Water Path

MAST Monterey Area Ship Track experiment

NCAR National Center for Atmospheric Research

NH Northern Hemisphere

OPA Océan Parallélisé

ORCHIDEE Organizing Carbon and Hydrology In Dynamic EcosystEms

PACE Parameterization of the Aerosol Climatic Effects

PDF Probability Density Function

PNNL Pacific Northwest National Laboratory

POLDER POLarization and Directionality of the Earth's Reflectances

PPH Plane-Parallel Homogeneity

PW Precipitable Water

RACE Radiation, Aerosol, and Cloud Experiment

RAMS Regional Atmospheric Modeling Section

RH Relative Humidity

SA Service d'Aéronomie

ScaRaB Scanner of the Earth Radiation Budget

SCM Single-Column Model

SH Southern Hemisphere

SST Sea Surface Temperature

SW Shortwave

TIROS Television Infrared Observation Satellite

TOA Top Of the Atmosphere

TOVS ↑TIROS-N Operational Vertical Sounder

TRMM Tropical Rainfall Measuring Mission

A.2. Notation list

α Albedo (often also used for parameter constants)

$\alpha\tau$ POLDER aerosol index

A_l Activation rate of cloud droplets, [m^{-3} s^{-1}]

A_i Nucleation rate of ice crystals, [m^{-3} s^{-1}]

c_p Specific heat of dry air at constant pressure, 1004.64 J kg^{-1} K^{-1}

D_j Effective diameter of cloud or precipitation species j, [m]

D_v Coeff. of vapor diffusion in air, [m^2 s^{-1}]

ϵ Emissivity

E_{jk} Collision efficiency between species j and k

e_{sat} Saturation vapor pressure, [hPa]

ΔF Radiative forcing, [Wm^{-2}]

f Cloud fraction of grid cell

$f_{\textsf{act}}$ Fraction of $\mathrm{N_{CCN}}$ activated

F_{rs} Freezing rate of rain drops to form snow, [m^{-3} s^{-1}]

F_{li} Freezing rate of liquid water droplets to form ice crystals, [m^{-3} s^{-1}]

g Asymmetry parameter

H Cloud geometrical thickness, [m]

I Radiative impact, [Wm^{-2}]

k Exponent in droplet activation

λ Climate sensitivity parameter, [K W^{-1} m^2]

λ_j Slope of size distribution of species j, [m^{-1}]

L_v Latent heat of vaporization of water, 2.501×10^6 J kg^{-1}

L_s Latent heat of sublimation of water, 2.834×10^6 J kg^{-1}

L_f Latent heat of freezing of water, 0.333×10^6 J kg^{-1}

m_j Mass of particle of species j, [kg]

m_a Initial mass of activated droplets, [kg]

m_0 Initial mass of nucleated ice crystals, 10^{-12} kg

N_j Number concentration of species j, [m^{-3}]

N_{CCN} Number concentration of CCN, [m^{-3}]

N_{IN} Number concentration of IN, [m^{-3}]

N_{IC} Number concentration of contact-freezing nuclei, [m^{-3}]

N_a Number concentration of aerosols, [m^{-3}]

n_{HM} Rate of formation of ice splinter by Hallett-Mossop-process, [kg^{-1}]

ω_0 Single scattering albedo

P_j Rate of precipitation of species j, [m s^{-1}]

Δq Parameter in Condensation scheme (“ratqs”), [kg kg^{-1}]

q_t Total water mixing ratio, [kg kg^{-1}]

q_c Condensed water mixing ratio, [kg kg^{-1}]

q_j Mixing ratio of species j, [kg kg^{-1}]

$q_{sat,j}$ Saturation vapor mixing ratio w.r.t. species j, [kg kg^{-1}]

ρ_{air} Air density, [kg m^{-3}]

ρ_j Density of precipitation species j, [kg m^{-3}]

r Correlation coefficient

r_0 Minimum radius for autoconversion, 0.8×10^{-5} m

r_{dv} Volume-mean cloud droplet radius, [m]

r_e Cloud droplet effective radius, [m]

r_{jk} Collision rate between species j and k, [m^{-3} s^{-1}]

σ Stefan-Boltzmann constant, 0.67 10^{-8} J K^{-4} m^{-2} s-1

S_j Supersaturation w.r.t. species j

T Temperature, [K]

T_s Surface emperature, [K]

T_0 Freezing temperature of water, 273.15 K

T_i Temperature, below which no supercooled water exists, 258.15 K

t Time, [s]

Δt Time step [s]

$\bar{V}_j$ Terminal fall speed of cloud or precipitation species j, [m s^{-1}]

w Updraft speed, [m s^{-1}]

$x_{\textsf{ice}}$ Ice mass fraction in a cloud

Δz Layer thickness, [m]

Indexes

v Water vapor

l Liquid water cloud droplets

i Ice crystals

r Rain water

g Graupel

s Snow

Bibliography

Abdul-Razzak, H., and S. J. Ghan, A parametrization of aerosol activation: 2. Multiple aerosol types, *J. Geophys. Res.*, *105*, 6837–6844, 1999.

Abdul-Razzak, H., S. J. Ghan, and C. Rivera-Carpio, A parametrization of aerosol activation: 1. Single aerosol type, *J. Geophys. Res.*, *103*, 6123–6131, 1998.

Ackerman, A. S., O. Toon, D. E. Stephens, A. J. Heymsfield, V. Ramanathan, and E. J. Welton, Reduction of tropical cloudiness by soot, *Science*, *288*, 1042–1047, 2000a.

Ackerman, A. S., O. B. Toon, J. P. Taylor, D. W. Johnson, P. V. Hobbs, and R. J. Ferek, Effects of aerosols on cloud albedo: Evaluation of Twomey's parameterization of cloud susceptibility using measurements of ship tracks, *J. Atmos. Sci.*, *57*, 2684–2695, 2000b.

Albrecht, B. A., Aerosols, cloud microphysics, and fractional cloudiness, *Science*, *245*, 1227–1230, 1989.

Anderson, T. L., R. J. Charlson, S. E. Schwartz, R. Knutti, O. Boucher, H. Rodhe, and J. Heintzenberg, Climate forcing by aerosols - a hazy picture, *Science*, *300*, 1103–1104, 2003.

Bartlett, J. T., The growth of cloud droplets by coalescence, *Q. J. R. Meteorol. Soc.*, *92*, 93–104, 1966.

Beheng, K. D., A parametrization of warm cloud microphysical conversion processes, *Atmos. Res.*, *33*, 193–206, 1994.

Bergeron, T., *On the physics of cloud and precipitation*, Procès-verbaux des séances de l'association de météorologie, Union Géodésique et Géophysique Internationale, Lisbon, 1933.

Bony, S., and K. A. Emanuel, A parameterization of the cloudiness associated with cumulus convection; evaluation using TOGA COARE data, *J. Atmos. Sci.*, *58*, 3158–3183, 2001.

Boucher, M., and J. Quaas, Testing and developing cloud parametrisations in the LMDZ GCM by using POLDER satellite data, *Geophys. Res. Lett.*, *submitted*, 2003.

Boucher, O., Aircraft can increase cirrus cloudiness, *Nature*, *397*, 30–31, 1999.

Boucher, O., and T. L. Anderson, General circulation model assessment of the sensitivity of direct climate forcing by anthropogenic sulfate aerosols to aerosol size and chemistry, *J. Geophys. Res.*, *100*, 26,117–26,134, 1995.

Boucher, O., and J. Haywood, On summing the components of radiative forcing of climate change, *Clim. Dyn.*, *18*, 297–302, 2001.

Boucher, O., and U. Lohmann, The sulfate–CCN–cloud albedo effect - a sensitivity study with two general circulation models, *Tellus*, *47B*, 281–300, 1995.

Boucher, O., and M. Pham, History of sulfate aerosol radiative forcings, *Geophys. Res. Lett.*, *29*, 1308, doi:10.1029/2001GL014048, 2002.

Boucher, O., H. Le Treut, and M. B. Baker, Precipitation and radiation modeling in a general circulation model: Introduction of cloud microphysical processes, *J. Geophys. Res.*, *100*, 16,395–16,414, 1995a.

Boucher, O., Z.-X. Li, and H. Le Treut, Introduction du schéma de convection de Tiedtke dans les MCGs du LMD, *Tech. rep.*, Laboratoire de Météorologie Dynamique, Paris, 20pp, 1995b.

Boucher, O., M. Pham, and C. Venkataraman, Simulation of the atmospheric sulfur cycle in the Laboratoire de Météorologie Dynamique general circulation model. Model description, model evaluation, and global and European budgets, in *Note scientifique de l'IPSL*, vol. 23, edited by J.-P. Boulanger and Z.-X. Li, IPSL, Paris, 26pp., 2002.

Brenguier, J.-L., Parameterization of the condensation process: A theoretical approach, *J. Atmos. Sci.*, *48*, 264–282, 1991.

Brenguier, J.-L., P. Chuang, Y. Fouquart, D. W. Johnson, F. Parol, H. Pawlowska, J. Pelon, L. Schüller, F. Schröder, and J. Snider, An overview of the ACE–2 CLOUDYCOLUMN closure experiment, *Tellus*, *52B*, 815–827, 2000a.

Brenguier, J.-L., H. Pawlowska, L. Schüller, R. Preusker, J. Fischer, and Y. Fouquart, Radiative properties of boundary layer clouds: Droplet effective radius versus number concentration, *J. Atmos. Sci.*, *57*, 803–821, 2000b.

Brenguier, J.-L., H. Pawlowska, and L. Schüller, Cloud microphysical and radiative properties for parameterization and satellite monitoring of the indirect effect of aerosol on climate, *J. Geophys. Res.*, *108*, 8632, doi:10.1029/2002JD002682, 2003.

Bréon, F.-M., and S. Colzy, Global distribution of cloud droplet effective radius from POLDER polarization measurements, *Geophys. Res. Lett.*, *27*, 4065–4068, 2000.

Bréon, F.-M., and P. Goloub, Cloud droplet effective radius from spaceborne polarization measurements, *Geophys. Res. Lett.*, *25*, 1879–1882, 1998.

Bréon, F.-M., D. Tanré, and S. Generoso, Aerosol effect on cloud droplet size monitored from satellite, *Science*, *295*, 834–838, 2002.

Buriez, J. C., C. Vanbauce, F. Parol, P. Goloub, M. Herman, B. Bonnel, Y. Fouquart, P. Couvert, and G. Sèze, Cloud detection and derivation of cloud properties from POLDER, *Int. J. Remote Sensing*, *18*, 2785–2813, 1997.

Calahan, R. F., Bounded cascade clouds: albedo and effective thickness, *Nonlin. Proc. Geoph.*, *1*, 156–167, 1994.

Carlin, B., Q. Fu, U. Lohmann, G. D. Mace, K. Sassen, and J. M. Comstock, High-cloud horizontal inhomogeneity and solar albedo bias, *J. Clim.*, *15*, 2321–2339, 2002.

Cess, R. D., G. Potter, J. P. Blanchet, G. Boer, A. Genio, M. Dequé, V. Dymnikov, V. Galin, W. Gates, S. Ghan, T. Kiehl, A. Lacis, H. Le Treut, Z. Li, X.-Z. Liang, B. McAvaney, V. Meleshko, J. Mitchell, J.-J. Morcrette, D. Randall, L. Rikus, E. Roeckner, J. Roer, U. Schlese, D. Sheinin, A. Slingo, A. Sokolov, K. E. Taylor, W. Washington, R. T. Wetherald, I. Yagai, and M.-H. Zhang, Intercomparison and interpretation of climate feedback processes in nineteen atmospheric general circulation models, *J. Geophys. Res.*, *95*, 16,601–16,615, 1990.

Cess, R. D., M.-H. Zhang, G. L. Potter, H. W. Barker, R. A. Colman, D. A. Dazlich, A. D. Del Genio, M. Esch, J. R. Fraser, V. Galin, W. Gates, J. J. Hack, W. J. Ingram, J. T. Kiehl, A. A. Lacis, H. Le Treut, Z.-X. Li, X.-Z. Liang, J.-F. Mahfouf, B. J. McAvaney, V. P. Meleshko, J.-J. Morcrette, D. A. Randall, E. Roeckner, J.-F. Royer, A. P. Sokolov, P. V. Sporyshev, K. E. Taylor, W.-C. Wang, and R. T. Wetherald, Uncertainties in carbon dioxide radiative forcing in atmospheric general circulation models, *Science*, *262*, 1252–1255, 1993.

Chameides, W. L., C. Luo, R. Saylor, D. Streets, Y. Huang, M. Bergin, and F. Giorgi, Correlation between model-calculated anthropogenic aerosols and satellite-derived cloud optical depths: Indication of indirect effect?, *J. Geophys. Res.*, *107*, 4085, doi:10.1029/2000JD000208, 2002.

Charlson, R. J., J. E. Lovelock, M. O. Andreae, and S. G. Warren, Sulphate aerosols and climate, *Nature*, *340*, 437–438, 1989.

Charlson, R. J., J. H. Seinfeld, A. Nenes, M. Kulmala, A. Laaksonen, and M. C. Faccini, Reshaping the theory of cloud formation, *Science*, *292*, 2025–2026, 2001.

Cheinet, S., The parameterization of clear and cloudy convective boundary layers, Ph.D. thesis, Ecole Polytechnique, Palaiseau, 139pp., 2002.

Cheinet, S., A multiple mass-flux parameterization for the surface-generated convection. Part I: Dry plumes, *J. Atmos. Sci.*, *60*, 2313–2327, 2003.

Cheinet, S., and J. Teixara, A simple formulation for the eddy-diffusivity parameterization of cloud-topped boundary layers, *Geophys. Res. Lett.*, *30*, 1930, doi:10.1029/2003GL017377, 2003.

Chuang, C. C., J. E. Penner, K. E. Taylor, A. S. Grossman, and J. J. Walton, An assessment of the radiative effects of anthropogenic sulfate, *J. Geophys. Res.*, *102*, 3761–3778, 1997.

Coakley, Jr., J. A., and C. D. Walsh, Limits to the aerosol indirect radiative effect derived from observations of ship tracks, *J. Atmos. Sci.*, *59*, 668–680, 2002.

Coakley Jr., J. A., R. L. Bernstein, and P. A. Durkee, Effect of ship-track effluents on cloud reflectivity, *Science*, *237*, 1020–2022, 1987.

Coakley Jr., J. A., P. A. Durkee, K. Nielsen, J. P. Taylor, S. Platnick, B. A. Albrecht, D. Babb, F.-L. Chang, W. R. Tahnk, C. S. Bretherton, and P. V. Hobbs, The appearance and disappearance of ship tracks on large spatial scales, *J. Atmos. Sci.*, *57*, 2765–2778, 2000.

Conover, J. H., Anomalous cloud lines, *J. Atmos. Sci.*, *23*, 778–785, 1966.

Conover, W. J., *Practical Nonparametric Statistics*, 2nd ed., John Wiley and Sons, New York, 493pp., 1980.

Cusack, S., J. M. Edwards, and R. Kershaw, Estimating the subgrid variance of saturation, and its parameterization for use in a GCM cloud scheme, *Q. J. R. Meteorol. Soc.*, *125*, 2057–3076, 1999.

Dai, A., A. D. Del Genio, and I. Y. Fung, Clouds, precipitation and temperature range, *Nature*, *368*, 665–666, 1997.

Dai, A., K. E. Trenberth, and T. R. Karl, Effects of clouds, soil moisture, and water vapor on diurnal temperature range, *J. Clim.*, *12*, 2451–2473, 1999.

Dai, A., T. M. L. Wigley, B. A. Boville, J. T. Kiehl, and L. E. Buja, Climates of the twentieth and twenty-first centuries simulated by the NCAR climate system model, *J. Clim.*, *14*, 485–519, 2001.

de Rosnay, P., J. Polcher, M. Bruen, and K. Laval, Impact of a physically based soil water flow and soil-plant interaction representation for modeling large scale land surface processes, *J. Geophys. Res.*, *107*, 4118, doi:10.1029/2001JD000634, 2002.

Del Genio, A. D., M.-S. Yao, W. Kovari, and K. K.-W. Lo, A prognostic cloud water parameterization for global climate models, *J. Clim.*, *9*, 270–304, 1996.

DeMott, P. J., K. Sassen, M. R. Poellot, D. Baumgardner, D. C. Rogers, S. D. Brooks, A. J. Prenni, and S. M. Kreidenweis, African dust aerosols as atmospheric ice nuclei, *Geophys. Res. Lett.*, *14*, 1732, doi:10.1029/2003GL017410, 2003.

Deschamps, P., F. Bréon, M. Leroy, A. Podaire, A. Bricaud, J. Buriez, and G. Sèze, The POLDER mission: Instrument characteristics and scientific objectives, *IEEE Trans. Geosc. Rem. Sens.*, *32*, 598–615, 1994.

Deuzé, J.-L., M. Herman, P. Goloub, D. Tanré, and A. Marchand, Characterization of aerosols over ocean from POLDER/ADEOS-1, *Geophys. Res. Lett.*, *26*, 1421–1424, 1999.

Deuzé, J. L., P. Goloub, M. Herman, A. Marchand, G. Perry, S. Susana, and D. Tanré, Estimate of the aerosol properties over the ocean with POLDER, *J. Geophys. Res.*, *105*, 15,329–15,346, 2000.

Deuzé, J. L., F. M. Bréon, C. Devaux, P. Goloub, M. Herman, B. Lafrance, F. Maignan, A. Marchand, F. Nadal, G. Perry, and D. Tanré, Remote sensing of aerosols over land surfaces from POLDER- ADEOS-1 polarized measurements, *J. Geophys. Res.*, *106*, 4913–4926, 2001.

Di Giuseppe, F., The effect of unresolved vertical cloud structure on radiative transfer calculations, *EGS/AGU/EUG Joint Assembly, 6 - 11th April 2003, Nice, France*, 2003.

Donner, L. J., C. J. Seman, B. J. Soden, R. S. Hemler, J. C. Warren, and J. S. K.-N. Liou, Large-scale ice clouds in the GFDL SKYHI general circulation model, *J. Geophys. Res.*, *102*, 21,745–21,768, 1997.

Doutriaux-Boucher, M., J.-C. Buriez, G. Brogniez, L. C.-Labonnote, and A. J. Baran, Sensitivity of retrieved POLDER directional cloud optical thickness to various ice particle models, *Geophys. Res. Lett.*, *27*, 109–112, 2000.

Dufresne, J.-L., C. Gautier, P. Ricchiazzi, and Y. Fouquart, Longwave scattering effects of mineral aerosols, *J. Atmos. Sci.*, *59*, 1959–1966, 2002.

Durkee, P. A., R. E. Chartier, A. Brown, E. J. Trehubenko, S. D. Rogerson, C. Skupniewicz, K. E. Nielsen, S. Platnick, and M. D. King, Composite ship track characteristics, *J. Atmos. Sci.*, *57*, 2542–2553, 2000.

Easterling, D. R., B. Horton, P. D. Jones, T. C. Peterson, T. R. Karl, D. E. Parker, M. J. Salinger, V. Razuvayev, N. Plummer, P. Jamason, and C. K. Folland, Maximum and minimum temperature trends for the globe, *Science*, *277*, 364–367, 1997.

Emanuel, K., A scheme for representing cumulus convection in large–scale models, *J. Atmos. Sci.*, *48*, 2313–2335, 1991.

Feichter, J., U. Lohmann, and I. Schult, The atmospheric sulfur cycle in ECHAM-4 and its impact on the shortwave radiation, *Clim. Dyn.*, *13*, 235–246, 1997.

Feingold, G., Modeling of the first indirect effect: Analysis of measurement requirements, *Geophys. Res. Lett.*, *30*, 1997, doi:10.1029/2003GL017967, 2003.

Feingold, G., L. A. Remer, J. Ramaprasad, and Y. J. Kaufman, Analysis of smoke impact on clouds in Brazilian biomass burning regions: An extension to Twomey's approach, *J. Geophys. Res.*, *106*, 22,907–22,922, 2001.

Feingold, G., W. L. Eberhard, D. E. Veron, and M. Previdi, First measurements of the Twomey indirect effect using ground-based remote sensers, *Geophys. Res. Lett.*, *30*, 1287, doi: 10.1029/2002GL016633, 2003.

Fitzgerald, J. W., Dependence of the supersaturation spectrum of CCN on aerosol size distribution and composition, *J. Atmos. Sci.*, *30*, 628–634, 1973.

Flatau, P. J., G. J. Tripoli, J. Verlinde, and W. R. Cotton, *The CSU-RAMS cloud microphysics module: General theory and documentation*, *Atmos. Sci. Paper*, vol. 451, Dept. Atmos. Sci., Colorado State University, Fort Collins, Colorado, 88pp., 1989.

Folland, C. K., T. R. Karl, J. R. Christy, R. A. Clarke, G. V. Gruza, J. Jouzel, M. E. Mann, J. Oerlemans, M. J. Salinger, and S.-W. Wang, Observed climate variability and change, in *Climate change 2001 – The scientific basis. Contribution of working group I to the Third Assessment Report of the Intergovernmental Panel on Climate Change*, edited by J. T. Houghton, Y. Ding, D. J. Griggs, M. Noguer, P. J. van der Linden, X. Dai, K. Maskell, and C. A. Johnson, pp. 99–182, Cambridge University Press, Cambridge, 2001.

Fouquart, Y., and B. Bonnel, Computations of solar heating of the Earth's atmosphere: A new parameterization, *Contr. Atmos. Phys.*, *53*, 35–62, 1980.

Fowler, L. D., D. A. Randall, and S. A. Rutledge, Liquid and ice cloud microphysics in the CSU general circulation model. Part I: Model description and simulated microphysical processes, *J. Clim.*, *9*, 489–529, 1996.

Georgii, H.-W., *Über die Eiskeimbildung in unterkühlten Wolken in ihrer Abhängigkeit von atmoshärischem Aerosol*, *Berichte des Deutschen Wetterdienstes*, vol. 58, Deutscher Wetterdienst, Offenbach, 43pp., 1959.

Ghan, S. J., L. R. Leung, and R. C. Easter, Prediction of cloud droplet number in a general circulation model, *J. Geophys. Res.*, *102*, 21,777–21,794, 1997a.

Ghan, S. J., L. R. Leung, and Q. Hu, Application of cloud microphysics to NCAR CCM2, *J. Geophys. Res.*, *102*, 16,507–16,527, 1997b.

Ghan, S. J., L. R. Leung, and J. McCaa, A comparison of three different modeling strategies for evaluating coud and radiation parameterizations, *Mon. Weather Rev.*, *127*, 1967–1984, 1999.

Ghan, S. J., R. C. Easter, E. G. Chapman, H. Abdul-Razzak, Y. Zhang, L. R. Leung, N. S. Laulainen, R. D. Saylor, and R. A. Zaveri, A physically based estimate of radiative forcing by anthropogenic sulfate aerosol, *J. Geophys. Res.*, *106*, 5279–5393, 2001.

Giraud, V., O. Thouron, J. Riedi, and P. Goloub, Analysis of direct comparison of cloud top temperature and infrared split window signature against independant retrievals of cloud thermodynamic phase, *Geophys. Res. Lett.*, *28*, 983–986, 2001.

Goloub, P., and O. Arino, Verification of the consistency of POLDER Aerosol Index over land with ASTR-2/ERS-2 fire product, *Geophys. Res. Lett.*, *27*, 899–902, 2000.

Goloub, P., M. Herman, H. Chepfer, J. Riedi, G. Brogniez, P. Couvert, and G. Sèze, Cloud thermodynamical phase classification from the POLDER spaceborne instrument, *J. Geophys. Res.*, *105*, 14,747–14,759, 2000.

Guibert, S., J. Snider, and J.-L. Brenguier, The aerosol activation in marine stratocumulus clouds. 1. Measurement validation for a closure study, *J. Geophys. Res.*, *108*, 8628, doi: 10.1029/2002JD002678, 2003.

Guilyardi, E., and G. Madec, Performance of the OPA/ARPEGE–T21 global ocean-atmosphere coupled model, *Clim. Dyn.*, *13*, 149–165, 1997.

Gunn, K., and J. Marshall, The distribution with size of aggregate snowflakes, *J. Meteorol.*, *15*, 452–461, 1957.

Hallett, J., and S. Mossop, Production of secondary ice particles during the riming process, *Nature*, *249*, 26–28, 1974.

Han, Q., W. B. Rossow, and A. A. Lacis, Near–global survey of effective droplet radii in liquid water clouds using ISCCP data, *J. Clim.*, *7*, 465–497, 1994.

Han, Q., W. B. Rossow, J. Chou, and R. M. Welch, Global survey of the relationship of cloud albedo and liquid water path with droplet size using ISCCP, *J. Clim.*, *11*, 1516–1528, 1998.

Han, Q., W. B. Rossow, J. Zeng, and R. Welch, Three different behaviours of liquid water path of water clouds in aerosol-cloud interactions, *J. Atmos. Sci.*, *59*, 726–736, 2002.

Hansen, J., M. Sato, and R. Ruedy, Radiative forcing and climate response, *J. Geophys. Res.*, *102*, 6831–6864, 1997.

Hansen, J. E., M. Sato, and R. Ruedy, Long-term changes of the diurnal temperature cycle: Implications about mechanisms of global climate change, *Atmos. Res.*, *37*, 175–209, 1995.

Hartmann, D. L., and M. L. Michelsen, No evidence for iris, *Bull. Am. Meteorol. Soc.*, *83*, 249–254, 2003.

Hauglustaine, D. A., F. Hourdin, L. Jourdain, M.-A. Filiberti, S. Walters, and J.-F. Lamarque, Interactive chemistry in the Laboratoire de Météorologie Dynamique general circulation model: Description and background tropospheric chemistry evaluation, *J. Geophys. Res.*, *submitted*, 2003.

Haywood, J. M., and O. Boucher, Estimates of the direct and indirect radiative forcing due to tropospheric aerosols: A review, *Rev. of Geophysics*, *38*, 513–543, 2000.

Haywood, J. M., and S. R. Osborne, The effect of overlying absorbing aerosol layers on remote sensing retrievals of cloud effective radius and cloud optical depth, *Q. J. R. Meteorol. Soc.*, *submitted*, 2003.

Heymsfield, A. J., and L. J. Donner, A scheme for parameterizing ice–cloud water content in general circulation models, *J. Atmos. Sci.*, *47*, 1865–1877, 1990.

Hocking, L. M., The collision efficiency of small drops, *Q. J. R. Meteorol. Soc.*, *85*, 44–50, 1959.

Hogan, R. J., and A. J. Illingworth, Deriving cloud overlap statistics from radar, *Q. J. R. Meteorol. Soc.*, *126*, 2903–2910, 2000.

Houze, R. A., *Cloud Dynamics*, 573 pp., Academic Press, San Diego, 1993.

Hudson, J. G., and S. S. Yum, Maritime-continental drizzle contrasts in small cumuli, *J. Atmos. Sci.*, *58*, 915–926, 2001.

Huffman, G., R. Adler, P. Arkin, A. Chang, R. Ferraro, A. Gruber, J. Janowiak, A. McNab, B. Rudolf, and U. Schneider, The Global Precipitation Climatology Project (GPCP) combined precipitation data set, *Bull. Am. Meteorol. Soc.*, *78*, 5–20, 1997.

Jakob, C., and S. A. Klein, The role of vertically varying cloud fraction in the parametrization of microphysical processes in the ECMWF model, *Q. J. R. Meteorol. Soc.*, *125*, 941–965, 1999.

Johnson, D. B., The role of giant and ultragiant aerosol particles in warm rain initiation, *J. Atmos. Sci.*, *39*, 448–460, 1982.

Jones, A., and A. Slingo, Predicting cloud–droplet effective radius and indirect sulphate aerosol forcing using a general circulation model, *Q. J. R. Meteorol. Soc.*, *122*, 1573–1595, 1996.

Jones, A., D. Roberts, and A. Slingo, A climate model study of indirect radiative forcing by anthropogenic sulphate aerosols, *Nature*, *370*, 450–453, 1994.

Jones, A., D. L. Roberts, M. J. Woodage, and C. E. Johnson, Indirect aerosol forcing in a climate model with an interactive sulphur cycle, *Tech. Rep. 25*, Hadley Centre, Bracknell, 34pp., 2001.

Jones, P. D., and A. Moberg, Hemispheric and large-scale surface air temperature variations: An extensive revision and an update to 2001, *J. Clim.*, *16*, 206–223, 2003.

Junge, C., and E. McLaren, Relationship of cloud nuclei spectra to aerosol size distribution and composition, *J. Atmos. Sci.*, *28*, 382–390, 1971.

Kandel, R., M. Viollier, P. Raberanto, J.-P. Duvel, L. A. Pakhomov, V. A. Golovko, A. P. Trishchenko, J. Mueller, E. Raschke, R. Stuhlmann, and the International ScaRaB Scientific Working Group (ISSWG), The ScaRaB earth radiation budget dataset, *Bull. Am. Meteorol. Soc.*, *79*, 765–783, 1998.

Kärcher, B., and U. Lohmann, A parameterization of cirrus cloud formation: Homogeneous freezing of supercooled aerosols, *J. Geophys. Res.*, *108*, 4698, doi:10.1029/2002JD003220, 2003.

Karl, T. R., P. D. Jones, R. W. Knight, G. Kukla, N. Plummer, V. Razuvayev, K. P. Gallo, J. Lindesay, R. J. Charlson, and T. C. Peterson, Asymmetric trends of daily minimum and maximum temperature, *Bull. Am. Meteorol. Soc.*, *74*, 1007–1023, 1993.

Kaufman, Y., and R. S. Fraser, The effect of smoke particles on clouds and climate forcing, *Science*, *277*, 1636–1639, 1997.

Kaufman, Y. J., and T. Nakajima, Effect of Amazon smoke on cloud microphysics and albedo - analysis from satellite imagery, *J. Appl. Meteorol.*, *32*, 729–744, 1993.

Kawamoto, K., and T. Nakajima, Seasonal variation of cloud particle size as derived from AVHRR remote sensing, *Geophys. Res. Lett.*, *30*, 1810, doi: 10.1029/2003GL017437, 2003.

Kessler, E., *On the Distribution and Continuity of Water Substance in Atmospheric Circulation*, *Meteorological Monographs*, vol. 10, Mass, Boston, 84pp., 1969.

Khairoutdinov, M., and Y. Kogan, A new cloud physics parameterization in a large-eddy simulation model of marine stratocumulus, *Mon. Weather Rev.*, *128*, 229–243, 2000.

Kiehl, J. T., and K. E. Trenberth, Earth's annual global mean energy budget, *Bull. Am. Meteorol. Soc.*, *78*, 197–208, 1997.

Krinner, G., Impact of lakes and wetlands on boreal climate, *J. Geophys. Res.*, *108*, 4520, doi: 10.1029/2002JD002597, 2003.

Kristjánsson, J. E., Studies of the aerosol indirect effect from sulfate and black carbon aerosols, *J. Geophys. Res.*, *107*, 4246, doi:10.1029/2001JD000887, 2002.

Kristjánsson, J. E., J. M. Edwards, and D. L. Mitchell, A new parametrization scheme for the optical properties of ice crystals for use in general circulation models of the atmosphere, *Phys. Chem. Earth*, *24*, 231–236, 1999.

Le Treut, H., and Z.-X. Li, Sensitivity of an atmospheric general circulation model to prescribed SST changes: Feedback effects associated with the simulation of cloud optical properties, *Clim. Dyn.*, *5*, 175–187, 1991.

Le Treut, H., and B. McAvaney, A model intercomparison of equilibrium climate change in response to CO_2 doubling, in *Note scientifique de l'IPSL*, vol. 18, edited by J.-P. Boulanger and Z.-X. Li, IPSL, Paris, 27pp., 2002.

Le Treut, H., M. Forichon, O. Boucher, and Z.-X. Li, Sulfate aerosol indirect effect and CO_2 greenhouse forcing: Equilibrium response of the LMD GCM and associated cloud feedbacks, *J. Clim.*, *11*, 1673–1684, 1998.

Le Van, P., Description de directives pour l'utilisation de la nouvelle dynamique du modèle de circulation générale, *Tech. Rep. 147*, Laboratoire de Météorologie Dynamique du C.N.R.S., Paris, 1989.

Li, Z.-X., Ensemble atmospheric GCM simulation of climate interannual variability from 1979 to 1994, *J. Clim.*, *12*, 986–1001, 1999.

Liepert, B. G., and U. Lohmann, A comparison of surface observations and ECHAM4–GCM experiments and its relevance to the indirect aerosol effect, *J. Clim.*, *14*, 1078–1091, 2001.

Lin, B., B. A. Wielicki, L. H. Chambers, Y. Hu, and K.-M. Xu, The iris hypothesis: A negative or positive cloud feedback?, *J. Clim.*, *15*, 3–7, 2002.

Lindzen, R., M.-D. Chou, and A. Hou, Does the earth have an adaptive infrared iris?, *Bull. Am. Meteorol. Soc.*, *82*, 417–432, 2001.

Liu, J. Y., and H. D. Orville, Numerical modeling of precipitation and cloud shadow effects on mountain-induced cumuli, *J. Atmos. Sci.*, *26*, 1283–1298, 1969.

Locatelli, J. D., and P. V. Hobbs, Fallspeed and masses of solid precipitation particles, *J. Geophys. Res.*, *79*, 2185–2197, 1974.

Lock, A. P., A. R. Brown, M. R. Bush, G. M. Martin, and R. N. B. Smith, A new boundary layer mixing scheme. Part I: Scheme description and single-column model tests, *Mon. Weather Rev.*, *128*, 3187–3199, 2000.

Lohmann, U., A glaciation indirect aerosol effect caused by soot aerosols, *Geophys. Res. Lett.*, *29*, 1052, doi:10.1029/2001GL014357, 2002a.

Lohmann, U., Possible aerosol effects on ice clouds via contact nucleation, *J. Atmos. Sci.*, *58*, 647–656, 2002b.

Lohmann, U., and B. Kärcher, First interactive simulations of cirrus clouds formed by homogeneous freezing in the ECHAM GCM, *J. Geophys. Res.*, *107*, 4105, doi:10.1029/2001JD000767, 2002.

Lohmann, U., and G. Lesins, Stronger constraints on the anthropogenic indirect aerosol effect, *Science*, *298*, 1012–1015, 2003a.

Lohmann, U., and G. Lesins, Comparing continental and oceanic cloud susceptibilities to aerosols, *Geophys. Res. Lett.*, *30*, 1791, doi: 10.1029/2003GL017828, 2003b.

Lohmann, U., and E. Roeckner, Design and performance of a new cloud microphysics scheme developed for the ECHAM general circulation model, *Clim. Dyn.*, *12*, 557–572, 1996.

Lohmann, U., J. Feichter, C. C. Chuang, and J. E. Penner, Prediction of the number of cloud droplets in the ECHAM GCM, *J. Geophys. Res.*, *104*, 9169–9198, 1999.

Lohmann, U., J. Feichter, J. Penner, and R. Leaitch, Indirect effect of sulfate and carbonaceous aerosols: A mechanistic treatment, *J. Geophys. Res.*, *105*, 21,193–12,206, 2000a.

Lohmann, U., G. Tselioudis, and C. Tyler, Why is the cloud albedo - particle size relationship different in optically thick and optically thin clouds?, *Geophys. Res. Lett.*, *27*, 1099–1102, 2000b.

Marshall, J. S., and W. M. Palmer, The distribution of raindrops with size, *J. Meteorol.*, *5*, 165–166, 1948.

Martin, G. M., D. W. Johnson, and A. Spice, The measurement and parameterization of effective radius of droplets in warm stratocumulus clouds, *J. Atmos. Sci.*, *51*, 1823–1842, 1994.

Maynard, K., and J. Polcher, Impact of land-surface processes on the interannual variability of tropical climate in the LMD GCM, *Clim. Dyn.*, *20*, 613–633, 2002.

Meerkötter, R., U. Schumann, D. R. Doelling, P. Minnis, T. Nakajima, and Y. Tsushima, Radiative forcing by contrails, *Ann. Geophysicæ*, *17*, 1080–1094, 1999.

Menon, S., A. D. Del Genio, D. Koch, and G. Tselioudis, GCM simulations of the aerosol indirect effect: Sensitivity to cloud parameterization and aerosol burden, *J. Atmos. Sci.*, *59*, 692–713, 2002.

Menon, S., J.-L. Brenguier, O. Boucher, P. Davison, A. D. Del Genio, J. Feichter, S. Ghan, S. Guibert, X. Liu, U. Lohmann, H. Pawlowska, J. E. Penner, J. Quaas, D. L. Roberts, L. Schüller, and J. Snider, Evaluating cloud-aerosol process parameterizations with single column models and ACE-2 cloudy column observations, *J. Geophys. Res.*, *in press*, 2003.

Meyers, M. P., P. DeMott, and W. Cotton, New primary ice–nucleation parameterizations in an explicit cloud model, *J. Appl. Met.*, *31*, 708–721, 1992.

Mitchell, J. F. B., D. J. Karoly, G. C. Hegerl, F. W. Zwiers, M. R. Allen, and J. Marengo, Detection of climate change and attribution of causes, in *Climate change 2001 – The scientific basis. Contribution of working group I to the Third Assessment Report of the Intergovernmental Panel on Climate Change*, edited by J. T. Houghton, Y. Ding, D. J. Griggs, M. Noguer, P. J. van der Linden, X. Dai, K. Maskell, and C. A. Johnson, pp. 695–738, Cambridge University Press, Cambridge, 2001.

Morcrette, J.-J., Evaluation of model–generated cloudiness: Satellite–observed and model–generated diurnal variability of brightness temperature, *Mon. Weather Rev.*, *119*, 1205–1224, 1991.

Mossop, S. C., The origin and concentration of ice crystals in clouds, *Bull. Am. Meteorol. Soc.*, *66*, 264–273, 1985.

Myhre, G., A. Myhre, and F. Stordal, Historical evolution of radiative forcing of climate, *Atmos. Environ.*, *35*, 2361–2373, 2001.

Nakajima, T., A. Higurashi, K. Kawamoto, and J. E. Penner, A possible correlation between satellite-derived cloud and aerosol microphysical parameters, *Geophys. Res. Lett.*, *28*, 1171–1174, 2001.

Novakov, T., and J. E. Penner, Large contribution of organic aerosols to cloud–condensation–nuclei concentrations, *Nature*, *365*, 823–826, 1993.

Parol, F., J. Descloitres, and Y. Fouquart, Cloud optical thickness and albedo retrievals from bidirectional reflectance measurements of POLDER instruments during ACE-2, *Tellus*, *52B*, 888–908, 2000.

Pawlowska, H., and J.-L. Brenguier, Microphysical properties of stratocumulus clouds during ACE–2, *Tellus*, *52B*, 868–887, 2000.

Pawlowska, H., and J.-L. Brenguier, An observational study of drizzle formation in stratocumulus clouds for general circulation model (GCM) parameterizations, *J. Geophys. Res.*, *108*, 8630, doi: 10.1029/2002JD002679, 2003.

Pawlowska, H., J.-L. Brenguier, and L. Schüller, Microphysical and radiative properties of stratocumulus, *Phys. Chem. Earth*, *24*, 927–932, 1999.

Peng, Y., U. Lohmann, R. Leaitch, C. Banic, and M. Couture, The cloud albedo-cloud droplet effective radius relationship for clean and polluted clouds from RACE and FIRE.ACE, *J. Geophys. Res.*, *107*, 4106, doi:10.1029/2000JD000281, 2002.

Peterson, T. C., T. R. Karl, P. F. Jamason, R. Knight, and D. R. Easterling, First difference method: Maximizing station density for the calculation of long-term global temperature change, *J. Geophys. Res.*, *103*, 25,967–25,974, 1998.

Pincus, R., and S. A. Klein, Unresolved spatial variability and microphysical process rates in large–scale models, *J. Geophys. Res.*, *105*, 27,059–27,065, 2000.

Planton, S., and B. Spagnoli, Quand la simulation numérique reproduit et explique le réchauffement des nuits d'été, *La Météorologie*, *42*, 4–5, 2003.

Pontikis, C. A., and E. M. Hicks, Droplet activation as related to entrainment and mixing in warm tropical maritime clouds, *J. Atmos. Sci.*, *50*, 1888–1896, 1993.

Pruppacher, H. R., and J. D. Klett, *Microphysics of Clouds and Precipitation*, 954 pp., Kluwer Academic Press, Dordrecht, 1997.

Quaas, J., Kopplung eines Atmosphärenmodells und eines Ozeanmodells auf einem Meta-Computer, Master's thesis, Institut für Geophysik und Meteorologie der Universität zu Köln, 90pp., 2000.

Quaas, J., O. Boucher, and F.-M. Bréon, Aerosol-cloud interactions in POLDER satellite data and in the LMDZ GCM, *J. Geophys. Res.*, *submitted*, 2003a.

Quaas, J., O. Boucher, J.-L. Dufresne, and H. Le Treut, Impacts of greenhouse gases and aerosol direct and indirect effects on clouds and radiation in atmospheric GCM simulations of the 1930-1989 period, *Clim. Dyn.*, *submitted*, 2003b.

Quaas, J., O. Boucher, J.-L. Dufresne, and H. Le Treut, Relative importance of greenhouse gas and aerosol forcings for climate trends of the 1950-1989 period in atmospheric GCM simulations, *J. Clim.*, *submitted*, 2003c.

Rädel, G., C. J. Stubenrauch, R. Holz, and D. L. Mitchell, Retrieval of effective ice crystal size in the infrared: Sensitivity study and global measurements for TIROS-N Operational Vertival Sounder, *J. Geophys. Res.*, *108*, 4281, doi: 10.1029/2002JD002801, 2003.

Ramanathan, P. Crutzen, J. Lelieveld, A. P. Mitra, D. Althausen, J. Anderson, M. O. Andreae, W. Cantrell, G. R. Cass, C. E. Chung, A. D. Clarke, J. A. Coakley Jr., W. D. Collins, W. C. Conant, F. Dulac, B. J. Heintzenberg, A. J. Heymsfield, B. Holben, S. Howell, C. J. Hudson, A. Jayaraman, J. T. Kiehl, T. N. Krishnamurti, D. D. Lubin, G. McFarquhar, T. Novakov, J. Ogren, E. I. A. Poddorny, K. Prather, K. Priestly, J. M. Prospero, F. P. K. Quinn, K. Rajeev, P. Rasch, S. Rupert, R. Sadourny, G. S. K. Satheesh, G. E. Shaw, P. Sheridan, and F. P. J. Valero, Indian Ocean Experiment: An integrated analysis of the climate forcing and effects of the great Indo-Asian haze, *J. Geophys. Res.*, *106*, 28,371–28,398, 2001a.

Ramanathan, V., P. J. Crutzen, J. T. Kiehl, and D. Rosenfeld, Aerosols, climate, and the hydrological cycle, *Science*, *294*, 2119–2124, 2001b.

Ramaswamy, V., O. Boucher, J. Haigh, D. Hauglustaine, J. Haywood, G. Myhre, T. Nakajima, G. Y. Shi, and S. Solomon, Radiative forcing of climate change, in *Climate change 2001 – The scientific basis. Contribution of working group I to the Third Assessment Report of the Intergovernmental Panel on Climate Change*, edited by J. T. Houghton, Y. Ding, D. J. Griggs, M. Noguer, P. J. van der Linden, X. Dai, K. Maskell, and C. A. Johnson, pp. 349–416, Cambridge University Press, Cambridge, 2001.

Rasch, P. J., and J. E. Kristjánsson, A comparison of the CCM3 model using diagnosed and predicted condensate parameterizations, *J. Clim.*, *11*, 1587–1614, 1998.

Rayner, N. A., D. E. Parker, E. B. Horton, C. K. Folland, L. V. Alexander, D. P. Rowell, E. C. Kent, and A. Kaplan, Global analyses of SST, sea ice and night marine air temperature since the late nineteenth century, *J. Geophys. Res.*, *108*, 4407, doi: 10.1029/2002JD002670, 2003.

Reddy, M. S., and O. Boucher, A study of the global cyle of carbonaceous aerosols in the LMDZT general circulation model, *J. Geophys. Res.*, *submitted*, 2003.

Reid, J. S., P. V. Hobbs, A. L. Rangno, and D. A. Hegg, Relationshiphs between cloud droplet effective radius, cloud liquid water content, and droplet concentration for warm clouds in Brazil embedded in biomass smoke, *J. Geophys. Res.*, *104*, 6145–6153, 1999.

Reynolds, R. W., and T. M. Smith, A high-resolution global sea surface temperature climatology, *J. Clim.*, *8*, 1571–1583, 1995.

Riedi, J., M. Doutriaux-Boucher, P. Goloub, and P. Couvert, Global distribution of cloud top phase from POLDER/ADEOS I, *Geophys. Res. Lett.*, *27*, 1707–1710, 2000.

Rosenfeld, D., TRMM observed first direct evidence of smoke from forest fires inhibiting rainfall, *Geophys. Res. Lett.*, *26*, 3105–3108, 1999.

Rosenfeld, D., Suppression of rain and snow by urban and industrial air pollution, *Science*, *287*, 1793–1796, 2000.

Rosenfeld, D., and I. M. Lensky, Satelite–base insights into precipitation formation processes in continental and maritime convective clouds, *Bull. Am. Meteorol. Soc.*, *79*, 2457–2476, 1998.

Rossow, W. B., and R. Schiffer, ISCCP cloud data products, *Bull. Am. Meteorol. Soc.*, *72*, 2–20, 1991.

Rotstayn, L. D., A physically based scheme for the treatment of stratiform clouds and precipitation in large–scale models. I: Description and evaluation of the microphysical processes, *Q. J. R. Meteorol. Soc.*, *123*, 1227–1282, 1997.

Rotstayn, L. D., On the "tuning" of autoconversion parameterizations in climate models, *J. Geophys. Res.*, *105*, 15,495–15,507, 2000.

Rotstayn, L. D., and J. E. Penner, Indirect aerosol forcing, quasi–forcing and climate response, *J. Clim.*, *14*, 2960–2975, 2001.

Rutledge, S., and P. Hobbs, The mesoscale and microscale structure and organization of clouds and precipitation in midlatitude cyclones. VIII: A model for the "seeder–feeder" process in warm–frontal rainbands, *J. Atmos. Sci.*, *40*, 1185–1206, 1983.

Sassen, K., and G. C. Dodd, Homogeneous nucleation rate for highly supercooled cirrus cloud droplets, *J. Atmos. Sci.*, *45*, 1357–1369, 1988.

Schüller, L., J.-L. Brenguier, and H. Pawlowska, Retrieval of microphysical, geometrical, and radiative properties of marine stratocumulus from remote sensing, *J. Geophys. Res.*, *108*, 8631, doi: 10.1029/2002JD002680, 2003.

Schwartz, S. E., Harshvardhan, and C. M. Benkovitz, Influence of anthropogenic aerosol on cloud optical depth and albedo shown by satellite measurements and chemical transport modeling, *Proc. Nat. Acad. Sci. USA*, *99*, 1784–1789, 2002.

Sexton, D. M. H., H. Grubb, K. P. Shine, and C. K. Folland, Design and analysis of climate model experiments for the efficient estimation of anthropogenic signals, *J. Clim.*, *16*, 1320–1336, 2003.

Slingo, A., A GCM parameterization for the shortwave radiative properties of water clouds, *J. Atmos. Sci.*, *42*, 1419–1427, 1989.

Slingo, J. M., The development and verification of a cloud prediction scheme for the ECMWF model, *Q. J. R. Meteorol. Soc.*, *113*, 899–927, 1987.

Smith, L. D., and D. A. Randall, *Parameterization of Cloud Microphysical Processes in the CSU General Circulation Model*, *Atmos. Sci. Papers*, vol. 491, Department of Atmospheric Sciences, Colorado State University, Colorado, 58pp., 1992.

Smith, R. N., A scheme for predicting layer clouds and their water content in a general circulation model, *Q. J. R. Meteorol. Soc.*, *116*, 435–460, 1990.

Snider, J. R., and J.-L. Brenguier, Cloud condensation nuclei and cloud droplet measurements during ACE–2, *Tellus*, *52B*, 828–842, 2000.

Sommeria, G., and J. W. Deardorff, Subgrid-scale condensation models of non-precipitating clouds, *J. Atmos. Sci.*, *34*, 344–355, 1977.

Spagnoli, B., S. Planton, M. Déqué, O. Mestre, and J.-M. Moisselin, Detecting climate change at a regional scale: The case of France, *Geophys. Res. Lett.*, *29*, 1450, doi:10.1029/2001GL014619, 2002.

Spice, A., D. W. Johnson, P. R. A. Brown, A. G. Darlison, and C. P. R. Saunders, Primary ice nuceleation in orographic cirrus clouds: A numerical simulation of the microphysics, *Q. J. R. Meteorol. Soc.*, *125*, 1637–1667, 1999.

Squires, P., An estimate of the anthropogenic production of cloud nuclei, *J. Rech. Atmos.*, *2*, 297–308, 1966.

Stephens, G. L., Radiation profiles in extended water clouds. II: Parameterization schemes, *J. Atmos. Sci.*, *35*, 2123–2132, 1978.

Stone, D. A., and A. J. Weaver, Factors contributing to diurnal temperature range trends in twentieth and twenty-first century simulations of the CCCma coupled model, *Clim. Dyn.*, *20*, 435–445, doi:10.1007/s00382-002-0288-y, 2003.

Stubenrauch, C., A. D. Del Genio, and W. B. Rossow, Implementation of subgrid cloud vertical structure inside a GCM and its effect on the radiation budget, *J. Clim.*, *10*, 273–287, 1997.

Stubenrauch, C. J., F. Eddounia, and G. Rädel, Correlations between microphysical properties of large-scale semi-transparent cirrus and the state of the atmosphere using satellite TIROS-N Operational Vertical Sounder observations and ECMWF ERA-40 reanalyses, *Atmos. Res.*, *submitted*, 2003.

Suhre, K., V. Crassier, C. Mari, R. Rosset, D. Johnson, S. Osborne, R. Wood, M. Andreae, B. Bandy, and T. Bates, Chemistry and aerosols in the marine boundary layer: 1-D modelling of the three ACE-2 Lagrangian experiments, *Atmos. Environ.*, *34*, 5079–5094, doi:10.1016/S1352-2310(00)00221-1, 2000.

Sun, B., and R. S. Bradley, Solar influences on cosmic rays and cloud formation: A reassessment, *J. Geophys. Res.*, *107*, 4211, doi:10.1029/2001JD000560, 2002.

Sundqvist, H., A parameterization scheme for non–convective condensation including prediction of cloud water content, *Q. J. R. Meteorol. Soc.*, *104*, 677–690, 1978.

Svensmark, H., and E. Friis-Christensen, Variation of cosmic ray flux and global cloud coverage - a missing link in solar-climate relationships, *J. Atmos. Sol.-Terr. Physics*, *59*, 1225–1232, 1997.

Takemura, T., H. Okamoto, A. Numaguti, A. Higurashi, and T. Nakajima, Global three-dimensional simulation and radiative forcing of various aerosol species, in *Current Problems in Atmospheric Radiation*, edited by W. L. Smith and Y. M. Timofeyev, IRS 2000, pp. 733–736, A. Deepak Publishing, 2000.

Tanré, D., F.-M. Bréon, J. L. Deuzé, M. Herman, P. Goloub, F. Nadal, and A. Marchand, Global observation of anthropogenic aerosols from satellite, *Geophys. Res. Lett.*, *28*, 4555–4558, 2001.

Taylor, J. P., M. D. Glew, J. A. Coakley Jr., W. R. Tahnk, S. Platnick, P. V. Hobbs, and R. J. Ferek, Effects of aerosols on the radiative properties of clouds, *J. Atmos. Sci.*, *57*, 2656–2670, 2000.

Tetens, O., Über einige meteorologische Begriffe, *Zeitschrift für Geophysik*, *6*, 297–309, 1930.

Thouron, O., Développement d'un schéma microphysique adapté à la modélisation des cirrus à méso-échelle. Apport des instruments de télédétection active pour sa validation, Ph.D. thesis, Université des Sciences et Technologies (Lille I), Lille, 130pp., 2003.

Tiedtke, M., A comprehensive mass flux scheme for cumulus parameterization in large-scale models, *Mon. Weather Rev.*, *117*, 1779–1800, 1989.

Tompkins, A., A prognostic parameterization for the subgrid-scale variability of water vapor and clouds in large-scale model and its use to diagnose cloud cover, *J. Atmos. Sci.*, *59*, 1917–1942, 2002.

Travis, D. J., A. M. Carleton, and R. G. Lauritsen, Contrails reduce daily temperature range, *Nature*, *418*, 601, 2002.

Trenberth, K. (Ed.), *Climate System Modeling*, 788 pp., Cambridge University Press, 1995.

Tripoli, G. J., and W. R. Cotton, A numerical investigation of several factors contributing to the observed variable intensity of deep convection over South Florida, *J. Appl. Meteorol.*, *19*, 1037–1063, 1980.

Twomey, S., The nuclei of natural cloud formation. Part II: The supersaturation in natural clouds and the variation of cloud droplet concentration, *Geofis. Pura Appl.*, *43*, 243–249, 1959.

Twomey, S., Pollution and the planetary albedo, *Atmos. Environ.*, *8*, 1251–1256, 1974.

United Nations, United nations framework convention on climate change, Available on http://unfccc.int/resource/docs/convkp/conveng.pdf, 25pp., 1992.

United Nations, Report of the world summit on sustainable development, Available on http://www.un.org/jsummit/, 173pp., 2002.

Vali, G., Atmospheric ice nucleation: A review, *J. Rech. Atmos.*, *19*, 105–115, 1985.

Vanbauce, C., J. C. Buriez, F. Parol, B. Bonnel, G. Sèze, and P. Couvert, Apparent pressure derived from ADEOS–POLDER observations in the oxygen a–band over ocean, *Geophys. Res. Lett.*, *25*, 3159–3162, 1998.

Verant, S., K. Laval, J. Polcher, and M. Castro, Sensitivity of the continental hydrological cycle to the spatial resolution over the Iberian peninsula, *J. Hydrometeorology*, *submitted*, 2003.

Webb, M., C. Senior, S. Bony, and J.-J. Morcrette, Combining ERBE and ISCCP data to assess clouds in the Hadley Centre, ECMWF and LMD atmospheric climate models, *Clim. Dyn.*, *17*, 905–922, 2001.

Wetzel, M. A., and L. L. Stowe, Satellite-observed patterns in stratus microphysics, aerosol optical thickness, and shortwave radiative forcing, *J. Geophys. Res.*, *104*, 31,287–31,299, 1999.

White, P. W., IFS Documentation. Part IV: Physical processes (CY25R1), *Tech. rep.*, ECMWF, Reading, 166pp., 2002.

Wigley, T. M. L., Possible climate change due to SO_2-derived cloud condensation nuclei, *Nature*, *339*, 365–367, 1989.

Williams, K. D., A. Jones, D. L. Roberts, C. A. Senior, and M. J. Woodage, The response of the climate system to the indirect effects of anthropogenic sulfate aerosol, *Clim. Dyn.*, *17*, 845–856, 2001.

Wilson, D., and S. Ballard, Microphysically based precipitation scheme for the UK meteorological office unified model, *Q. J. R. Meteorol. Soc.*, *125*, 1607–1636, 1999.

Wobrock, W., A. I. Flossmann, M. Monier, J.-M. Pichon, L. Cortez, J.-F. Fournol, A. Schwarzenböck, S. Mertes, J. Heintzenberg, P. Laj, G. Orsi, L. Ricci, S. Fuzzi, H. T. Brink, P. Jongejan, and R. Otjes, The Cloud Ice Mountain Experiment (CIME) 1998: experiment overview and modelling of the microphysical processes during the seeding by isentropic gas expansion, *Atmos. Res.*, *58*, 231–265, doi:10.1016/S0169-8095(01)00094-1, 2001.

Wood, R., P. R. Field, and W. R. Cotton, Autoconversion rate bias in stratiform boundary layer cloud parameterizations, *Atmos. Res.*, *65*, 109–128, 2002.

Young, K. C., A numerical simulation of wintertime, orographic precipitation: Part I. Description of model microphysics and numerical techniques, *J. Atmos. Sci.*, *31*, 1735–1748, 1974a.

Young, K. C., The role of contact nucleation in ice phase initiation in clouds, *J. Atmos. Sci.*, *31*, 768–776, 1974b.

Ziegler, C. L., Retrieval of thermal and microphysical variables in observed convective storms. Part 1: Model development and preliminary testing, *J. Atmos. Sci.*, *42*, 1487–1509, 1985.

Remerciements

Le soutien par mon directeur de thèse Hervé Le Treut m'a été précieux pour tout mon travail ainsi que pour l'établissement des contacts par les écoles d'été, les collaborations avec des scientifiques externes et les conférences.

Je tiens à remercier mon co-directeur de thèse Olivier Boucher qui a inspiré presque toutes les études, qui m'a repondu dans innombrables méls ou pendant nos réunions à toutes mes questions, et qui m'a appris le fonctionnement du monde scientifique.

Je suis reconnaissant à Jean-Louis Brenguier pour tout son soutien.

Avec Marie Boucher, Surabi Menon, Jean-Louis Dufresne et François-Marie Bréon j'ai collaboré fructueusement, et je leur en remercie.

Pour avoir eu la gentillesse d'être les rapporteurs de ma thèse je remercie Ulrike Lohmann et Yves Fouquart, et également Serge Planton et Michael Schulz d'avoir participé au jury.

L'ensemble de l'équipe de modélisation du LMD m'a accueilli chaleureusement, et je suis très reconnaissant pour tous les conseils pratiques et scientifiques, et pour toute leur amitié.